

Report No. UT-03.32

***IN-SITU TESTS OF THREE
BENTS AT SOUTH TEMPLE
BRIDGE ON INTERSTATE 15 –
FINAL REPORT***

**By: Chris Pantelides, Ph.D.
Lawrence Reaveley, Ph.D.
Jeffrey Duffin
Jon Ward
Chris Delahunty**

**Civil & Environmental
Engineering Department
University of Utah
Salt Lake City, Utah**

**Utah Department of Transportation
Research Division**

June 2003



**Report No.
CVEEN-02/2003**

**IN-SITU TESTS OF THREE BENTS AT
SOUTH TEMPLE BRIDGE ON
INTERSTATE 15 - FINAL REPORT**

by

CHRIS P. PANTELIDES

JEFFREY B. DUFFIN

JON P. WARD

CHRIS A. DELAHUNTY

LAWRENCE D. REAVELEY

**Report to Sponsors:
Utah Department of Transportation**

June 2003

**Civil & Environmental Engineering
College of Engineering
University of Utah
Salt Lake City, Utah**

UDOT RESEARCH & DEVELOPMENT REPORT ABSTRACT

1. Report No. UT-03.32		2. Government Accession No.		3. Recipient's Catalog No.	
4. Title and Subtitle In-Situ Tests of Three Bents at South Temple Bridge on Interstate 15 – Final Report		5. Report Date June 2003			
		6. Performing Organization Code			
7. Author(s) Chris Pantelides, Ph.D. Lawrence Reaveley, Ph.D. Jeffrey Duffin Jon Ward Chris Delahunty		8. Performing Organization Report No. CVEEN-02/2003			
9. Performing Organization Name and Address University of Utah Civil and Environmental Engineering Department 122 So. Central Campus Dr. Rm. 104 Salt Lake City, UT 84112		10. Work Unit No.			
		11. Contract No. 00-9162			
12. Sponsoring Agency Name and Address Utah Department of Transportation Research Division 4501 South 2700 West Salt Lake City, Utah		13. Type of Report and Period Covered			
		14. Sponsoring Agency Code			
15. Supplementary Notes					
16. Abstract <p>The present report describes the test procedures and results of three in-situ full-scale tests carried out in Salt Lake City, Utah in 2000. The tests were carried out on the southbound lanes of the South Temple Bridge at Interstate 15, in Salt Lake City. The first test was carried out on a three- column bridge bent without the road deck (Bent #4S), the second test was carried out on an identical three-column bridge with half the gravity load present from the deck (Bent #5S), and the third test was carried out on Bent #6S, with half the gravity load from the deck, which was seismically retrofitted with carbon fiber reinforced polymer (CFRP) composites. For all three bents, the foundation was retrofitted through a reinforced concrete grade beam overlay and through pinning of the pile caps to the piles. The report provides detailed information on the test setup, the loading scheme used to simulate seismic loads, a description of the condition of the as-is bridge bents, the design of the CFRP composite for seismic retrofit of Bridge Bent #6S, and an assessment of the performance of the three bridge bents. It was found that the grade beam improved the simulated seismic performance of all three bents. For Bent #6S, which had the CFRP composite seismic retrofit in addition to the grade beam, the seismic retrofit goal of increasing the displacement ductility of the bridge by a factor of two was achieved.</p>					
17. Key Words			18. Distribution Statement Available: UDOT Research Division P.O. Box 148410 Salt Lake City, UT 84114-8410 www.udot.utah.gov		
19. Security Classification (of this report) <div style="text-align: center;">N/A</div>	20. Security Classification (of this page) <div style="text-align: center;">N/A</div>	21. No. of Pages <div style="text-align: center;">223</div>	22. Price		

FORWARD

University of Utah Professors Chris P. Pantelides and Lawrence D. Reaveley obtained a research grant from the Utah Department of Transportation (UDOT) for performing a research study regarding the evaluation of capacity and seismic retrofit of three reinforced concrete systems, consisting of a three column bent without a deck and two three-column bents joined by the existing deck. The Southbound lanes of the South Temple Bridge, at Interstate 15 were the site for performing these tests. The tests were performed in April and May of 2000. Two of the bents were retrofitted with a grade beam at the foundation level and the third was also retrofitted with a grade beam but in addition it was reinforced with carbon fiber reinforced polymer (FRP) composites.

Principal investigator for the project was Professor Chris P. Pantelides, and co-principal investigator was Professor Lawrence D. Reaveley of the Department of Civil and Environmental Engineering. Mr. Jeffrey B. Duffin, Mr. Jon Ward, and Mr. Chris Delahunty, graduate students at the Civil and Environmental Engineering Department, were the research assistants for the project.

This document constitutes the Final Report for the project. The UDOT managers for the project were Mr. Samuel Musser, P.E., Research Program Manager, and Daniel Avila, P.E., Development & Implementation Program Manager.

EXECUTIVE SUMMARY

Results from in-situ lateral load tests of three R/C bridge bents, whose design was inadequate under current seismic codes are presented. The first test involved an as-built bent without any deck, which demonstrated column bar pullout at the bent cap-column joints and subsequent lap splice failure. Details of a R/C grade beam seismic retrofit design are provided. A nonlinear analysis model including soil-structure interaction predicted the experimental results with reasonable accuracy. Structural displacement ductility and that resulting from bent cap and foundation flexibility were compared to theoretical relations. Limiting strains and stresses for reinforcement in columns, bent cap-column joints, lap splices, and pile cap-column joints were measured and compared to the literature. Comparison of the experimental column plastic hinge length to predictive relationships shows that the latter slightly underestimate the measured plastic hinge length. Damage indices based on energy were used to evaluate the performance. Comparison with a test of a bridge bent without a grade beam retrofit shows that the foundation seismic retrofit was successful in enhancing the performance of the system.

The in-situ tests demonstrated that application of an external CFRP composite seismic retrofit to reinforced concrete bridges with inferior design details enhances the displacement ductility and seismic performance; this provides an economic alternative to rebuilding. The lessons learned from the tests were used in developing improved recommendations for the seismic retrofit design of R/C bridges using CFRP jackets. The performance-based design procedure includes a nonlinear pushover static analysis of the as-is bent, determination of the column CFRP jacket thickness for plastic hinge confinement, column shear strengthening, and column lap splice clamping. A second analysis of the CFRP retrofitted bent with an iterative design of the T-joints is then carried out; the CFRP jacket in the T-joints consists of three elements: (1) diagonal FRP composite sheets for resisting diagonal tension; (2) FRP composite sheets in the direction of the beam cap axis for shear strengthening and increased flexural capacity; and (3) U-straps that are clamped at the column faces and go over the beam cap, whose purpose is to anchor the longitudinal column bars that typically terminate prematurely, and to provide additional flexural strength. An equilibrium approach combined with strain compatibility is used to design all three CFRP elements. It was found that the design procedure compared favorably with experimental results carried out in the I-15 in-situ tests.

The tests revealed that the CFRP composite retrofit design placed an additional demand on the substructure system, which needs to be addressed when considering a seismic retrofit design of this type. The additional strength of the retrofit design of the superstructure caused yielding in the piles and additional stresses on the pile caps. It will be shown that during the testing, the structural frame actually transitioned into three unique frame types defined as: Phase I ($0\% < \text{drift} < 4\%$) fixed-fixed column ends; Phase II ($4\% < \text{drift} < 6\%$) plastic hinged-hinged for the exterior columns and plastic hinged-plastic hinged for the middle column; and Phase III ($6\% < \text{drift} < 6.8\%$) semi fixed-hinged for the exterior columns and semi fixed-plastic hinged for the interior column. However, the CFRP composite retrofitted bent was able to achieve the goal of doubling the displacement ductility of the as-is bent.

ACKNOWLEDGEMENTS

The authors would like to thank the following individuals for their support and encouragement throughout the project. Samuel Musser, Research Program Manager, Mr. Doug Anderson, Research Engineer, and Daniel Avila, Development & Implementation Program Manager of the Research Division of the Utah Department of Transportation; Dr. Larry Cercone, Chief Scientist, Air Logistics Corporation; Mr. Scott Isaac of Sika Corporation; Dr. Evert Lawton and Dr. Steve Bartlett, Professors of Civil and Environmental Engineering, University of Utah, and Dr. Kyle Rollins Professor of Civil Engineering, Brigham Young University.

In addition, the authors would like to thank the following students from the Department of Civil and Environmental Engineering, University of Utah for their assistance: Danny Alire, B.Sc., Chandra Clyde, M.Sc., Curtis Cook, M.Sc., Jon Hansen, M.Sc., Robert Haight, M.Sc., Nicole Marriott, B.Sc., Paul McMullin, M.Sc., Jason Rapich, B.Sc., Morgan Sandall, B.Sc., and Yasuteru Okahashi, Ph.D. candidate.

Finally, the authors would like to thank Wasatch Constructors for their assistance in the project.

TABLE OF CONTENTS

ABSTRACT.....	ii
FORWARD.....	iii
EXECUTIVE SUMMARY	iv
ACKNOWLEDGEMENTS.....	v
LIST OF FIGURES	x
LIST OF TABLES.. ..	xvii
1. INTRODUCTION	1
FRP Composite Confinement.....	1
Seismic Strengthening with FRP Composites	2
Seismic Retrofit Design with FRP Composites	4
Large Scale Tests of Bridge Systems with FRP Composites.....	5
Objectives	7
2. BRIDGE BENT #4S WITH GRADE BEAM RETROFIT WITHOUT THE DECK.....	8
Bridge Bent Description	8
<i>Vertical Load</i>	11
<i>Condition of Bent #4S in 2000</i>	11
Grade Beam Design for Foundation Retrofit.....	13
Material Properties.....	14
<i>Steel</i>	14
<i>Concrete</i>	16
Loading System	17
<i>Load Frame Footings</i>	17
<i>Load Frame</i>	18
<i>Push and Pull Interface System</i>	20
Instrumentation	22
<i>Cable-Extension Displacement Transducers</i>	22
<i>Linear Variable Differential Transformers</i>	22
<i>Strain Gages</i>	22
Test Procedure and Structural Response.....	24
<i>Load</i>	26
<i>Displacement of the Entire System</i>	28
<i>Displacement of Grade Beam</i>	29
<i>Displacement of the Superstructure</i>	30
Hysteretic Behavior of System	30
<i>System Stiffness</i>	32
<i>System Energy</i>	32
<i>Behavior of Structural Elements</i>	34
Performance Levels and Damage Assessment for Bent	35

<i>Zone 1: East Column-Bent Cap Joint: Damage Assessment</i>	36
<i>Zone 2: Center Column-Bent Cap Joint: Damage Assessment</i>	41
<i>Zone 3: West Column-Bent Cap Joint: Damage Assessment</i>	45
<i>Zone 4: East Column Base Damage Assessment</i>	51
<i>Zone 5: Center Column Base Damage Assessment</i>	55
<i>Zone 6: West Column Base Damage Assessment</i>	60
Overall Structural Performance	64
<i>Performance Levels for Bent #4S</i>	64
<i>Displacement Ductility for Bent #4S</i>	66
3. BRIDGE BENT #5S WITH GRADE BEAM RETROFIT AND GRAVITY LOAD	68
Bridge Bent Description	68
<i>Superstructure</i>	68
<i>As-Built Foundation</i>	70
<i>Comparison with AASHTO and ACI Requirements</i>	70
<i>Gravity Load</i>	71
Grade Beam Seismic Retrofit	72
<i>Material Properties</i>	75
Experimental Investigation of Bridge Bent	75
<i>Instrumentation</i>	76
<i>Test Procedure</i>	76
Experimental Results	77
Behavior of Structural Elements	79
<i>Columns</i>	80
<i>Bent Cap-Column Joints</i>	85
<i>Grade Beam and Pile Caps</i>	86
Performance Assessment	87
Comparison with Bent #4S of the Southbound Bridge – Test 2000.....	90
Comparison with Bent #5N of the Northbound Bridge – Test 1998	91
Damage Index using Energy	91
4. BRIDGE BENT #6S: SEISMIC RETROFIT WITH GRADE BEAM AND CFRP	
COMPOSITE.....	94
Condition of Bent #6S Prior to Retrofit.....	98
Surface Preparation	100
<i>Removal of Delaminated Concrete (1)</i>	100
<i>Shotcrete Application (2)</i>	101
<i>Chamfered Column and Beam Cap Corner Preparation (3)</i>	102
<i>CFRP Application (4)</i>	102
Bent #6S 2000 CFRP Retrofit Design Based on Previous Design of Bent #6N 1998	
Experiment.....	102
<i>Flexural Hinge Confinement of Columns</i>	103
<i>Lap Splice Clamping</i>	104
<i>Shear Strengthening of Columns</i>	105
<i>Flexural Hinge Confinement of Cap Beam</i>	106
<i>Required Layers after Assessment of Column and Cap Beam Deficiencies</i>	106

<i>Shear Strengthening of Column-Cap Beam Joint-Ankle Wrap</i>	107
<i>Anchorage of Column Bars—U-Strap</i>	108
<i>Dywidag Bar Installation</i>	110
<i>Foundation Design</i>	111
Test Setup.....	114
<i>Load Frame Foundations</i>	115
<i>Load Frame</i>	116
<i>Road Deck Fixity on Bents #5S and #6S</i>	118
Instrumentation	118
<i>Internal Strain Gages Attached to the Steel Reinforcement</i>	118
<i>Load Frame Strain Gages</i>	119
<i>Grade Beam and Dywidag Strain Gages</i>	120
<i>Strain Gages Installed on the CFRP Composite Layers</i>	121
<i>Columns</i>	121
<i>Cap Beam</i>	121
<i>Linear Variable Differential Transducers (LVDT) Setup</i>	124
<i>Volume LVDTs</i>	124
<i>Linear Column Array</i>	124
<i>Cable Extension Displacement Transducers (DT)</i>	125
<i>Horizontal Cable Extension Displacement Transducers (DT)</i>	125
<i>Vertical Cable Extension Displacement Transducers (DT)</i>	125
Experimental Conditions and Testing.....	128
Experimental Data	128
<i>Displacements</i>	128
<i>Horizontal Displacements</i>	128
<i>Vertical Displacements</i>	130
<i>Hysteresis Curve Development</i>	134
<i>Force/Displacement Development</i>	136
<i>Discussion of Figures 4.50-4.55 and Table 4.4</i>	140
<i>Stiffness of Structures</i>	140
<i>Peak Horizontal Load Considerations</i>	141
<i>Peak Horizontal Displacement Considerations</i>	142
Ductility Relationships for Bent #5S, #6S (2000) and Bent #6N (1998)	143
<i>Discussion of Figures 4.58-4.63 and Table 4.5</i>	146
<i>Comparisons of Curve Fitting vs. FEMA 273</i>	146
<i>FEMA 273 Observations and Recommendations</i>	150
Energy Relationships	151
<i>Discussion on Hysteretic Energy Capacity Absorption</i>	154
Performance Levels and Damage Assessment for Bent #6S	158
<i>Damage Assessment of Bent #6S</i>	158
<i>General Reinforcement Steel Yielding and Concrete Crushing</i>	158
Specific Bent #6S 2000 Test Joint Damage Assessment.....	166
<i>East Column-Cap Beam Joint: Mechanical and Material Evaluation</i>	166
<i>Ankle Wrap (Diagonal) Layers</i>	166
<i>Zero Layers</i>	166
<i>U-Straps</i>	168

<i>Yielding Reinforcement Steel and Concrete Crushing</i>	168
<i>Joint Longitudinal Reinforcement Steel Pullout</i>	170
<i>Middle Column-Cap Beam Joint: Mechanical and Material Evaluation</i>	174
<i>Ankle Wrap (Diagonal) Layers</i>	174
<i>Zero Layers</i>	175
<i>U-Straps</i>	176
<i>Column Confinement Layers (6 Layers) Adjacent to the Joint</i>	176
<i>Yielding Reinforcement Steel and Concrete Crushing</i>	177
<i>Joint Longitudinal Reinforcement Steel Pullout</i>	179
<i>Volumetric Change in Joint</i>	179
<i>West Column-Cap Beam Joint: Mechanical and Material Evaluation</i>	184
<i>Ankle Wrap (Diagonal) Layers</i>	184
<i>U-Straps and Cap Beam Confinement Layers</i>	185
<i>Yielding Reinforcement Steel and Concrete Crushing</i>	186
<i>Column Longitudinal Reinforcing in the Joint Steel Pullout</i>	188
<i>Cap Beam Flexural Crack</i>	188
<i>Assessment of the East Column-Grade Beam Joint</i>	195
<i>Confinement Layers</i>	195
<i>Yielding of Steel Reinforcement and Concrete Crushing</i>	195
<i>Assessment of the Middle Column-Grade Beam Joint</i>	199
<i>Confinement Layers</i>	199
<i>Yielding of Steel Reinforcement and Concrete Crushing</i>	200
<i>Volumetric Change in Bottom Column-Grade Beam Joint</i>	201
<i>Assessment of the West Column-Grade Beam Joint</i>	204
<i>Confinement Layers</i>	204
<i>Yielding of Steel Reinforcement and Concrete Crushing</i>	204
Overall Bent #6S 2000 Test Damage Assessment.....	208
5. CONCLUSIONS.....	214
Bent #4S (2000)	214
Bent #5S (2000)	215
Bent #6S (2000)	215
Closure	217
6. REFERENCES	219

LIST OF FIGURES

Figure 2.1	As-built dimensions of Bent #4S.....	9
Figure 2.2	As-built rebar detail of Bent #4S.....	9
Figure 2.3	As-built steel details of Bent #4S.....	10
Figure 2.4	As-built footing plan section of Bent #4S.....	10
Figure 2.5	Spalling under cap beam of Bent #4S.....	12
Figure 2.6	Spalling due to reinforcement deterioration on cap beam of Bent #4S.....	12
Figure 2.7	Clear cover under cap beam barely attached on Bent #4S.....	13
Figure 2.8	As-built substructure of Bent #4S (2000): (a) plan, (b) elevation.....	14
Figure 2.9	Modified grade beam for Bent #4S: (a) plan, (b) elevation, (c) knee joint cross section, (d) mid-span, (e) overlay of existing pile cap, (f) overlay of existing pile cap around column.....	15
Figure 2.10	Stress/Strain curves for existing and grade beam concrete in Bent #4S.....	16
Figure 2.11	Load frame footings for Bent #4S.....	17
Figure 2.12	Load frame actuator extension modification.....	18
Figure 2.13	Side view of load frame with hydraulic actuator.....	19
Figure 2.14	Load frame front view.....	19
Figure 2.15	Load frame pad with 38mm threaded tie down rods and welded plates.....	20
Figure 2.16	Hydraulic actuator used in testing.....	20
Figure 2.17	Load cell with 2.76GN capacity.....	21
Figure 2.18	Load cell, clevis connection and push box with chucked pre-stress tendons located on the East side of Bent #4S.....	21
Figure 2.19	Pull box with pre-stressing tendons stressed to 4.45kN each, located on the west end of Bent #4S.....	22
Figure 2.20	Location of CEDT instruments.....	23
Figure 2.21	LVDT array: (a) South face of center column, cap-beam joint, (b) South face at the base of center column.....	24
Figure 2.22	Locations of strain gages on Bent #4S.....	25
Figure 2.23	Displacement of Bent #4S vs. time with steps and cycles.....	26
Figure 2.24	Cyclic Load history for Bent #4S.....	27
Figure 2.25	Difference in displacement readings of CEDT 1 and CEDT 3 during testing of Bent #4S.....	28
Figure 2.26	Displacement of the entire system, grade beam, and superstructure of Bent #4S.....	29
Figure 2.27	Hysteretic behavior of Bent #4S.....	31
Figure 2.28	Experimental stiffness degradation of Bent #4S.....	32
Figure 2.29	Energy absorbed by Bent #4S for each cycle.....	33
Figure 2.30	Cumulative Energy absorbed by Bent #4S.....	33
Figure 2.31	Shear Diagram for Bent #4S under maximum experimental load.....	34
Figure 2.32	Moment Diagram for Bent #4S under maximum experimental load.....	34
Figure 2.33	Six zones of interest for damage assessment.....	35
Figure 2.34	Performance levels and degradation phases.....	36
Figure 2.35	Strain gage SG33 showing reduction of strain due to bar pullout.....	37
Figure 2.36	Moment-curvature for East column-bent cap joint.....	38
Figure 2.37	Condition of East column-bent cap joint: (a) 1.5% drift, (b) 2% drift, (c) 4% drift, (d) 5% drift.....	40
Figure 2.38	Strain time-history for SG55, the first element to yield in the overall structure.....	41
Figure 2.39	Moment curvature for center bent cap-column joint.....	42
Figure 2.40	Damage to Center column-bent cap joint at the end of 5% drift.....	43
Figure 2.41	Damage to Center column-bent cap joint showing the buckled zone on the west face.....	44
Figure 2.42	Center column-bent cap joint buckled zone on the west face.....	44
Figure 2.43	Strain gage SG65 time history.....	45
Figure 2.44	Strain time-history for SG69 in the West column-bent cap joint.....	46

Figure 2.45 Strain time-history for SG70 in the West column-bent cap joint.....	46
Figure 2.46 Pullout pocket in column longitudinal bar in West column-bent cap joint; the pocket is 22mm long.....	47
Figure 2.47 Moment curvature for West column-bent cap joint	48
Figure 2.48 West column-bent cap joint at 2% drift ratio	49
Figure 2.49 West column-bent cap joint at 5% drift ratio	50
Figure 2.50 22mm long pullout pocket in column longitudinal bars at West column-bent cap joint.....	50
Figure 2.51 SG7 and SG 8 showing slip of lap splice in East column base	51
Figure 2.52 Moment-curvature for East column base	52
Figure 2.53 East column base: (a) 0.8mm cracks at 1.5% drift ratio, (b) 3mm to 5mm cracks at 5% drift ratio	54
Figure 2.54 East column base north face: 3mm to 5mm cracks at 5% drift ratio.....	54
Figure 2.55 SG23 and SG24 showing relative slip in lap splice of center column base	55
Figure 2.56 Center column base showing diagonal crack at a 5% drift ratio	56
Figure 2.57 Moment-curvature for Center column base.....	57
Figure 2.58 Center column base: (a) before test, (b) diagonal shear cracks at 2% drift.....	59
Figure 2.59 Center column base at 5% drift: (a) South face, (b) East face	59
Figure 2.60 Center column base at 5% drift: (a) West side and Southwest corner showing buckled bars, (b) North face.....	60
Figure 2.61 Strain gages SG51 and SG52 showing relative slip in the lap splice of West column base	61
Figure 2.62 Moment-curvature for West column base	62
Figure 2.63 West column base damage: (a) South face at 2% drift, (b) South face at 5% drift....	63
Figure 2.64 West column base post-test damage on South face at 5% drift.....	64
Figure 2.65 Displacement ductility of the Bent #4S.....	66
Figure 3.1 As-built Bent #5S (2000)	69
Figure 3.2 Steel reinforcement details for as-built Bent #5S (2000)	69
Figure 3.3 Cross-sectional reinforcement details for Bent #5S (2000)	70
Figure 3.4 Pile-to-pile cap connection details and retrofit.....	71
Figure 3.5 Grade beam retrofit: (a) elevation, and (b) plan.....	72
Figure 3.6 Design of grade beam for flexural and axial loads.....	73
Figure 3.7 Grade beam knee-joint reinforcement details.....	74
Figure 3.8 Grade beam reinforcement details: (a) elevation view, (b) plan view, and (c) Section A-A knee joint, Section B-B span between pile caps, and Section C-C overlay on existing pile caps.....	74
Figure 3.9 Grade beam reinforcement including Dywidag bars, cap overlay, and knee joint.....	75
Figure 3.10 Load frame setup showing actuator, steel yoke, and prestressing cables.....	76
Figure 3.11 Displacements of grade beam, superstructure, and total system for Bent #5S (2000)	77
Figure 3.12 Applied lateral load for Bent #5S (2000) from load cell reading.....	78
Figure 3.13 Hysteresis curve of total system for Bent #5S (2000).....	79
Figure 3.14 Degradation of lateral stiffness for Bent #5S (2000).....	79
Figure 3.15 Comparison of force-displacement envelopes from experiment and analytical model for Bent #5S (2000)	80
Figure 3.16 Location and sequence of experimental plastic hinge formation for Bent #5S (2000)	81
Figure 3.17 Damage to Bent #5S (2000) lap splice at bottom of center column: (a) after test, (b) detail showing buckled column bar, (c) lap splice after post-test investigation ...	83
Figure 3.18 Maximum strains in reinforcement at the bottom of the center column	84
Figure 3.19 Damage to Bent #5S (2000) at top of center column: (a) pullout of longitudinal reinforcement, (b) after test, (c) showing buckled column bar.....	84
Figure 3.20 Nominal joint shear in center column joint: (a) free-body diagram, (b) forces resolved into couples, (c) vertical shear, and (d) horizontal shear	85

Figure 3.21	Damage to bent cap-column joints of Bent #5S (2000): (a) center column joint at end of test, (b) east column joint after post-test investigation	86
Figure 3.22	Cracks in the grade beam at a drift ratio of 2.5%: (a) center pile cap, (b) close up on the top of the grade beam.....	87
Figure 3.23	Location of observed cracks in the grade beam	87
Figure 3.24	Displacement ductility of total system for Bent #5S (2000)	88
Figure 3.25	Force-deformation for Bent #5S (2000), Bent #4S (2000), and Bent #5N (1998)	90
Figure 3.26	Energy comparison for Bent #5S (2000), Bent #4S (2000), and Bent #5N (1998) ..	91
Figure 4.1	Typical bent structure for both the 1998 and 2000 bridge tests	94
Figure 4.2	Dry lay-up of epoxy resin applied to dry CFRP composite textile using roller and squeegee.....	95
Figure 4.3	North view of 2000 test site showing Bent #4S, Bent #5S, and Bent #6S.....	96
Figure 4.4	Wet lay-up epoxy resin machine with saturation reservoir	96
Figure 4.5	Foundation system for Bent #5N and Bent #6N in the 1998 tests	97
Figure 4.6	Loose cover concrete removed from Bent #6S showing cover concrete delamination and loss in vertical stirrup area in the bent cap	98
Figure 4.7	Elevation showing the original 1962 steel details	99
Figure 4.8	Column and beam cap section of 1962 reinforcement details.....	100
Figure 4.9	Water jet gun and nozzle used to remove debris prior to CFRP application	100
Figure 4.10	First step in retrofit of Bent #6S: Water Jet for removing loose concrete cover.....	101
Figure 4.11	Cap beam with cover layer restored to the original concrete cover thickness	101
Figure 4.12	Concrete stress-strain diagrams defining the unconfined and CFRP composite confined sections used in the analytical Drain-2DX model.....	103
Figure 4.13	Complete CFRP composite retrofit design of Bent #6S for the 2000 test (L = number of CFRP composite layers)	109
Figure 4.14	U-strap design for Bent #6S for the 2000 test	110
Figure 4.15	Location and overall dimensions of the existing piles	111
Figure 4.16	Design of both the interior and exterior pile-to-pile cap retrofitted connections	111
Figure 4.17	Plan view of the modified grade beam system.....	112
Figure 4.18	Cross-sections of the retrofitted grade beam	113
Figure 4.19	Hoop steel details used in the retrofitted grade beam.....	113
Figure 4.20	Longitudinal steel used in the retrofitted grade beam	114
Figure 4.21	Elevation of test set-up for the May 6 th and 9 th 2000 Bent #6S tests	114
Figure 4.22	Yoke assembly attached to the East haunch end of Bent #6S	115
Figure 4.23	Twenty 12.7 mm cable strands used to apply the pull portion of the load for Bent #6S	116
Figure 4.24	Plan view of a typical foundation and geopier system used to support the load frame used in the Bent #6S 2000 test.....	116
Figure 4.25	Elevation of the 2000 load frame detail with the 2.1 m extension	117
Figure 4.26	Formed concrete pedestals on Bent #5S cap- beam	118
Figure 4.27	Roller and roller runways located on Bent #6S bearing plates	118
Figure 4.28	Location of the internal strain gages on the reinforcement for the Bent #6S 2000 test	119
Figure 4.29	Location of the strain (F) gages on the North and South sides of the load frame	120
Figure 4.30	Strain gage locations in the grade beam and strain gages on the Dywidag bars in the foundations.....	120
Figure 4.31	Strain gages installed on the CFRP composite layers in the plastic hinge regions on the columns	121
Figure 4.32	Strain gages located on the diagonal and zero layers of the East joint.....	122
Figure 4.33	Strain gages located on the diagonal and zero layers of the Middle joint.....	122
Figure 4.34	Strain gages located on the diagonal, zero, and strap layers of the West joint	123

Figure 4.35 Complete view of all external strain gages installed on the load frame and Bent #6S for the 2000 test	123
Figure 4.36 Top and bottom LVDT box arrays and linear column arrays attached to the Middle column	124
Figure 4.37 Horizontal DTs used to monitor the horizontal displacements of the load frame and cap beam during the 2000 Bent #6S test.....	125
Figure 4.38 Vertical DTs used to monitor the vertical displacements of the of the cap beam and grade beam during the 2000 Bent #6S test	126
Figure 4.39 DTs used to monitor vertical displacements of the West column during the 9 May 2000 test	127
Figure 4.40 Horizontal displacement of load frame foundations (102 mm) on Bent #6S(2000)	129
Figure 4.41 Total System, Superstructure, and Grade Beam displacements for the complete Test of Bent #6S (2000).....	130
Figure 4.42 West column-cap beam joint showing a permanent 16mm gap in the longitudinal column bars.....	131
Figure 4.43 Permanent vertical deformation of the superstructure on the middle column DT12), Bent #6S 2000 test on Saturday 6 May 00	132
Figure 4.44 Permanent vertical deformation of the superstructure on the center span of the West portion (DT 5), Bent #6S test on Saturday 6 May 00	132
Figure 4.45 Total permanent vertical deformation of the superstructure on the West column Bent #6S 2000 test on (DT 8) and (DT 2), Saturday 6 May 00 and Tuesday 9 May 00..	133
Figure 4.46 Total permanent vertical deformation of the total system on the West Column Bent #6S 2000 test on Saturday 6 May 00 and Tuesday 9 May 00	133
Figure 4.47 Hysteresis diagram for Bent #6N 1998 test	134
Figure 4.48 Hysteresis diagram for Bent #5S 2000 test	135
Figure 4.49 Hysteresis diagram for Bent #6S 2000 test	135
Figure 4.50 Force/displacement plot of the total system of Bent #6S 2000 test interpolated by weighted average method	137
Figure 4.51 Force/displacement plot of the super structure of Bent #6S 2000 test interpolated by weighted average method	137
Figure 4.52 Force/displacement plot of the total system of Bent #6S 2000 push only interpolated by weighted average method	138
Figure 4.53 Force/displacement plot of the total system of Bent #6S 2000 pull cycles only interpolated by weighted average method	138
Figure 4.54 Force/displacement plot of the total system of Bent #6N 1998 test interpolated by weighted average method	139
Figure 4.55 Force/displacement plot of the total system of Bent #5S 2000 interpolated by weighted average method	139
Figure 4.56 Degradation of the total system Bent #6N 1998, and total system Bent #6S 2000 pull cycles, superstructure Bent #6S 2000, total system Bent #6S 2000, total system Bent #5S 2000, and total system Bent #6S 2000 push cycles	141
Figure 4.57 Average spline curves for the total system Bent #6N 1998, total system Bent #6S 2000 pull cycles, superstructure Bent #6S 2000, total system Bent #6S 2000, total system Bent #5S 2000, and total system Bent #6S 2000 push cycles	142
Figure 4.58 Total system Bent #6S 2000 mean average displacement ductility curve	143
Figure 4.59 Total system Bent #6S 2000 push cycles only displacement ductility curve.....	143
Figure 4.60 Total system Bent #6S 2000 pull cycles only displacement ductility curve	144
Figure 4.61 Super structure Bent #6S 2000 mean average displacement ductility curve.....	144
Figure 4.62 Total system Bent #5S 2000 displacement ductility curve	145
Figure 4.63 Total system Bent #6N 1998 displacement ductility curve.....	145
Figure 4.64 Push cycles of the backbone curve of the total system Bent #6S 2000 and the displacement ductility based on the FEMA guidelines.....	147

Figure 4.65 Push cycles of total system of FEMA curve and the 99% confidence intervals banded about $S(x)$ the mean average of the complete peak loads for Bent #6S 2000 test.....	148
Figure 4.66 Push cycles of the 99% confidence intervals plotted around $S(x)$ the mean average of the peak vs. the recommended FEMA intersection points for the ith and the $(ith - 1)$ cycles for each drift step	148
Figure 4.67 Pull cycles of the backbone curve of the total system Bent #6S 2000 and the ductility based on the FEMA guidelines.....	149
Figure 4.68 Pull cycles of total system of FEMA curve and the 99% confidence intervals banded about $S(x)$ the mean average of the complete peak loads for Bent #6S 2000.....	149
Figure 4.69 Pull cycles of the 99% confidence intervals plotted around $S(x)$ the mean average of the peak vs. the recommended FEMA intersection points for the ith and the $(ith - 1)$ cycles for each drift step.....	150
Figure 4.70 Hysteretic Energy absorbed for each cycle for the total system (Bent #6S 2000)....	151
Figure 4.71 Hysteretic Energy absorbed for each cycle for the superstructure (Bent #6S 2000)	152
Figure 4.72 Energy absorbed for each cycle for the total system (Bent #6N 1998 test)	152
Figure 4.73 Energy absorbed for each cycle for the total system (Bent #5S 2000 test).....	153
Figure 4.74 Cumulative hysteresis energy absorbed by the total system Bent #6S 2000, superstructure Bent #6S 2000, total system Bent #6N 1998, and total system Bent #5S 2000	153
Figure 4.75 Energy dissipation for any cycle i	154
Figure 4.76 Maximum lateral push-pull forces vs. time for each cycle of the Bent #6S 2000 test.....	159
Figure 4.77 Maximum lateral push/pull drift ratio vs. time for each cycle of the Bent #6S 2000 test.....	159
Figure 4.78 Bent #6S deflected shape for the 2000 test at the maximum lateral load and a drift ratio of 3.73%.....	160
Figure 4.79 Reinforcement steel yielding and concrete crushing of the as-built Bent #5S 2000 DRAIN-2DX model lateral force/displacement curve.....	161
Figure 4.80 Reinforcement steel yielding and concrete crushing of the retrofitted Bent #6S 2000 DRAIN-2DX model lateral force/displacement curve	161
Figure 4.81 Degradation sequence represented by the reinforcement steel yielding and concrete crushing of the as-built Bent #5S 2000 DRAIN-2DX model	162
Figure 4.82 Degradation sequence of the reinforcement steel yielding and concrete crushing of the retrofitted Bent #6S 2000 DRAIN-2DX model.....	163
Figure 4.83 Cap-beam external CFRP composite diagonal 2 layers located in the East column-cap beam region: strain vs. %drift pull cycles for strain gages 31, 32, and 33.....	167
Figure 4.84 Cap-beam external CFRP composite zero 2 layers located in the East column-cap beam region: strain vs. %drift push cycles for strain gages 67, 52, 51, 43, and 42.....	167
Figure 4.85 U-strap failure shown at 4.0% drift step.....	168
Figure 4.86 Cap-beam internal lateral reinforcement steel located in the East column-cap beam region: strain vs. % drift for SG29	169
Figure 4.87 Moment curvature for the East column-cap beam joint	170
Figure 4.88 Surface damage for East column-cap beam joint	172
Figure 4.89 Internal damage for East column-cap beam joint.....	173
Figure 4.90 No column reinforcement steel pullout and no damage sustained on the cap beam portion of the Middle column.....	174

Figure 4.91 Cap-beam external CFRP composite diagonal 2 layers located in the middle column-cap beam region: strain vs. %drift push cycles for strain gages 48, 49 and 50.....	175
Figure 4.92 Cap-beam external CFRP composite zero 1 layer located in the middle column-cap beam region: strain vs. %drift push cycles for strain gages 118, 117, 116, 115, and 114.....	175
Figure 4.93 Average displacement deflections of the cap beam indicating smaller tensile demands on the middle joint U-straps	176
Figure 4.94 Column external CFRP composite 6 confinement layers located on the middle column top region: strain vs. %drift pull cycles for strain gages 53, 54, 55, 57, 60, 59, 58, and 56.....	177
Figure 4.95 Excessive flexural demands applied to the upper column confinement layers adjacent to the cap beam soffit	178
Figure 4.96 Column longitudinal reinforcement steel strain vs. drift for SG44	179
Figure 4.97 Moment curvature for the Middle column-cap beam joint	180
Figure 4.98 Volumetric change in the Middle column-cap beam joint	180
Figure 4.99 Surface damage for Middle column-cap beam joint	182
Figure 4.100 Internal damage for Middle column-cap beam joint	183
Figure 4.101 Cap-beam external CFRP composite diagonal 2 layers located in the West column-cap beam region: strain vs. %drift pull cycles for strain gages 68, 69, and 70.....	184
Figure 4.102 West column-cap beam joint ankle (diagonal) wrap and U-strap damage up to the maximum drift of 6.8%	185
Figure 4.103 Push cycles for four CFRP composite layers SG119 and SG121; U-straps five layers SG123 and SG124	186
Figure 4.104 West column-cap beam joint after CFRP composite layers were removed exposing moderate flexural stresses in the plastic hinge regions of the upper	187
Figure 4.105 Degradation transition of the U-straps and column longitudinal reinforcement steel bond capacity	187
Figure 4.106 West column-cap beam moment curvature	188
Figure 4.107 Debonded column longitudinal bar observed in the joint after the concrete cover was removed from the West column-beam joint.....	189
Figure 4.108 Beginning of the tension crack at 4.0% displacement drift.....	189
Figure 4.109 Flexural tension cracked cap beam section east of the West column: beginning at 4.0% drift ratio and ending at 5.5% drift	190
Figure 4.110 Tension crack relative to the negative moment longitudinal reinforcement steel and the CFRP confinement adjacent to the West column.....	190
Figure 4.111 Surface damage for West column-cap beam joint.....	193
Figure 4.112 Cap beam reinforced by road deck diaphragm system preventing complete failure	193
Figure 4.113 Internal damage for West column-cap beam joint.....	194
Figure 4.114 Moment curvature diagram for the East column grade beam joint	196
Figure 4.115 Surface damage and deterioration for East column-grade beam joint	198
Figure 4.116 Column external CFRP composite 14 confinement layers located on the Middle column bottom region: strain vs. %drift push cycles for strain gages 19, 20, 21, 23, 26, 25, 24, and 22.....	199
Figure 4.117 Column external CFRP composite 2 confinement layers located on the Middle column bottom region: strain vs. %drift push cycles for strain gages 106, 107, 108, 109, 110, 111, 112, and 113.....	200
Figure 4.118 Moment curvature diagram for the Middle column-grade beam joint	201
Figure 4.119 Volumetric change in the bottom Middle column-grade beam joint	201
Figure 4.120 Surface damage and deterioration for East column-grade beam joint	203
Figure 4.121 Moment curvature diagram for the West column-grade beam joint	205

Figure 4.122 Surface damage and deterioration for West column-grade beam joint	207
Figure 4.123 Performance levels (Phases) for Bent #6S 2000 test.....	209
Figure 4.124 Phase I Bent #6S 2000 deflected shape between $0\% \leq \text{drift} \leq 4.0\%$	211
Figure 4.125 Onsite Phase I Bent #6S 2000 deflected shape between up to 4.0% drift ratio	211
Figure 4.126 Phase II Bent #6S 2000 deflected shape between $4.0\% \leq \text{drift} \leq 6.0\%$	212
Figure 4.127 Onsite Phase II Bent #6S 2000 deflected shape up to 6.0% drift ratio	212
Figure 4.128 Phase III Bent #6S 2000 deflected shape between $6.0\% \leq \text{drift} \leq 6.8\%$	213
Figure 4.129 Onsite Phase III Bent #6S 2000 deflected shape at 6.8% drift ratio	213

LIST OF TABLES

Table 2.1	Tensile rebar testing schedule for Bent #4S	14
Table 2.2	Steel rebar tensile characteristics for Bent #4S	15
Table 2.3	Concrete compressive strength characteristics	17
Table 2.4	Peak loads corresponding to cycles of testing for Bent #4S	27
Table 2.5	Peak displacements and drift ratios for Bent #4S	29
Table 2.6	Peak displacements of grade beam for Bent #4S	30
Table 2.7	Peak displacement values and % drift for the superstructure of Bent #4S	31
Table 2.8	Damage assessment for East column-bent cap joint	38
Table 2.9	Damage assessment for Center column-bent cap joint	42
Table 2.10	Damage assessment for West column-bent cap joint	48
Table 2.11	Damage assessment for East column base	53
Table 2.12	Damage assessment for Center column base	58
Table 2.13	Damage assessment for West column base	63
Table 2.14	Damage assessment of structure of Bent #4S	65
Table 3.1	Column plastic hinge length	82
Table 3.2	Bridge performance assessment	89
Table 3.3	Comparison of energy indices for three bents	92
Table 4.1	Confinement layers of CFRP composite and their locations on Bent #6S 2000	106
Table 4.2	Actual drift steps for the total system Bent #6S 2000 test	128
Table 4.3	Total, superstructure, and grade beam horizontal displacements for the 1998 and 2000 tests	130
Table 4.4	Load, stiffness, and displacement data for Figures 4.50–4.55	140
Table 4.5	Displacement ductility values for the 1998 and 2000 tests	146
Table 4.6	Maximum hysteric energy cycles for the 1998 and 2000 tests	155
Table 4.7	Peak load and displacement for the 1998 and 2000 tests	155
Table 4.8	The 80 % $S(x)_{\max}$ lateral load peak values in the 1998 and 2000 tests	156
Table 4.9	Energy, Work, and Damage Index for the 1998 and 2000 tests	156
Table 4.10	Strains for the reinforcement yielding and concrete crushing for the as-built Bent #5S 2000	164
Table 4.11	Strains for the reinforcement yielding and concrete crushing for the retrofitted Bent #6S 2000	165
Table 4.12	Damage assessment matrix for the East column-cap beam joint	171
Table 4.13	Damage assessment matrix for the Middle column-cap beam joint	181
Table 4.14	Damage assessment matrix for the West column-cap beam joint	192
Table 4.15	Damage assessment matrix for the East column-grade beam joint	197
Table 4.16	Damage assessment matrix for the Middle column-grade beam joint	202
Table 4.17	Damage assessment matrix for the West column-grade beam joint	206
Table 4.18	Overall Bent #6S 2000 test damage assessment	210

1. INTRODUCTION

The seismic force and displacement capacity of bridges is of interest for the purpose of establishing realistic estimates for performance-based seismic design and retrofit. In particular, assessment of existing bridges with deficient seismic details is important for evaluating their capacity and for suggesting seismic retrofit measures.

Laboratory studies have been carried out for design of new reinforced concrete (RC) bridges and for seismic retrofit of existing ones. Improvement of column longitudinal bar anchorage by addition of steel plates welded to the ends of the steel bars and replacement of the removed concrete using a cement-based mortar was demonstrated by Park et al. (1993). Seismic retrofit techniques for RC bridges involving steel jackets, concrete jackets, and fiber-reinforced polymer (FRP) composite jackets for columns have been used successfully (Priestley et al. 1996). Xiao et al. (1996) presented theoretical and experimental studies for seismic retrofit of bridge column footings. They found that reinforced concrete overlay retrofits may not develop an effective post-cracking mechanism. Eberhard and Marsh (1997) tested a three-span reinforced concrete bridge by inducing cyclic lateral loads on its bents. These tests determined the structure's stiffness under three conditions: (1) in-situ, (2) excavation of soil from abutments, and (3) isolation of the structure from the abutments. McLean and Marsh (1999) performed experimental studies on 1/3-scale models for retrofits of both pile-supported and spread footing column assemblages. It was found that a reinforced concrete overlay provided an effective retrofit. An as-built bridge joint with typical pre-1960 design details was tested at 75% scale by Sritharan et al. (1999). The design flaws were: (a) no joint reinforcement, and (b) the longitudinal column bars were prematurely terminated at the joint. The performance of the joint was not satisfactory; pronounced diagonal cracks across the joint were observed at a displacement ductility equal to 2.0 and the joint damage prevented the ideal strength of the system from being developed.

Other retrofit schemes include steel jackets connected to a base plate anchored to the footing (Darwish et al. 1999), post-tensioning of T-joints using RC bolsters (Lowes and Moehle 1999), and retrofitting of outrigger beam-column frames with concrete sleeving and column jacketing (Griezic et al. 1999). Pantelides et al. (1999, 2001) conducted in-situ cyclic, quasi-static lateral load tests on two bridge bents, one of which was retrofitted with carbon FRP (CFRP) composites, and the other was tested as-is; the foundations of both bents were improved with a plain concrete beam linking the pile caps and an external tension tie made up of two 36-mm Dywidag bars; it was found that the displacement ductility of the retrofitted bent with CFRP composites was significantly improved.

FRP Composite Confinement

The behavior of many structures including bridges under the effects of recent earthquakes such as the 1989 Loma Prieta, 1994 Northridge, and 1995 Kobe, has been the stimulus for developing and implementing new techniques and applications of modern materials, such as carbon and glass FRP composites for seismic retrofit. The unsatisfactory seismic performance of these structures has been attributed to poorly designed details and outdated design principles, which existed in older codes. The various applications of external FRP composite retrofit in bridges have shown that in most cases the implementation of FRP

composite materials provides adequate seismic detailing to the structure, and improves ductility and seismic performance; this provides an economic alternative to rebuilding.

Confinement effectiveness of FRP jackets in concrete columns depends on several parameters, including concrete strength, types of fibers and resin, fiber volume fraction and fiber orientation in the jacket, jacket thickness, shape of cross section, length-to-diameter ratio of the column, and the interface bond between the core and the jacket. The application of carbon fiber composite jackets for the three columns and cap beam of an existing concrete bridge pier was performed in September 1996, in Salt Lake City. The evaluation of the pier in the as-is condition, the rehabilitation objectives, and the composite wrap design were presented by Gergely et al. (1998). A bilinear stress-strain curve for the confinement model of circular and rectangular concrete sections with fiber-reinforced plastic composite jackets was used for performing pushover analyses. Mirmiran et al. (1998) studied the effects of shape, length, and bond on FRP-confined concrete. They show square sections to be less effective in confining concrete than their circular counterparts. Spoelstra and Monti (1999) developed a uniaxial model for concrete confined with FRP composites. The model, which is suitable to be inserted into fiber-type beam-column elements, explicitly accounts for the continuous interaction with the confining device due to the lateral strain of concrete, through an incremental-iterative approach. The relation between the axial and lateral strains is implicitly derived through equilibrium between the dilating confined concrete and the confining device. This relation allows one to trace the state of strain in the jacket and to detect its failure. The model is compared with a set of experimental tests and shows very good agreement in both the stress-strain and the stress-lateral strain response.

A new stress-strain model for concrete with a sufficient amount of confinement from FRP composites, which leads to significant compression strength enhancement has been presented by Lam and Teng (2002). A strain ductility based model, was developed for predicting the compressive behavior of normal strength concrete confined with FRP composite jackets by Moran and Pantelides (2002). The model is applicable to both bonded and non-bonded FRP confined concrete, and can be separated into two components: a strain softening component that accounts for unrestrained internal crack propagation in the concrete core, and a strain hardening component that accounts for strength increase due to confinement provided by the FRP composite jacket. A variable strain ductility ratio was used to develop the proposed stress-strain model. Equilibrium and strain compatibility were used to obtain the ultimate compressive strength and strain of FRP confined concrete as a function of the confining stiffness and ultimate strain of the FRP jacket.

Seismic Strengthening with FRP Composites

An investigation on the seismic strengthening of concrete columns with carbon fiber composites was conducted by Katsumata et al. (1988). Ten 1/4-scale column specimens with square cross-sections were tested, after the corners were rounded. The test results showed that wrapping of carbon fibers around the column greatly increased the earthquake-resistant capacity of the columns. Saadatmanesh et al. (1996), analyzed the seismic behavior of RC columns strengthened with FRP composite straps. Five concrete column-footing assemblages were constructed with a 1/5-dimensional scale factor. The unidirectional glass fabric straps were wrapped around the potential plastic hinge zone of the columns. All specimens were tested under inelastic reversal loading while simultaneously being subjected to a constant

axial load. Test results showed that seismic resistance of retrofitted concrete columns improves significantly as a result of the confining action of the FRP composite straps. The straps were highly effective in confining the core concrete and preventing the longitudinal reinforcement bars from buckling under cyclic loading.

Seismic retrofit methods focusing on the retrofit of RC bridge piers were studied by Machida (1997). Primarily, improvement of shear resistance strength is required for the improvement of seismic resistance of RC structures. In the old standards, shear resistance strength in the case of no placement of reinforcing steel bars was overestimated, and as a result, many structures had insufficient shear resistance strength. Conventional retrofitting methods include enhanced concrete placing and steel plating. To overcome these large-scale operations, the winding of carbon fiber sheet and the use of aramid fiber sheet were developed. In addition, FRP spraying was proposed and investigated as a retrofit method.

The flexural behavior of earthquake-damaged reinforced concrete columns repaired with prefabricated FRP wraps has been studied by Saadatmanesh et al. (1997a). Four column specimens were tested to failure under reversed inelastic cyclic loading to a level that could be considered higher than would occur in a severe earthquake. The columns were repaired with prefabricated FRP wraps and retested under simulated earthquake loading. The test specimens were designed to model single-bent, nonductile concrete columns in existing highway bridges constructed before the modern seismic design provisions were in place. FRP composite wraps were used to repair damaged concrete columns in the critically stressed areas near the column footing joint. Seismic performance of repaired columns in terms of their hysteretic response was evaluated and compared to those of the original and unretrofitted columns. The results indicate that the proposed repair technique was highly effective. Both flexural strength and displacement ductility of the repaired columns were higher than those of the original columns. The typical behavior of rectangular bridge columns with substandard design details for seismic forces was investigated by Saadatmanesh et al. (1997b). The poor performance of this type of column attested to the need for effective and economical seismic upgrading techniques. A method utilizing FRP composites to retrofit existing bridge columns was investigated. High-strength FRP straps were wrapped around the column in the potential plastic hinge region to increase confinement and to improve the behavior under seismic forces. Five rectangular columns with different reinforcement details were constructed and tested under reversed cyclic loading. Two columns were not retrofitted and were used as control specimens so that their hysteresis response could be compared with those for retrofitted columns. The results of this study indicated that significant improvement in ductility and energy absorption capacity could be achieved as a result of this retrofitting technique.

RC elements have also been strengthened with polyacetal-fiber (PAF) sheets. Typical properties of the polyacetal fiber are high strength, high strain capacity, high resistance to shear force, lightweight and ease of handling by preformability. Polyacetal fiber reinforced by special epoxy-resin that is optimized for the fiber offers an outstanding combination of properties not available from steel and other high strength fibers, such as glass, aramid and carbon fibers, which are used for the seismic retrofit of RC structures. The advantages realized were the overall cost savings and strengthening of RC elements in a short time. Tests conducted by Iihoshi et al. (1999) investigate the strengthening effect of concrete elements with polyacetal FRP. The lateral loading tests were performed on fourteen RC

columns in order to analyze the strengthening effect of polyacetal FRP on shear and ductility, and to clarify the possibility of this FRP as a material for seismic retrofit.

The use of FRP composite material wraps on aged and damaged concrete structures has been recognized as an effective method to restore the load carrying capacity and extend the service life of the structures (Lau and Zhou 2001). The investigation shows the behavior of the wrapped concrete cylinder with different wrapping materials and bonding dimensions using finite element (FEM) and analytical methods. The experimental results show that the deflection of the wrapped concrete cylinder in the load direction decreases with increasing length, thickness and modulus of the wrapping sheet. A reliable technique of CFRP prestressing has also been developed for retrofitting of some Japanese historical structures (Katsumata et al. 2001). Masuo et al. (2001) studied the seismic strengthening of RC columns with wing walls. In the proposed strengthening system, CF-anchors are jointed to CFRP sheets by passing anchor strands through the penetrating holes of the wing walls. It was shown that the load-deformation behavior of the columns strengthened by the system almost coincided with that of completely wrapped columns.

Seismic Retrofit Design with FRP Composites

FRP composite jacket design criteria, for various seismic column failure modes, were described by Seible et al. (1997). Detailed examples showed the application of the design criteria to retrofits of columns with circular and rectangular sections, different reinforcement ratios, and detailing. The carbon jacket designs were validated through large-scale bridge column model tests and were found to be just as effective as steel shell jackets in providing desired inelastic design deformation capacity levels.

In the aftermath of the 1995 Hyogo-Ken Nanbu Earthquake in which many failures of bridge piers occurred, numerous studies have been conducted on ways to retrofit existing RC columns and piers. Mutsuyoshi et al. (1999) studied and found that continuous fiber sheets offer a feasible means of retrofitting. Consequently, several design guidelines on the use of FRP sheets for retrofitting highway, railway and subway structures have been proposed in recent years. The JSCE (Japan Society for Civil Engineers) Concrete Committee on FRP Sheet, has been commissioned to establish a new design method for seismic retrofit of bridge columns and piers. It seeks to unify all the existing guidelines on a performance-based design concept. The new design method of shear strength and ductility of retrofitted RC structures using FRP sheet is described and the design equations for shear strength and ductility are also presented.

The rehabilitation of RC columns jacketed with carbon FRP composites for improving shear strength, confinement, and ductility has received considerable attention. However, research for improving the shear capacity of beam-column T-joints in bridges using FRP composite materials is in the early stages. Gergely et al. (2000) describe the experimental results of fourteen 1/3-scale tests of concrete beam-column joints. The variables considered were the composite system, the fiber orientation, and the surface preparation. The tests demonstrated the viability of carbon FRP composites for their use in improving the shear capacity of the joints as evidenced by the experimental results. Based on these experimental results, a design aid was developed for T-joints with inadequate confinement and shear reinforcement.

Monti et al. (2001) proposed a design equation to determine the optimal thickness of FRP jackets and to enhance the ductility of existing RC bridge piers with circular cross sections.

The equation allows the design of the optimal thickness of FRP jackets in terms of the desired upgrading index, mechanical characteristics of the selected composite material, and quantities defining the initial state of the pier section. Seible (2001) describes jacket design criteria for various seismic column failure modes, and provides detailed examples of their application to retrofits of columns with circular and rectangular column geometry, different reinforcement ratios, and detailing. The paper also shows that the retrofit criteria and guidelines are applicable to other advanced composite jacketing systems with appropriate consideration for differences in mechanical properties of the materials system, installation and curing technology, as well as jacket discontinuities.

Pantelides and Gergely (2002) presented analysis and design procedures for the CFRP composite seismic retrofit of an RC three-column bridge bent. The CFRP jacket was designed using performance-based criteria to provide a target displacement ductility based on seismic retrofit measures for the columns, bent cap, and bent cap-column joints. In situ quasi-static cyclic tests of a bent in the as-built condition and a bent retrofitted with the CFRP jacket were carried out in 1998. The seismic retrofit was successful, and the bridge bent retrofitted with CFRP composites reached a displacement ductility level in excess of the target ductility and double the hysteretic energy dissipation of the as-built bent. A description of the CFRP composite layout and validation of the design assumptions from the experimental results was presented. Recommendations for improvement of the original CFRP composite seismic retrofit design were offered based on the lessons learned from the in situ tests.

Large Scale Tests of Bridge Systems with FRP Composites

Seible et al. (1999) conducted a large scale test on one “as-built” and four composite jacketed rectangular flexural bridge spandrel columns to assess the effectiveness of different retrofit schemes using FRP composite jackets. Three of the four FRP retrofit systems only addressed the lap splice region, whereas the fourth system connected the column jacket to the arch rib to improve the column/arch rib interface response. Final damage patterns and failure modes showed that only the latter scheme improved the seismic response whereas the other systems resulted in a sliding failure mode without improving the displacement capacity, which for the prototype bridge response is less desirable than the original “as-built” lap splice debonding failure. All retrofit schemes successfully clamped the column reinforcement lap splice above the column pedestal construction joint. The tests showed that FRP composite jacketing systems clearly can be installed without affecting the overall geometry or appearance of the structure, and emphasized the importance of designing retrofit strategies to control the mode of failure. Retrofitting of one weakness without considering the next mode of failure could lead to ineffective and poor designs.

In-situ lateral load tests of two bridge bents were conducted on Interstate 15 in Salt Lake City to determine the strength and ductility of an existing concrete bridge and the improvements that could actually be achieved using a CFRP advanced composite retrofit (Pantelides et al. 1999). The design of the CFRP composite retrofit was developed based on rational guidelines for the columns, cap beam, and cap beam-column joints to double the displacement ductility of the as-built bent. The advanced composite was able to strengthen the cap beam-column joints effectively for an increase in shear stresses of 35%, while the peak lateral load capacity was increased by 16%. The displacement ductility was significantly improved from the as-built bent to the CFRP retrofitted bent.

Large scale tests have been performed for investigating the retrofit of double-deck viaducts which incorporated cap beam prestressing (Priestly et al. 1993), and in-situ tests have been carried out on FRP retrofitted columns (Gamble and Hawkins 1996) and FRP retrofitted bridge bents (Pantelides et al. 1999a, 2001). The tests showed that FRP composite jackets are as effective as comparable steel or concrete jacket systems. The seismic retrofit of the State Street Bridge on Interstate 80 in Salt Lake City has been recently completed with a CFRP composite seismic retrofit (Pantelides et al. 2003a, 2003b), in which many of the retrofit concepts and experience developed from previous in-situ tests were implemented.

Bridge columns and decks were strengthened with CFRP rods and strips by Alkhardji (2001). The first part of the research focused on strengthening and testing to failure of the bridge decks. One of the three simply supported decks was strengthened using near-surface mounted (NSM) DFRP rods while another deck was strengthened using externally bonded CFRP strips. This led to the conclusion that the addition of FRP reinforcement improved the flexural capacity of the decks and that the design strengths were achieved in the field. The second part of the research presented the strengthening and testing to failure of the bridge columns. This part of the research program aimed at investigating the feasibility and effectiveness of using NSM CFRP rods to improve the flexural capacity of the columns. Test results indicate that the proposed strengthening technique is feasible and effective for improving the flexural capacity of RC columns.

Saatcioglu and Grira (2001) carried out an experimental investigation to verify the use of FRP grids as transverse reinforcement in concrete structures, placing emphasis on concrete confinement and seismic loading. Column reinforcement cages consisted of ordinary steel reinforcement as longitudinal bars and FRP grids as transverse reinforcement. Test parameters included grid spacing and pattern, the volumetric ratio of grid reinforcement, and the level of axial load. Results indicate improved deformability of columns, when confined by properly designed grids.

Three in-situ tests were performed on two bents of a reinforced concrete bridge under quasi-static cyclic loads (Pantelides et al. 2001). The bridge was built in 1963 and did not possess the necessary reinforcement details for ductile performance. The tests included an as-built bent, a bent rehabilitated with CFRP composite jackets, and a damage bent repair with epoxy injection and CFRP composite jackets. Two new concepts of strengthening bridge bents with FRP composites were implemented; the first involves shear strengthening and confinement of beam cap-beam joints through an FRP composite “ankle-wrap”; the second is an FRP composite “U-strap” to improve anchorage of column longitudinal steel reinforcement extending into the joint. FRP composite jackets were implemented in the columns and beam cap. The performance of the bent in the as-built condition and that of the rehabilitated and repaired bents is described in terms of strength, stiffness, displacement ductility, and energy dissipation.

Sheikh (2001) tested columns retrofitted with CFRP and GFRP composites to improve the seismic resistance of the concrete columns. Twelve circular and sixteen square columns were tested under simulated earthquake loads while simultaneously subjected to gravity loads. The results showed moment curvature responses of the sixteen columns. The investigation explains that retrofitting with FRP of both circular and square columns can result in improving their brittle behavior to highly increased ductile behavior, thus significantly improving their seismic resistance.

It is clear from this literature review that FRP composites are well suited for seismic retrofit. The low weight, high strength and ease of application make these materials unique candidates for seismic retrofit. Even though the technology has been implemented, little data exists for verification of the performance of retrofitted structures in seismic events. Seible and Priestley (1999) reported that in the 1994 Northridge earthquake all bridge structures in the region of strong ground motion, that were retrofitted since the 1989 Loma Prieta earthquake, performed adequately without damage requiring repairs. Moreover, it was demonstrated that assessment analyses, performed on six bridges that collapsed due to column failure showed that collapse could have been prevented if existing column technology had been implemented before the 1994 Northridge earthquake.

Several improvements and developments are anticipated in the coming years. One area where little work has been done within the research community is seismic rehabilitation, i.e., repair of structures damaged during earthquakes. One such study of an in-situ test of a bridge, which was damaged and then rehabilitated with FRP composites and was tested again, has produced some encouraging results (Pantelides et al. 2001). In the future, more research needs to be carried out to determine the viability of FRP composites used alongside more commonly used materials for seismic rehabilitation.

Objectives

The present report describes the test procedures and results of three in-situ full-scale tests carried out in Salt Lake City, Utah in 2000. The tests were carried out on the southbound lanes of the South Temple Bridge at Interstate 15, in Salt Lake City. The first test was carried out on a three-column bridge bent without the road deck (Bent #4S), the second test was carried out on an identical three-column bridge with half the gravity load present from the deck (Bent #5S), and the third test was carried out on Bent #6S, with half the gravity load from the deck, which was seismically retrofitted with carbon fiber reinforced polymer (CFRP) composites. For all three bents, the foundation was retrofitted through a reinforced concrete grade beam overlay. The objective of this report is to report provide detailed information on the test setup, the loading scheme used to simulate seismic loads, a description of the condition of the as-is bridge bents, the design of the CFRP composite for seismic retrofit of Bridge Bent #6S, and an assessment of the performance of the three bridge bents.

2. BRIDGE BENT #4S WITH GRADE BEAM RETROFIT WITHOUT THE DECK

Interstate 15 through Salt Lake City was built in 1963 and a 17-mile portion, which included 142 bridges, was slated for reconstruction. In 1998, three lateral load tests on the northbound lanes of South Temple Bridge were performed on two bents (Pantelides et al. 2001); the first test was for an as-is Bent #5N (1998), the second for a CFRP retrofitted Bent #6N (1998), and the third was for Bent #5 repaired with epoxy injection and subsequently retrofitted with CFRP composites, which is test Bent #5R (1998). The southbound lanes of the South Temple Bridge consisted of eight three-column bents. Bridge bents #4S, #5S, and #6S were tested in 2000: Bent #4S was freestanding, with no superimposed dead load, whereas Bents #5S and #6S supported the section of road deck between them throughout testing. Bent #6S had been retrofitted with CFRP composites, whereas Bent #5S was tested in the as-is condition. This paper focuses on experimental observations of the test for Bent #4S (2000).

Reinforced concrete bridge structures are designed to allow ductile behavior and ultimately be either serviceable or repairable after a severe earthquake. Undoubtedly, the design of new structures is performed for the maximum possible earthquake energy dissipation, but what of existing structures too expensive to demolish and reconstruct? The objective of the test carried out of Bent #4S was to analyze such a structure to determine the following: (1) existing capacity, (2) failure mechanisms, and (3) through performance-based evaluation and damage level criteria, the adequacy of existing bridge systems.

Bridge Bent Description

Bent No. 4S of Bridge No. 58 was located at South Temple and 750 West. The structure was used as an overpass of a Union Pacific Railroad train junction in downtown Salt Lake City. Components of the bent include: (1) the Superstructure made of the Cap Beam and three Columns, and (2) the Substructure made of the Pile caps, Strut Beams, and the Piles. The cap beam is a 19.71m x 1.219m rectangle with ends that taper 0.31 m from 2.15m, which is the outer face of the two of the three columns, which support the cap beam. The two outer columns are spaced at equal increments from the centerline of the middle column, which is also the centerline of the system. The three columns are 0.914m square extending from the top of the pile cap to the bottom of the cap beam, a total distance of 6.947m; complete dimensions are provided in Figure 2.1.

The internal details of the cap beam are denoted by the rebar detail in Figure 2.2 and the cross-section details in Figure 2.3. A clear cover of 63.5mm was used in the cap beam, and 89 mm of clear cover was used in the columns. There are two notable details at the column ends. The first interesting detail is the lap splices, located from the cold joint at the top of the pile caps to approximately 762mm into the columns. This is an important detail, as the splice slips during the test and the strain values disappear. The second point is the cold joint at the top of the column. The columns were cast and cured before the cap beam was cast. The rebar details in the Utah Department of Transportation (UDOT) original drawings call for a lap splice piece of bar to continue to the top of the cap beam. Whether installation was neglected at the time of construction or if it was an oversight is yet to be determined, but it proves to be a mistake as the column bars stop 356mm from the top of the cap-beam, as indicated in Figure 2.2. Thus, there were four design/construction deficiencies: (1) inadequate confinement of the columns, of the column lap splice region, and plastic hinge regions; (2) inadequate shear capacity of columns; (3) lack of hoop reinforcement in the bent cap joint regions; and (4) inadequate anchorage of the column longitudinal reinforcement into the bent cap and pile caps.

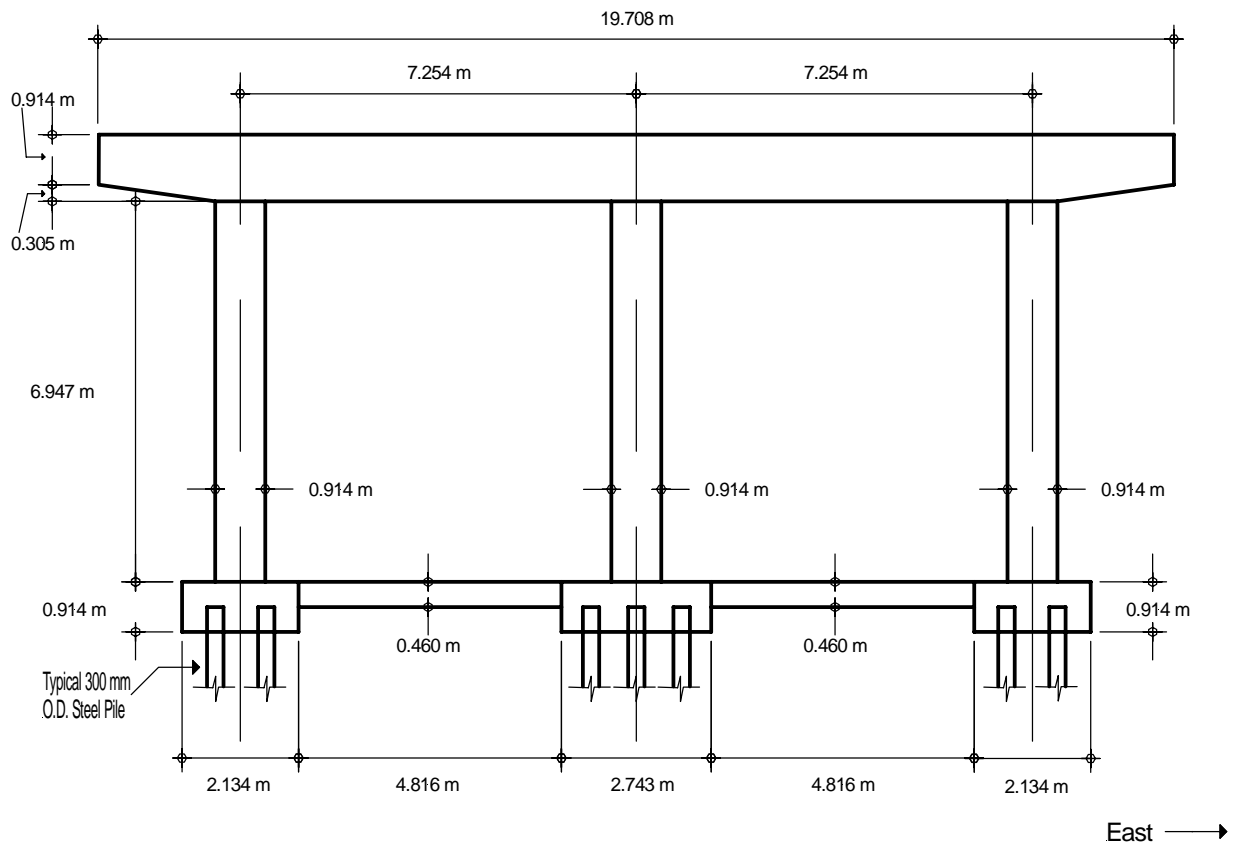


Figure 2.1 As-built dimensions of Bent #4S

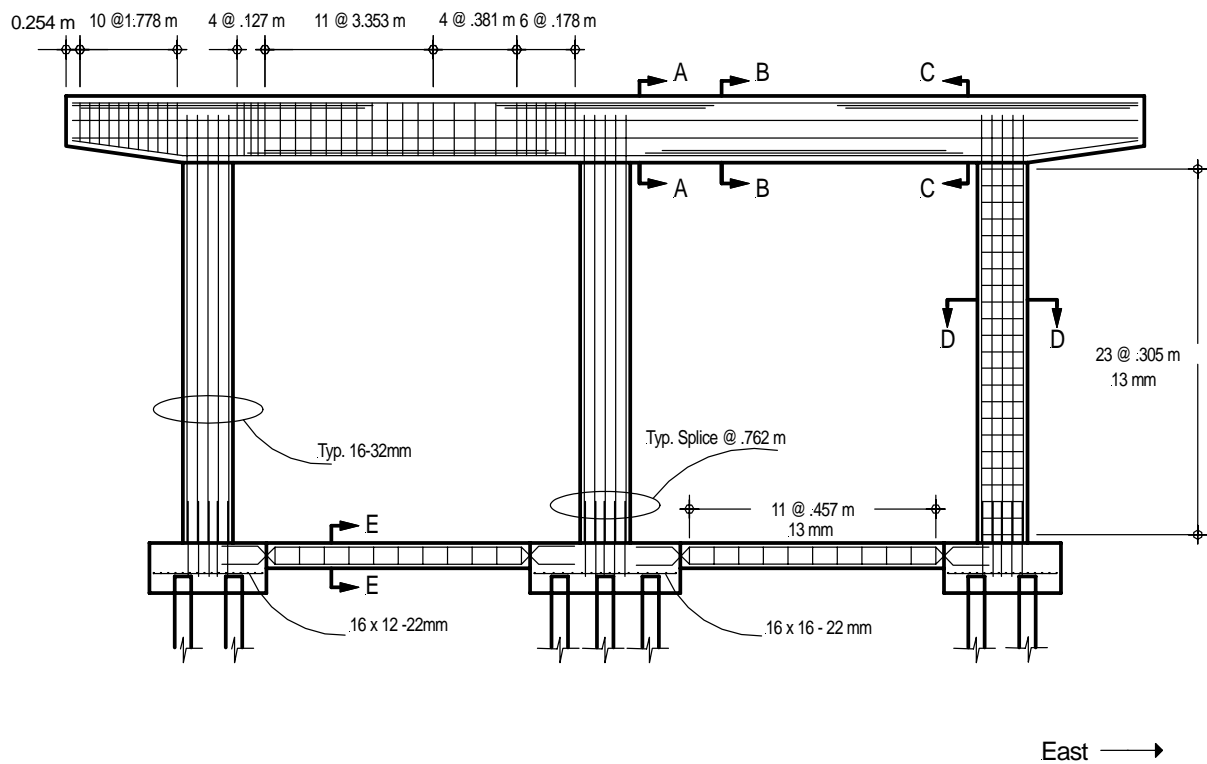


Figure 2.2 As-built rebar detail of Bent #4S

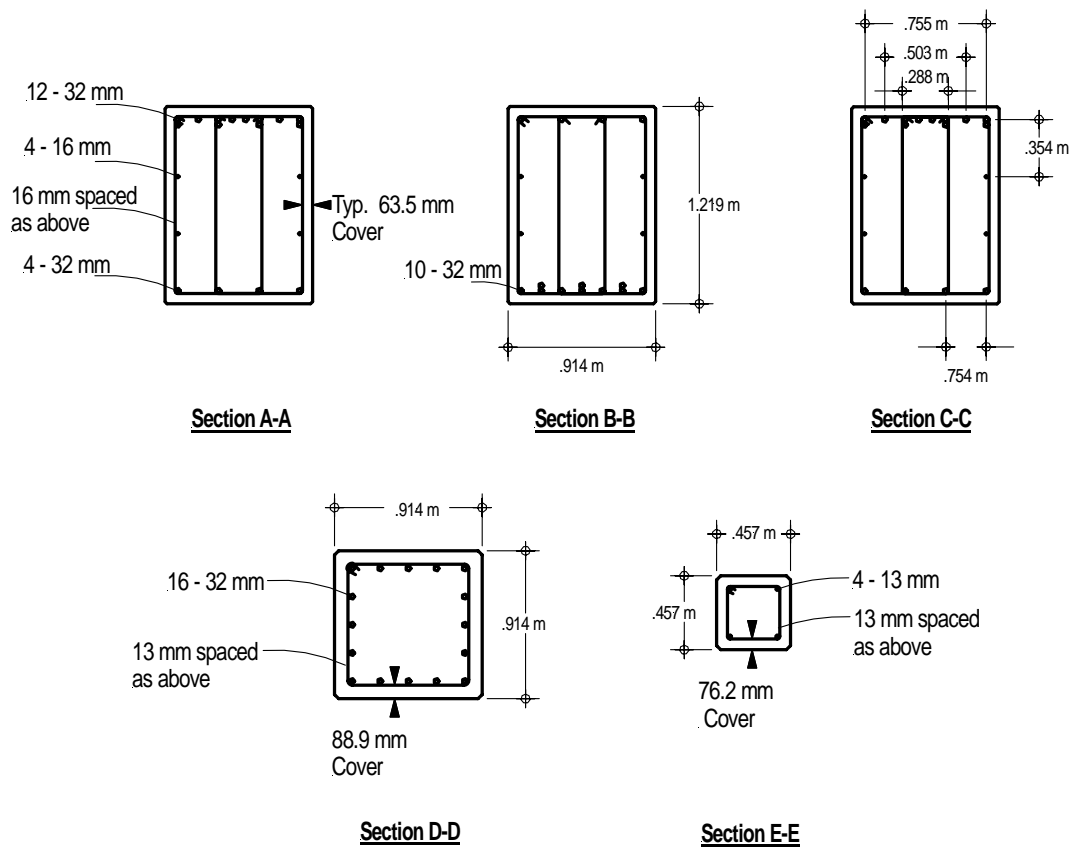


Figure 2.3 As-built steel details of Bent #4S

The first components of the substructure are the piles and the pile caps as shown in Figure 2.4. The piles are 300mm diameter, with a 7-gage steel wall thickness, driven to approximately 23.16m then filled with concrete. Three separate pile groups exist; the exterior pile groups include four piles set in a 1.219m square pattern, and the interior pile group has five piles in a 1.829m square with one pile placed in the center. A rebar mat of [12 x 16] - 22mm (#7) for the exterior pile groups and a [16 x 16] - 22mm mat for the center pile group, lies on top. There are three individual pile caps that correspond to the three columns.

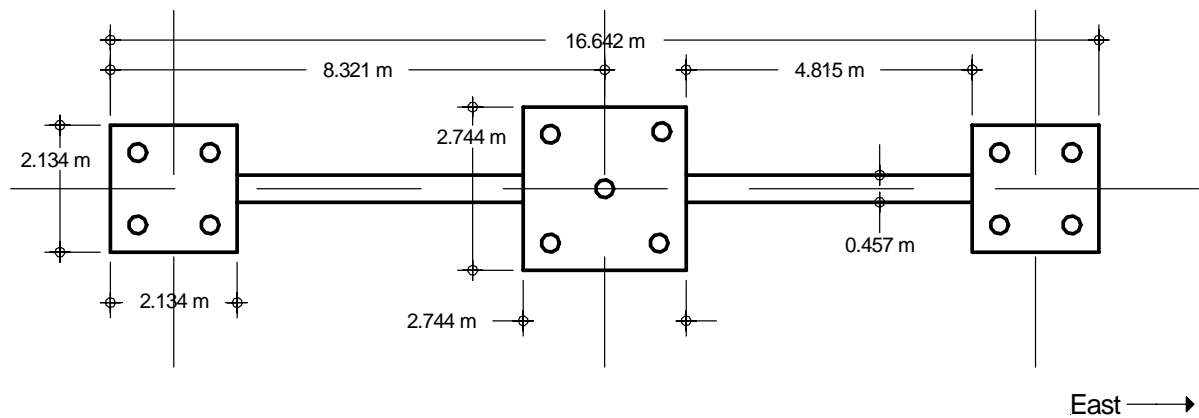


Figure 2.4 As-built footing plan section of Bent #4S

The exterior pile caps are similar in dimension 2.13m square by 914mm thick encompassing the rebar mat and the top 305mm of the pile groups. The center pile cap is 2.743m square and 914mm thick; it also encompasses the rebar mat and the top 305mm of the pile group. The second component of the substructure is the strut beams; these are essentially “spacers” to keep the pile caps properly spaced and tied to each other. The general dimension is 457mm square x 4.815m long. There are 4-25mm longitudinal bars set in the corners with 76 mm of clear cover. They tie into the pile caps via lap splices on the strut side. There are 11-13mm transverse reinforcement closed hoops spaced at 457mm, as shown in Figures 2.2 and 2.3.

Vertical Load

Bent #4S was for all purposes the baseline control in the 2000 tests. It was the only bent that had no superimposed dead load on it while undergoing testing. It only retained the dead loads generated by self-weight; 503kN total weight of the cap beam and 138kN per column. It did however see a lifetime of load bearing service. The total dead load for these bents in service was approximately 4780 kN per bent (Duffin 2003). This load was distributed to eight points located along the top of the cap beam. Thus, it can be inferred that Bent #4S had barely 16.1% of the in-service dead load, whereas Bent #5S and Bent #6S had a dead load equal to 58.0% of the in-service dead load. Alternatively, during the 2000 tests, Bent #4S had only 27.7% of the dead load that Bent #5S and #6S had when they were tested.

Condition of Bent #4S in 2000

The general condition of Bent #4S in the spring of 2000 was as follows: the vertical columns had very minor cracking and hardly any spalling, and the horizontal cap beam had practically lost its clear cover. There had been severe spalling on various sections of the 37 year old structure due to concrete degradation brought on by rebar corrosion/expansion and freeze/thaw action. Although the significant spalling appeared to be restricted to the cap beam on the bottom face between the columns and the three vertical faces of both tapered ends, the entire cap beam vertical faces had many hollow sounding spots that rendered the clear cover of the cap beam useless. These areas of the cap beam also revealed longitudinal and transverse reinforcement that had been severely weathered. The columns, strut-beams and pile caps were all clean and intact. Photographs of spalling are provided in Figures 2.5, 2.6, and 2.7. Clearly, the state of the cap beam was in serious deterioration; more details for an in-depth study of the impact of the corrosion on the shear capacity can be found in the study for the northbound bridge tests carried out in 1998 (Pantelides et al. 2000).

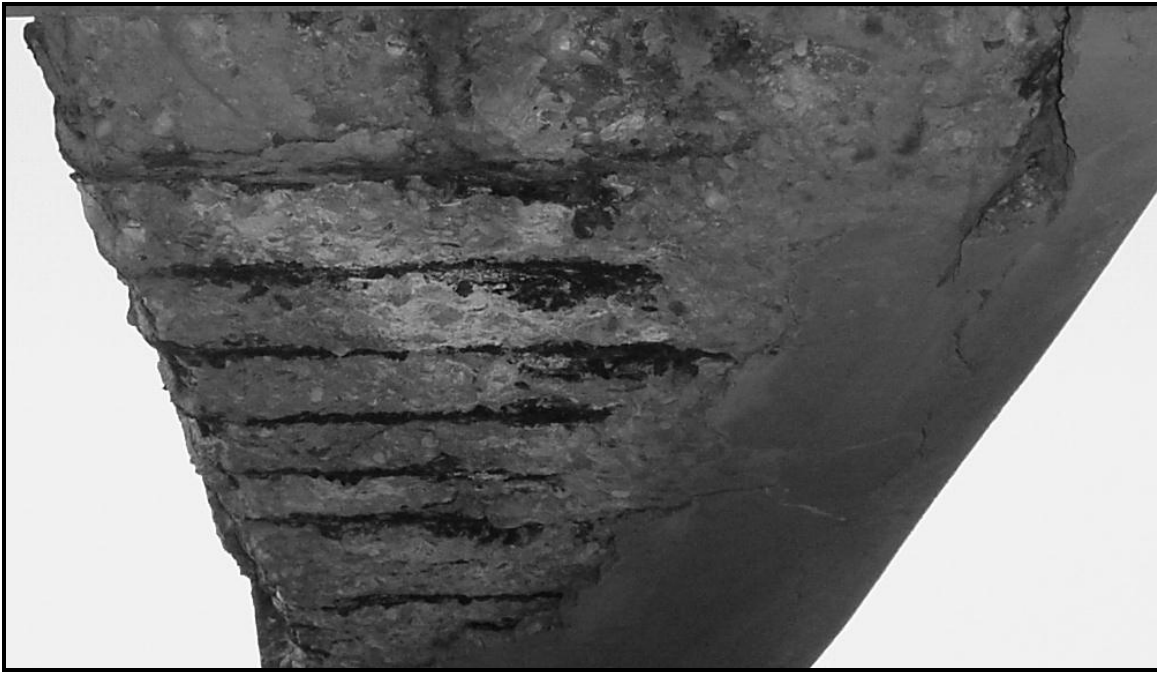


Figure 2.5 Spalling under cap beam of Bent #4S

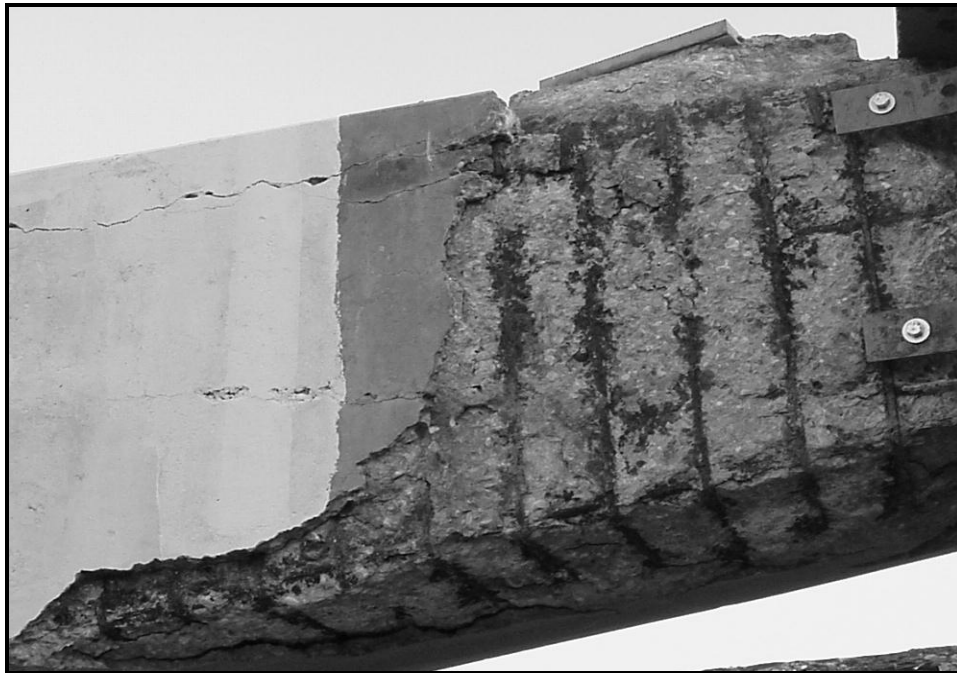


Figure 2.6 Spalling due to reinforcement deterioration on cap beam of Bent #4S



Figure 2.7 Clear cover under cap beam barely attached on Bent #4S

Grade Beam Design for Foundation Retrofit

The grade beam was developed in order to close the compression/tension load path to be created in the structure during lateral loading. The larger mass would also make it harder to displace the entire structure, making the system act more like a fixed base. There was also a safety issue related to disassociating the pile caps from the piles in shear and or moment before reaching the capacity of the system. For the above reasons, a reinforced concrete grade beam was cast monolithically around the existing columns, pile caps and struts as shown in Figure 2.8.

In order to keep the pile caps from de-bonding off of the piles, holes were cored 1.524m into the piles and 35mm (#11) Dwyidag bars were epoxied in place, one in each corner pile of each pile cap, for a total of 16 bars. After the grade beam cured a 152mm square x 25mm thick plate was fastened down to the new grade beam, so as to keep the piles, cap, and grade beam in compression, thereby reducing the probability of pullout. The overall dimensions of the reinforced grade beam were 762mm x 2.133m x 17.557m. The overall depth of the entire beam was 762mm, with the exception of the depth over the pile caps, which was 305mm. The grade beam extended past the exterior pile caps 457mm, with a knee joint return of 762mm in depth. Twenty-four 25mm bars run the length of the grade beam, 12 on the top and 12 on the bottom spaced evenly at 185mm. For the long runs to the north and the south of the columns these longitudinal bars are spliced 1.525m over the mid-spans between the columns as shown in Figure 2.9(a). Transverse reinforcement consisted of 10mm bars in one of four configurations, which can be seen in Figures 2.9(c)-(f). Transverse reinforcement is spaced at 152mm or 406mm as shown in Figure 2.9(b).

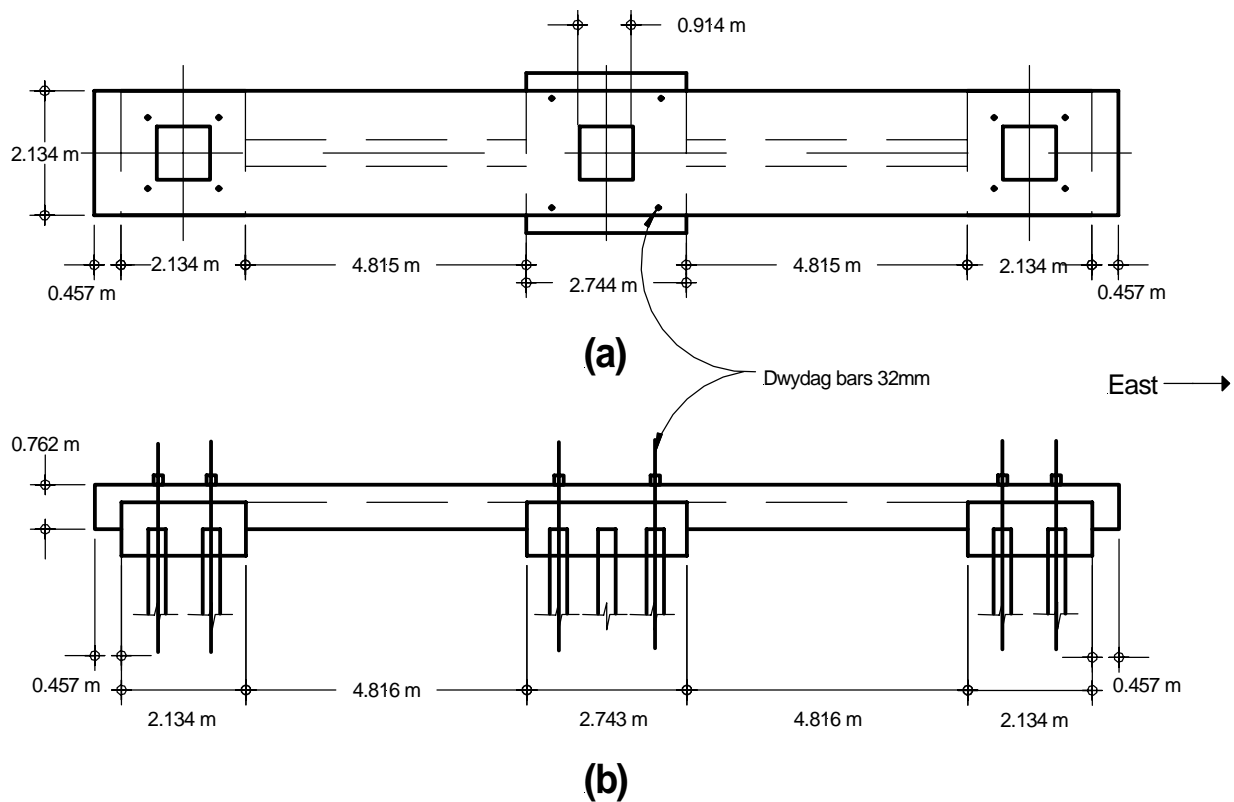


Figure 2.8 As-built substructure of Bent #4S (2000): (a) plan, (b) elevation

Material Properties

The material properties of Bent #4S were determined by obtaining concrete cores and rebar from the mid-height of the columns.

Steel

Tensile tests were performed on the rebar to determine: (1) yield stress (σ_y), (2) ultimate strength (σ_u), (3) yield strain (ϵ_y), and (4) ultimate strain, (ϵ_u). The number of bars and bar sizes included in the test is shown in Table 2.1. This includes the tests done for the new grade beam steel as well.

Table 2.1 Tensile rebar testing schedule for Bent #4S

No. of samples		Diameter (mm)
Existing Bent Structure		
4		32
1		19
3		16
New Grade Beam		
2		25
2		10

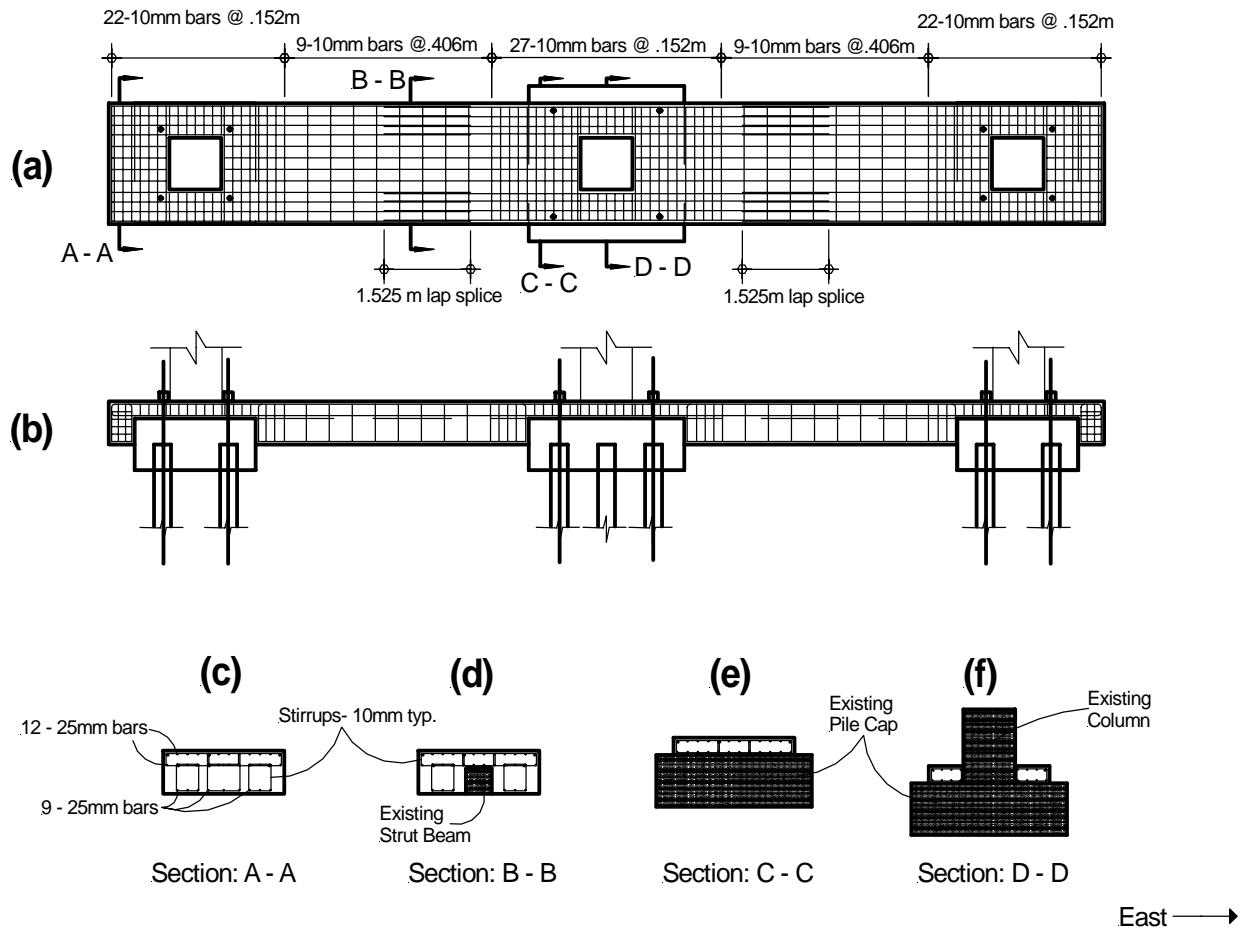


Figure 2.9 Modified grade beam for Bent #4S: (a) plan, (b) elevation, (c) knee joint cross section, (d) mid-span, (e) overlay of existing pile cap, (f) overlay of existing pile cap around column

The Young's Modulus of steel E was found as 199.9GPa from the average stress/strain curve that best represented the steel properties of the entire system. The original design specification obtained from the UDOT plans called for rebar reinforcement of grade 276MPa. The yield stress of the tested rebar was determined to be 363Mpa. This is 24% stronger than the original design considerations. The rebar that was put into the grade beam underwent similar testing and it was determined that the strength was 469MPa compared to the design value of 414MPa, resulting in 11% strength increase. Material properties for Bent #4S steel are tabulated and shown in Table 2.2.

Table 2.2 Steel rebar tensile characteristics for Bent #4S

Specimen	Bar Grade	F_y (MPa)
Existing Bent	40	364.4
New Grade Beam	60	454.7

Concrete

Using ASTM C 42/C - 42/M -99, cylindrical cores were extracted from the centers of the columns. Four 102 mm diameter x 402mm length cylinders are the basis of the concrete strength characteristics for Bent #4S. With the load/cross-sectional area and the strains measured during the tests, the stress strain curves could be plotted with the equations given by Hognestad et al. (1955) as shown in Figure 2.10:

$$f_c = f'_c \left[\frac{2\varepsilon}{0.0024} - \left(\frac{\varepsilon}{0.0024} \right)^2 \right] \quad (2.1)$$

for $\varepsilon \leq 0.0024$ mm/mm

$$f_c = f'_c [1 - Z(\varepsilon - 0.0024)] \quad (2.2)$$

for $0.002 < \varepsilon \leq 0.004$ mm/mm, and $Z = 80$ for confined concrete in the core; in Figure 2.10 the lower curve is the existing bent concrete and the upper curve is the new grade beam concrete. The value of concrete compressive strength used in the theoretical calculation and analytical program for Bent 4 was taken to be 34.0MPa, which is the ultimate strength of the actual tests and is shown in Table 2.3; this value is 23% higher than the specified concrete strength of 27.6MPa. The average compressive strength of the new grade beam concrete was obtained from cylinders made at concrete casting and was found as 39.3MPa.

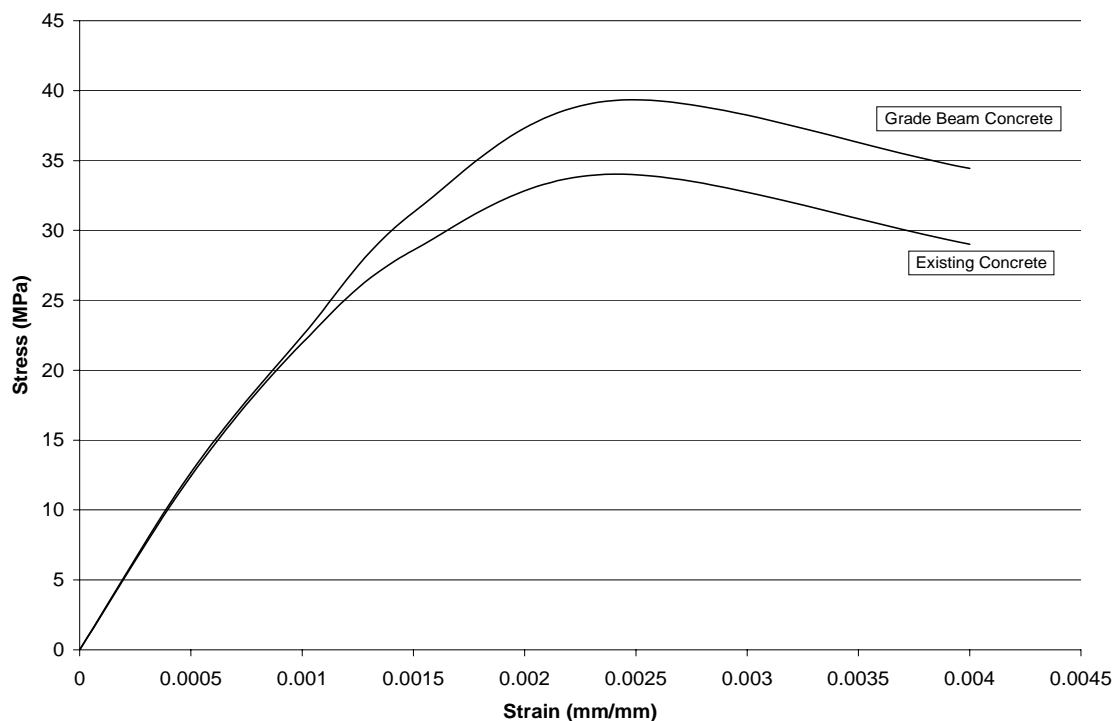


Figure 2.10 Stress/Strain curves for existing and grade beam concrete in Bent #4S

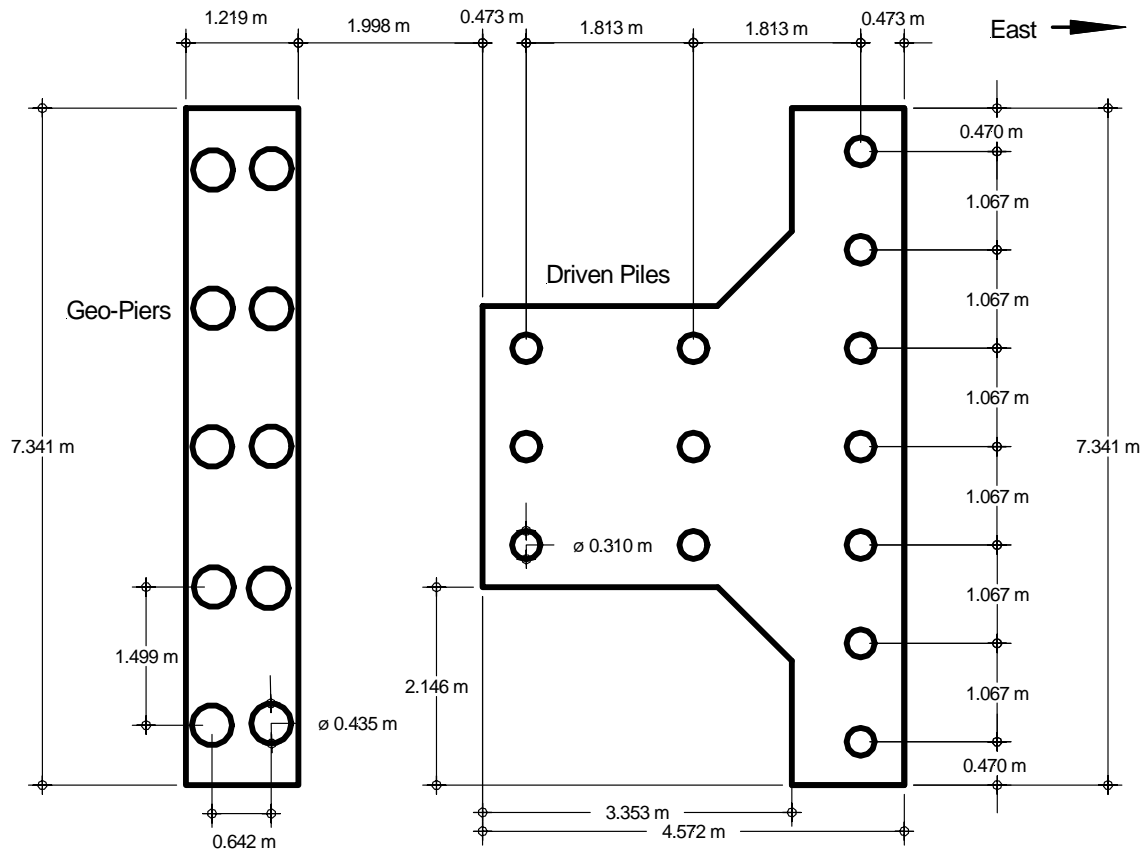
Table 2.3 Concrete compressive strength characteristics

Specimen	f'c (MPa)
Existing Bent	34.0
New Grade Beam	39.3

Loading System

Load Frame Footings

The loading of Bent 4S during the test was a quasi-static cyclic load. There were two separate footings supporting the load frame; the rear footing shown in Figure 2.11, was a reinforced concrete T-shaped pad 1.524m thick; the footing set upon 13-310mm steel piles that were driven to 15m depths. The front footing sits 1.99m to the west of the rear footing, oriented in the same plane; the footing is also 1.524m thick, with a rectangular shape; this footing is set on 10-435mm rock columns called geo-piers. These foundations provided the uplift and shear resistance required to support the load frame.

**Figure 2.11** Load frame footings for Bent #4S

Load Frame

The original structure was built for testing of the northbound bridge bents in 1998 (Pantelides et al. 2000). Some modifications were made to the load frame in order to allow it to reach the bents during the tests. An extension was made from a 609mm diameter and 19mm wall thickness structural pipe, which extended from the front face of the stiffened box between the apexes of the two A-frames, as shown in Figure 2.12. The design calculations used to size the members in this load frame are included elsewhere (Delahunty 2003). This structure was made of several components, of which the first two components are A-frame structures made of AISC steel wide flange shapes as shown in Figures 2.13 and 2.14. W12x65 members made up the exterior shape, which includes the base. The vertical interior members were W8x31 shapes. The horizontal and diagonal members in the A-frames were 102mm diameter structural pipes with 13mm wall thickness that were notched and welded into 13mm knife plates, which were in turn welded to the flanges of the W12x65 and W8x31 members. The first tier horizontal structural pipe member was located 1.60m from the top of the footing, the second tier 3.15m above the footing, the third tier 4.65m above the footing, and the apex of the A-frame was 7.672m above the footing.

The load frame was placed onto the footings around 16-38mm stainless steel threaded rods, and then leveled so as to ensure the hydraulic actuator would be level with the bent at the center point of the cap beam. If any air gaps existed between the four pads of the load frame and the footings, a non-shrink grout was packed into the voids to ensure that the load frame would not flex during the loading cycles. The excess voids in and around the embedded stainless steel tie down rods filled with a high strength epoxy to ensure the frame would not slip around during loading. After the grout and epoxy had cured, a 25mm thick x 102mm wide x 203mm long plate with a 38mm hole was placed over each tie down rod and welded to the load frame pads as shown in Figure 2.15. Only then were the nuts placed on the rods to secure the load frame to the footings.



Figure 2.12 Load frame actuator extension modification

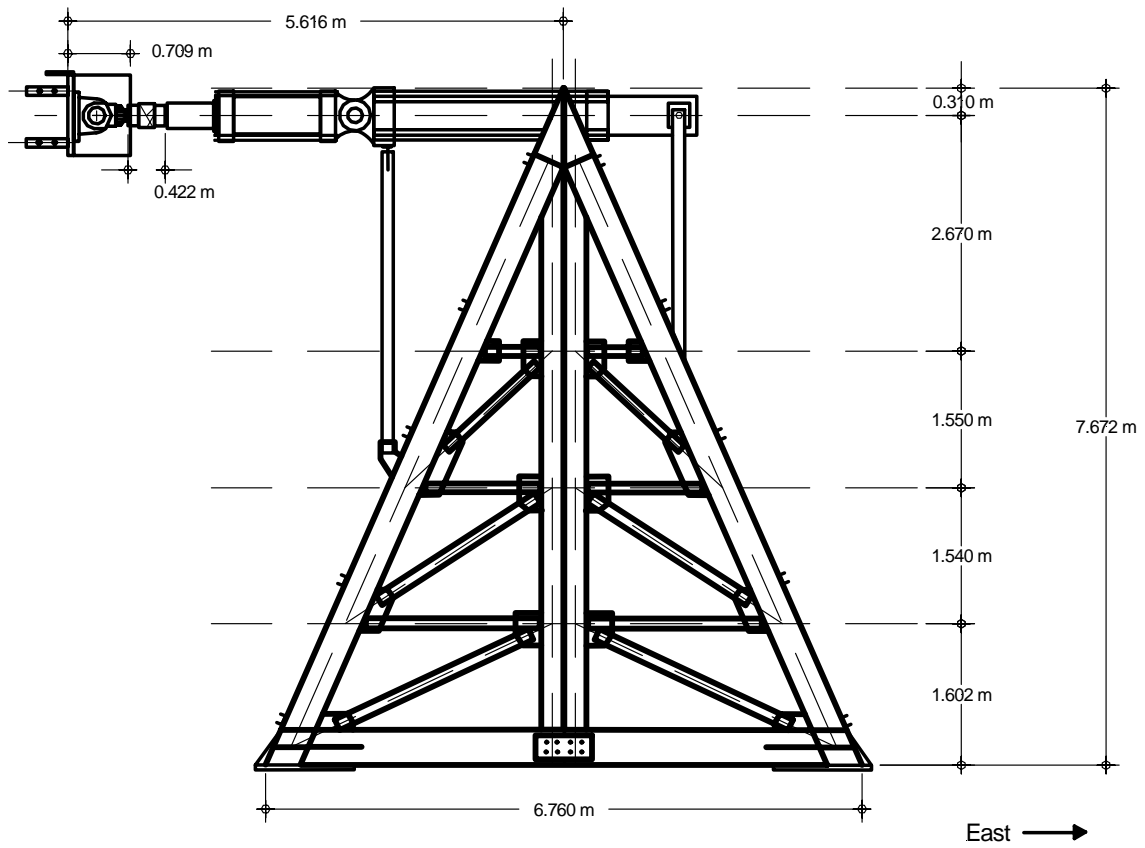


Figure 2.13 Side view of load frame with hydraulic actuator



Figure 2.14 Load frame front view



Figure 2.15 Load frame pad with 38mm threaded tie down rods and welded plates

Push and Pull Interface System

The hydraulic actuator used in the tests was a 406mm bore, 203mm rod, with 762mm stroke, tie rod cylinder as shown in Figure 2.16. This actuator was serviceable up to 2.68MN of extensive force. The load cell used was a 2.76GN capacity strain based transducer; it was placed onto the actuator rod by means of 102mm NPT connection milled into the rods, as shown in Figure 2.17.

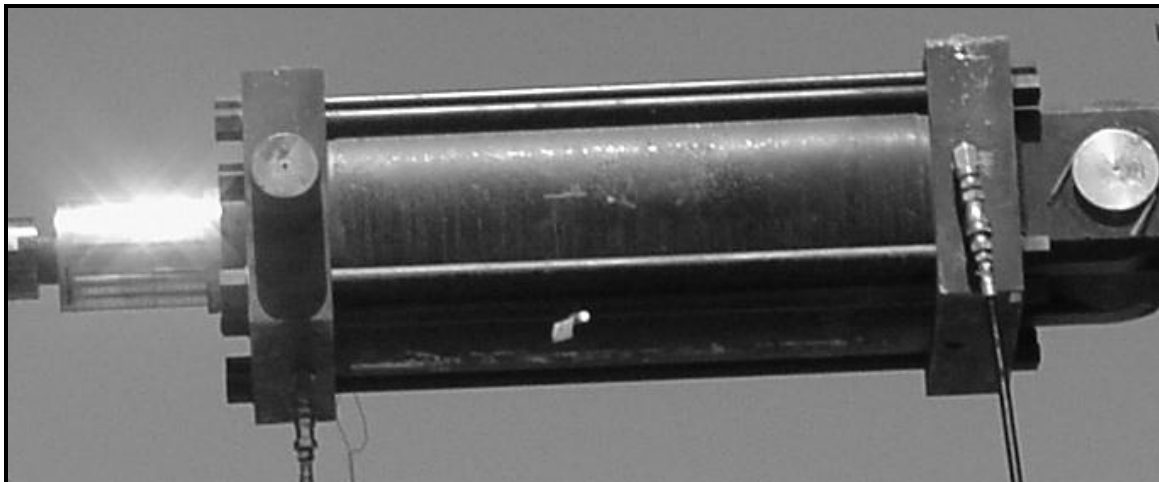


Figure 2.16 Hydraulic actuator used in testing

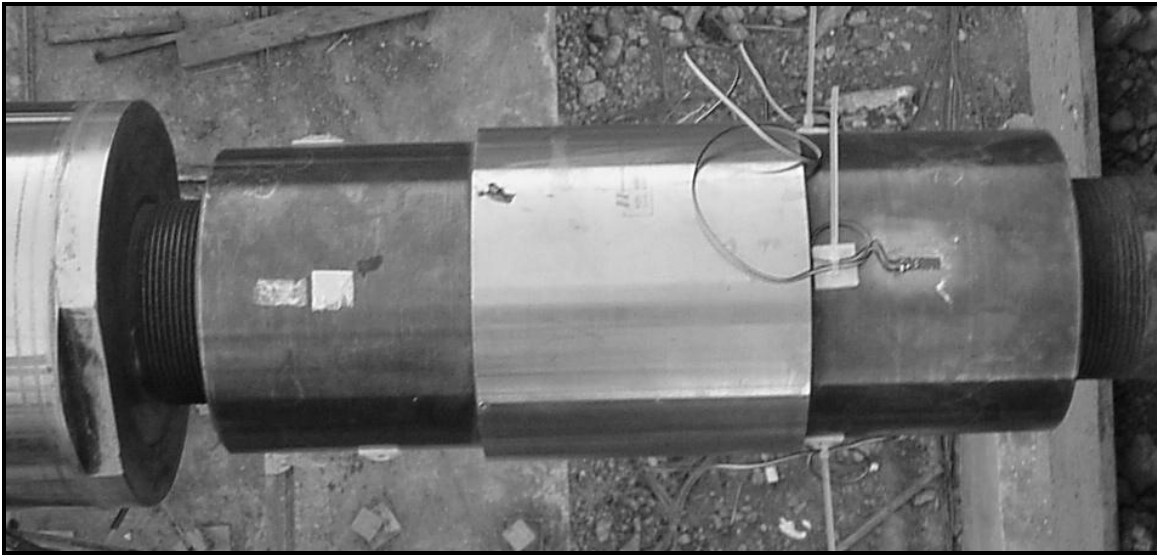


Figure 2.17 Load cell with 2.76GN capacity

To apply a cyclic load the bridge bent had to be pulled to a given displacement, which required a system that would act as if the actuator was actually pushing from the west end instead of pulling from the east. A system of two steel boxes (Figure 2.18) that were 51mm wider than the cap ends, was placed on the two beam cap ends, and 20 strands (ten on each side) of high-strength 13mm, seven wire pre-stressing cable was threaded through the holes in the steel boxes and chucked as not to slip through the holes. The pre-stressing cables were then stressed one by one to 4.45kN per strand (See Figure 2.19).

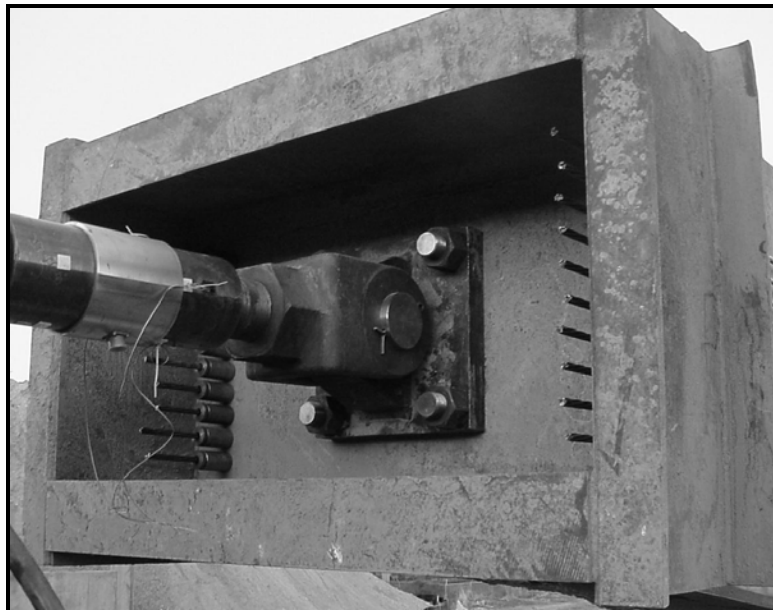


Figure 2.18 Load cell, clevis connection and push box with chucked pre-stress tendons located on the East side of Bent #4S



Figure 2.19 Pull box with pre-stressing tendons stressed to 4.45kN each, located on the west end of Bent #4S

Instrumentation

Cable-Extension Displacement Transducers

The use of Cable-Extension Displacement Transducers (CEDT or DT) to measure critical displacements of the entire bent system, including the on screen display for displacement step and cycle control was critical. A total of fourteen DT's were used to record various points on the bent. Two sets of three-tier tall scaffolding were erected, one on the east side of the loading frame, and the other on the west end of the bent. These scaffolds served as the anchor points for most of the DT's. As detached points from the system there was no influence of motion on the fixed end of the DT, and eliminated the possibility of error in displacement values. Two DT's were attached to the outer and upper most East and West edges of the cap-beam to record the maximum displacement of the system as shown in Figure 2.20. The remaining DT's were implemented to enable calculations relating to curvature of the column faces. Three sets of three DT's were placed on the West scaffold corresponding to the top and bottom 458mm of the west face of the center and west columns.

Linear Variable Differential Transformers

On and around the joints of the bent a device that can measure small displacements is necessary to understand certain behaviors that can not be captured by a DT. The linear variable differential transformer (LVDT) is a well suited device for such measurement. A total of 17 LVDT arrays were employed on Bent #4S. These sensors are located primarily around the base of the center column and the center column/cap-beam joint. This was done to monitor deformation in the joint, buckling and curvature of the columns. The locations of the LVDT arrays are shown in Figure 2.21.

Strain Gages

As strain gages are usually bonded to isotropic materials, it became necessary to core into Bent #4S at strategic locations, in order to attach the gages to the rebar set behind an average of

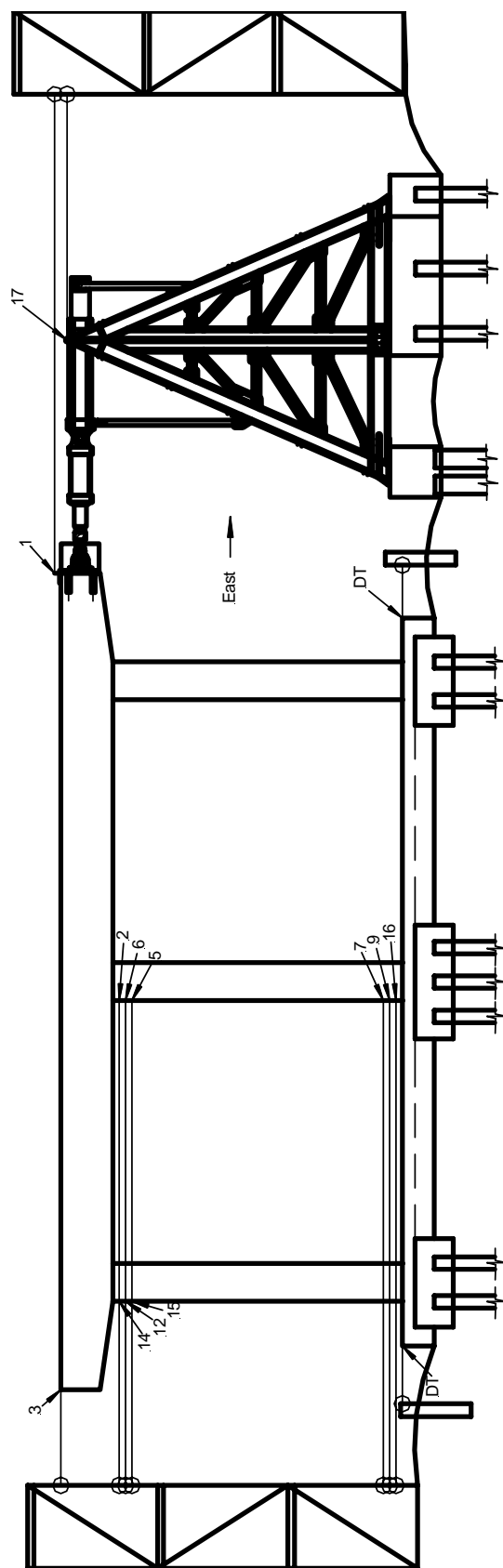


Figure 2.20 Location of CEDT instruments

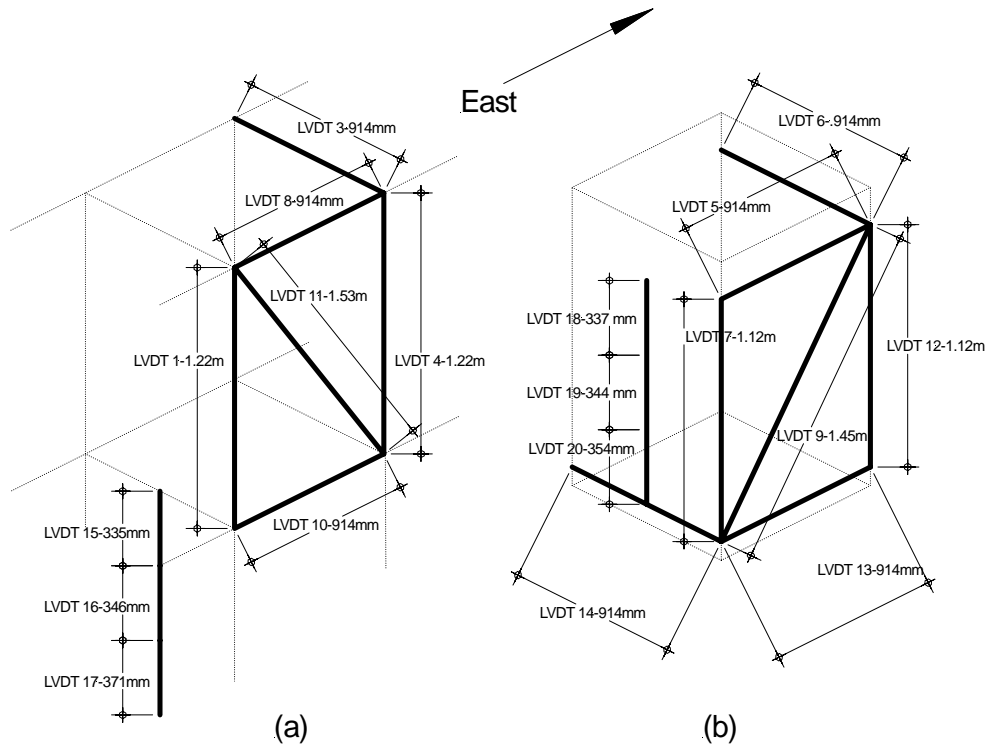


Figure 2.21 LVDT array: (a) South face of center column, cap-beam joint, (b) South face at the base of center column

70mm of concrete. The coring was stopped just short of the steel bars, as not to damage them. A total of 82 individual gages were installed in Bent #4S (2000), as shown in Figure 2.22. All strain gages on the columns are on the East faces of their respective columns. The strain gages located at the bottoms of the columns are strategically placed over the top of the lap splices. All strain gages on the cap-beam are set on the North face of the structure. All strain gages set in the grade beam are evenly spaced across the width of the beam. The strain gages in the driven piles are attached to the Dwyidag bars which were installed into the piles.

Test Procedure and Structural Response

A uniaxial cyclic compression (push) and tension (pull) procedure was the basis of motion for this experiment. The testing protocol was displacement-based increments, determined by the drift ratio. The actuator under hydraulic pressure was made to push to the desired positive displacement then stopped, retracted to the starting (zero) point then retracted further to the corresponding negative displacement then stopped and returned to the original (zero) starting point; this single cycle is denoted as the first cycle. The cycle is repeated two more times at the exact displacement levels as the first. The three cycles to the same displacement increments are denoted as the first step as shown in Figure 2.23. The drift of the system is calculated as

$$Drift = \frac{d_l}{H_s} \quad (2.3)$$

where d_l is the lateral displacement of the system at the hydraulic actuator level, and $H_s=7.709\text{m}$.

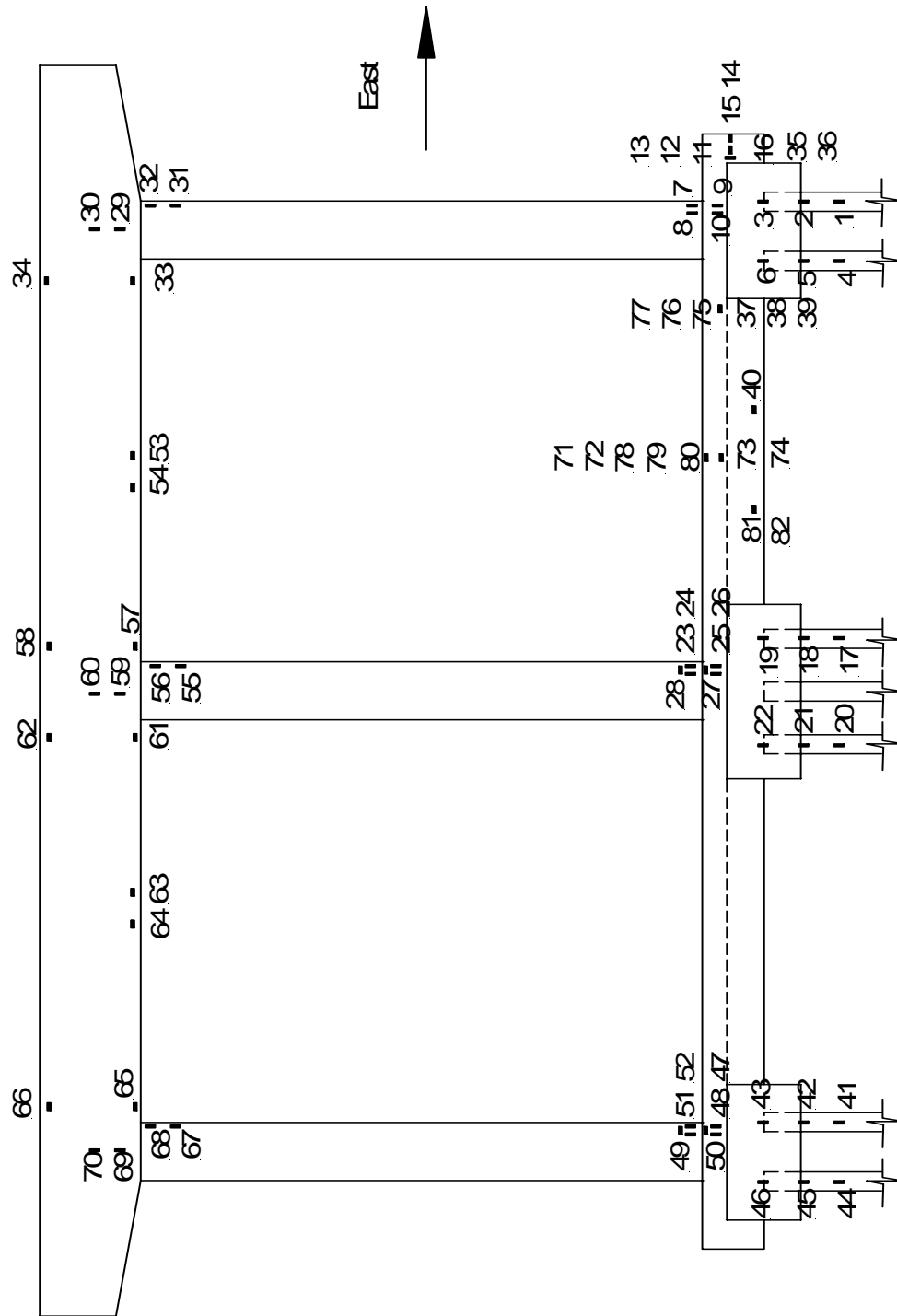


Figure 2.22 Locations of strain gages on Bent #4S

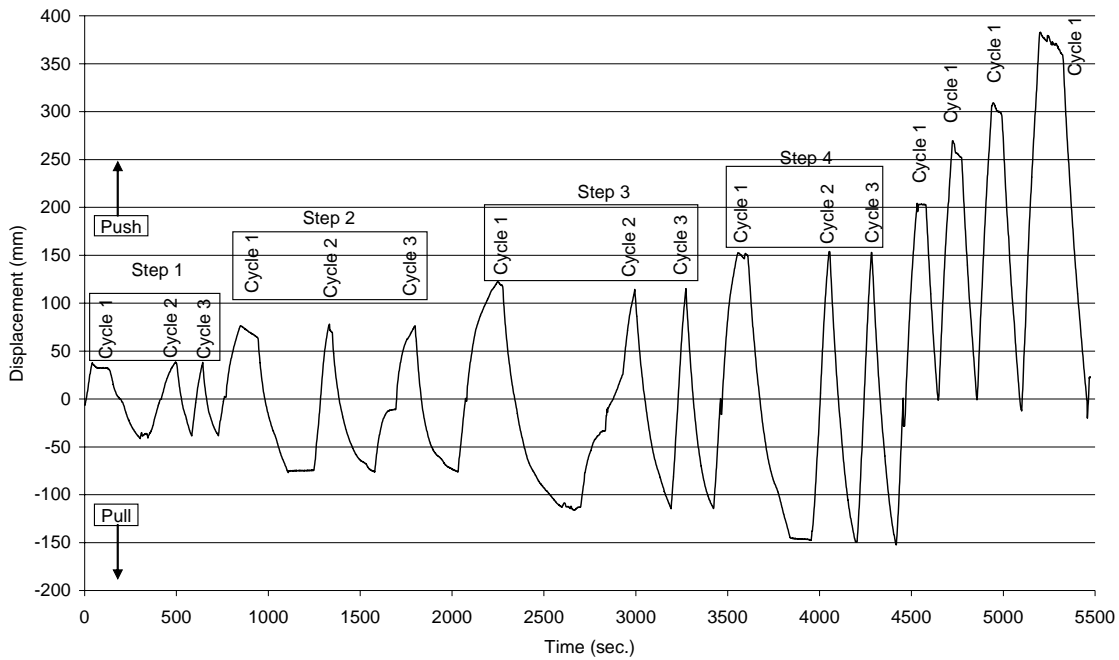


Figure 2.23 Displacement of Bent #4S vs. time with steps and cycles

The maximum pull or push displacement that the hydraulic actuator was capable of was $\pm 381\text{mm}$. The percent drift ratio (displacement) corresponding to the steps of the experiment was: 0.5% (39mm), 1.0% (78mm), 1.5% (117mm), and 2.0% (156mm). At this point in the experiment, the test was continued at push steps only with one cycle per step. The final drift ratio (displacement) was as follows: 2.6% (203mm), 3.29% (254mm), 3.95 % (304mm), and 4.94% (381mm). Limitations in the load capacity on the pull side of the system, moving load frame footings, slightly moving system footings, and elastic stretching of the pre-stress tendons all contributed to missing the desired drift ratio of 5%.

Load

The loading of the system was acquired via the tension/compression load cell attached in series with the actuator. The load history is shown in Figure 2.24, from which it is seen that the maximum force readings come at the first cycle of each step. The maximum load of the first step was 1157kN in the push direction and 1192kN in the pull direction. The maximum load of the second step was 1580kN in the push direction and 1576kN in the pull direction. The maximum load of the third step was 1573kN in the push direction and 1575kN in the pull direction. The maximum load of the fourth step was 1428kN in the push direction and 1429kN in the pull direction. Finally, the maximum load of the fifth step was 1474kN in the push direction and 723kN in the pull direction. The corresponding peak loads to cycles pushed or pulled are given in Table 2.4.

The reason behind relatively low load values on the pull side of the last step was due to the degradation observed at the east cap beam-column joint and a concern that the joint would fall off; thus the last four cycles were only in the push direction, where the beam cap returned to zero displacement and was pushed only. The overall maximum push load occurred in the fourth cycle at 1580.58kN. The last push maximum recorded was in the sixteenth cycle at 1352.78kN. The overall drop in push load capacity was 227.8kN, a drop of 14.4%.

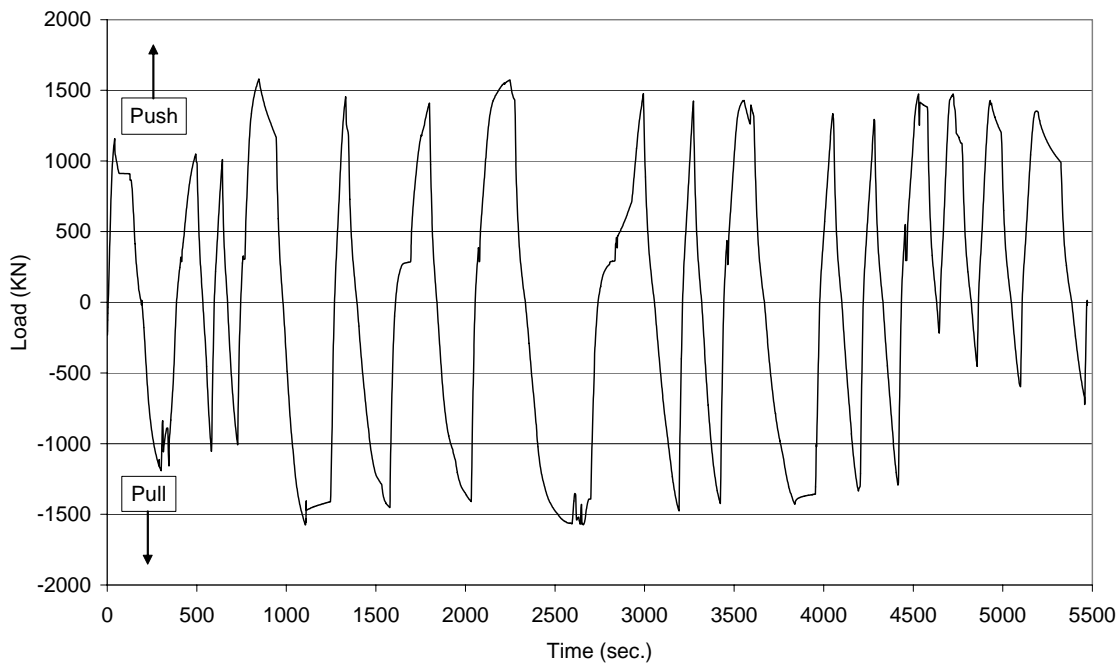


Figure 2.24 Cyclic Load history for Bent #4S

Table 2.4 Peak loads corresponding to cycles of testing for Bent #4S

		Max Load (push) (kN)	Min Load (pull) (kN)
First Step	First Cycle	1157.49	-1192.24
	Second Cycle	1049.00	-1055.82
	Third Cycle	1009.18	-1008.23
Second Step	Fourth Cycle	1580.58	-1576.86
	Fifth Cycle	1455.37	-1452.76
	Sixth Cycle	1410.14	-1410.06
Third Step	Seventh Cycle	1573.76	-1575.13
	Eighth Cycle	1476.33	-1476.25
	Ninth Cycle	1424.34	-1424.38
Fourth Step	Tenth Cycle	1428.35	-1429.54
	Eleventh Cycle	1334.89	-1336.09
	Twelfth Cycle	1293.79	-1293.12
Fifth Step	Thirteenth Cycle	1474.12	-218.38
	Fourteenth Cycle	1474.12	-454.23
	Fifteenth Cycle	1427.97	-596.97
	Sixteenth Cycle	1352.78	-723.07

As the final four cycles of the test were actually steps, as each cycle was to a new displacement level, and the fact that there was no real pull phase to the push phase the results of this test will be in general inclusive of cycles 1 through 12. This means that the overall loss in the peak push load capacity would be 1580.58kN to 1293.79kN, a difference of 286.79kN, and a drop of 18.1%. For the pull side, the peak load value occurred in the fourth cycle at 1576.86kN, and

the last peak load value in the twelfth cycle was 1293.12kN. This is a difference of 283.74kN and a drop of 17.9%.

Displacement of the Entire System

The displacement of the entire system was recorded in two CEDT. As shown in Figure 2.20, CEDT 1 and CEDT 3 measure this overall displacement including any motion in the bent cap, columns, grade beam, pile caps, piles, and soil. One CEDT would have been ample for this task, but a second was added as a redundant, and in the unlikely event that a massive localized failure would allow different displacement values of the same structure from one end to the other. The overall difference in data readings between CEDT 1 and CEDT 3 is shown in Figure 2.25. These differences show a maximum of 7.9mm in the push side during the last step, and a maximum of 10.5mm in the pull side, also accruing during the last step. These differences are easily explained: as the test progressed more damage occurred in the structure causing cracks to open and give different CEDT readings.

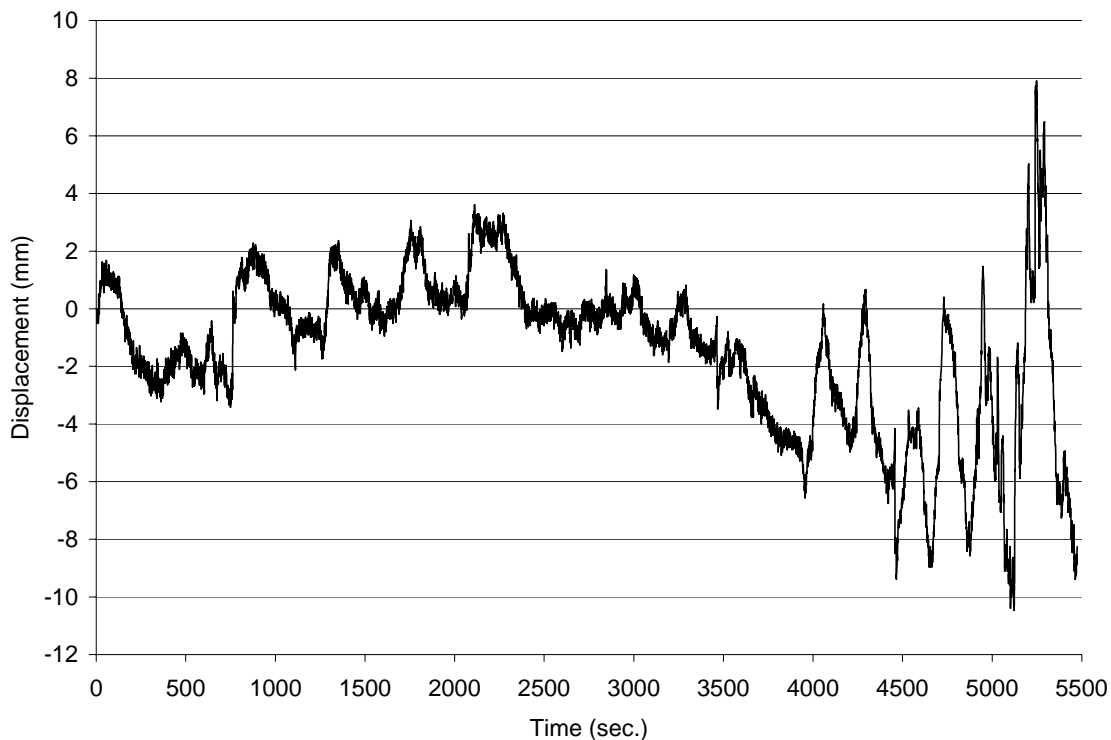


Figure 2.25 Difference in displacement readings of CEDT 1 and CEDT 3 during testing of Bent #4S

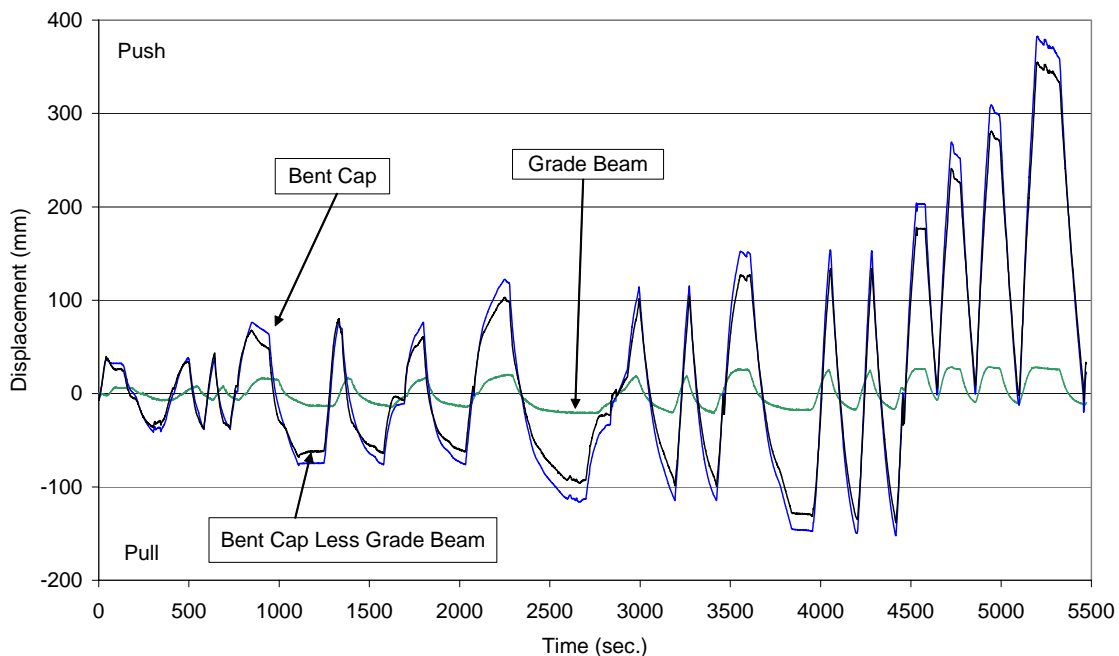
Because of small differences in the two CEDT data readings and to keep the displacement data consistent with the point of application, CEDT 1 is taken as the basis of the displacement measurement and not the average of the two CEDT. The maximum push and pull data obtained by CEDT 1 is tabulated by cycle and shown with corresponding actual % drift and the target drift for the entire test in Table 2.5.

Table 2.5 Peak displacements and drift ratios for Bent #4S

		Max Displacement (push) (mm)	% Drift	Min Displacement (pull) (mm)	% Drift	Target Drift
First Step	First Cycle	37.8	0.49	-41.3	-0.54	0.5
	Second Cycle	38.6	0.50	-38.5	-0.50	0.5
	Third Cycle	38.3	0.50	-38.3	-0.50	0.5
Second Step	Fourth Cycle	76.3	0.99	-77.0	-1.00	1.0
	Fifth Cycle	78.0	1.01	-76.2	-0.99	1.0
	Sixth Cycle	76.5	0.99	-76.2	-0.99	1.0
Third Step	Seventh Cycle	122.5	1.59	-116.2	-1.51	1.5
	Eighth Cycle	114.4	1.48	-114.6	-1.49	1.5
	Ninth Cycle	115.3	1.50	-114.5	-1.49	1.5
Fourth Step	Tenth Cycle	152.5	1.98	-147.6	-1.92	2.0
	Eleventh Cycle	153.9	2.00	-149.4	-1.94	2.0
	Twelfth Cycle	153.1	1.99	-152.5	-1.98	2.0
Fifth Step	Thirteenth Cycle	204.2	2.65	-1.4	-0.02	2.5
	Fourteenth Cycle	269.5	3.50	-0.7	-0.01	3.5
	Fifteenth Cycle	309.1	4.01	-12.6	-0.16	4.0
	Sixteenth Cycle	383.0	4.97	-20.0	-0.26	5.0

Displacement of Grade Beam

CEDTs measured the displacement of the entire system; the grade beam moved during the testing as shown by the CEDTs attached to the grade beam at the West and East ends (Figure 2.20). The motion of the grade beam relative to the overall system is small, but it can no be ignored. Figure 2.26 displays the motion of the overall system as per CEDT 1, the motion of the grade beam, and the difference of CEDT 1 less the grade beam motion.

**Figure 2.26** Displacement of the entire system, grade beam, and superstructure of Bent #4S

The maximum displacements of the grade beam for both push and pull are shown in Table 2.6. The maximum lateral motion of the grade beam for the push, neglecting the last four cycles was 26.3mm and 21.1mm for the pull. This motion accounts for 17.2% and 18.1% for the push (cycle 10) and pull (cycle 9) peak displacements respectively.

Table 2.6 Peak displacements of grade beam for Bent #4S

		Max Displacement (push) (mm)	Min Displacement (pull) (mm)
Step First Step	First Cycle	7.3	-8.0
	Second Cycle	8.4	-7.2
	Third Cycle	8.3	-7.4
Second Step	Fourth Cycle	17.2	-14.1
	Fifth Cycle	17.3	-14.6
	Sixth Cycle	17.5	-14.5
Third Step	Seventh Cycle	20.7	-21.1
	Eighth Cycle	18.9	-20.4
	Ninth Cycle	19.1	-21.1
Fourth Step	Tenth Cycle	26.3	-17.8
	Eleventh Cycle	25.5	-17.4
	Twelfth Cycle	24.8	-17.1
Fifth Step	Thirteenth Cycle	26.8	-7.0
	Fourteenth Cycle	28.5	-9.3
	Fifteenth Cycle	28.4	-10.6
	Sixteenth Cycle	28.5	-11.9

Displacement of the Superstructure

The displacements and drifts of the superstructure alone are somewhat less than that of the entire system. By subtracting the values of Table 2.6 from Table 2.5, the actual displacement of the superstructure with the corresponding drift ratio can be obtained as shown in Table 2.7. This determines that the superstructure and the entire system behave similarly but with moderate differences in the maxima; because of this, the major portion of this chapter will deal with the overall system, with periodic reference to the superstructure characteristics alone.

Hysteretic Behavior of System

The hysteretic behavior shown by the hysteresis curve is simply the relationship between load behavior and displacement behavior of a system. This relationship is important in understanding how a system dissipates the energy imparted into it, how a system degrades in terms of stiffness, and in understanding the displacement ductility. The energy of a system at a known displacement and corresponding load can be found by calculating the area of the closed loops using calculus integration techniques if the equation of the loops is known, or by using a cubic spline technique in order to determine the equation of loops. The hysteresis diagram for the Bent #4S entire system is shown in Figure 2.27.

Table 2.7 Peak displacement values and % drift for the superstructure of Bent #4S

		Max Displacement (push) (mm)	% Drift	Min Displacement (pull) (mm)	% Drift
First Step	First Cycle	30.5	0.40	-33.3	-0.43
	Second Cycle	30.1	0.39	-31.3	-0.41
	Third Cycle	30.0	0.39	-31.0	-0.40
Second Step	Fourth Cycle	59.1	0.77	-62.9	-0.82
	Fifth Cycle	60.8	0.79	-61.6	-0.80
	Sixth Cycle	59.0	0.77	-61.8	-0.80
Third Step	Seventh Cycle	101.9	1.32	-95.1	-1.23
	Eighth Cycle	95.5	1.24	-94.2	-1.22
	Ninth Cycle	96.2	1.25	-93.4	-1.21
Fourth Step	Tenth Cycle	126.2	1.64	-129.8	-1.68
	Eleventh Cycle	128.4	1.67	-132.0	-1.71
	Twelfth Cycle	128.3	1.66	-135.3	-1.76
Fifth Step	Thirteenth Cycle	177.5	2.30	5.6	0.07
	Fourteenth Cycle	241.1	3.13	8.5	0.11
	Fifteenth Cycle	280.8	3.64	-2.0	-0.03
	Sixteenth Cycle	354.5	4.60	-8.1	-0.11

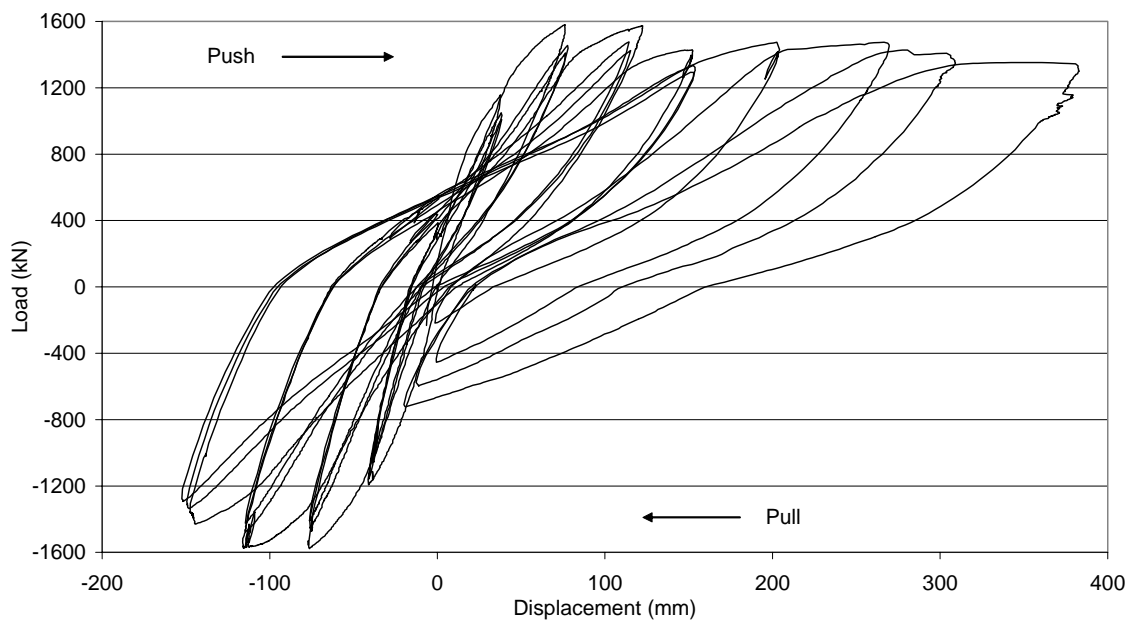


Figure 2.27 Hysteretic behavior of Bent #4S

System Stiffness

The stiffness of the system at any cycle is the slope of the hysteresis curve and it can be found by using the maximum values in Tables 2.4 and 2.5. The stiffness of the system as shown in Figure 2.28 decreases with each subsequent cycle. The initial elastic stiffness, k_e of 58.6 kN/mm was reduced 48% in the first step and finally reduced 94% in the final cycle.

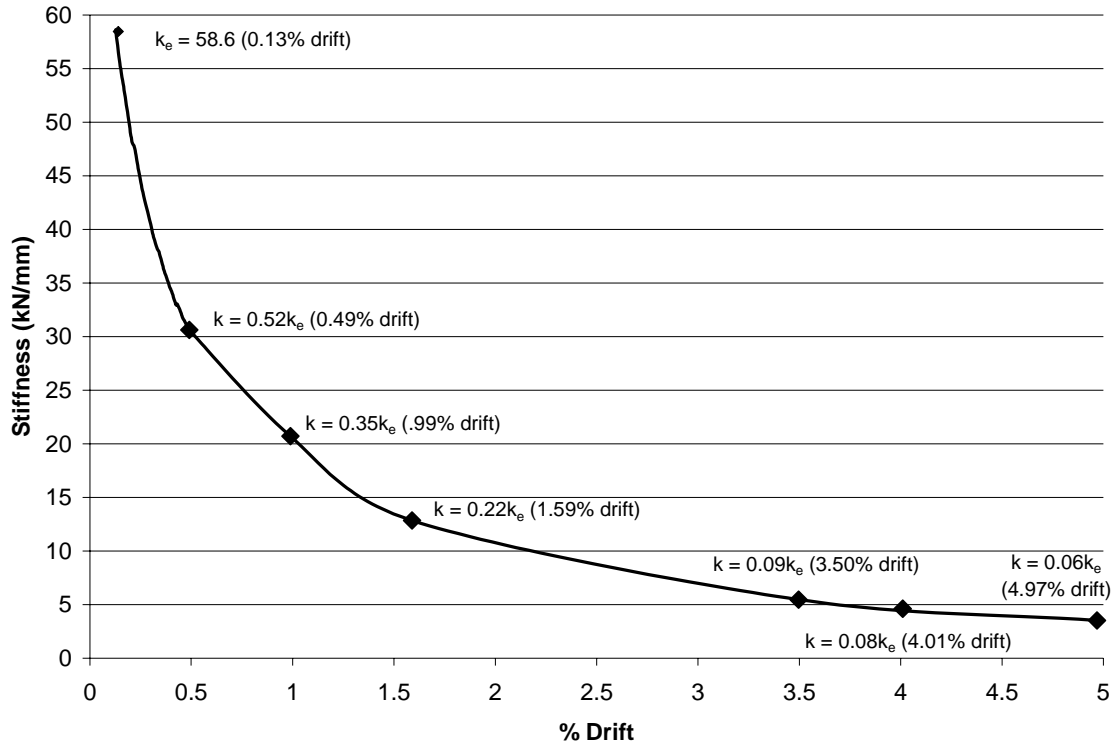


Figure 2.28 Experimental stiffness degradation of Bent #4S

System Energy

In order to obtain the energy absorbed by the system each cycle was plotted in a Cartesian system. Each loop was fit piecewise with a high order polynomial; these polynomials were also given an R squared value in order to determine closeness of fit. These equations were then used to determine the area under the curves by integrating the polynomials along the maximum and minimum bounds. The area under the hysteresis curve has energy units (kN-m). Figure 2.29 shows how much energy is absorbed by the structure per cycle, and Figure 2.30 shows the cumulative energy absorbed.

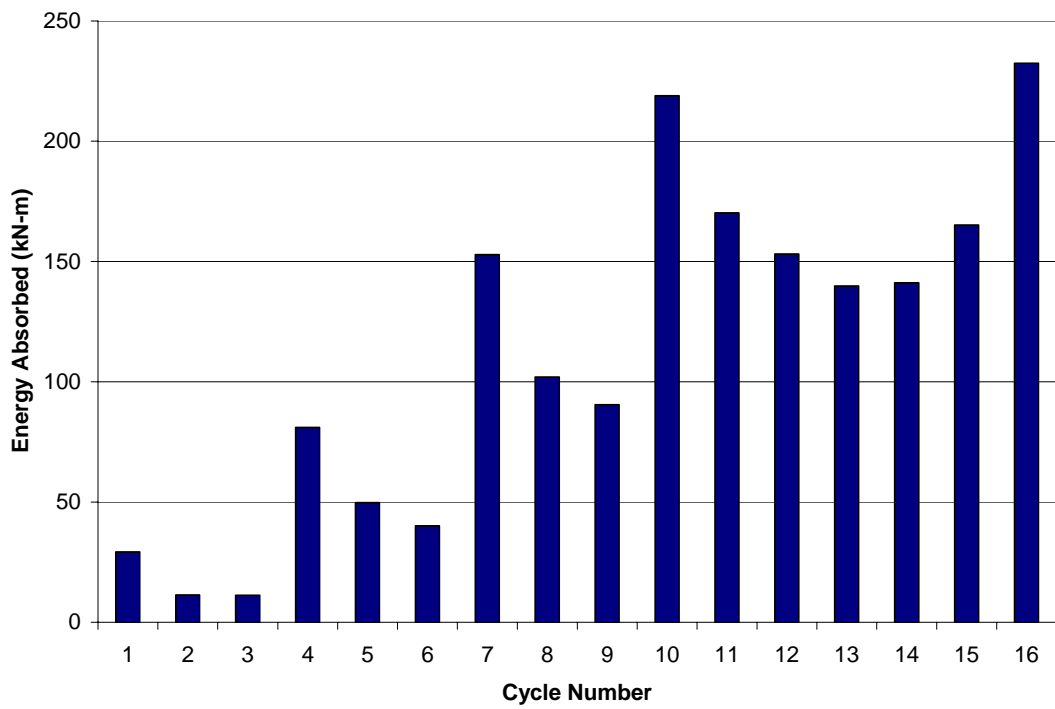


Figure 2.29 Energy absorbed by Bent #4S for each cycle

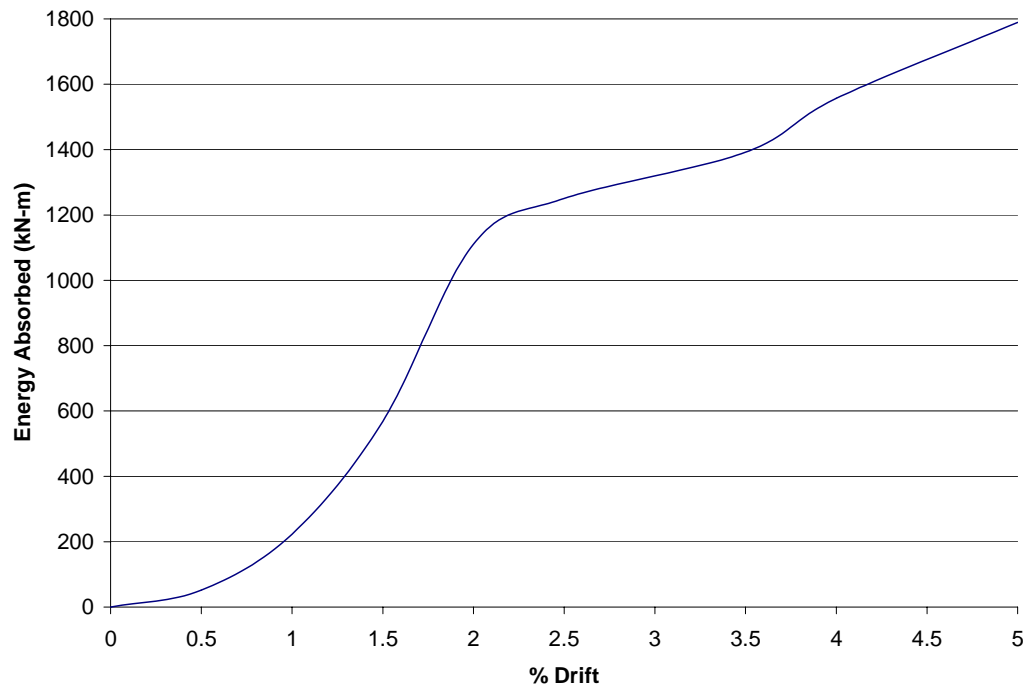


Figure 2.30 Cumulative Energy absorbed by Bent #4S

Behavior of Structural Elements

An extensive non-linear analysis including the soil/structure and soil/pile interaction was done using the program DRAIN-2DX (Prakash et al. 1993). The maximum push and pull load/displacement points were averaged to give a positive backbone curve which is an envelope used to compare the pushover curve of the analytical model. Once the analytical model was found to adequately represent the experimental results, the actual loads were input into the program and the structural analysis produced shear forces and bending moments at various elements of the structure. The shear and moment diagrams for the maximum experimental lateral loads are shown in Figures 2.31 and 2.32, respectively.

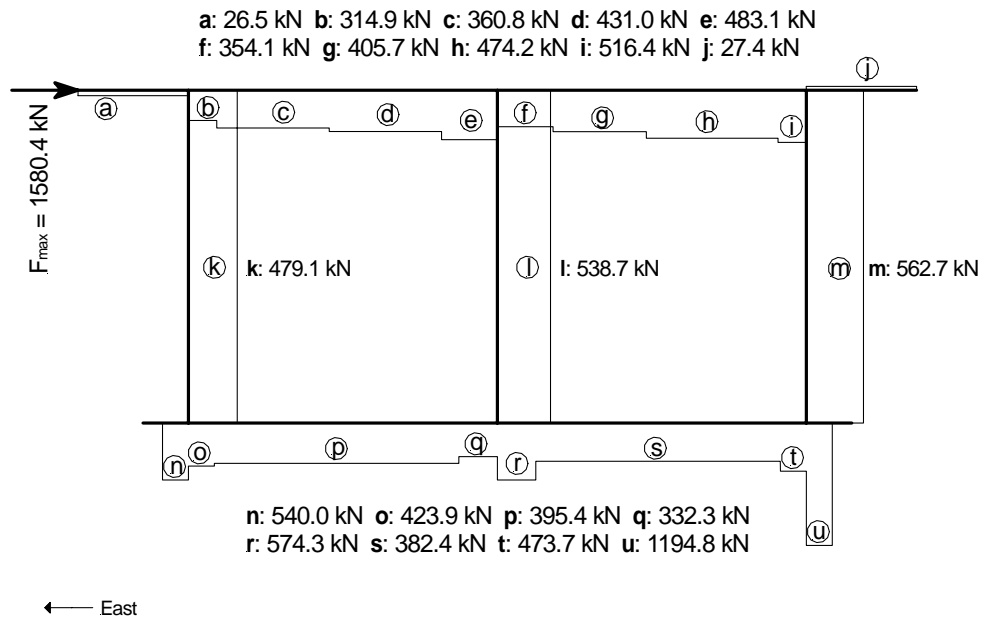


Figure 2.31 Shear Diagram for Bent #4S under maximum experimental load

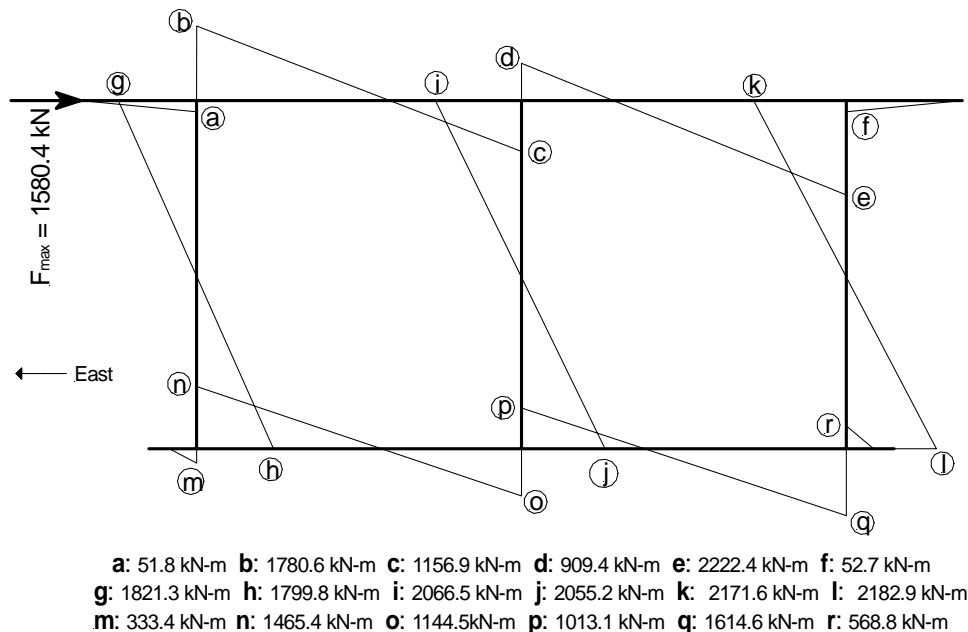


Figure 2.32 Moment Diagram for Bent #4S under maximum experimental load

Performance Levels and Damage Assessment for Bent #4S

An overall description of the damage sustained by Bent #4S in the 2000 test is given below. The assessed damage can be related to three failure performance levels or stages. For the benefit of understanding the damage mechanisms behind the entire structure, this section will deal with the six zones of the structure where nearly all the damage occurred. These zones are outlined as in Figure 2.33.

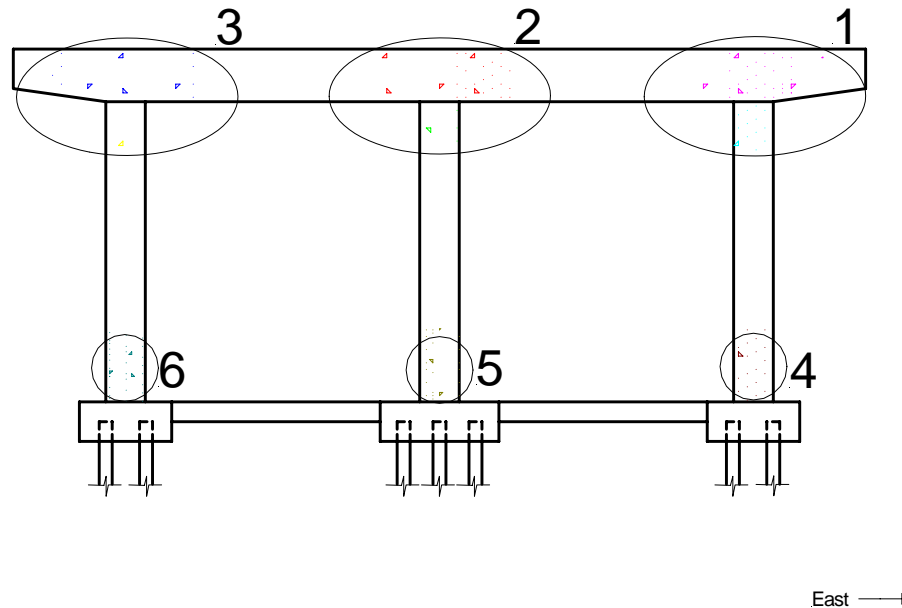


Figure 2.33 Six zones of interest for damage assessment

Each of the six zones has its own unique results; the bent cap and upper portion of the columns have been split on purpose as to describe the differences that each zone portrays. These six zones will be examined on the basis of what damage was experienced and how the damaged progressed. Onsite field notes correlate the visible external cracking with internal sensor readings, as well as physical mechanisms such as buckling, pullout, and lap splice slip.

Figure 2.34 shows the three distinct performance levels or phases associated with the performance of Bent #4S. Each of the six zones had visibly observable mechanical and material degradation, which is associated with the unseen internally developed mechanisms based on the three performance levels coincident with three drift ratios. These drift ratios are chosen to best represent the damage as observed in the field, by readings from sensors and from analytical pushover analysis. These drift ratio intervals are as follows: (a) $0.5\% < drift \leq 1\%$, (b) $1\% < drift \leq 2\%$, and (c) $2\% < drift \leq 5\%$. Figure 2.34 shows the three drift intervals with respect to the load vs. drift ratio curve. Performance level I is defined as the drift ratio of 1% at which the structure yields; performance level II is defined as the drift ratio of 2% at which the column longitudinal bars pull out of the bent cap; performance level III is defined as the drift ratio of 5% at which the column to pile cap lap splices have practically pulled out and are no longer transferring the tensile forces from the columns to the pile caps effectively.

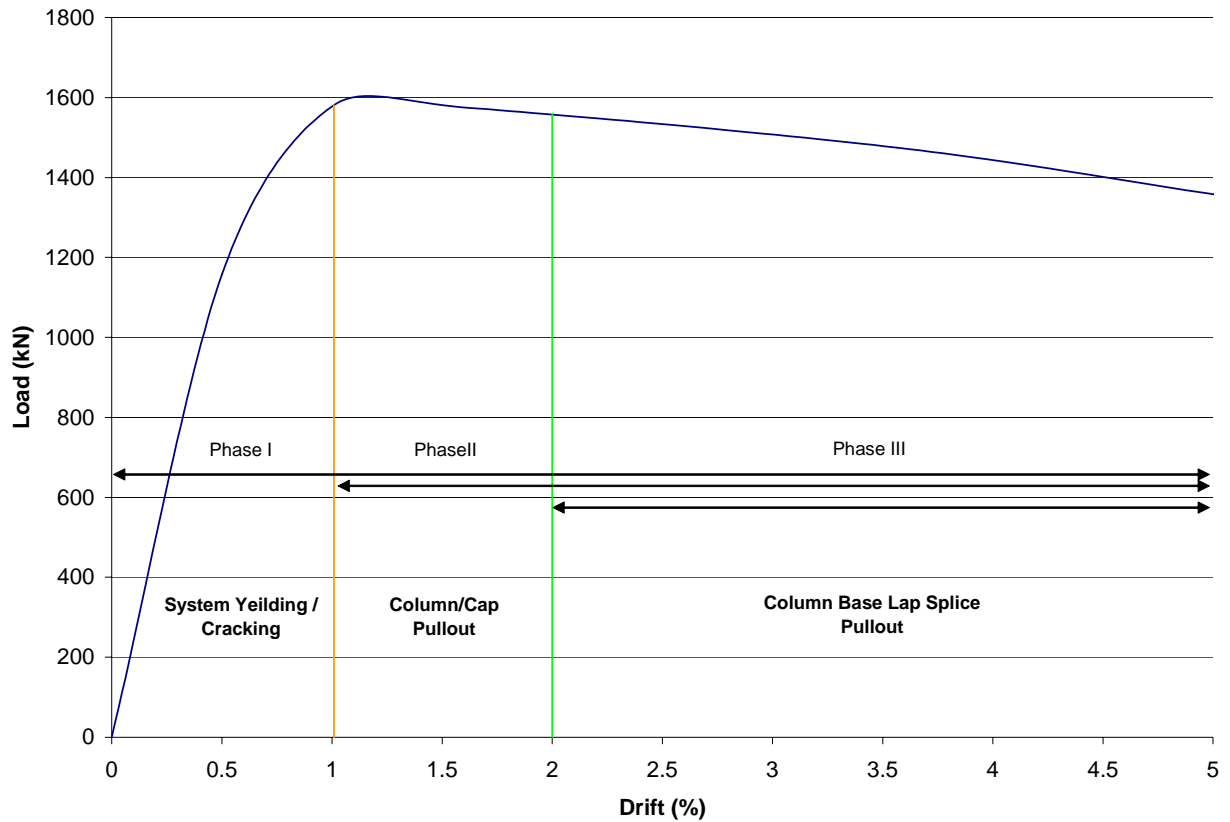


Figure 2.34 Performance levels and degradation phases

Zone 1: East Column-Bent Cap Joint: Damage Assessment

Six strain gages numbered SG29, SG30, SG31, SG32, SG33, and SG34, were placed in Zone 1 as shown in Figure 2.22. The maximum tensile strain recorded in these strain gages was $1640\mu\epsilon$ which is 136% of yield for SG 32, $1400\mu\epsilon$ or 116% yield for SG31 and SG33 was $960\mu\epsilon$ or 80% of yielding strain. The maximum compressive strain for SG32 was $719\mu\epsilon$ or 60% of yield, SG31 produced 19% of yield strength at $226\mu\epsilon$, and SG33 has a strain of $372\mu\epsilon$ or 31% of yielding strain. Strain data given by SG33, and SG34 show a trend in that the strain builds as each progressive drift is achieved without yielding until in the 8th cycle in the 1.5% drift step. From that point on, the strain gage records a reducing strain reading as is seen in Figure 2.35. This is indicative of the mechanism of de-bonding or pullout.

Strain gages SG33 and SG34 were located on the north face of the cap beam on the upper and lower rebar. The north and south faces of the bent cap were particularly corroded; in many areas the rebar was actually visible due to the missing concrete clear cover. It is then easy to see why these bars will debond at low drift levels.

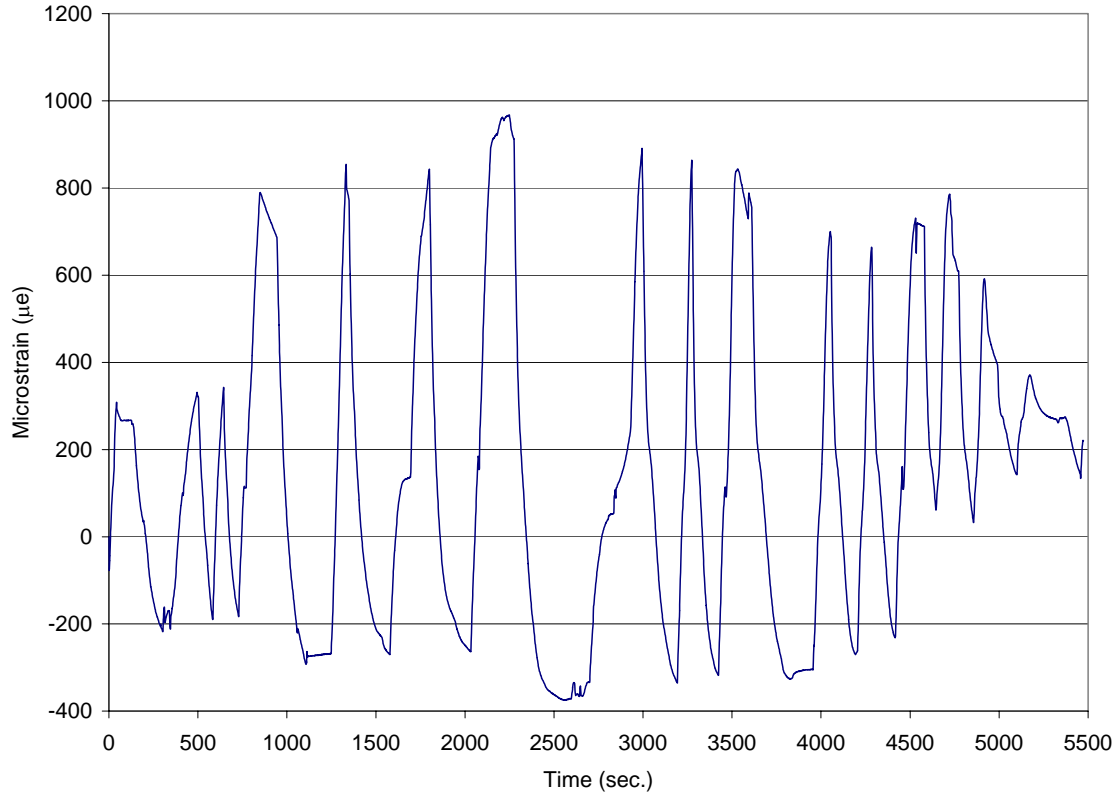


Figure 2.35 Strain gage SG33 showing reduction of strain due to bar pullout

Although there was insufficient data to determine the strains on the longitudinal bars ending in Zone 1 with SG29 and SG30, the DRAIN-2DX pushover analysis for Bent #4S shows that the strains reached at the centerline of the cap beam over the East column, was $2710\mu\epsilon$, which is 2.25 times the yielding strain. The strain in the bent cap reinforcement that correlates to SG33 from the DRAIN-2DX pushover analysis is $1011\mu\epsilon$ in tension, which is 84% of yield, and compares well to the value of 80% of yield that was measured in the experiment.

A moment-curvature diagram has been constructed for the east column-bent cap joint from analytical results, as shown in Figure 2.36. The east column-bent cap joint moment demand increases up to 4.0% drift, and then displays no increase. The curvature ductility for the east column-bent cap joint was determined to be equal to 9.8 using the expression:

$$\Phi_d = \phi_u / \phi_y \quad (2.4)$$

where the ratio of the ultimate to the yield curvature is used to define the curvature ductility.

A summary of the performance of the East column bent cap joint is given in Table 2.8, according to the three performance levels.

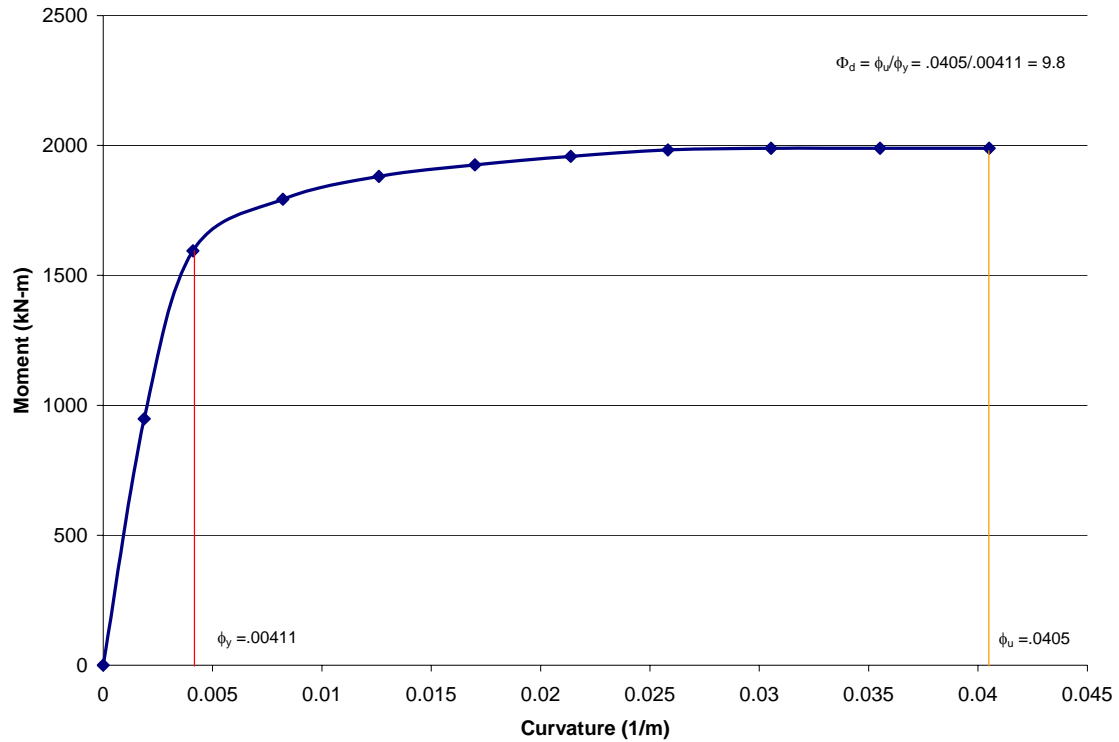


Figure 2.36 Moment-curvature for East column-bent cap joint

Table 2.8 Damage assessment for East column-bent cap joint

	Phase I $0.5 < \text{drift} \leq 1.0$	Phase II $1.0 < \text{drift} \leq 2.0$	Phase III $2.0 < \text{drift} \leq 5.0$
Steel	SG31 and SG32 both yield in tension first pull cycle of 1.0% drift	SG31 and SG32 are strain hardening through the pull cycles	n/a
Concrete	0.2mm-1.0mm cracks develop from 0 – 1m in length	1.0mm-4mm cracks lengthening of the shear cracks which develop plastic hinge and pulverizes concrete in the joint	4.0mm - 6.5mm cracks developing as drift increases due to prying action at toe of knee joints. Shear mechanism is fully developed and plastic hinge is well formed releasing moment so flexure doesn't occur at top of column
Column-bent cap joint	n/a	n/a	Pullout occurs at column-bent cap joint. Corroded bars pullout around 2.0% drift. Best estimate is that pullout occurs in this drift range around 3.5-4.0%drift

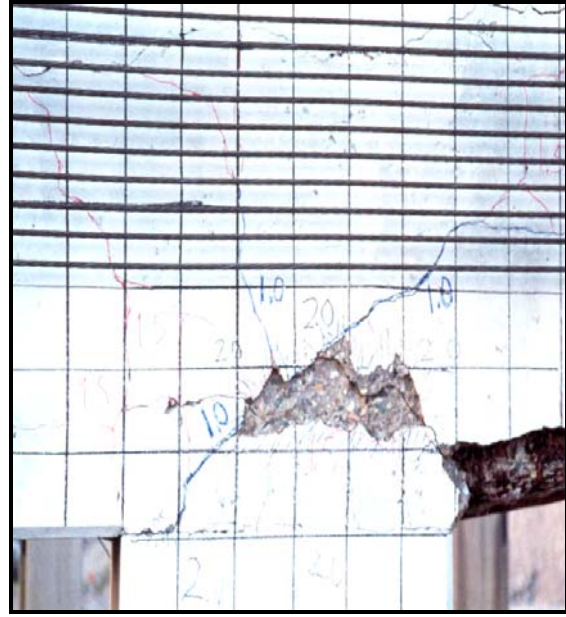
Field Notes for East column-bent cap joint: South face

- 1.) 0.2mm cracks @ 0.5% drift
- 2.) 1.0mm shear crack developing @ 1.0% drift
- 3.) 3.0mm diagonal shear cracks @ 1.5% drift, no flexural cracks have developed at the top of the column, which would be expected, plastic hinge is observed to form approximately 279mm above column in the cap beam
- 4.) 4.0mm diagonal shear cracks, and $185\text{mm}^2 \times 25\text{mm}$ spalling along column/cap-beam interface @ 2.0% drift
- 5.) 5.0mm cracks @ 3.5% drift
- 6.) Two main diagonal shear cracks reach 1.24m and 1.11m in length by 5.0% drift and measure 6.5mm wide with the majority of the clear cover de-bonded, but still hanging, still no flexural cracks at top of column. Pure pin has formed in the cap beam

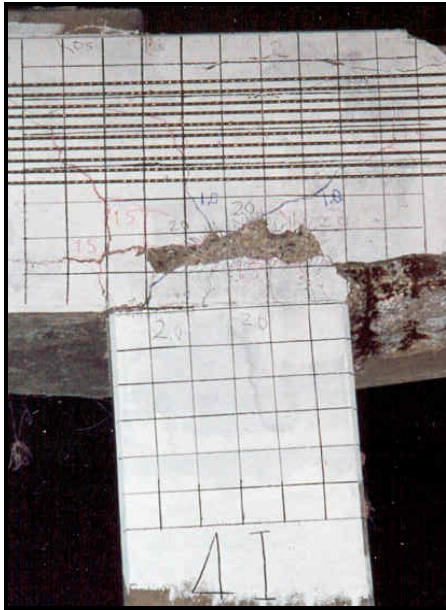
After removing the de-bonded clear cover, the column longitudinal reinforcement was found to end 355mm below the top of the Cap beam, and that all of the bars on the south face had pulled out with an average of 16mm. The plans called for a splice piece to be attached to each of the vertical bars, but apparently it was neglected. If early pullout has occurred it makes sense as to why no flexural cracks developed at the top of the column.



(a)



(b)



(c)



(d)

Figure 2.37 Condition of East column-bent cap joint: (a) 1.5% drift, (b) 2% drift, (c) 4% drift, (d) 5% drift

Zone 2: Center Column-Bent Cap Joint: Damage Assessment

Eight strain gages numbered SG55, SG56, SG57, SG58, SG59, SG60, SG61 and SG62, were placed in Zone 2 as shown in Figure 2.22. The maximum tensile strain recorded out of these strain gages was $1970\mu\epsilon$, which is 164% of yield in SG55. The maximum compressive strain for SG55 was $1620\mu\epsilon$ or 135% of yield. SG55 was the first element to yield in the overall structure during testing; this yielding occurred in the pull direction of the first cycle at 0.5% drift. The time record of the strain for SG55 is given in Figure 2.38.

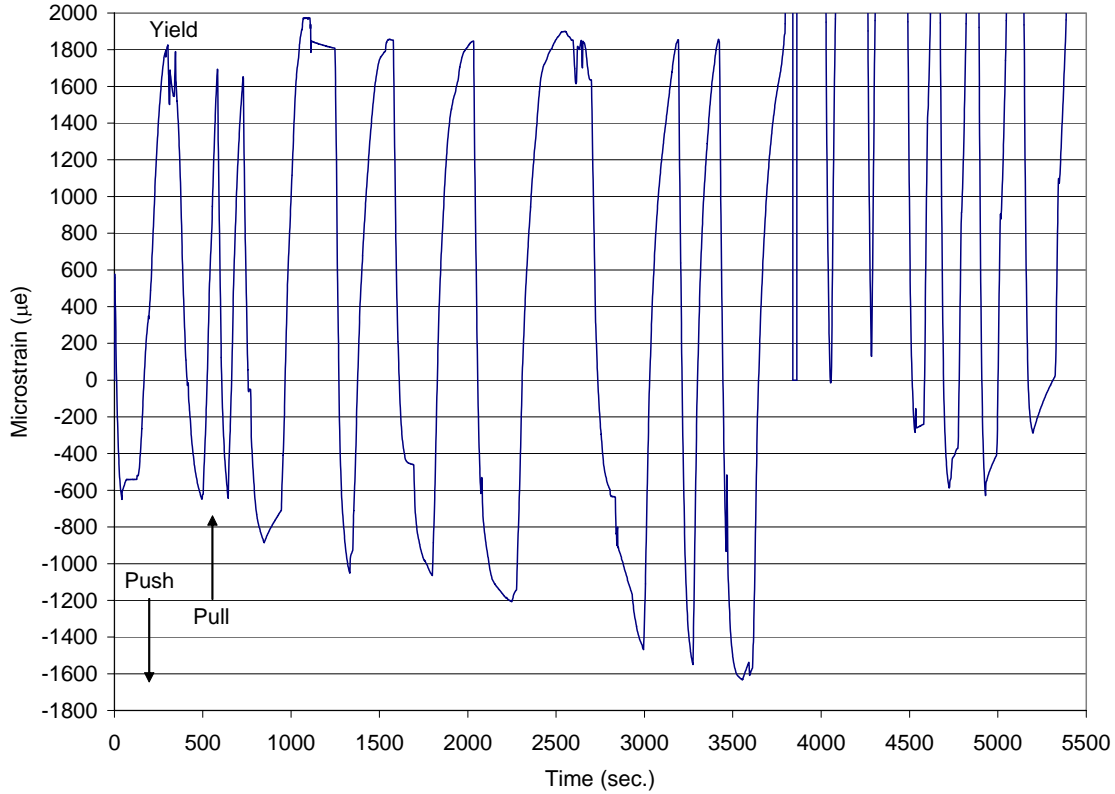


Figure 2.38 Strain time-history for SG55, the first element to yield in the overall structure

The bent cap over the center column joint throughout the test experienced relatively little damage. The upper part of the column however, in the plastic hinge region took almost all of the damage. This is because the cap beam with dimensions 0.914m x 1.23m was 33% larger in cross-sectional area, but also more than twice as stiff as the column. The strain gages applied to the cap beam showed low level of strain. This is because the moments were forced to the top of the column where it was least stiff.

A moment curvature diagram was constructed for the center bent cap-column joint; the moment demand increases up to 4.0% drift, and then displays no increase. The moment curvature curve is shown in Figure 2.39; the curvature ductility was determined from Equation 2.4 as 11.4.

A summary of the performance of the Center column bent cap joint is given in Table 2.9, according to the three performance levels.

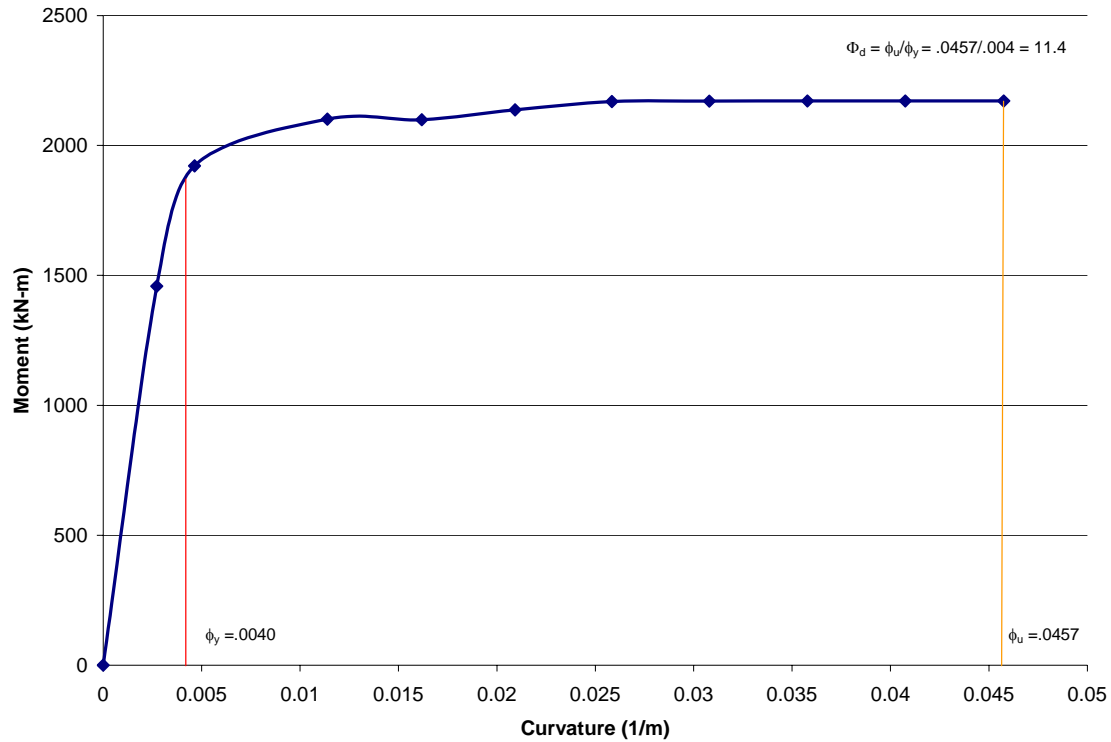


Figure 2.39 Moment curvature for center bent cap-column joint

Table 2.9 Damage assessment for Center column-bent cap joint

	Phase I $0.5 < \text{drift} \leq 1.0$	Phase II $1.0 < \text{drift} \leq 2.0$	Phase III $2.0 < \text{drift} \leq 5.0$
Steel	SG55 yields in tension first pull cycle of 0.5% drift	SG55 yield in compression in the push of seventh cycle	SG55 strain hardens represents all axial column bars just under cap beam
Concrete	0.15mm minimal shear cracks in cap beam 0.5mm-1.5mm flexural cracks develop from 0 – 0.9m in length around cold joint and 304mm below cold joint	Existing Flexural cracks grow to 3.0mm; At 1.5%drift, spalling of clear cover on SE corner. Possible buckle Existing Flexural cracks grow to 5.0mm at 2.0%drift	South face of center column has largest 14mm open crack, east face largest crack is 8.0mm, north face largest crack is 8.0mm, west face largest crack is 17.0mm all cracks are flexural, no shear
Column-bent cap joint	n/a	Spalling of clear cover on SE corner. Possible buckle, no clear signs of pullout	Visible joint expansion around top of center column with visible bulges along 3.0-3.5% drift

Field Notes for Center column-bent cap joint: South face unless otherwise noted

- 1.) 0.15mm shear cracks @ 0.5% drift 150mm long
- 2.) 1.5mm flexure crack developing along cold joint and 0.6mm flexural crack developing at 304mm below cold joint @ 1.0% drift
- 3.) 3.0mm flexural cracks along cold joint, and 2.5 mm cracks at 304mm below cold joint during 1.5% drift, spalled area falls off at top of column below cold joint on south east corner; buckling is observed
- 4.) 5.0mm flexural cracks at 2.0% drift
- 5.) visible joint expansion around top of center column with visible bulges along 3.0-3.5% drift maybe local buckling
- 6.) South face of center column has largest 14mm open crack, east face largest crack is 8.0mm, north face largest crack is 8.0mm, west face largest crack is 17.0mm all cracks are flexural, no shear

After removing the de-bonded clear cover, the column longitudinal reinforcement on the east and west faces were found to have buckled. The buckling on the west face was displaced 90mm out. The east face buckling was less severe, only 12mm. The main buckled area was approximately 304mm below the cap/column cold joint as seen in Figure 2.40. Figures 2.41 and 2.42 show the column rebar buckling which occurred mainly on the west face.



Figure 2.40 Damage to Center column-bent cap joint at the end of 5% drift



Figure 2.41 Damage to Center column-bent cap joint showing the buckled zone on the west face



Figure 2.42 Center column-bent cap joint buckled zone on the west face

Zone 3: West Column-Bent Cap Joint: Damage Assessment

Six strain gages numbered SG65, SG66, SG67, SG68, SG69, and SG70 were placed in Zone 3 as shown in Figure 2.22. The maximum tensile strain recorded out of these strain gages was $2340\mu\epsilon$, which is 195% of yield in SG 68 located at the top of the west column on the east face just below the cap beam. The maximum compressive strain found in SG67 was $1400\mu\epsilon$, or 116% yield. Strain data given by SG65 and SG66 located on the cap beam south face and attached to the top and bottom longitudinal bars, show very similar results to SG33 and SG34 located in the mirror position on the east column. The time history of SG65 is shown in Figure 2.43. Figure 2.43 shows that SG65 has the same tendency of the rebar to lose strain with larger displacement; it reached yield in the tension phase of the 5th cycle at 2% drift, and yielding each subsequent cycle in tension up to $1550\mu\epsilon$, after which the strain drops off indicating that the bar has de-bonded. SG69 and SG70 similarly loose strain starting slowly around 1.5% and totally lose strain by the end of 2.5% drift, as shown in Figures 2.44 and 2.45. Gages SG69 and SG70 were attached to the center longitudinal rebar in the west column. As this particular rebar is near the neutral axis of the column, when the cycles change between push and pull the rebar always shows a tensile strain. The graphs therefore always stay above the x-axis. The drop in tensile strain correlates to insufficient embedment and premature pullout, which is visually verified by the 22mm pocket located at the top end of the rebar located 0.355m from the top of the bent cap, which can be seen in Figure 2.46.

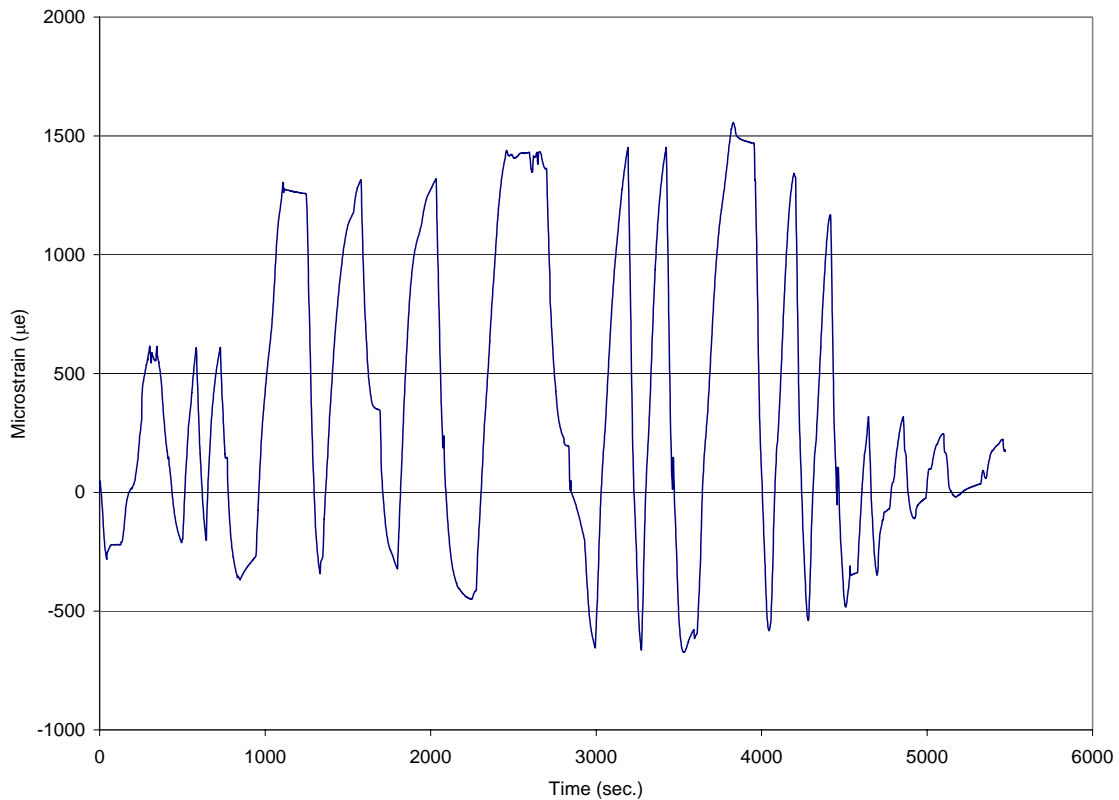


Figure 2.43 Strain gage SG65 time history

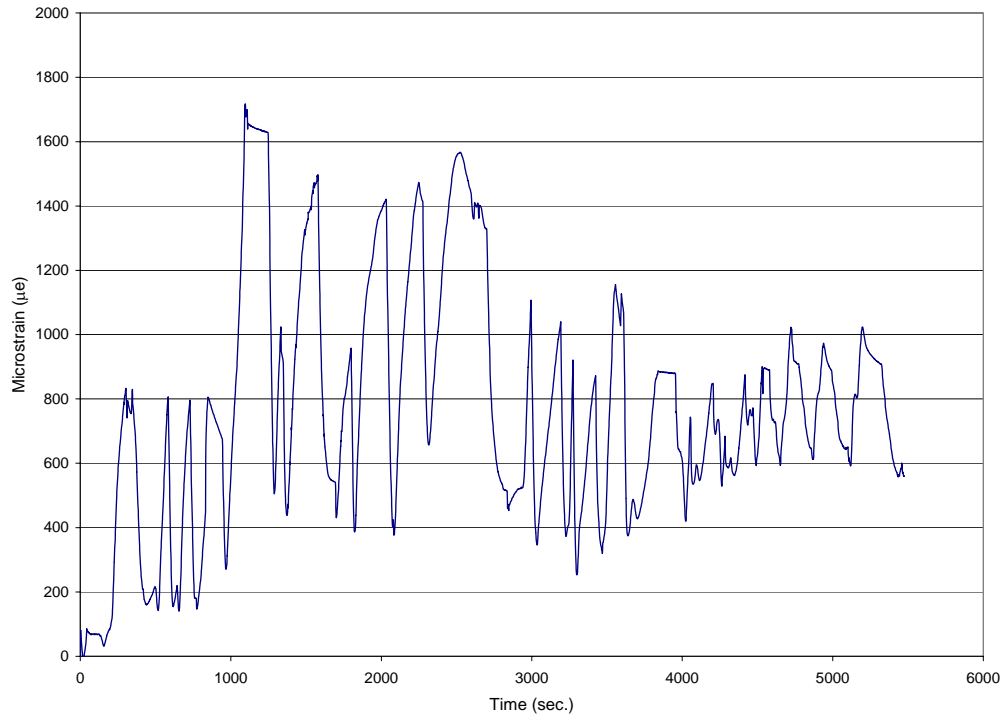


Figure 2.44 Strain time-history for SG69 in the West column-bent cap joint

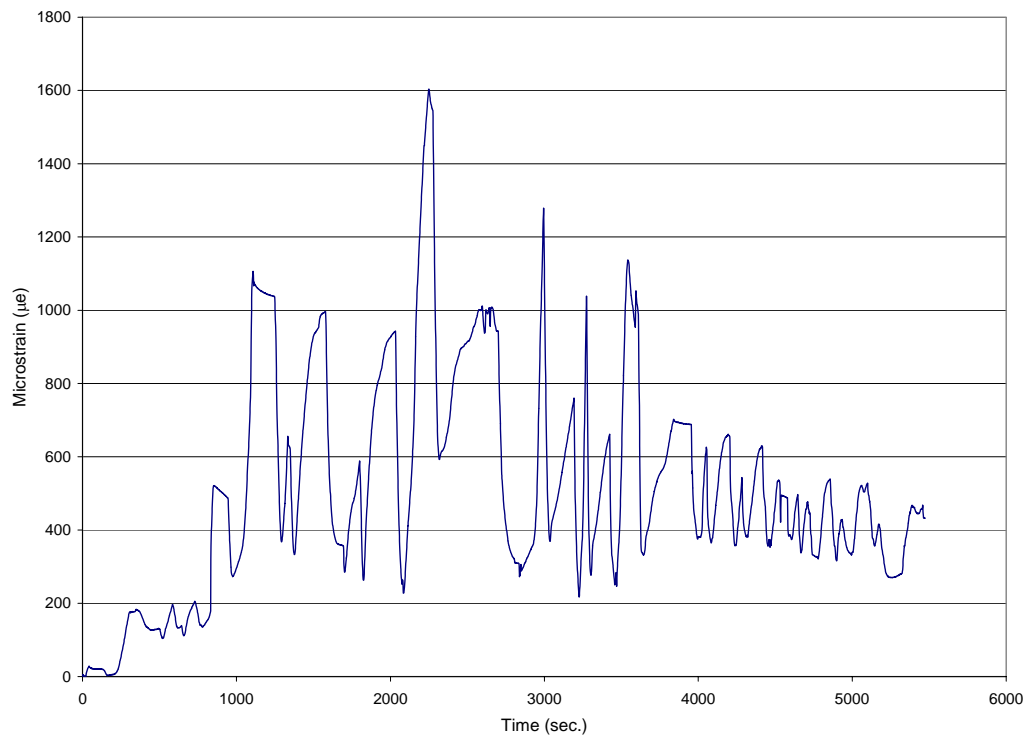


Figure 2.45 Strain time-history for SG70 in the West column-bent cap joint

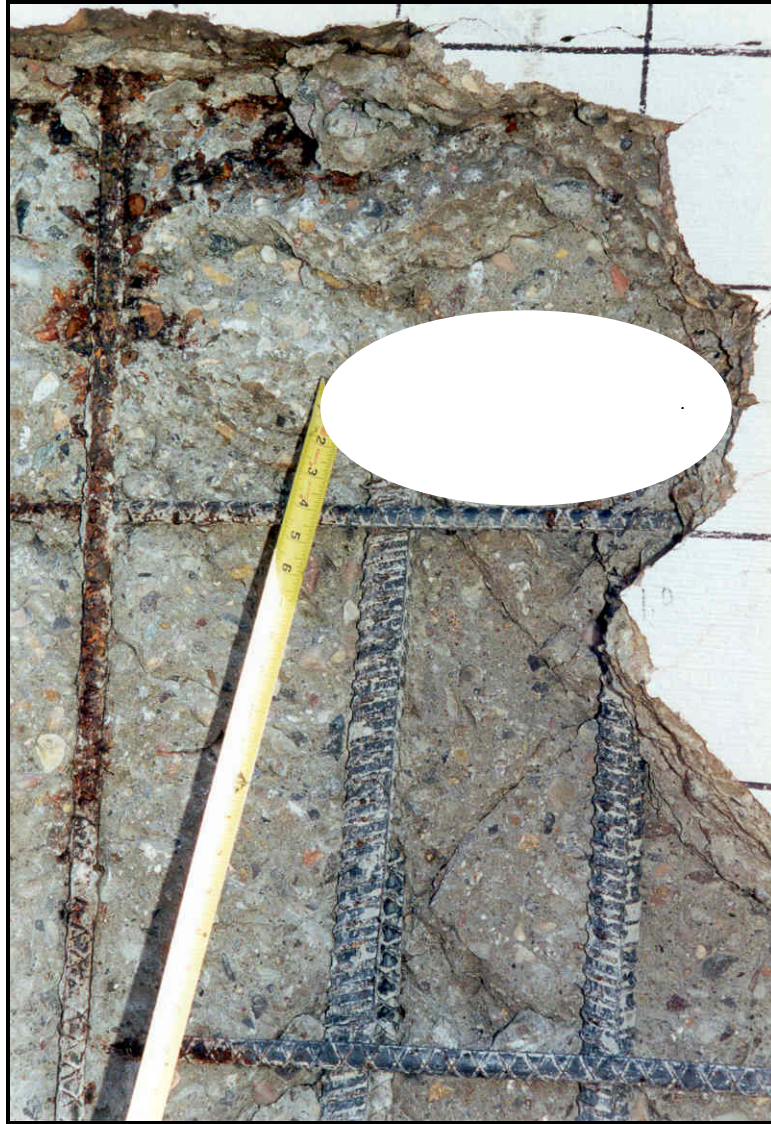


Figure 2.46 Pullout pocket in column longitudinal bar in West column-bent cap joint; the pocket is 22mm long

A moment curvature diagram was constructed for the West column-bent cap joint; the moment demand increases to 4.0% drift, and then displays no increase or decrease. The moment vs. curvature curve is shown in Figure 2.47, and the curvature ductility is determined to be 10.8.

A summary of the performance of the West column bent cap joint is given in Table 2.10, according to the three performance levels. The condition of the joint at 2% and 5% drift ratio is shown in Figures 2.48 and 2.49, respectively.

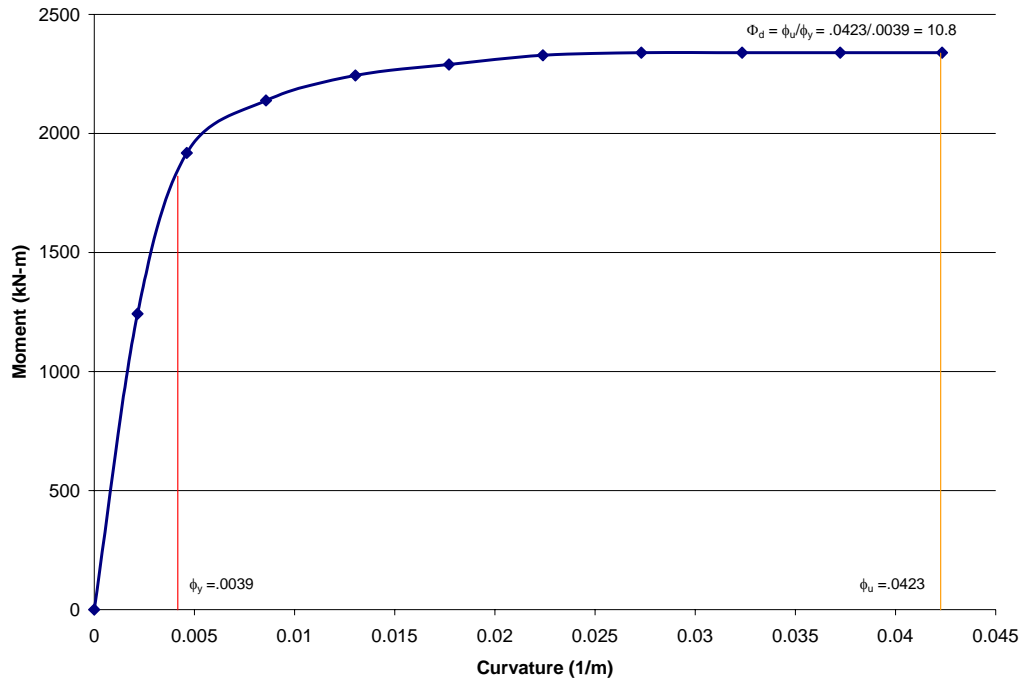


Figure 2.47 Moment curvature for West column-bent cap joint

Table 2.10 Damage assessment for West column-bent cap joint

	Phase I $0.5 < \text{drift} \leq 1.0$	Phase II $1.0 < \text{drift} \leq 2.0$	Phase III $2.0 < \text{drift} \leq 5.0$
Steel	SG67 and SG68 both yield in tension first pull cycle of 0.5% drift. SG67 reaches max strain in 1.0% drift	SG67 yield in compression at 2% and SG65 yields in tension a 2.0% are strain hardening through the pull cycles	Strain hardening for SG65, SG67, SG68
Concrete	0.15mm shear cracks @ 0.5% drift 15mm-155mm long, 0.15mm crack developing along cold joint 1mm diagonal shear cracks 155mm-200mm long, 1.5mm flexure crack developing along cold joint and 0.6mm flexural crack developing at 381mm below cold joint @ 1.0% drift 0.15mm flexural crack developing 685mm below cold joint @ 1.0% drift flexural cracks are visible on all faces	3.0mm diagonal shear cracks @ 1.5% drift extending to 234mm with the development of a plastic hinge in the center of the column 381mm up from the cold joint 4.0mm diagonal shear cracks, @ 2.0% drift, minor concrete spalling. Flexural cracks not developing Plastic hinge is fully developed	South face of west column /bent cap joint has largest 14mm open crack, east face largest crack is 3.0mm, north face largest crack is 7.0mm, west face largest crack is 3.0mm Heavy shear damage and a well developed hinge
Column-bent cap joint	n/a	Cap Beam corner bars de-bond locally @ 1.5% drift SG65 and SG66 show reducing strain	Pullout definitely occurs for SG69 and SG70 denoting the longitudinal rebar in the column where it ends in the cap beam 2.0% -2.5% drift

Field Notes for West column-bent cap joint: South face unless otherwise noted

- 1.) 0.15mm shear cracks @ 0.5% drift 15mm-155mm long, 0.15mm crack developing along cold joint
- 2.) 1mm diagonal shear cracks 155mm-200mm long, 1.5mm flexure crack developing along cold joint and 0.6mm flexural crack developing at 381mm below cold joint @ 1.0% drift, 0.15mm flexural crack developing 685mm below cold joint @ 1.0% drift flexural cracks are visible on all faces
- 3.) 3.0mm diagonal shear cracks @ 1.5% drift extending to 234mm with the development of a plastic hinge in the center of the column 381mm up from the cold joint, as the shear cracks develop and release the moment, flexural cracks have stopped developing at the top of the column, which would be expected
- 4.) 4.0mm diagonal shear cracks, @ 2.0% drift, minor concrete spalling which is probably already loose clear cover. Flexural cracks not developing but plastic hinge is fully developed
- 5.) South face of west column /bent cap joint has largest 14mm open crack, east face largest crack is 3.0mm, north face largest crack is 7.0mm, west face largest crack is 3.0mm; heavy shear damage and a well developed plastic hinge

After removing the de-bonded clear cover the column longitudinal reinforcement on the south face, the column longitudinal rebar had been found pulled out by 35mm, as shown in Figure 2.50.

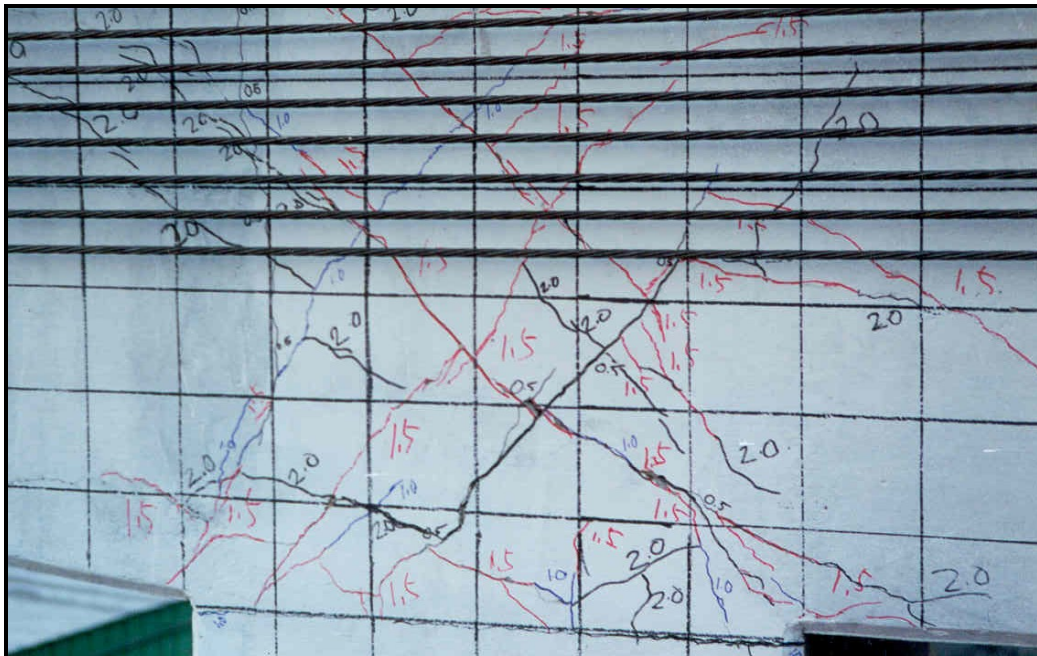


Figure 2.48 West column-bent cap joint at 2% drift ratio



Figure 2.49 West column-bent cap joint at 5% drift ratio



Figure 2.50 22mm long pullout pocket in column longitudinal bars at West column-bent cap joint

Zone 4: East Column Base Damage Assessment

The East column base was instrumented with four strain gages located on the east face of the column 451mm above the pile cap; the strain gages are numbered SG7, SG8, SG9 and SG10, as shown in Figure 2.22. These four strain gages are strategically located as to have one gage on each bar of the lap splice that connects the column longitudinal bar to the pile cap rebar protruding through the cold joint. The intent was to have strain readings across the splice to be able to determine whether the splice was long enough to develop the tensile forces, or whether the splice would slip. As anticipated, the splice was not long enough and lap splice failure occurred. The maximum tensile strain recorded by these strain gages was $1000\mu\epsilon$, which is 83% of yield by SG8. The maximum compressive strain was from SG8 as well, and it was $700\mu\epsilon$ or 58% of yield. The results of monitoring SG7 and SG8 on two bars shows that the lap splice has two distinct strain levels that can be seen in Figure 2.51. From $0\% < \text{drift} < 0.5\%$, the strain levels are perfectly aligned. From $0.5\% < \text{drift} < 1\%$, the tensile strains lay right on top of each other, but the compression strains start to deviate. At 2.0% drift, the tensile strains start to part and the slip in the lap splice starts developing. From there on, the slip develops further and it is evident that the two bars are straining differently.

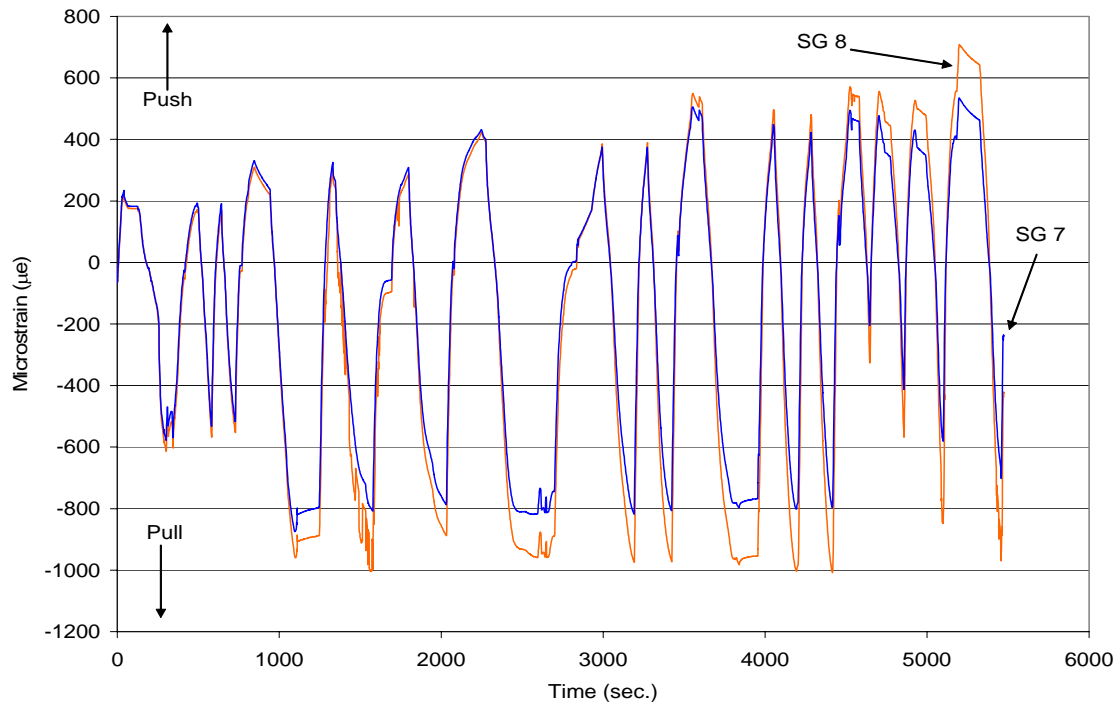


Figure 2.51 SG7 and SG 8 showing slip of lap splice in East column base

A moment curvature diagram was constructed for the lower portion of the East column; the moment increased up to 3.0% drift, and then displayed no increase or decrease. The moment curvature for the east column bottom is shown in Figure 2.52, from which the curvature ductility was determined as 17.7; this is 1.8 times the curvature ductility of the East column-bent cap joint indicating that the bottom of the column suffered more damage than the top.

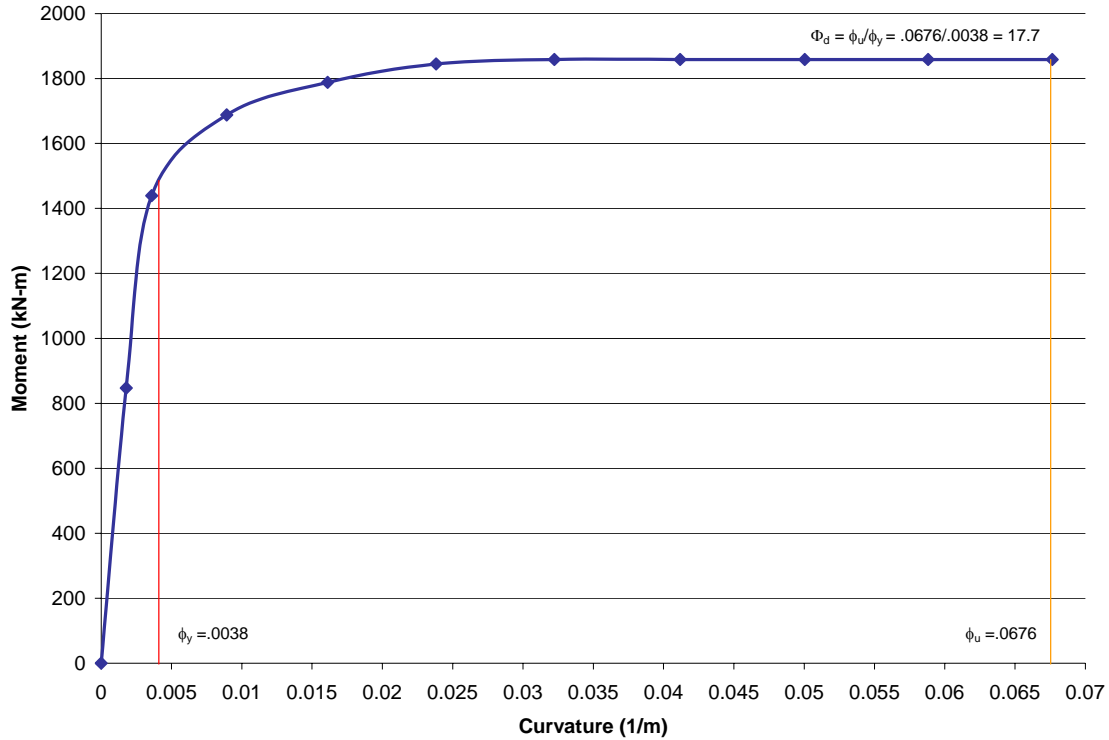


Figure 2.52 Moment-curvature for East column base

Field Notes for East column base: South face unless otherwise noted

- 1.) No visible flexural or shear cracks @ 0.5% drift
- 2.) Hairline flexural cracks start to develop at 279mm and 1.7m above the grade beam. They start in the middle of the south face and wrap around the west face and end in the center of the north face of the east column @ 1.0% drift
- 3.) 0.8mm flexural cracks propagate from hairline; @ 1.5% drift more flexural cracks appear with the half column formation mentioned above; 2.0mm cracks develop 279mm above pile cap
- 4.) 1.5mm flexural cracks open on the east half of the column 914mm above pile cap; No shear cracks have developed yet at 2.0% drift
- 5.) South face largest crack 3mm, west face largest crack 5mm, north face largest crack 3mm, east face largest crack 5mm at 5.0% drift

A summary of the performance of the East column base is given in Table 2.11, according to the three performance levels. The condition of the column base at various drift levels is shown in Figures 2.53 and 2.54.

Table 2.11 Damage assessment for East column base

	Phase I $0.5 < \text{drift} \leq 1.0$	Phase II $1.0 < \text{drift} \leq 2.0$	Phase III $2.0 < \text{drift} \leq 5.0$
Steel	n/a	n/a	n/a
Concrete	No visible flexural or shear cracks at 0.5%	Hairline flexural cracks start to develop at 279mm and 1.7m above the grade beam. They start in the middle of the south face and wrap around the west face and end in the center of the north face of the east column; At 1.0% drift 0.8mm flexural cracks propagate from the hairlines; At 1.5% drift more flexural cracks appear with the half column formation mentioned above.	0.8mm flexural cracks propagate from the hairlines; At 1.5% drift more flexural cracks appear with the half column formation mentioned above; 2.0mm cracks develop 279mm above pile cap South face largest crack 3mm, west face largest crack 5mm, north face largest crack 3mm, east face largest crack 5mm
Lap Splice Slip/Bucklin	n/a < 1% difference in SG7 and SG8 in tension; 9% difference in compression.	Column motion starts to pry the rebar and small strain drop occurs on compression phases; At 1.5% drift 14% difference in compression, still < 1.0% in tension; At 2.0% drift there is an 8% difference in tension and 18% difference in compression strain	At 3.3% drift the column bar is still picking up strain but the pile cap bar is slipping; At 5.0% drift the tensile strain difference is 24%



(a)



(b)

Figure 2.53 East column base: (a) 0.8mm cracks at 1.5% drift ratio, (b) 3mm to 5mm cracks at 5% drift ratio



Figure 2.54 East column base north face: 3mm to 5mm cracks at 5% drift ratio

Zone 5: Center Column Base Damage Assessment

The center column base designated as zone 5 contained six strain gages. Four of these gages SG 23, SG24, SG25, and SG26 are oriented in the same manner as the east column over a splice; the other two gages SG27 and SG28 are adhered to the confining hoop steel, as shown in Figure 2.22. Similar to the East column base, the importance of knowing how the lap splice behaves is the purpose of this instrumentation.

The lap splice held together well until a 1.5% drift ratio, after which the strains started to deviate; SG23 which was attached to the column rebar did exactly what was expected as seen in Figure 2.55. In the 6th cycle, SG23 reached the yield point and continued to increase in tensile strain with each cycle; on the other hand, the lap splice bar containing SG24 almost hit yield but then experienced slip at a 1.5% drift ratio; the next couple of cycles show some slipping then at 2.0% drift the slip degrades sharply, and this continues through to 5.0% drift. Strain gage SG28 located on the hoop steel recorded only 42% of its yield strength.

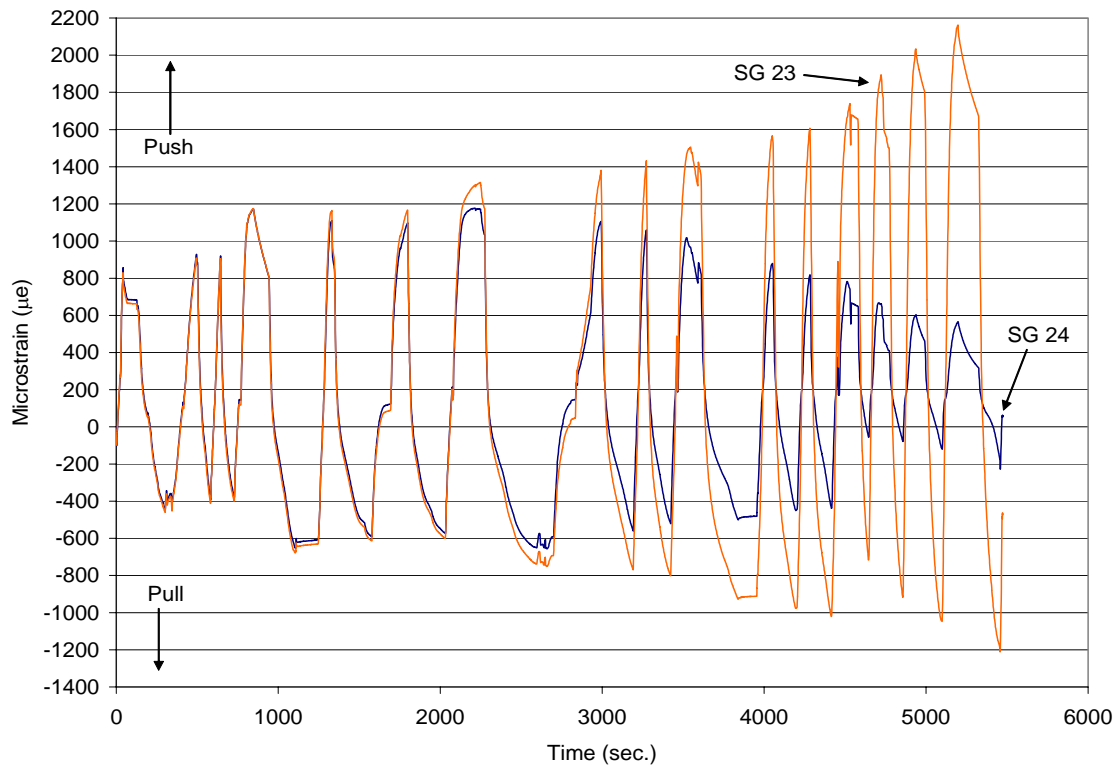


Figure 2.55 SG23 and SG24 showing relative slip in lap splice of center column base

In the analytical modeling of Bent #4S, the Center column bottom joint was the first to develop a plastic hinge; however, during testing it occurred after the Center column-bent cap joint has developed a plastic hinge. In actuality, plastic hinges formed at approximately 660mm above the grade beam (or 965mm above the pile cap), whereas the plastic hinge for the column-bent cap joint formed around 381mm below the bent cap. The mode of failure for the Center column bottom joint was shear induced buckling followed by lap splice failure, while for the Center column-bent cap joint the failure mode was flexural induced buckling. The damage for the Center column base, started at the corner intersection of the column and

[illegible]

A moment curvature diagram was constructed for the Center column base, as shown in Figure 2.57; the moment demand increased up to a 3.0% drift ratio, and then displayed no increase or decrease. The curvature ductility for the Center column base was determined to be 19.4, which is 1.7 times that of the Center column-bent cap joint, and signifies more damage.

56

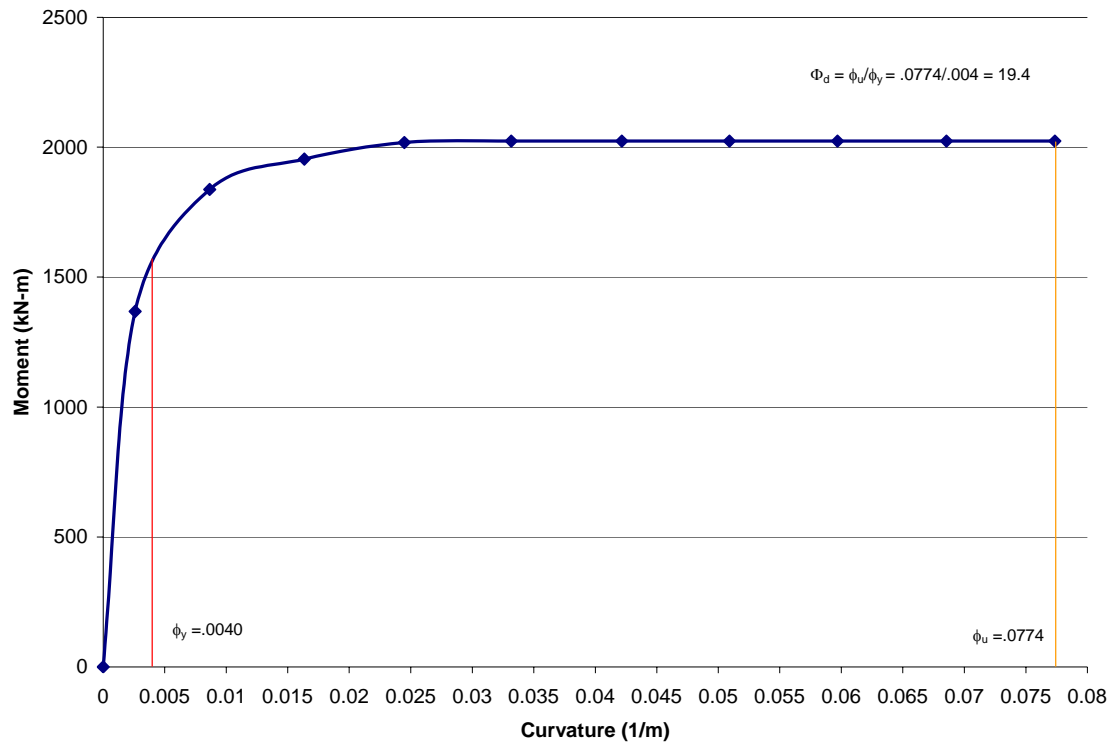


Figure 2.57 Moment-curvature for Center column base

Field Notes for Center column base: South Face unless otherwise noted; all measurements are taken from top of grade beam unless otherwise noted

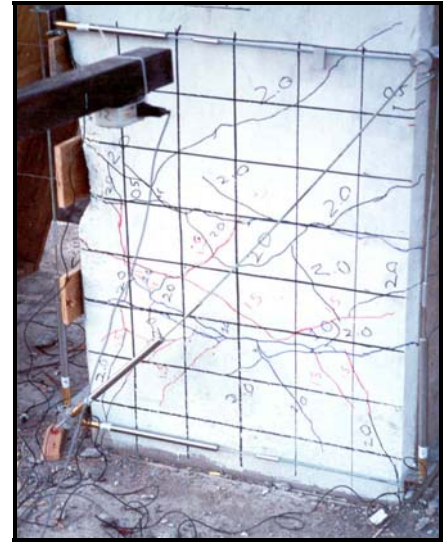
- 1.) 0.1mm flexural crack develops on all four sides at 762mm at 0.5% drift
- 2.) 1.5mm flexural/shear cracks develop between 76mm and 600mm at 1.0% drift
- 3.) 2.5mm flexural cracks propagate @ 1.5% drift from the previous drift step; more flexural cracks appear. Flexural cracks are 3.0mm wide by end of 1.5% drift step. Shear cracks start to develop quickly from the flexural cracks at centerline of column and are 2.0mm by end of 1.5% drift step
- 4.) Shear degradation is main mode of failure in the 2.0% drift step with 4.0mm shear cracks at the opening ends of the east/west faces and tapering to 1.0mm at the closing ends
- 5.) Around a 3.3% drift ratio the buckling mechanism on the West face is visible and evident as the volume change of the area, large (5.0mm) permanent cracks
- 6.) Largest crack experienced by the end of the 5.0% drift ratio last cycle was 11.0mm on South face near the buckling zone of the west face, 7.0mm on the West face again associated with the buckling zone, 7.0mm, 16mm, and 19mm cracks on the North side, as shown in see Figure 2.60(b), and 10 mm cracks on the East face along the buckling zone

Table 2.12 Damage assessment for Center column base

	Phase I $0.5 < \text{drift} \leq 1.0$	Phase II $1.0 < \text{drift} \leq 2.0$	Phase III $2.0 < \text{drift} \leq 5.0$
Steel	n/a	SG23 yields on first 1.5% drift-push cycle at about 1.2% drift	Almost all axial bars have yielded with the exception of those close to the neutral axis on the North and South faces
Concrete	0.1mm flexural crack develops on all four sides at 762mm at 0.5% drift 1.5mm flexural/shear cracks develop between 76mm and 600mm at 1.0% drift	2.5mm flexural cracks propagate at 1.5% drift from the previous drift step; more flexural cracks appear. Flexural cracks are 3.0mm wide by end of 1.5% drift step. Shear cracks start to develop quickly from the flexural cracks at centerline of column and are 2.0mm by end of 1.5% drift step. Shear degradation is main mode of failure in the 2.0% drift step with 4.0mm shear cracks at the opening ends of the East/West faces and tapering to 1.0mm at the closing ends	Largest cracking experienced by the end of the 5.0% drift cycle was 11.0mm on South face near buckle zone of West face, 7.0mm on West face again associated with the buckle zone, 7.0mm, 16mm, and 19mm cracks on North side, see Figure 2.60(b), and 10 mm cracks on the East face along the buckle zone
Lap Splice Slip/Buckling	n/a	Column motion starts to pry the rebar and small strain drop occurs on compression phases at 1.5% drift ratio with a 10% difference in strain readings across SG23 and SG24	Around 3.3% drift the buckling mechanism on the west face is visible and evident by the volume change and large (5.0mm) permanent cracks. At 2% drift the column bar is still picking up strain but the pile cap bar is slipping, the difference in strain is 33%. There is 64% difference at 3.3% drift and 73% difference at 5%drift



(a)



(b)

Figure 2.58 Center column base: (a) before test, (b) diagonal shear cracks at 2% drift



(a)



(b)

Figure 2.59 Center column base at 5% drift: (a) South face, (b) East face

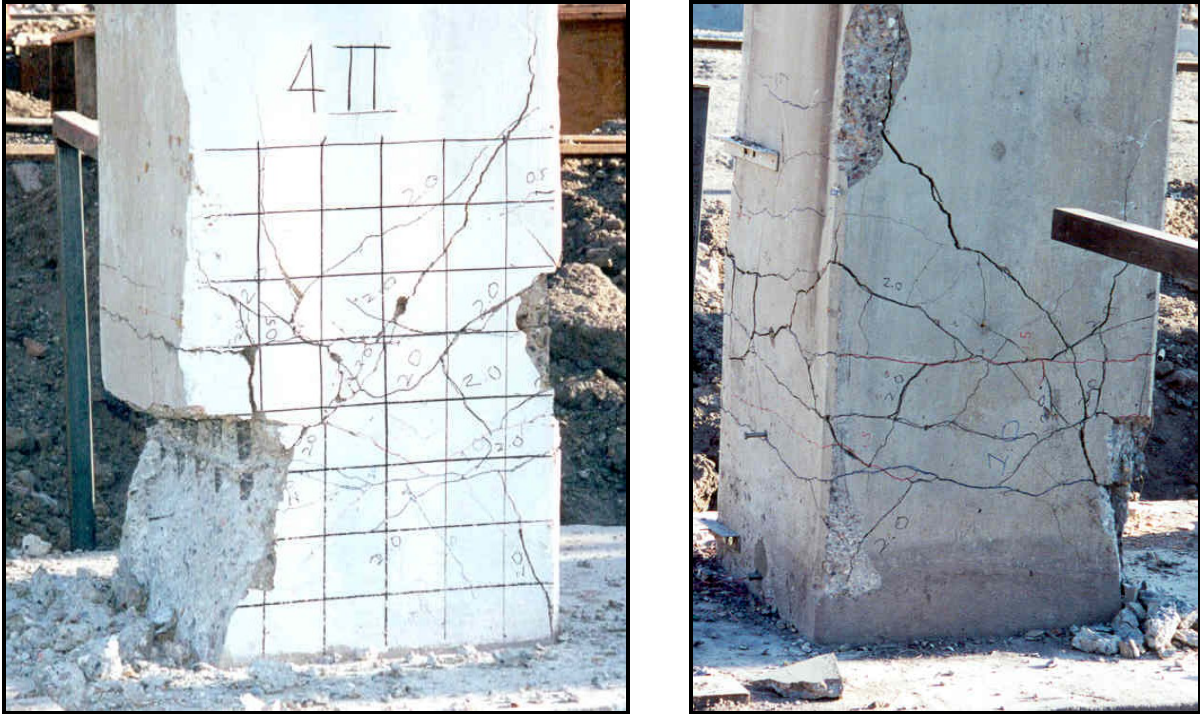


Figure 2.60 Center column base at 5% drift: (a) West side and Southwest corner showing buckled bars, (b) North face

Zone 6: West Column Base Damage Assessment

The West column base, designated as zone 6, contained six strain gages; four of these gages SG 47, SG48, SG51, and SG52 were oriented in the same manner as the Center and East columns over the lap splice. The other two gages SG49 and SG50 were attached to the confining hoop steel. Similar to the other column bases, the goal of the instrumentation was to understand how the lap splice functioned. The lap splice held together well up to a 1.5% drift ratio, with a 7% strain difference between the column and foundation bars and then the strains started to deviate. Strain gage SG51, which was attached to the column rebar yielded in the third cycle and kept increasing in strain as shown in Figure 2.61.

The bar containing SG52 almost hit yield in the sixth cycle at 2.0% drift and experienced a 13% difference in strain from SG51. At 3.3% drift, the slip degraded quickly showing a 33% difference in strain, and at 5.0% drift the difference was 51%. Strain gage SG28 located on the hoop steel was stressed to a fraction of its yield strength at $200\mu\text{s}$, or 16% of its yield strength.

In the analytical model the West column base was the last to develop a plastic hinge. A plastic hinge formed 571mm above the grade beam. There was no apparent buckling around the West or East faces, even though there was lap splice failure and yielding. This confirms that the analytical model was correct in predicting this to be one of the last hinges to form. From observations during the test, the plastic hinge was still developing and was not a full mechanism at 5% drift ratio.

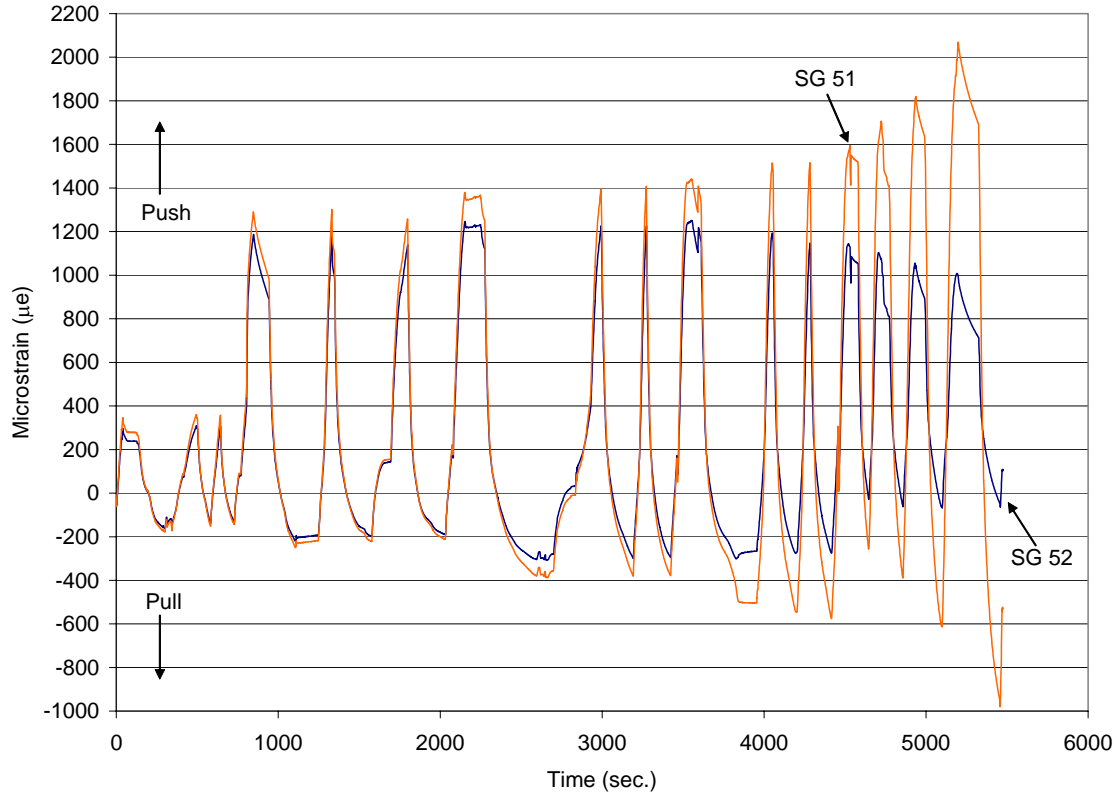


Figure 2.61 Strain gages SG51 and SG52 showing relative slip in the lap splice of West column base

A moment curvature diagram was constructed for the West column base, as shown in Figure 2.62; the moment demand increased up to 3.0% drift, and then displayed no increase or decrease. The moment-curvature ductility for west column bottom joint was determined to be 16.9, which is 1.6 times that of the West column-bent cap joint, and signifies more damage.

A summary of the performance of the West column base is given in Table 2.13, according to the three performance levels. The condition of the column base at various drift levels is shown in Figures 2.63 and 2.64.

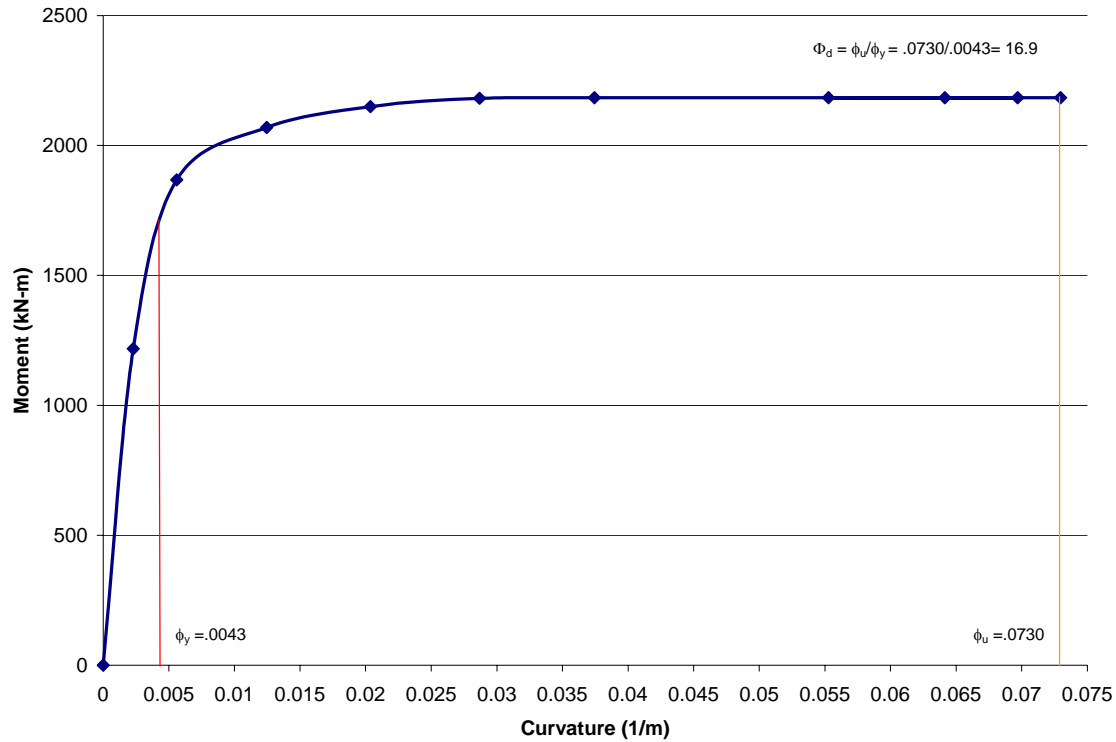


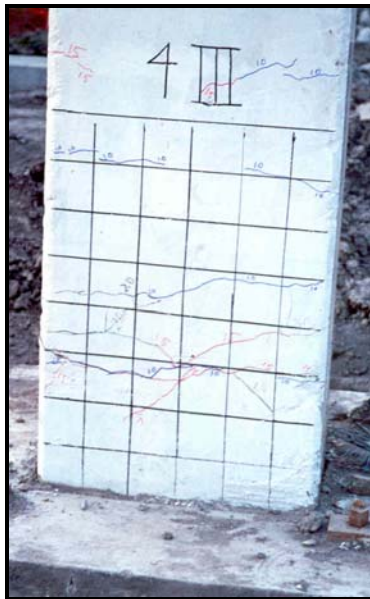
Figure 2.62 Moment-curvature for West column base

Field Notes for West column base: South face unless otherwise noted; all measurements are taken from top of grade beam unless otherwise noted

- 1.) No visible flexural or shear cracks @ 0.5%
- 2.) Hairline flexural cracks @ 1.0% drift start to develop at 419mm, 723mm, 1.1m, and 1.5m above the grade beam. They start in the middle of the South face and wrap around the West and East faces and end in the center of the North face of the East column. The cracks do not align to form one continuous ring around the column; they are staggered
- 3.) 1.0mm flexural cracks propagate from the hairlines @ 1.5% drift in the 419mm height range
- 4.) 1.0mm flexural cracks start migrating to the corners of the column and grade beam to develop the shearing mechanism @ 2.0% drift
- 5.) A triangular chunk of concrete is cracked and hanging in place on the West face. The largest crack on the South face was 11mm, on the West face the largest crack was 4.7mm, on the North face the largest crack was 6mm, and on the east face the largest crack was 9mm at 5.0% drift

Table 2.13 Damage assessment for West column base

	Phase I $0.5 < \text{drift} \leq 1.0$	Phase II $1.0 < \text{drift} \leq 2.0$	Phase III $2.0 < \text{drift} \leq 5.0$
Steel	SG51 yields in tension (push) in 3 rd cycle of 1.0% drift	SG52 yields in tension on first push cycle of 1.5% drift	Almost all rebars have yielded with the exception of those close to the neutral axis on the north and south faces
Concrete	No visible flexural or shear cracks at 0.5%; Hairline flexural cracks at 1.0% drift start to develop at 419mm, 723mm, 1.1m, and 1.5m above the grade beam; they start in the middle of the South face and wrap around the West and East faces and end in the center of the North face of the East column. The cracks do not align to form one continuous ring around the column; they appear to be staggered	1.0mm flexural cracks propagate from the hairlines at 1.5% drift in the 419mm height range. 1.0mm flexural cracks start bending to the corners of the column and grade beam to develop a shear mechanism at 2.0% drift	A triangular chunk of concrete is cracked and hanging in place on the West face. The South face largest crack is 11mm, west face largest crack 4.7mm, north face largest crack 6mm, east face largest crack 9mm at 5.0% drift
Lap Splice Slip/Buckling	0.5% drift shows 5% difference in strain reading; 1.0% drift shows 7% difference	Column motion starts to pry the rebar but the difference still remains 7% at a 1.5% drift ratio. By the end of 2.0% drift, there is a 13% difference	At 3.3% drift the column bar is still picking up strain but the pile cap bar is slipping, the difference in strain is 33%. At 5.0% drift the difference is 51%



(a)



(b)

Figure 2.63 West column base damage: (a) South face at 2% drift, (b) South face at 5% drift

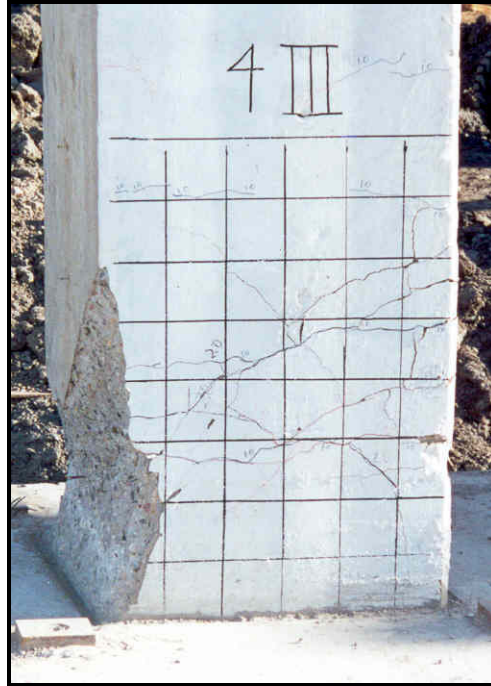


Figure 2.64 West column base post-test damage on South face at 5% drift

Overall Structural Performance

Performance Levels for Bent #4S

There were three performance levels for Bent #4S as evidenced by analysis of the test data: (1) System yielding at 1% drift ratio, (2) Longitudinal column bar pullout from the East and West column-bent cap joints at 2% drift ratio, and (3) Lap-splice failure at the base of all three columns by 5% drift ratio. These three performance levels define then important phases of the tests and the damage experienced by the structure, which is summarized in Table 2.14

Table 2.14 Damage assessment of structure of Bent #4S

	Element	Phase I 0.5% < drift ≤ 1.0%	Phase II 1.0% < drift ≤ 2.0%	Phase III 2.0% < drift ≤ 5.0%
Column-Bent Cap Joints	Steel	Center and West Bent cap yield in tension first pull cycle of 0.5% drift; East Bent cap yields first pull cycle of 1% drift	Strain hardening through the pull cycles in East and West Bent cap	Strain hardening in Center Bent cap
	Concrete	0.2mm-1.5mm flexural cracks 1mm diagonal shear cracks 155mm-200mm long	1.0mm-5mm cracks lengthening of the shear cracks which develop plastic hinges; buckling of column bars in Center column	4mm- 6.5mm cracks developing; Shear mechanism is fully developed; South face of center column has 17mm open flexural crack
	Column Bar Pullout / Buckling	n/a	Corner bars de-bond locally at 1.5% drift at West column; Spalling of clear cover on SE corner of Center column; buckling initiation	Column bar pullout begins at 2% drift on East and West column; bar buckling in Center column at 3% drift
Column Bases	Steel	n/a	Center column steel yields at 1.2% drift and West column at 1.5% drift	Almost all axial rebar yields in Center and West columns with the exception of those close to the neutral axis on the north and south faces
	Concrete	1.5mm flexure/ shear cracks in Center column at 1% drift; Hairline flexural cracks in West column at 1% drift	0.8mm flexural cracks at 1.5% drift in East column; Shear degradation is main mode of failure in Center column at the 2% drift step with 4mm shear cracks at the opening ends of the east/west faces; 1mm flexural cracks start migrating to the corners of the West column and grade beam to develop the shearing mechanism at 2% drift	Flexural cracks appear in west and east faces of East column largest crack is 5mm; At 3.3% drift buckling on the west face of the Center column is visible; Permanent cracks vary from 7mm on west face to 19mm cracks on north face of Center column; For West column permanent cracks reach 11mm
	Lap Splice Slip / Buckling	At 1.0% drift 7% difference in strain between spliced bars on West column, 9% on East column	Column motion starts to pry the rebar; At 2.0% drift there is an 8% difference in tension and 18% difference in compression strain between spliced bars of East column; at 1.5% drift ratio there is a 10% difference in strain readings between spliced bars in Center column; at 2% drift there is 13% difference between spliced bars of West column	At 5.0% drift the tensile strain difference between spliced bars of the East column is 24%; In the Center column at 2% drift the column bars are still picking up strain but the pile cap bar is slipping, the difference in strain is 33%. There is 64% difference at 3.3% drift and 73% difference at 5% drift; In the West column the difference in strain is 33% and at 5.0% drift the difference is 51%

Displacement Ductility for Bent #4S

The displacement ductility of Bent #4S was calculated based on a spline interpolation of the load vs. deformation envelope curve obtained during the test from Figure 2.27. However, it should be noted that the last four cycles, which did not consider complete load reversal in Figure 2.23, were not included; this is justified on the basis of wanting to carry out a direct comparison between all three tests. Thus, the yield displacement is equal to $\Delta_y = 59.8\text{mm}$ and the ultimate fully reversed displacement is equal to $\Delta_{\max} = 151.5\text{mm}$, which gives a displacement ductility of $\mu_{\Delta} = \Delta_{\max} / \Delta_y = 2.53$.

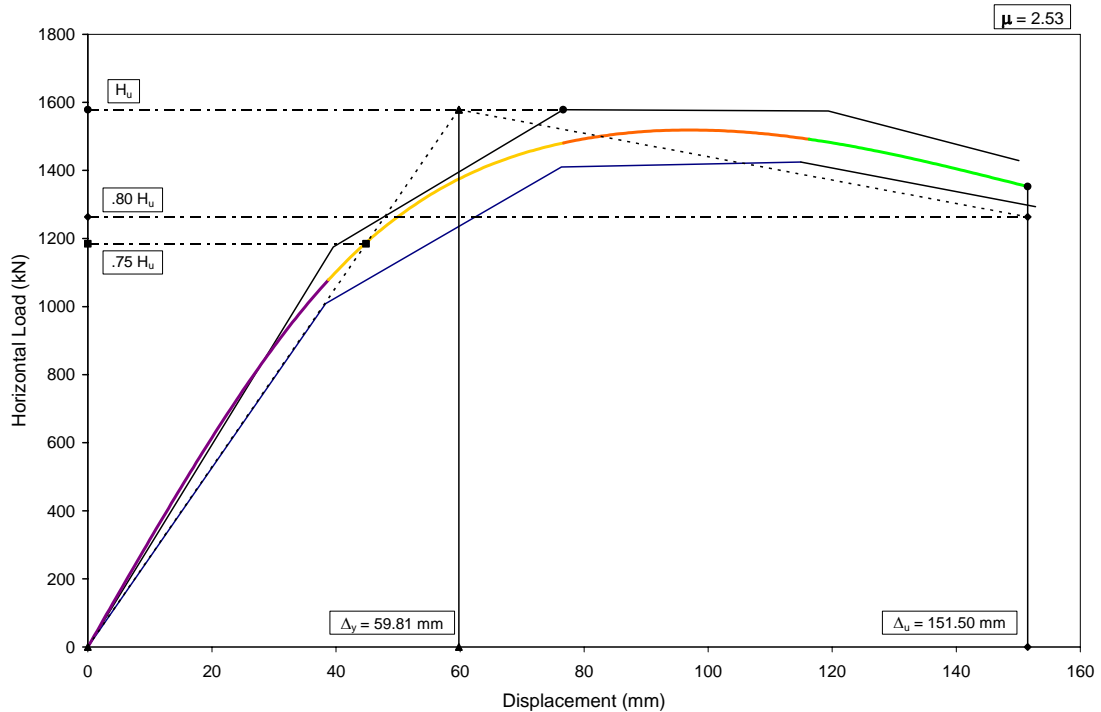


Figure 2.65 Displacement ductility of the Bent #4S

From the results of the test outlined in the preceding paragraphs with respect to the six zones, it can be observed that systematic degradation of Bent #4S occurred by means of four mechanisms. In Phase I the initial system yielding allows for further displacement with increasing lateral loading. This is accompanied by two mechanisms: (1) many local reinforcing bars yield at the top and bottom of the columns, and (2) cracking of the concrete in the six zones which begins producing stiffness degradation.

In Phase II the third mechanism of longitudinal column bar pullout from the bent cap joints further weakens the structural system. As bars pull out, the structural system loses continuity, and forces and moments that the system should collectively resist are transferred to other components within the system. These components are then overstressed and begin failing more quickly. This bar pull occurred in the interval from 1.0% to 2.0% drift ratio.

However, although the pullout has a large effect on the structure at this time, it should not be taken that pullout is the only mechanism occurring. The structural system is still experiencing localized yielding, and the effects of concrete cracking and crushing.

Phase III starts to materialize after the 2.0% drift cycles. At increasingly larger displacements, the rotations in the base joints become larger, and the prying forces on the reinforcement spread the lap splices apart. Because of this lap splice slip mechanism at or around 2.0% drift, a steady degradation in the strength of the structure is seen; each cycle produces a little more slip and therein the strength has a steady linear drop off.

3. BRIDGE BENT #5S WITH GRADE BEAM RETROFIT AND GRAVITY LOAD

The main objective of test Bent #5S (2000) was to determine the in-situ performance of a bridge bent carrying half the in-service gravity load, using a reinforced concrete grade beam seismic retrofit connecting the three pile caps, under simulated earthquake lateral loads. The information gained is useful in assessing the bridge bent capacity, the potential damage that could be caused by earthquakes to bridges of similar construction, and the effectiveness of the grade beam seismic retrofit. An analytical model of the bridge bent was developed which included the soil-pile-structure interaction conditions (Ward 2001, Cook et al. 2002). Even though the bridge bent had inadequate details other than the foundation, these were not retrofitted in the present test; the results of the present test are important in establishing the deficiencies of the superstructure excluding those of the foundation system. The performance of the bridge bent in the present test was compared to that of a bent with identical details (Bent #6S 2000), which was seismically retrofitted both with a grade beam in the foundation and with CFRP composites in the superstructure (Pantelides et al. 2002). Comparisons were carried out for a similar experiment of an identical bridge bent (Bent #5N 1998) without the grade beam seismic retrofit (Pantelides et al. 2001), and Bent #4S (2000) with identical details including the grade beam retrofit but without the deck described in Chapter 2.

Bridge Bent Description

Superstructure

The superstructure of Bent #5S (2000) consisted of three columns, a bent cap, steel girders, and the deck. The 7.188-m high columns were 0.914 m square, while the bent cap was 19.660 m long, 0.914 m wide, and 1.219 m high, tapering to 0.914 m from the exterior columns to the ends, as shown in Figure 3.1. Each column had sixteen 32 mm reinforcing bars around its perimeter extending from the pile cap to within 310 mm of the bent cap top fiber, as shown in Figures 3.2 and 3.3. The transverse reinforcement consisted of 13 mm single hoops starting at 152 mm from the base of the column and spaced at 305 mm up to the bent cap bottom fiber, as shown in Figures 3.2 and 3.3. At the base of each column, there were 16 dowels of the same dimension in lap splices extending 0.762 m (24 bar diameters) above the pile cap, as shown in Figure 3.3. There was no transverse reinforcement in the bent cap-column joints or in the pile caps.

The bent cap flexural reinforcement consisted of 32 mm and 16 mm bars as shown in Figure 3.3. For transverse reinforcement 16 mm double stirrups were used, as shown in Figure 3.3, at a spacing that was varied along the length of the bent cap, as shown in Figure 3.2. There were no vertical stirrups present in the bent cap-column joints. The concrete cover was 51 mm over the surface of the bent cap and 89 mm over the columns.

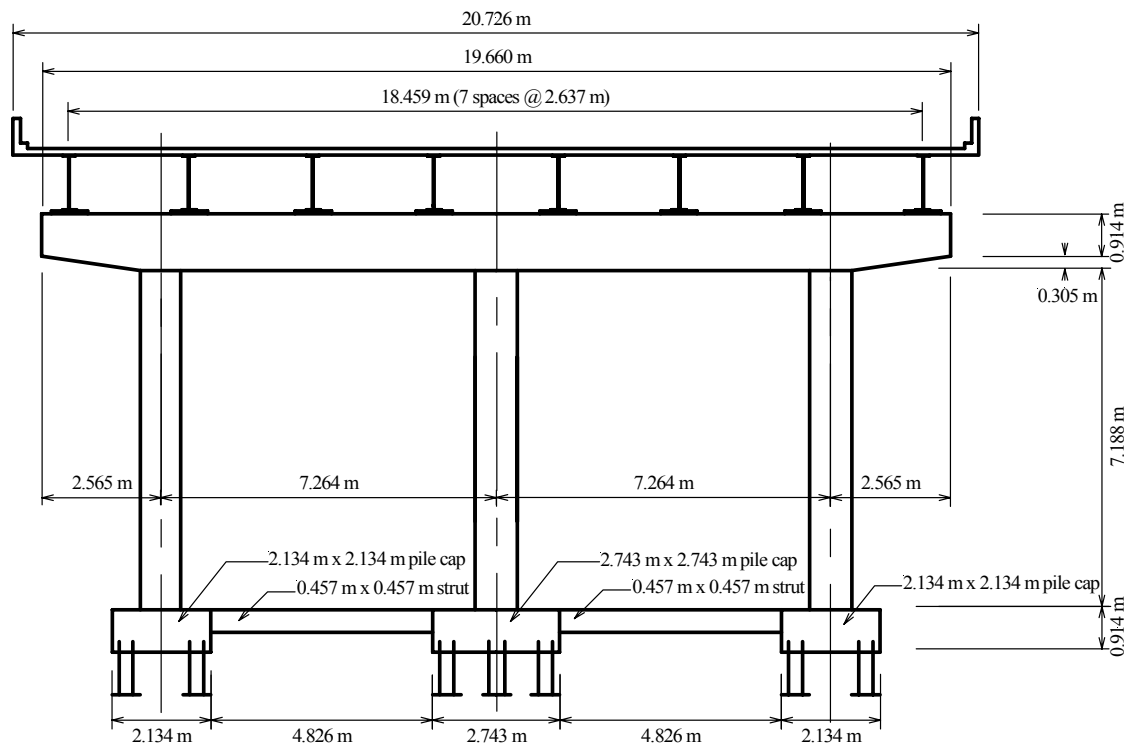


Figure 3.1 As-built Bent #5S (2000)

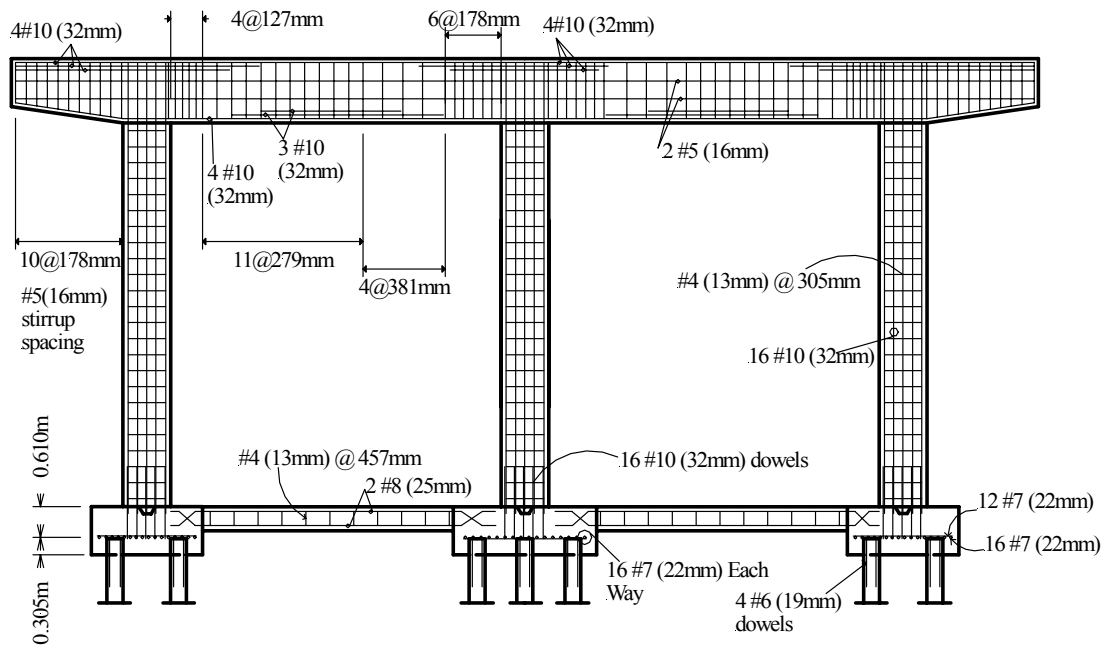


Figure 3.2 Steel reinforcement details for as-built Bent #5S (2000)

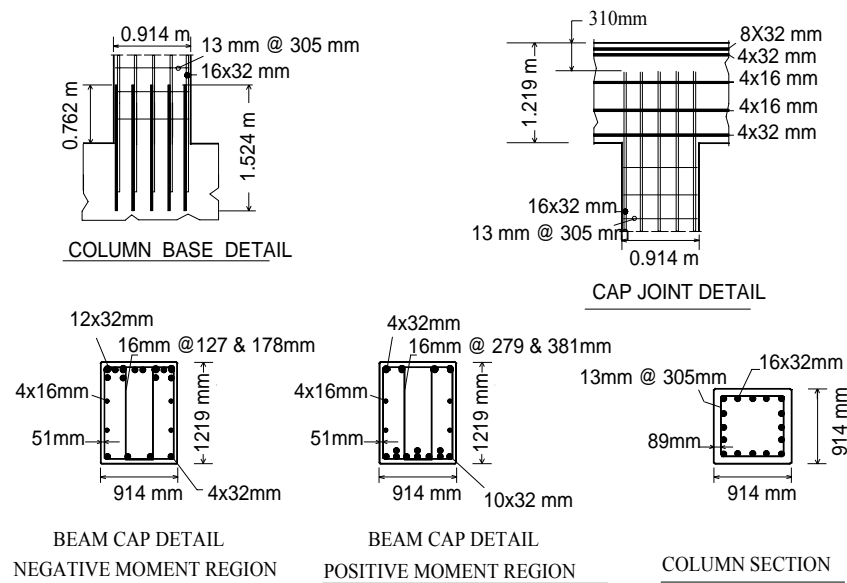


Figure 3.3 Cross-sectional reinforcement details for Bent #5S (2000)

As-Built Foundation

The three columns were supported on reinforced concrete pile caps. The two exterior caps measured 2.134 m square and 0.914 m high; they were supported on four cylindrical concrete filled steel piles, 0.305 m in diameter and approximately 18.30 m deep. The interior cap was 2.743 m square, 0.914 m high, and was supported on five piles. Connecting each pile cap was a 0.457 m square concrete strut beam, reinforced with four 25 mm bars with 13 mm stirrups spaced at 457 mm, as shown in Figure 3.2. The exterior pile caps were each reinforced by a row of sixteen 22 mm bars running perpendicular to the plane of the bent, and a row of twelve 22 mm bars running parallel to it. This reinforcement was located 0.610 m below the top of the pile cap. The interior pile cap was reinforced similarly except that the parallel row had sixteen 22 mm bars.

The 305-mm diameter concrete filled steel piles were embedded into the 0.914-m thick pile cap a distance of 0.305 m as shown in Figure 3.4. The piles were connected to the pile cap with four 19 mm bars extending 0.305 m into the pile cap, as shown in section A-A of Figure 3.4. For the lateral loads predicted from the analysis, the anchorage length would have been insufficient to resist pullout failure of the piles. A 38-mm hole was cored through the pile cap and into the pile for a distance of 2.438 m as shown in Figure 3.4, and the pile was anchored to the pile cap using a 32 mm Dywidag bar (1,030 MPa ultimate stress) epoxied into the hole. This detail was implemented for the four corner piles of each pile cap; the fifth pile of the interior cap was underneath the interior column, it was not accessible and thus it was not retrofitted.

Comparison with AASHTO and ACI Requirements

The reinforcement details of the bridge bent were compared to the AASHTO requirements for seismic zones 3 and 4 (AASHTO 1998). With respect to the area of longitudinal column reinforcement, the existing columns had a steel ratio of 1.6%, which satisfied the requirement that the steel ratio should be between 1% and 6%. In terms of the transverse reinforcement for confinement of the columns, the AASHTO requirement calls for

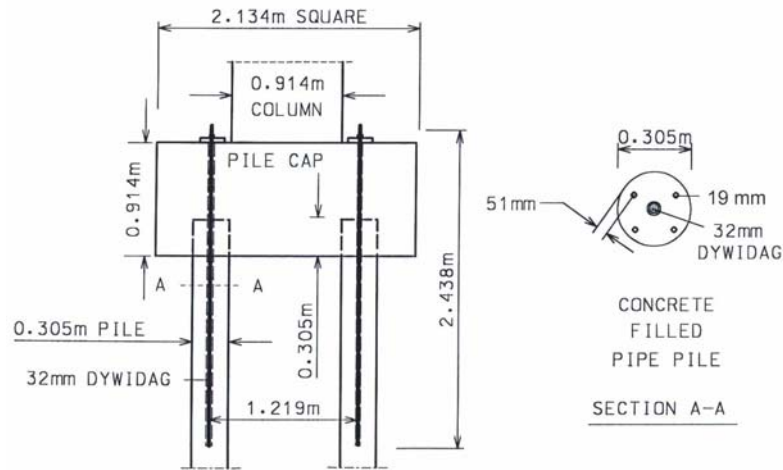


Figure 3.4 Pile-to-pile cap connection details and retrofit

transverse reinforcement to be provided at a maximum of 100 mm for the top and bottom 1.198 m of the columns, which was violated by the existing details; in addition, the cross-sectional area of the transverse reinforcement was only 43% of the area required. Currently, lap splices are permitted only within the center half of the column height and the splice length should not be less than 60 bar diameters; in the bridge bent tested, the splice was in the plastic hinge region at the bottom of the column, and the lap splice length was only 24 bar diameters; in addition, the requirement for spacing of transverse reinforcement in the splice region of 100 mm was violated since the spacing of the ties was 305 mm. The hoops provided also violated the AASHTO requirements of a closed tie with 135-degree hooks having a 75 mm extension at each end. The development length of the longitudinal steel into the bent cap required by AASHTO is 881 mm and this was met in part, since the column steel extended 909 mm into the bent cap; however, the existing bent details violate the requirement which calls for column transverse reinforcement extending a distance of 380 mm from the face of the column connection into the adjoining members, since no transverse reinforcement was provided in either the bent cap joints or the pile caps.

ACI committee 318 (1999) states that the positive moment capacity of the bent cap near the column support should be more than half the negative moment capacity at that same support, i.e. $M^+/M^- \geq 0.5$, where M^+ = bent cap positive moment capacity near the support (1186 kN-m), and M^- = bent cap negative moment capacity near the support (3366 kN-m). This ratio was 0.35 in the present case, which violates significantly the design stipulation.

Gravity Load

The gravity load was provided by the road deck, which was left in place connecting Bents #5S and #6S. The deck was supported on eight wide flange steel girders that rested on steel bearing plates and concrete pedestals built on top of the bent cap at 2.637 m, on centers, as shown in Figure 3.1. The weight of the deck was calculated as 3843 kN. Because the deck rested on two bents, the load per bent was 1922 kN, i.e. half the in-service gravity load, or 240 kN per girder per bent. The weight of the bent cap (503 kN), and that of the columns (425 kN) were included in the analytical model. Thus, the exterior columns had an axial load of $0.033 f'_c A_g$, and the interior column a ratio of $0.038 f'_c A_g$, where f'_c = concrete compressive strength, and A_g = column gross cross-sectional area. In order to minimize the torsional effects and carry out the test safely, the deck was fixed to Bent #5S and allowed to move on rollers at Bent #6S.

Grade Beam Seismic Retrofit

From a static pushover analysis of the bent, it was concluded that the foundation with the existing reinforcement details would not be able to resist the forces resulting from the lateral load and displacement applied to the bent, and would fail before the capacity of the superstructure would be reached; this was evident at the pile to pile cap connections. A reinforced concrete grade beam overlay was constructed at the bottom of the bent, around the pile caps and struts, as shown in Figures 3.5 through 3.9; its purpose was to complete the tension and compression load path at the base of the bent, improve shear and negative moment capacity of the foundation, and allow the pile caps to displace uniformly, so that failure at the pile to pile cap connections would be prevented.

In order to improve the connection of the piles to the pile cap, a hole was cored 1.524 m into each pile through the 0.914-m pile cap, and a 32-mm vertical Dywidag bar was set into place with a high strength epoxy grout as shown in Figures 3.4 and 3.9; this was done for the four corner piles of each pile cap as shown in Figure 3.5; a 25 mm steel plate washer was placed on the grade beam, and a nut was used to tighten the Dywidag assembly together. The grade beam thickness was 0.762 m between two pile cap faces and 0.305 m over the pile caps; the width was 2.134 m, and extended 0.457 m past each end pile cap, as shown in Figure 3.5. The critical sections were at the pile cap-grade beam overlay connection points, as shown in Figure 3.6, and the midspan of the grade beam between two pile cap faces. The design followed ACI 318 (1999) procedures for flexural and axial member design. The beam was designed to resist positive and negative moments of 1153 kN-m and 668 kN-m, respectively, at the middle of the span between two pile cap faces, and a 373 kN-m negative moment at the pile cap overlay. The positive and negative moment capacities of the grade beam within the span were 1122 kN-m and 2876 kN-m, and the overlay had a 590 kN-m negative moment capacity. The grade beam was designed to carry a 450 kN shear load. According to ACI 318 (1999), the shear capacity of the grade beam within the span was 1573 kN and 2744 kN over the pile caps.

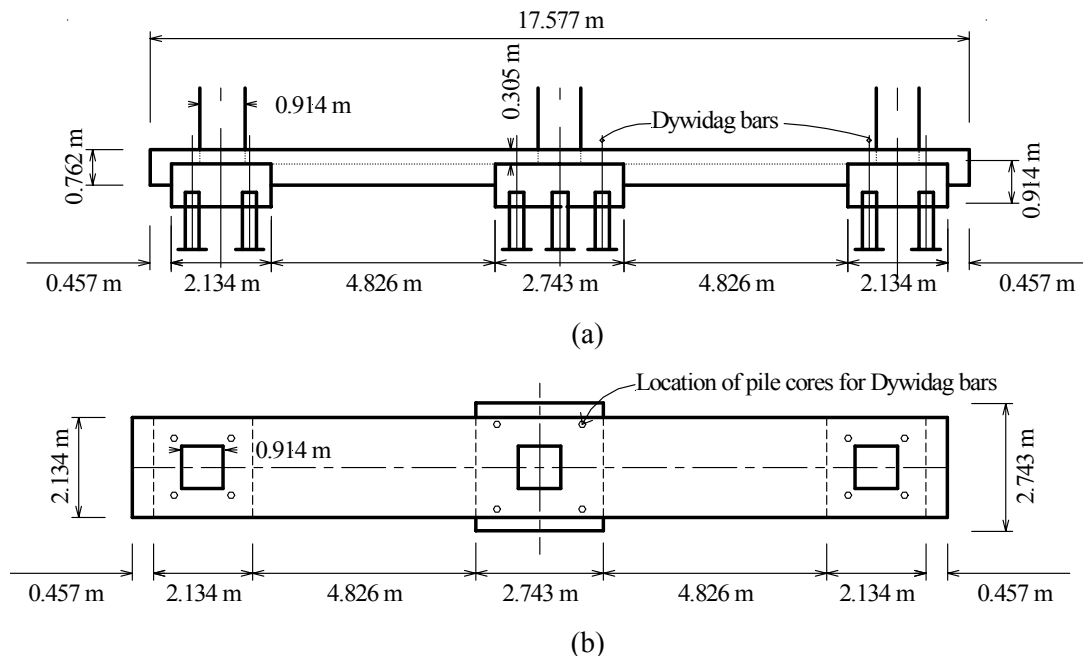


Figure 3.5 Grade beam retrofit: (a) elevation, and (b) plan

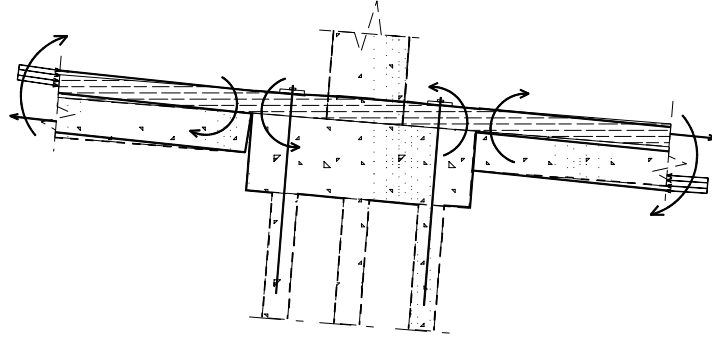


Figure 3.6 Design of grade beam for flexural and axial loads

The knee joints at the ends of the grade beam were designed for closing and opening moments using equations and reinforcement details given by Park and Paulay (1975). The horizontal area of one joint stirrup is given as:

$$a_{s-horz} = 1.5 \frac{s_{vert}}{d_{vert}} A_s \quad (3.1)$$

where s_{vert} = vertical spacing of horizontal stirrups, d_{vert} = vertical depth of concrete section, and A_s = area of longitudinal reinforcement. Similarly, the area of one vertical joint stirrup is given as:

$$a_{s-vert} = 1.5 \frac{s_{horz} d_{vert}}{d_{horz}} A_s \quad (3.2)$$

where s_{horz} = horizontal spacing of vertical stirrups, and d_{horz} = horizontal depth of concrete section. Application of Equations 3.1 and 3.2 resulted in the knee joint reinforcement details shown in Figures 3.7 through 3.9. The longitudinal reinforcement consisted of twelve 25 mm bars along the top, and two groups of three 25 mm bars along the bottom, between the pile caps. The shear reinforcement was 10 mm stirrups spaced at 152 mm over the pile caps and for a distance of 0.610 m beyond the pile caps, and a spacing of 406 mm along the two spans, as shown in Figure 3.8.

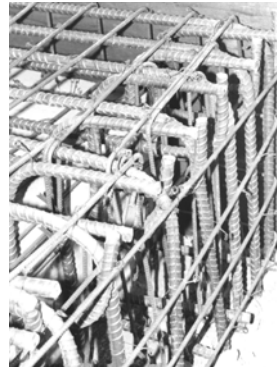
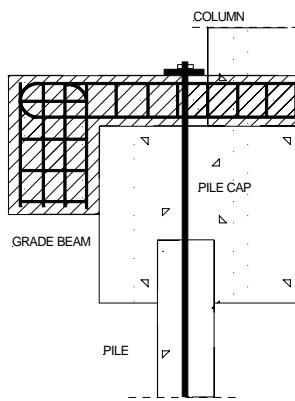


Figure 3.7 Grade beam knee-joint reinforcement details

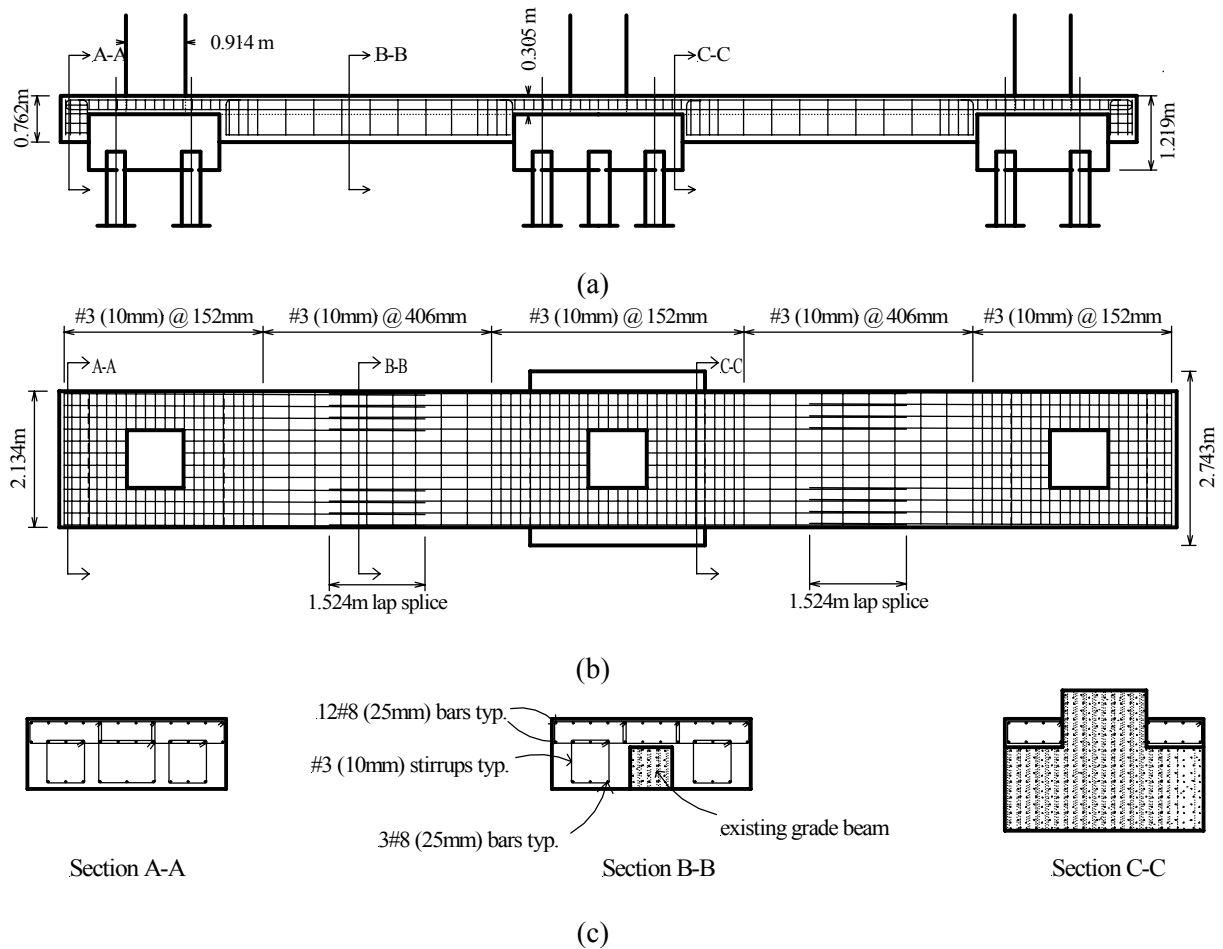


Figure 3.8 Grade beam reinforcement details: (a) elevation view, (b) plan view, and (c) Section A-A knee joint, Section B-B span between pile caps, and Section C-C overlay on existing pile caps



Figure 3.9 Grade beam reinforcement including Dywidag bars, cap overlay, and knee joint

Material Properties

Several samples of 32 mm, 19 mm, and 16 mm diameter bars were taken from the existing bridge and cut into 0.61-m lengths; in addition, 25 mm and 10 mm diameter new bars from the grade beam retrofit were tested. For the existing structure, the steel had a yield stress of 326 MPa or 1.21 times the design yield strength, and for the grade beam steel, it had a yield stress of 469 MPa. Four concrete cylinders, 102 mm in diameter and 204 mm in height, were cored from the existing bent. The concrete cores were tested according to ASTM C 42/C 42M – 99 (ASTM 1999). The average concrete compressive strength of the existing structure was 33 MPa or 1.23 times the design strength. The average compressive strength of the new grade beam concrete was 34 MPa.

Experimental Investigation of Bridge Bent

The experiment for Bent #5S (2000) was conducted as a quasi-static cyclic lateral load test. A cyclic load was applied at the bent cap centerline using a 2700 kN-capacity hydraulic actuator mounted at the top of a steel load frame on the west end of the bent. The steel frame sat upon two foundations, one supported by piles, and the other supported by geopiers. The actuator was connected to a steel yoke, which provided a flat surface and distributed the pressure evenly across the entire end face of the bent cap when pushing to the east, as shown in Figure 3.10. On the opposite end, there was a similar yoke, joined to the first by twenty 13 mm-diameter prestressing steel cables. These cables provided enough tension to pull the entire structure to the west when the actuator was retracting. However, the cables were prestressed only to take out the sag and did not interfere with the bent cap capacity.



Figure 3.10 Load frame setup showing actuator, steel yoke, and prestressing cables

Instrumentation

In order to determine the strain levels in the steel reinforcement, strain gauges were attached to the reinforcement in selected locations, including the base and top of the columns, in the bent cap-column joints, and along the top and bottom longitudinal reinforcement of the bent cap. In addition, there were strain gauges attached to the Dwyidag bars at the pile cap/pile interface, and 305 mm above and below this interface. Several gauges were placed in the grade beam on longitudinal, transverse, and shear reinforcement.

Linear variable differential transducers (LVDTs) were placed in two types of arrays. One box array was placed at the base of the center column, and another around the center bent cap-column joint. A box array consisted of two vertical LVDTs, two horizontal, one diagonal, and one each on the lower west and upper east of the array, perpendicular to the others. The box arrays were used to measure joint shear strain, and the end-to-end arrays were used to measure column curvature. In order to measure the displacement of the system, several cable extension displacement transducers (DTs) were used. A DT was attached to each end of the bent cap to measure the overall horizontal displacement, on the grade beam to measure the foundation movement, and one DT was attached to the top of the load frame to record its movement.

Test Procedure

The experiment was performed using a cyclic, quasi-static load. Each cycle was repeated three times for each load step. At the end of each load step the test was paused for making observations and the test resumed, but at a larger displacement, as shown in Figure 3.11. The

displacements were implemented at preselected drift ratio increments, as a percentage of lateral displacement at the bent cap level divided by the column height (0.25%, 0.5%, 1%, 1.5%, 2%, 2.5%, etc.). This continued until the actuator reached its maximum stroke in the push direction, which occurred at a drift ratio of 2.7%; at that point, the test was continued by pushing to the maximum displacement, and pulling 25 mm farther than the previous step; this continued for three more load steps; when the actuator reached its maximum stroke in the pull direction, which occurred at a drift ratio of 3.8%, the test was terminated.

Experimental Results

A load cell attached to the hydraulic actuator recorded the applied load as shown in Figure 3.12. The maximum load in the push direction was 2046 kN, and the last push reading was 1741 kN, a drop of 15%; the displacement corresponding to this load drop was used for evaluating the displacement ductility. The maximum load recorded by the load cell in the pull direction was -1877 kN, and the last reading in the pull direction was -1847 kN, a drop of 2%. To measure the absolute displacement of the bent, a DT was attached to each end of the bent cap. The average value was then calculated and labeled “Displacement of Total System.” The “Displacement of the total System” included the displacement from the top of the bent cap to the piles, including the deformation contribution of the piles, the soil around the piles, the pile caps, the grade beam, the columns, and the bent cap. In Figure 3.11, the displacement on the top of the grade beam included the deformation contribution of the piles, the soil around the piles, the pile caps and the grade beam; the superstructure displacement included the deformation contribution of the columns, and the bent cap.

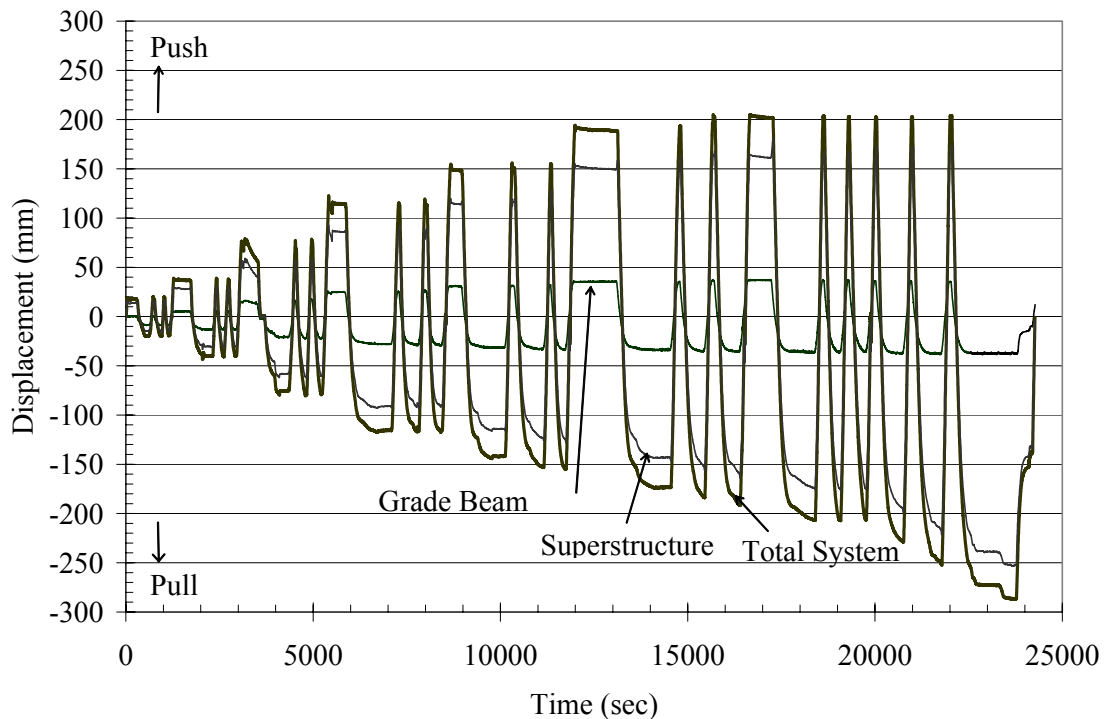


Figure 3.11 Displacements of grade beam, superstructure, and total system for Bent #5S (2000)

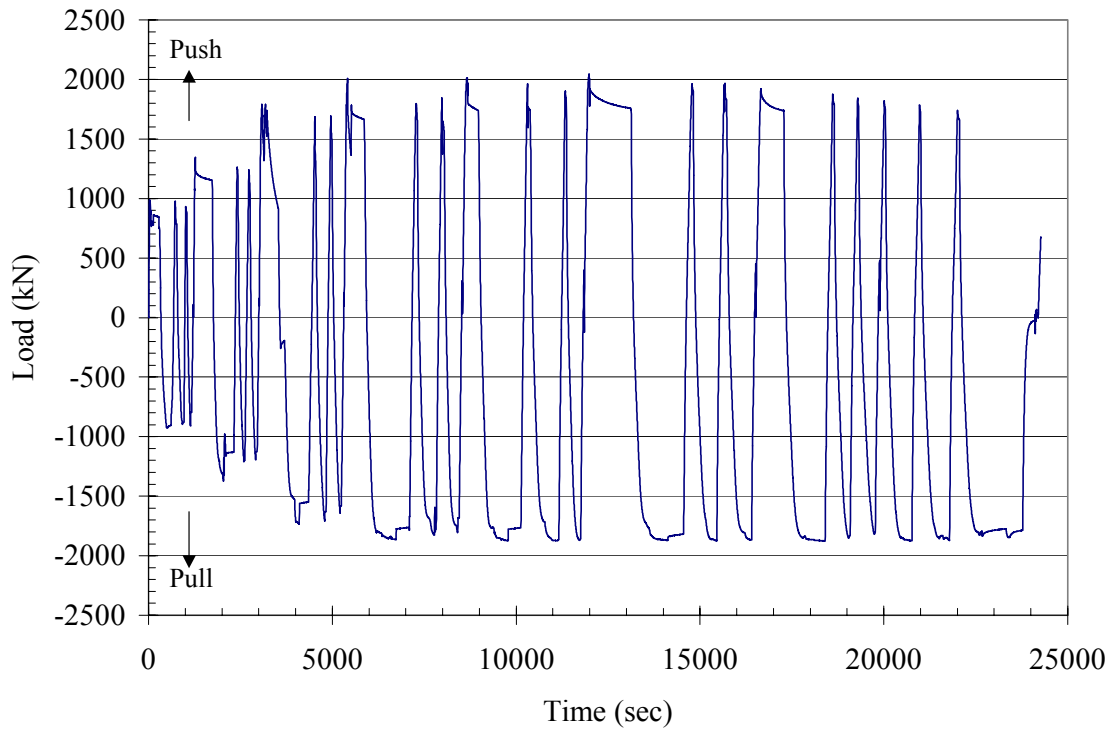


Figure 3.12 Applied lateral load for Bent #5S (2000) from load cell reading

The maximum displacement recorded in the push direction (to the east) was 205 mm, a 2.7% drift ratio, and in the pull direction (to the west) was -287 mm, a 3.8% drift ratio, as shown in Figure 3.11. Several DTs were placed on the grade beam and load frame foundations to measure their movement. The maximum displacement of the grade beam to the east (push direction) was recorded as 38 mm, and that to the west (pull direction) was -39 mm, as shown in Figure 3.11. By subtracting the displacement of the grade beam from the displacement of the total system, the displacement of the superstructure was obtained, as shown in Figure 3.11. Thus, the maximum relative displacement to the east (push direction) was recorded as 182 mm, a 2.4% relative drift ratio, and that to the west (pull direction) was recorded as -254 mm, a 3.3% relative drift ratio. Thus, approximately 11% of the total displacement was due to the flexibility of the grade beam, pile caps, piles, and soil.

The hysteresis diagram showing the force-displacement behavior of the structure for the total system, including both the superstructure and the grade beam is shown in Figure 3.13. Stable behavior is observed dissipating a large amount of energy. The lateral stiffness of the bent for each cycle is shown in Figure 3.14. The initial elastic stiffness, k_e , was reduced to 13% of k_e at a superstructure drift ratio of 2.8%, or total system drift ratio of 3.3%.

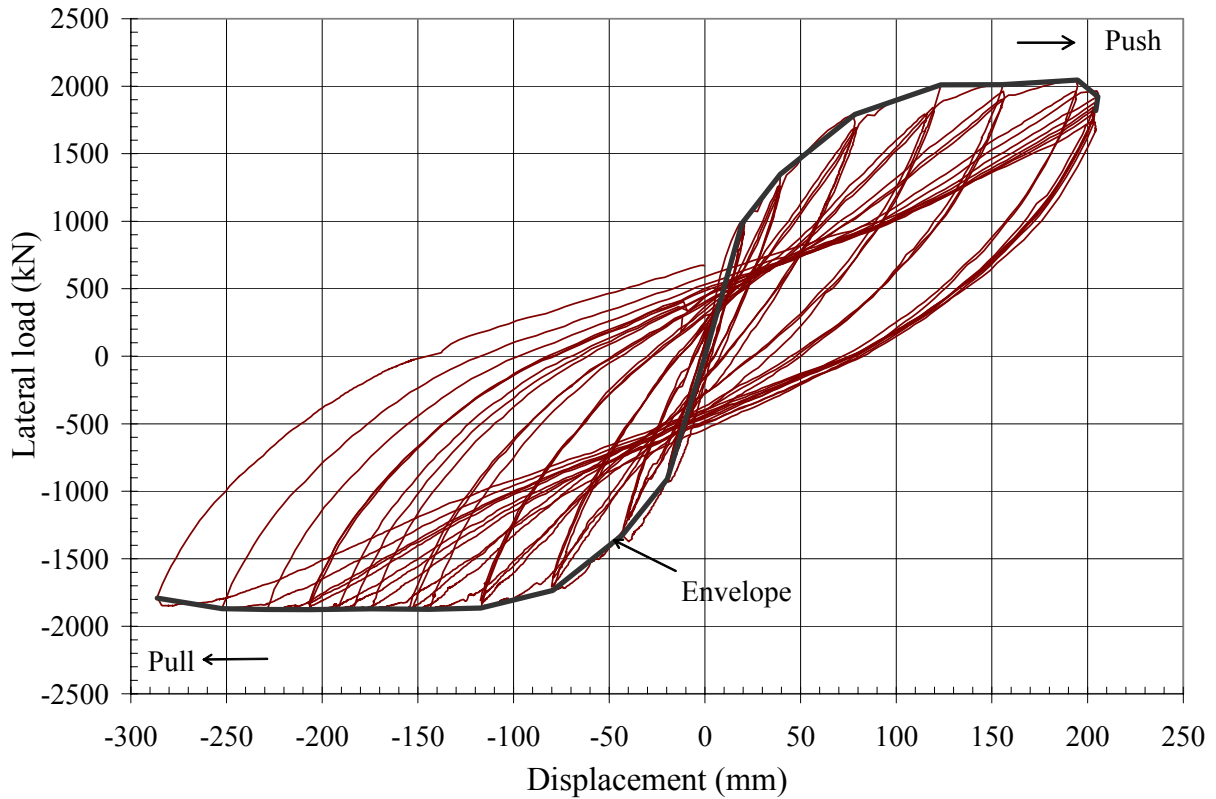


Figure 3.13 Hysteresis curve of total system for Bent #5S (2000)

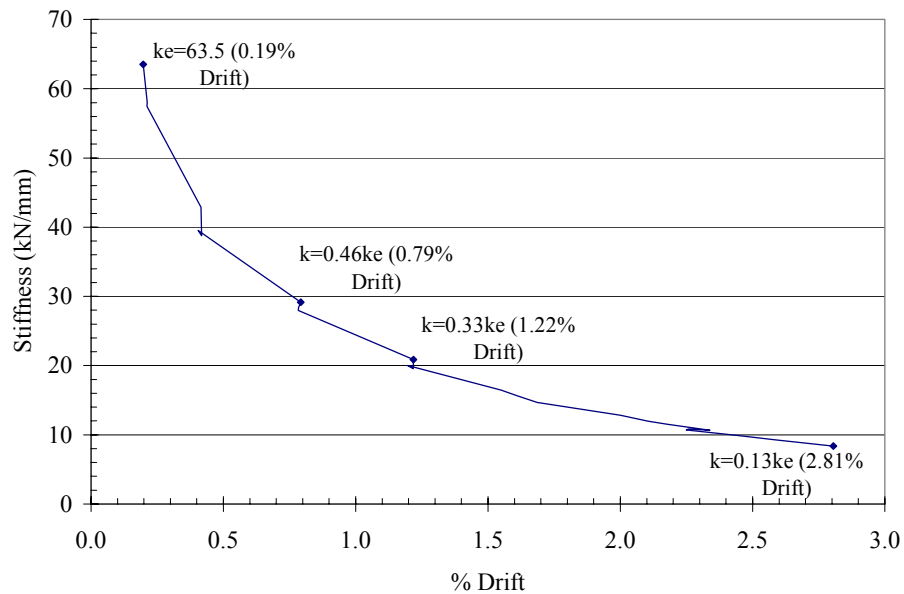


Figure 3.14 Degradation of lateral stiffness for Bent #5S (2000)

Behavior of Structural Elements

Results of an analytical model developed for the purpose of numerically simulating the bridge bent response to the lateral load, predicted the experimental results very closely (Ward 2001). The analytical model was used to calculate the applied shear forces and bending

moments in the columns, bent cap, joints and grade beam. The model uses a two-dimensional structural component model of the three-column bent. The properties of the structural elements, the grade beam, pile caps, piles, and soil are included in the numerical model. The program DRAIN-2DX was used (Prakash et al. 1993), where the main structural members were modeled using a fiber beam-column element. The soil resistance on the piles and the embedded pile caps was modeled using Winkler springs; a footing test was used to determine the horizontal frictional springs (Cook et al. 2002). Figure 3.15 shows a comparison of the experimental envelope from Figure 3.13, and the analytical force displacement envelope from the DRAIN-2DX computer model. It can be observed that agreement is good up to a lateral displacement of 190 mm; the analytical model estimated the displacement contribution of the substructure in a satisfactory manner.

Columns

The column shear forces were calculated from the applied lateral load on the bent cap at each load step. The maximum shear force resisted by the east column was 746 kN, and the maximum bending moment was 2825 kN-m. The curvature at the top and bottom of the center column was found experimentally, and the plastic hinge locations in the structure were found by observing the strain at yielding of the reinforcement and the concrete damage as a function of compressive strain. The top of the columns yielded first, followed by the bent cap-column joints, and finally the bottom of the columns as shown in Figure 3.16. The yielding sequence is influenced by the extra reinforcement and the stiffening effect from the grade beam overlay retrofit. The last observed yielding point (node 9 in Figure 3.16) was in the grade beam itself, at approximately the midspan of the east and center pile cap faces.

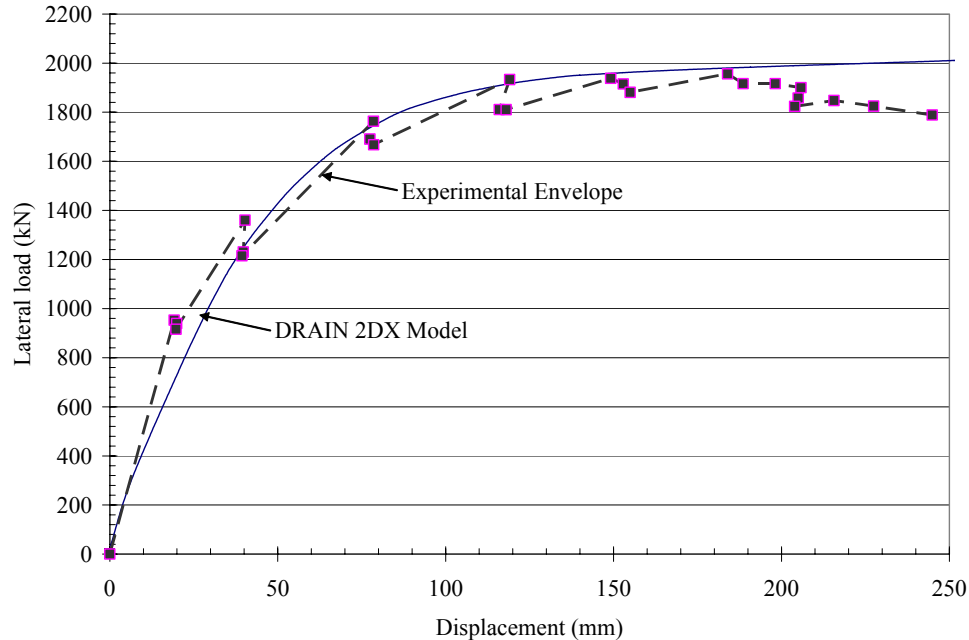


Figure 3.15 Comparison of force-displacement envelopes from experiment and analytical model for Bent #5S (2000)

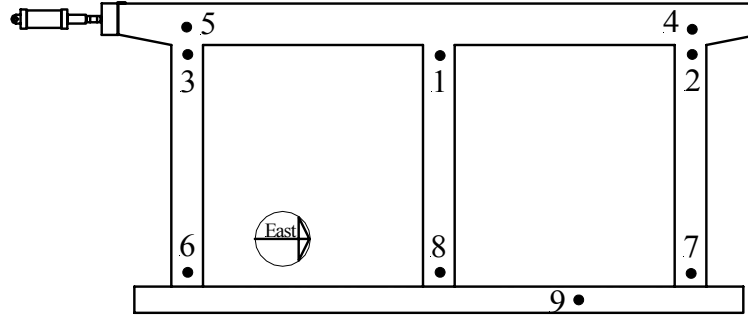


Figure 3.16 Location and sequence of experimental plastic hinge formation for Bent #5S (2000)

The plastic hinge length at the column end was calculated by using the curvature at the top of the center column. The plastic hinge length can be obtained from the displacement ductility factor, μ_Δ , as follows:

$$\mu_\Delta = \frac{\Delta_u}{\Delta_y} = 1 + \frac{\Delta_p}{\Delta_y} \quad (3.3)$$

where Δ_u = ultimate displacement, Δ_y = system yield displacement, and Δ_p is defined as:

$$\Delta_p = \left(\frac{M_u}{M_n} - 1 \right) \Delta_y + L_p (\phi_u - \phi_y) (L - L_p) \quad (3.4)$$

where M_u = maximum moment, M_n = yield moment, ϕ_u = curvature at ultimate displacement, ϕ_y = curvature at system yield, L_p = plastic hinge length, and L = distance from the top face of the grade beam support to the bottom face of the bent cap. For the given bent, it can be shown that the yield displacement for a column in double curvature is:

$$\Delta_y = \frac{\phi_y L^2}{6} \quad (3.5)$$

The actual point of contraflexure was approximately at midheight of the column, within an error of 3% of the column length, which establishes that Equation 3.5 is reasonably accurate in this case. Therefore, the displacement ductility using Equations 3.3 through 3.5 is:

$$\mu_\Delta = \frac{M_u}{M_n} + 6(\mu_\phi - 1) \frac{L_p}{L} \left(1 - \frac{L_p}{L} \right) \quad (3.6)$$

where μ_ϕ = curvature ductility, which is defined as the ultimate curvature divided by the yield curvature. From Equation 3.6, the plastic hinge length can be back-calculated if the displacement ductility is known; the following ultimate and yield moments, and curvature ductility at the top of the center column were used based on the experimental findings: $M_u = 2248$ kN-m, $M_n = 2137$ kN-m, $\mu_\phi = 7.4$ (Ward 2001); the displacement ductility of the

superstructure alone $\mu_d = 4.1$ as shown in a later section, and the clear column height $L = 6.883$ m; with these parameters, the plastic hinge length was found as $L_p = 600$ mm.

The value calculated for L_p , is compared to the value given by Priestley et al. (1996), which is based on analysis and test results as:

$$L_p = 0.08L_1 + 0.022f_{ye}d_{bl} \geq 0.044f_{ye}d_{bl} \quad (3.7)$$

where $L_1 = 3.442$ m is the distance from the critical section of the plastic hinge to the point of contraflexure, f_{ye} = yield strength of steel (326 MPa), and d_{bl} = diameter of longitudinal steel (32 mm). The observed value of the plastic hinge was also compared to the expression given by Panagiotakos and Fardis (2001), which is based on a mechanics approach and is given as:

$$L_p = 0.12L_s + 0.014\alpha_s f_{ye}d_{bl} \quad (3.8)$$

where L_s = shear span of column ($M/V = 3.442$ m). In Equation 3.8, α_s equals 1.0 if slippage of longitudinal steel from its anchorage zone beyond the section of maximum moment is possible or 0.0 if it is not. Equation 3.7 yields $L_p = 505$ mm, which is 84% of the value obtained using Equation 3.6. Equation 3.8 yields $L_p = 559$ mm for $\alpha_s = 1.0$, which is 93% of the value given by Equation 3.6 and is closer to the observed value. The values of the plastic hinge length are summarized in Table 3.1. The predictive relationships slightly underestimate the experimentally obtained plastic hinge length. The physical condition of the plastic hinge and lap splice at the bottom of the center column is shown in Figure 3.17, where buckling of the column bars is visible.

Table 3.1 Column plastic hinge length

Method	Plastic Hinge Length (mm)	Percent of Experimental (%)
Experimental	600	100
Priestley et al. (1996)	505	84
Panagiotakos and Fardis (2001)	559	93

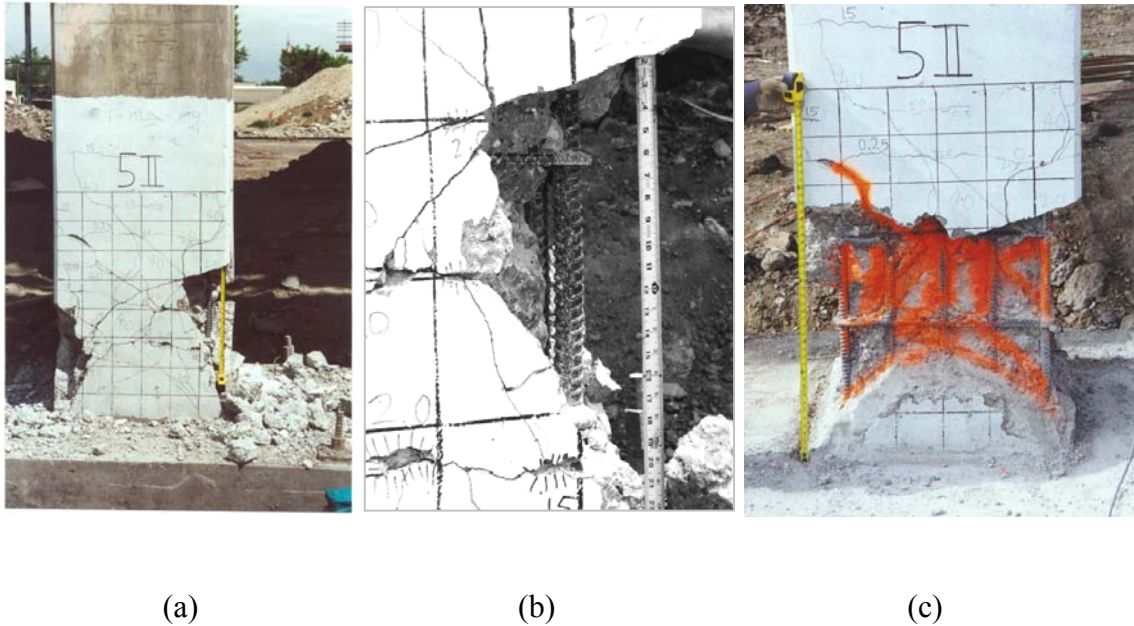


Figure 3.17 Damage to Bent #5S (2000) lap splice at bottom of center column: (a) after test, (b) detail showing buckled column bar, (c) lap splice after post-test investigation

Strain gauge readings in the lap splice region of the columns, and on the longitudinal reinforcement extending into the bent cap-column joints indicated that pullout of column reinforcing bars had occurred. Insufficient anchorage causes weakening of the entire structure and a greater propensity for loss of capacity. The strain gauge reading on the longitudinal reinforcement at the column bottom was subtracted from the reading at the anchorage dowels coming up from the pile cap; this difference determined the strain at which slippage had occurred in the lap splice. As shown in Figure 3.18, at a drift ratio of 2%, the center column lap splice began slipping at a differential strain of 1 mm/m (or a strain of 1.4 mm/m in the column bars); this slip gradually increased causing a drop in the structure's strength. It is obvious that a 24 bar diameter splice is not effective.

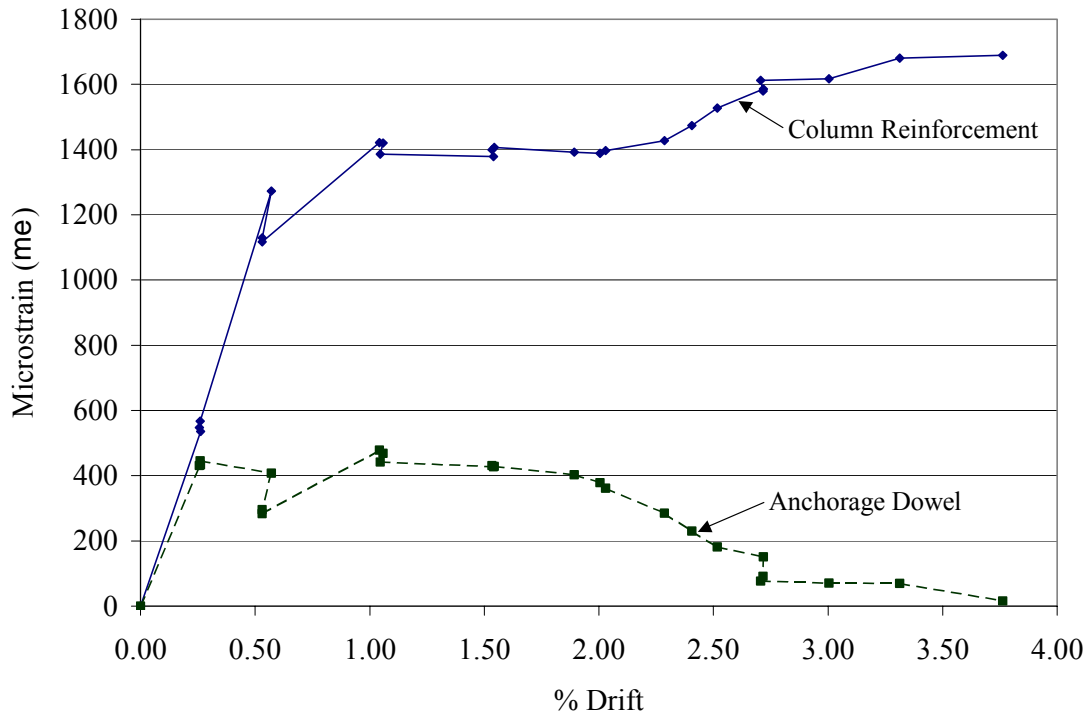


Figure 3.18 Maximum strains in reinforcement at the bottom of the center column

Similarly, at the top of the columns, the column longitudinal reinforcement started losing anchorage in the bent cap-column joint at a strain from 1.2 mm/m to 1.6 mm/m and a drift ratio of 2.0%. A 3 mm pullout of the longitudinal reinforcement at the top of the east column was observed at completion of the test, as shown in Figure 3.19a; the damage at the top of the center column at termination of the test is shown in Figure 3.19b and 3.19c, which included bar buckling. This indicates insufficient anchorage of the column bars in the bent cap, since no transverse reinforcement was provided in the bent cap column joint; insufficient anchorage of column bars is a known deficiency of older bridges (Park et al. 1993).

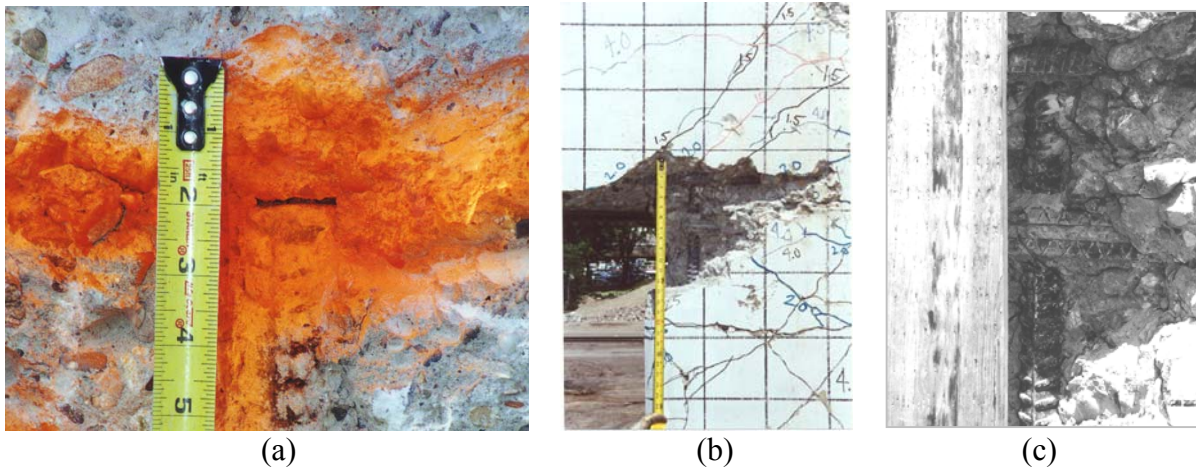


Figure 3.19 Damage to Bent #5S (2000) at top of center column: (a) pullout of longitudinal reinforcement, (b) after test, (c) showing buckled column bar

Bent Cap-Column Joints

The shear in the center column bent cap-column joint was calculated using the maximum lateral load from the analytical DRAIN-2DX model results of Figure 3.15. The average of the vertical and horizontal shear forces were calculated, as shown in Figure 3.20, to find the nominal joint shear stress:

$$\tau_{xy} = \frac{v_v + v_h}{2} \quad (3.9)$$

where v_v and v_h , are vertical and horizontal shear stresses, given as:

$$v_v = \frac{V_v}{A_{jv}} \quad ; \quad v_h = \frac{V_h}{A_{jh}} \quad (3.10)$$

where V_v = vertical shear force (2655 kN), V_h = horizontal shear force (1910 kN), A_{jv} = vertical joint area (1.115 m²), and A_{jh} = horizontal joint area (0.836 m²). The vertical and horizontal shear stresses were found from Equation 3.10 as 2.38 MPa and 2.28 MPa, respectively. From Equation 3.9, the nominal joint shear stress was 2.33 MPa or $0.40 \sqrt{f'_c}$.

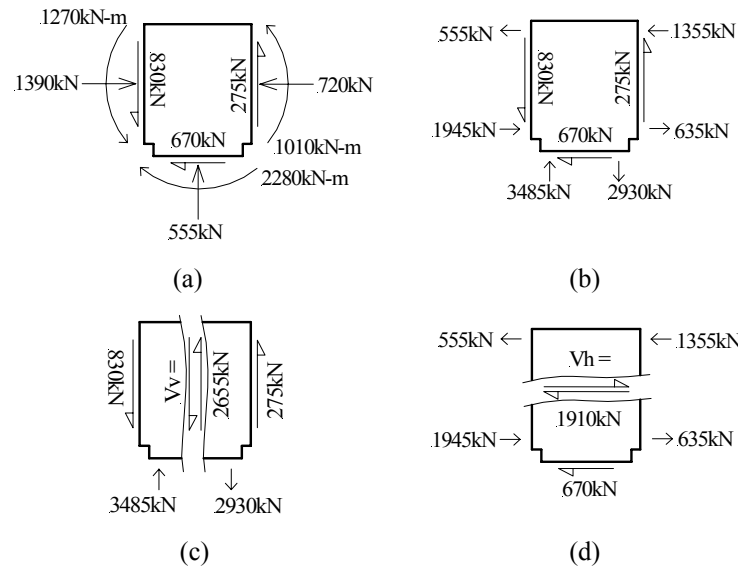


Figure 3.20 Nominal joint shear in center cap-column joint: (a) free-body diagram, (b) forces resolved into couples, (c) vertical shear, and (d) horizontal shear

The principal stresses, $\sigma_{t,c}$, were calculated using:

$$\sigma_{t,c} = \frac{\sigma_x + \sigma_y}{2} \pm \sqrt{\left(\frac{\sigma_x - \sigma_y}{2}\right)^2 + \tau_{xy}^2} \quad (3.11)$$

where σ_x and σ_y = compressive stresses in the joint in the x- and y-directions (0.95 MPa and 0.66 MPa, respectively), and τ_{xy} = shear stresses in the joint (2.33 MPa). The principal tensile stress was $\sigma_t = 3.14$ MPa or $0.55 \sqrt{f'_c}$, and the principal compressive stress was found

as $\sigma_c = -1.53 \text{ MPa}$ or $0.05 f'_c$. Priestley et al. (1996) indicate that joint degradation will likely occur at a principal tension exceeding $0.42 \sqrt{f'_c}$ (MPa) for a curvature ductility, μ_ϕ , less than 3.0, and a principal tension exceeding $0.29 \sqrt{f'_c}$ (MPa) for a curvature ductility greater than 7.0; in addition, degradation occurs when the principal compression stress exceeds $0.3 f'_c$. In the present case the curvature ductility exceeds 7.0, so the capacity for principal tension is $0.29 \sqrt{f'_c}$ (MPa) which was exceeded by a factor of 1.7. It is evident that the center joint experienced degradation due to diagonal tensile stresses, which can be observed from Figure 3.21.

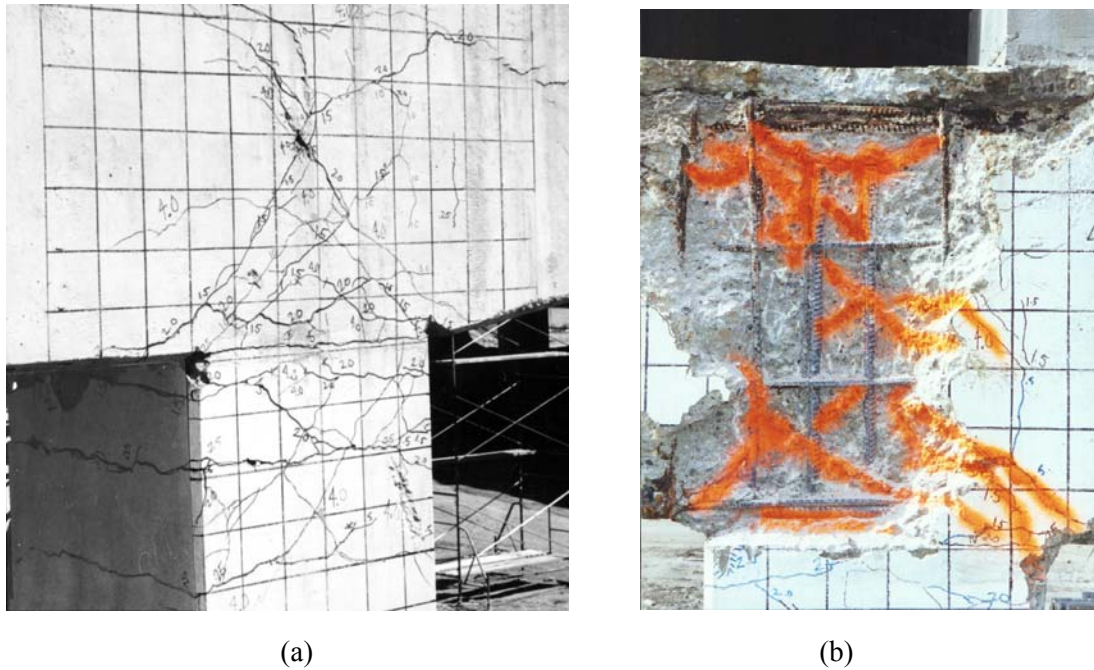


Figure 3.21 Damage to bent cap-column joints of Bent #5S (2000): (a) center column joint at end of test, (b) east column joint after post-test investigation

Grade Beam and Pile Caps

In the grade beam, the maximum tensile strain in the longitudinal reinforcement was 3.08 mm/m or 184% of the yield strain. This occurred at the grade beam midspan between the east and center pile cap faces during the 3.0% drift ratio cycle, (node 9 in Fig. 3.16). The principal tensile stress in the pile cap-column joint was $0.68 \sqrt{f'_c}$ (MPa), which is higher than $0.42 \sqrt{f'_c}$ (MPa), and indicates joint degradation. The maximum tensile strain measured in the Dywidag bars was 1.26 mm/m or 57% of the yield strain, at a drift of 2.8%, indicating that these bars served their intended purpose of anchoring the pile caps to the piles below and did not yield.

The grade beam capacity calculated using ACI 318 (1999) was compared to the forces applied to the foundation system during the test. The shear capacity of the grade beam and pile cap was large enough to prevent any shear damage. This is because the grade beam overlay and the pile cap were clamped together by the Dywidag assembly and acted as one

unit. However, the negative moment near the center pile cap was 33% higher than the capacity, causing the grade beam to undergo flexural stresses and deformations high enough to induce cracking. These cracks developed in the grade beam overlay at a 2.5% drift ratio above the vertical faces of the existing pile cap, on both sides of the center column, as shown in Figures 3.22 and 3.23.



Figure 3.22 Cracks in the grade beam at a drift ratio of 2.5%: (a) center pile cap, (b) close up on the top of the grade beam

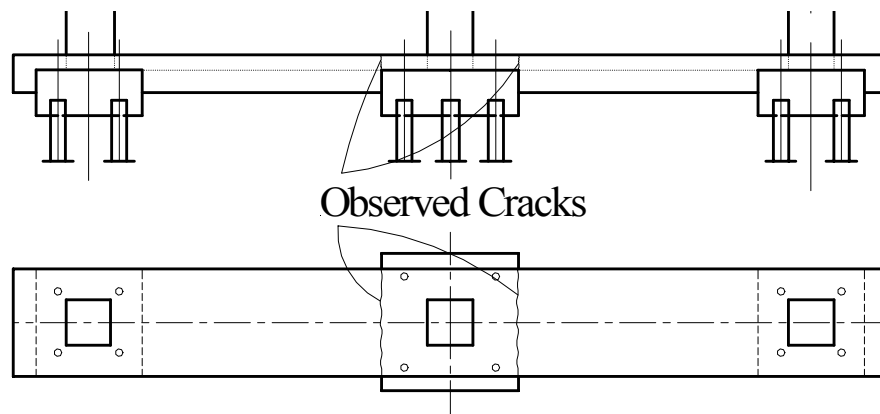


Figure 3.23 Location of observed cracks in the grade beam

Performance Assessment

The Pacific Earthquake Engineering Research Center (PEER) has developed a bridge performance database for assessment of reinforced concrete bridges (Hose et al. 2000). This evaluation is based on five performance levels: (I) Cracking, (II) Yielding, (III) Initiation of local mechanism, (IV) Full development of local mechanism, and (V) Strength degradation. The displacement ductility, as defined in Equation 3.3, was found by using the method

suggested by Légeron and Paultre (2000). The intersection of the yield line and equal energy line determines the system yield, as shown in Figure 3.24. Thus, the total system including the superstructure and foundation had a displacement ductility of $\mu_{\Delta f} = 3.7$. The superstructure alone had a displacement ductility of $\mu_{\Delta r} = 4.1$; the yield displacement for the total system was $\Delta_y = 66$ mm. Relationships have been established in the literature for accounting for bent cap and foundation flexibility in multicolumn bents. A relationship between the structural displacement ductility capacity and that resulting from bent cap and foundation flexibility is (Priestley et al. 1996):

$$\mu_{\Delta f} = 1 + \frac{\mu_{\Delta r} - 1}{1 + f_a}; \quad f_a = \frac{\Delta_b + \Delta_f}{\Delta_c} \quad (3.12)$$

where f_a is a flexibility coefficient, Δ_b = bent cap displacement, Δ_f = foundation displacement, and Δ_c = structural deformation of the columns. Using the above values from the test, the bent cap and foundation flexibility coefficient is evaluated from Equation 3.12 as $f_a = 14.8\%$; the value of this coefficient, and the fact that the foundation flexibility was measured as 11%, demonstrates that the bent cap flexibility is small and that foundation flexibility is the dominant effect; the contribution of the bent cap flexibility is thus only 3.8%.

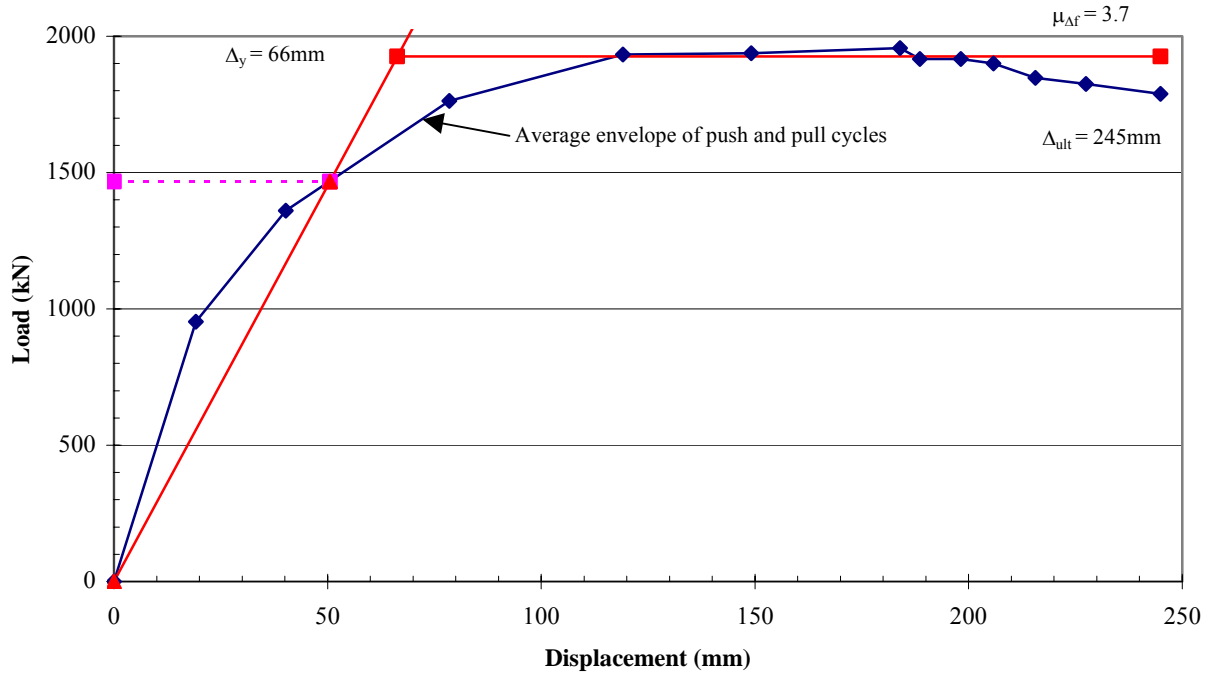


Figure 3.24 Displacement ductility of total system for Bent #5S (2000)

The equivalent viscous damping ratio ξ_{eq} is defined as:

$$\xi_{eq} = \frac{1}{4\pi} \left(\frac{E_d}{E_s} \right) \quad (3.13)$$

where E_d = energy dissipation per cycle, and E_s = elastic strain energy. The equivalent damping ratio reached a maximum of 0.074 at a drift ratio of 3.8%, whereas at a 2% drift

ratio, the equivalent damping ratio was 0.050. The joint shear strength coefficient of the bent cap-column joints, γ , is defined as:

$$\gamma = \frac{\tau_{xy}}{\sqrt{f'_c}} \quad (3.14)$$

where τ_{xy} = nominal joint shear stress. The maximum joint shear strength coefficient γ was 0.397 (MPa). The bent cap-column joint crack widths were noted throughout the experiment and are recorded for each performance level in Table 3.2, which presents the performance of the bent in quantitative terms including crack width, lateral load, and bent cap-column joint shear strength for each of the five performance levels. In addition, Figures 3.17, 3.19, 3.21, and 3.22 show the damage to the columns, bent-cap column joints, and grade beam at the end of the test; the longitudinal column bars buckled at both ends of the columns, which signifies impending strength degradation. As can be seen, the PEER performance parameters capture the damage sequence experienced by the bent during the test in a satisfactory manner. The crack width data is unique and could be used in post-earthquake capacity evaluation of R/C bridges with similar details.

Table 3.2 Bridge performance assessment

Level	Qualitative Performance Description	Quantitative Performance Description	Load Step	Lateral Load (kN)	Crack Width (mm)	Drift Ratio (%)	γ (MPa)	ξ_{eq} (%)
I	Onset of hairline cracks	Initial cracking in joint	1	985.3	Hairline	0.25	0.184	1.7
II	First yield of longitudinal reinforcement	Tops of columns yield, flexural crack widths in bases of columns < 1 mm	2	1347.9	0.08 columns	0.53	0.305	2.6
III	Initiation of local mechanism	Spalling in bent cap and columns, flexural cracks in bases of columns > 1mm, large shear crack forming in west bent cap-column joint	4	2010.6	2.0 joint interface	1.56	0.377	4.6
IV	Development of local mechanism	Spalling, flexure cracks in bases of columns > 2mm, shear cracks in bent cap-column joints > 2mm	5	1963.4	3.0 joint interface	2.01	0.383	5.0
V	Strength degradation	Extensive spalling, flexural cracks in columns > 4mm, joint shear cracks > 3mm for 2/3 of joint depth, vertical cracks > 2m tall, buckling of column bars	10	1847.2	4.5 for columns 3.0 for joints 1.0 for grade beam	3.31	0.397	7.4

Comparison with Bent #4S of the Southbound Bridge – Test 2000

The performance of Bent #5S (2000) was compared to that of a bridge bent without the deck (Bent #4S) of the Southbound Bridge tested in 2000, as described in Chapter 2. Bent #4S (2000) of the Southbound Bridge was retrofitted with a grade beam of the same dimensions and reinforcement as Bent #5S (2000), and was identical to it except that the deck was demolished and thus the superimposed dead load was absent. The experimental force-deformation envelope for Bent #5S (2000) was compared to the force-deformation envelope for Bent #4S (2000), as shown in Figure 3.25. The maximum lateral load resisted by Bent #4S (2000) was 1579 kN, while Bent #5S (2000) resisted 1957 kN, or 1.24 times higher. The cumulative energy absorbed by Bent #5S (2000) was 3566 kN-m, or 1.95 times that absorbed by Bent #4S (2000), which was 1827 kN-m, as shown in Figure 3.26. The gravity load due to the presence of the deck was beneficial even though it amounted to only 3.3% (exterior column) and 3.8% (interior column) of $f'_c A_g$. Under service conditions, this effect would be even more pronounced because the gravity load would be approximately twice due to the presence of the deck on both sides of the bent.

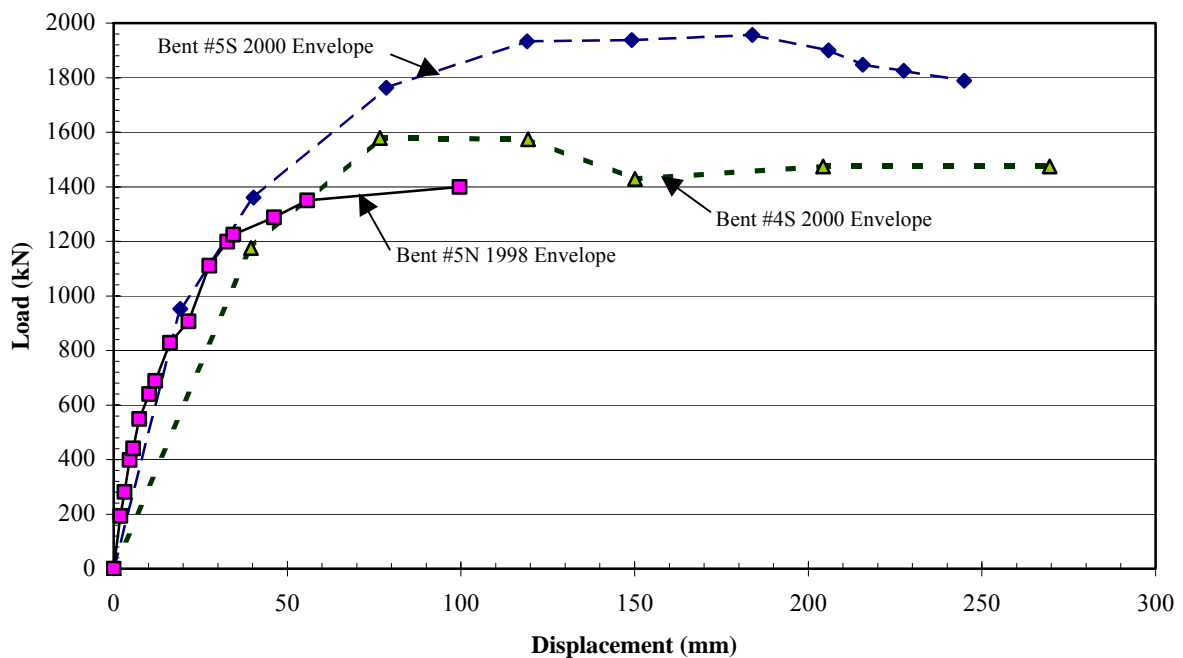


Figure 3.25 Force-deformation for Bent #5S (2000), Bent #4S (2000), and Bent #5N (1998)

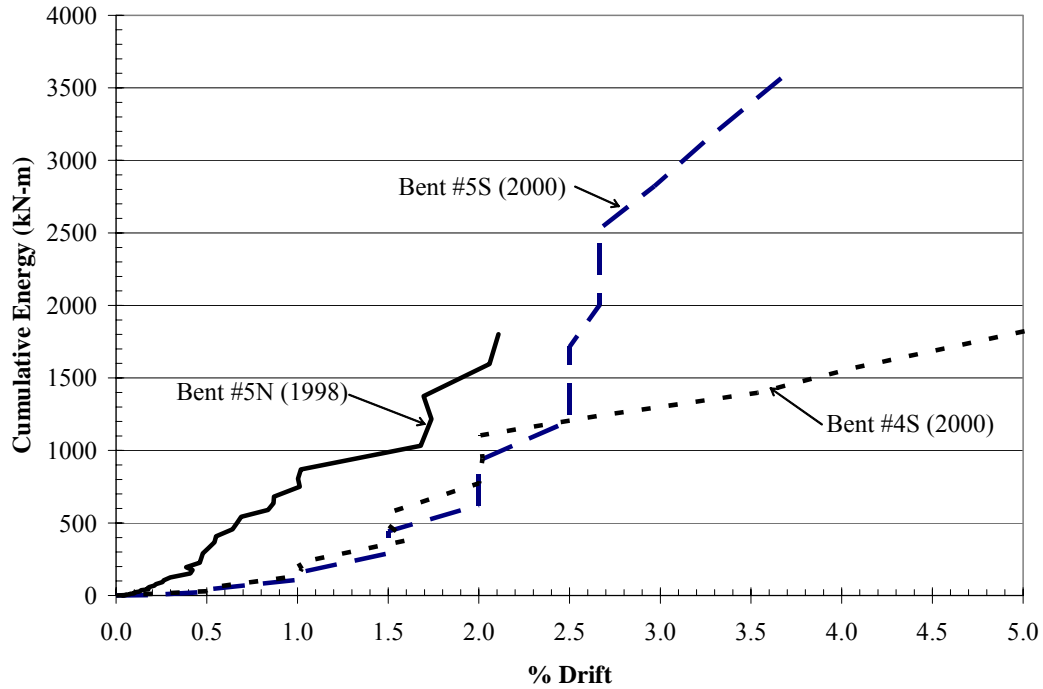


Figure 3.26 Energy comparison for Bent #5S (2000), Bent #4S (2000), and Bent #5N (1998)

Comparison with Bent #5N of the Northbound Bridge – Test 1998

The northbound lanes of the South Temple Bridge were tested in 1998 using a similar procedure (Pantelides et al. 2001). Bent #5N (1998) was tested in the as-is condition without a grade beam retrofit but with a similar dead load from the deck. In place of the grade beam, the foundation for Bent #5N (1998) was secured by two 36-mm Dywidag bars cast into the load frame foundations and extending to the pile cap at the far end, where they were anchored to a wide flange steel beam to form a tensile tie; a compression strut was created by linking the pile caps using a plain concrete beam, and by connecting the pile caps to the load frame foundation using a short reinforced concrete beam (Pantelides et al. 2001). The envelope of the hysteresis loops for Bent #5N (1998) is shown in Figure 3.25. The maximum lateral load resisted by Bent #5N (1998) was 1400 kN, which is 0.71 times the capacity of Bent #5S (2000). The hysteretic energy absorbed by Bent #5N (1998) was 1801 kN-m, or 0.50 times that absorbed by Bent #5S (2000), as shown in Figure 3.26.

Damage Index using Energy

In order to relate the quantities of energy absorbed by a particular system to the actual damage, three indices have been used: (1) the relationship by Légeron and Paultre (2000), which defines E_N as the normalized dissipated energy:

$$E_N = \frac{1}{H'_{\max} \Delta_{y/l}} \sum_{i=1}^n E_i \quad (3.15)$$

where H'_{max} = maximum load on envelope curve, Δ_{yl} = system yield displacement, and E_i = energy dissipation for cycle i ; (2) the work index I_W , proposed by Gosain et al. (1977) defined as:

$$I_W = \sum_{i=1}^n \frac{H_i \Delta_i}{H'_{max} \Delta_{yl}} \quad (3.16)$$

where H_i = average of maximum and minimum load for cycle i , Δ_i = average of maximum and minimum displacement for cycle i , and H'_{max} and Δ_{yl} were defined previously; and (3) the damage index D_{EW} proposed by Ehsani and Wight (1990), which combines the cyclic dissipated energy with the elastic energy:

$$D_{EW} = \frac{1}{H'_{max} \Delta_{yl}} \sum_{i=1}^n E_i \left(\frac{K_i}{K_{yl}} \right) \left(\frac{\Delta_i}{\Delta_{yl}} \right)^2 \quad (3.17)$$

where K_i = stiffness of cycle i , and K_{yl} = ideal elastic stiffness of system. The damage indices given by Equations 3.15-3.17 are shown for the three bents in Table 3.3. From this comparison, Bent #5S (2000) had an energy index, E_N , 1.7 times that of Bent #4S (2000), a work index, I_W , 1.6 times that of Bent #4S (2000), and a damage index, D_{EW} , 3.9 times that of Bent #4S (2000). In addition, Bent #5S (2000) had an energy index 18.1 times that of Bent #5N (1998), a work index, I_W , 5.5 times that of Bent #4S (2000), and a damage index 31.9 times that of Bent #5N (1998). All three indices recognize that Bent #5S (2000) performed better than Bent #5N (1998), indicating that the grade beam seismic retrofit was effective. In addition, all three indices recognize the beneficial effect of the gravity load, since Bent #5S (2000) has a higher index than Bent #4S (2000).

Table 3.3 Comparison of energy indices for three bents

Test	E_N	I_W	D_{EW}
Bent #5S (2000)	38.26	45.32	109.81
Bent #4S (2000)	22.71	27.68	27.85
Bent #5N (1998)	2.11	8.18	3.44

The displacement ductility was calculated for Bent #5N (1998) as 2.8 (Pantelides et al. 2001). This is compared to the total system ductility of 3.7 for Bent #5S (2000), which is a 32% increase. It is clear that the performance of Bent #5S (2000) was superior to that of Bent #5N (1998), and that the grade beam retrofit proved to be an effective solution for enhancing the seismic performance of this type of bridge bent.

In summary, the reinforced concrete grade beam seismic retrofit enhanced the performance of a bridge bent under simulated seismic loads. The maximum drift ratio reached at the bent cap level was 3.8% in the pull direction and 2.7% in the push direction.

Approximately 11% of the total displacement of the bridge system was due to the movement of the grade beam, foundation, piles and pile caps. The displacement ductility of the bent, including the bent cap and foundation flexibilities, the latter being the dominant effect, was found to be 3.7, which shows that the grade beam was very effective.

The effect of the grade beam retrofit was evaluated by comparing the present test with a test of an otherwise identical bent (Bent #5N), which was tested in 1998, but did not have a grade beam retrofit. The lateral load resisted by Bent #5S (2000) was 1.4 times that of Bent #5N (1998), and the hysteretic energy dissipation was 1.98 times that of the Bent #5N (1998). These results were confirmed by comparing energy-based damage indices found in the literature. The grade beam retrofit provided higher base fixity which in turn generated more redundancy and ductility for the foundation-superstructure system. The grade beam retrofit was successful in improving the seismic performance of a bent with substandard reinforcement details and should be considered in the seismic retrofit design of similar bridges.

4. BRIDGE BENT #6S: SEISMIC RETROFIT WITH GRADE BEAM AND CFRP COMPOSITE

A typical bent superstructure was constructed with a cap beam section 0.914m wide by 1.22m deep that was supported by three equally spaced square 0.914m columns. Each cap beam supported eight steel girders whose longitudinal span lengths were 21.87m simply supported between adjacent bents. The girders supported a 305mm thick reinforced bridge deck and the exterior girders supported two parapet retaining walls located on both sides of the deck perimeter. Each of the three columns was supported by a deep pile foundation system. A square 2.13m X 2.13m by 0.914m thick pile cap supported the two exterior columns. The exterior pile caps were supported by four 305mm steel cased, reinforced concrete circular piles. A square 2.34m X 2.34m by 0.914m thick pile cap supported the interior center column, and the pile cap was supported by five 305mm, steel cased, reinforced concrete circular piles as shown in Figure 4.1.

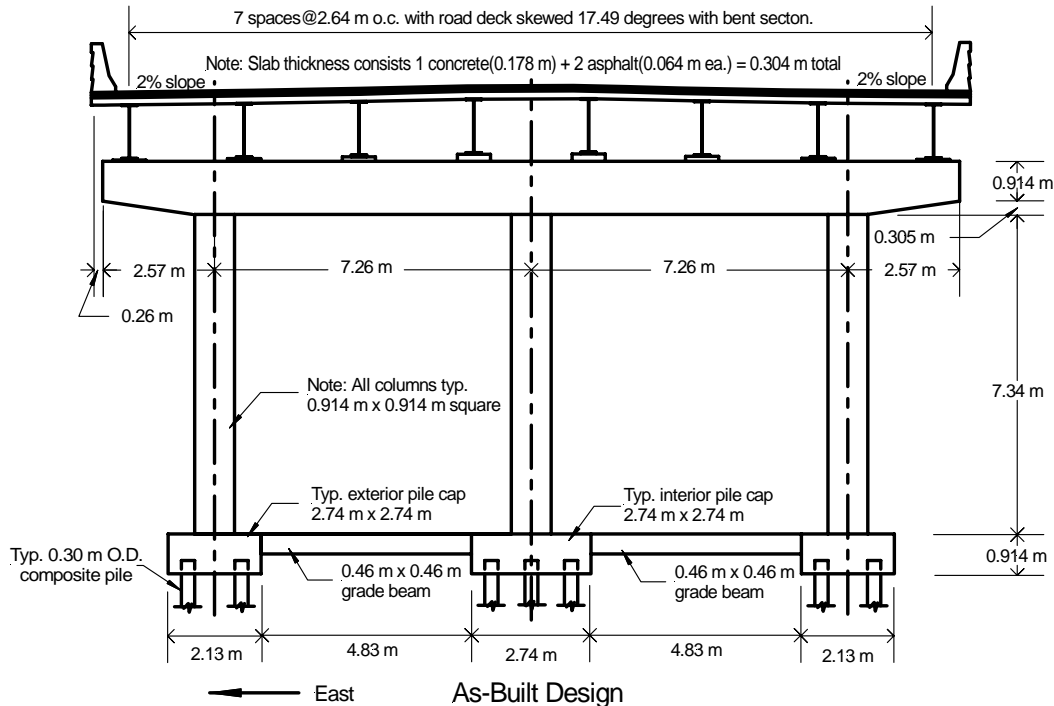


Figure 4.1 Typical bent structure for both the 1998 and 2000 bridge tests

There were two main research objectives for the two bridges tested in 1998 and 2000. The first objective was to retrofit a typical existing reinforced concrete bridge structure to improve its seismic performance according to current code standards. The project was located in the west section of Salt Lake City where the seismic zone rating is 4. The second objective was to double the displacement ductility of the existing bridge bents using Fiber Reinforced Polymer (FRP) composites; this is an arbitrary measure that has been used in the past to gauge the effectiveness of FRP composite retrofitted columns in laboratory tests

(Seible et al. 1997). In the original bridge design, the only considerations for lateral load forces were for wind loading.

The first phase of testing done in 1998 was conducted using two bent structures, Bent #5N and Bent #6N. In the 1998 test, Bent #5 was tested as an existing or as-is structure whereas Bent #6 was seismically retrofitted with a dry lay-up Carbon Fiber Reinforced Polymer (CFRP) composite. The deck section was left in place between Bent #5N and Bent #6N, which provided half the original axial load during the test. The definition, used in this reports, for dry lay-up is in reference to how the epoxy resin is applied to the CFRP composite fiber sheet. The dry lay-up procedure that was used in 1998 for Bent #6N consisted of pouring epoxy resin onto a precut carbon fiber sheet. Next, by using hand tools the resin was spread evenly over the entirety of the precut carbon sheet. The hand tools used were paint rollers, large metal and plastic scrapers and squeegees as shown in Figure 4.2. The lay up and design of the CFRP in the 2000 tests was different as shown in a later section.

The second phase of testing was conducted in 2000 on three bent structures Bent #4, Bent #5S, and Bent #6S, as shown in Figure 4.3. Bent #4S was tested to simulate a bent structure without any deck (no axial loading) and was used to compare the influence of axial loading with Bent #5S that was tested with half the deck load (Ward 2001). Bent #5S was tested in the as-is condition with half the deck load.



Figure 4.2 Dry lay-up of epoxy resin applied to dry CFRP composite textile using roller and squeegee

Bent #6 was tested in 2000 as a seismic retrofit with a wet lay-up CFRP composite and half the original axial loading. A wet lay-up application was used, in which a carbon fiber



Figure 4.3 North view of 2000 test site showing Bent #4S, Bent #5S, and Bent #6S

sheet is precut to a desired length and then fully submerged in a reservoir of epoxy resin. Next, it is run through two tightly spaced rollers to squeeze out any excessive resin from the material before it is applied, as seen in Figure 4.4.

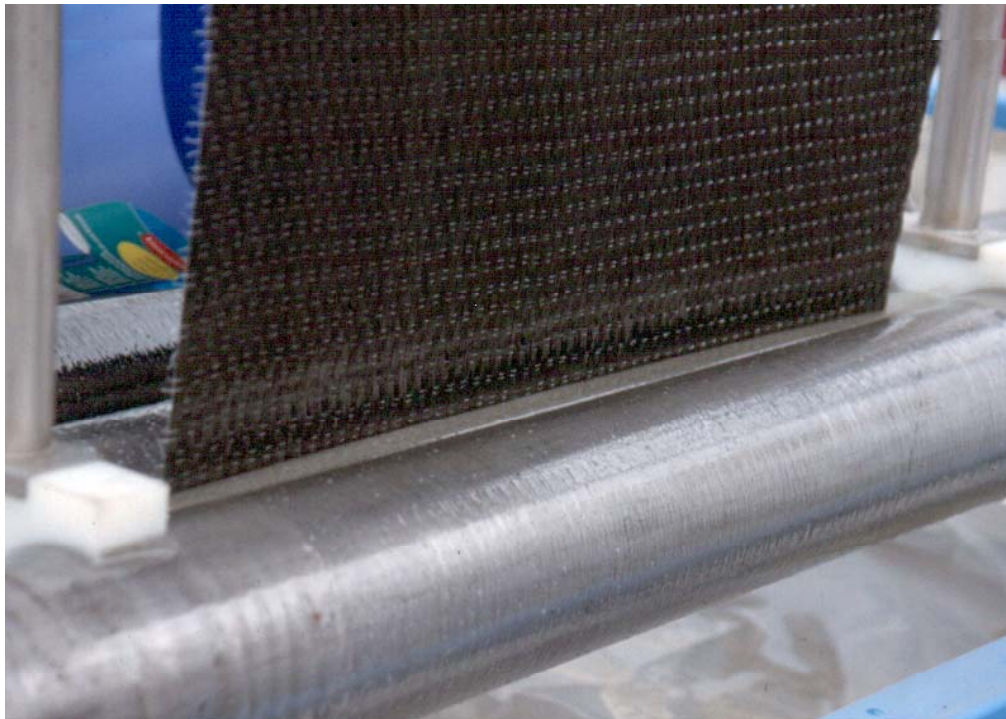


Figure 4.4 Wet lay-up epoxy resin machine with saturation reservoir

In the initial design stage, a typical bent structure was analyzed using a static pushover-analysis, which provided an estimate of the anticipated peak load and displacement that the bent structure could support. The computer program used for the analysis is the structural analysis program DRAIN-2DX (Prakash et al. 1993). It was found that in the proposed test, the existing pile anchorage would not provide adequate uplift capacity for the foundation system. The required additional uplift capacity was provided in both the 1998 and 2000 tests by anchoring high strength Dywidag bars in all the pile-to-pile cap connections of the five bents tested. Two different foundation systems were used for the 1998 and 2000 tests. Both foundation systems were designed to address the shear, displacement and uplift demands that had been evaluated with the modeling program DRAIN-2DX. Increasing the foundation capacity was essential for preventing premature failure of the foundation structures while testing the bridge bent. This was important since the main objective was to assess the capacity of the as-is and retrofitted bent super structures.

The 1998 foundation retrofit was accomplished by casting two new unreinforced concrete struts on both sides of the original square 0.46m x 0.46m strut beams. The new struts were used as lateral bracing between the three pile caps supporting the super structure. In addition, an unreinforced beam was cast between the load frame foundation and the end pile-cap to form a continuous compression strut for the entire foundation system. To address the required tension capacity, two non-prestressed 36mm Dywidag bars (1,030 MPa ultimate stress) were placed in the new grade beam strut that linked the entire foundation system together end to end (Pantelides et al. 2001) as shown in Figure 4.5. The foundation retrofit provided the additional capacity for a successful 1998 test.

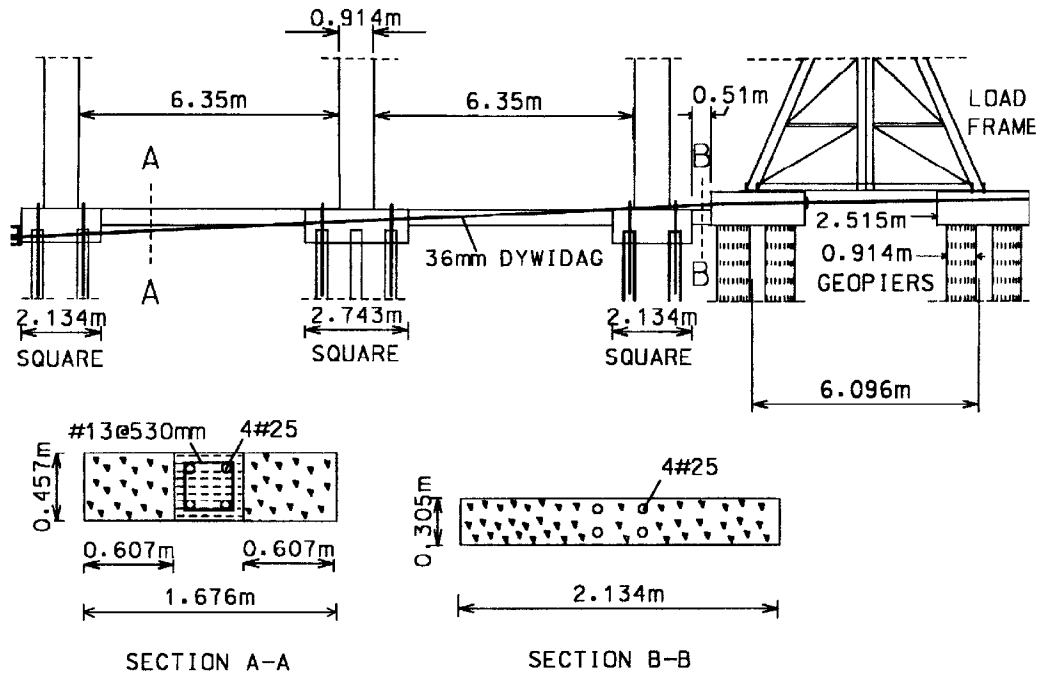


Figure 4.5 Foundation system for Bent #5N and Bent #6N in the 1998 tests

A major difference in the foundation design between the 1998 and 2000 tests was that in the 2000 tests the load frame foundation was not attached to the bent structure foundations. In addition, a new reinforced concrete foundation grade beam overlay 305mm thick was cast on top of the existing pile caps and strut beam. This foundation grade beam was cast to a total width of 2.13m on both sides of the existing strut beam as described in Chapter 3.

Condition of Bent #6S Prior to Retrofit

The columns and pile caps of Bent #6S were found to be in excellent condition; however, the cap beam showed signs of heavy corrosion due to freeze and thaw cycling and application of de-icing salt on the deck. Approximately 50% of the cover concrete on the cap beam was delaminated from the hoop reinforcement. The vertical stirrups in the cap beam had an overall loss of approximately 13% of steel area due to corrosion, as shown in Figure 4.6.



Figure 4.6 Loose cover concrete removed from Bent #6S showing cover concrete delamination and loss in vertical stirrup area in the bent cap

An assessment of the original reinforcement details showed that there were four reinforcement deficiencies in the original 1962 steel details. The first deficiency was an inadequate amount of longitudinal reinforcement in the lap splice regions located at the base of the columns. Second, there was inadequate anchorage of the longitudinal steel in both the pile cap and cap beam. Third, there was no transverse hoop steel in the column-cap beam joints. Finally, the confining steel in the columns was not sufficient by today's codes. The as-built reinforcement details are as shown in Figures 4.7 and 4.8. There was one variation in

the actual construction of the Bent #6 2000 structure from the as-built drawings. In the drawings the column-cap beam joints, the lateral column longitudinal reinforcement steel is shown to extend to the top longitudinal reinforcement of the cap beam. After the Bent #6S 2000 test, the cover concrete was removed from the joint and it was found that the column's reinforcement steel ended an average of 380mm from the top surface of the cap beam as shown in Figure 4.89(c).

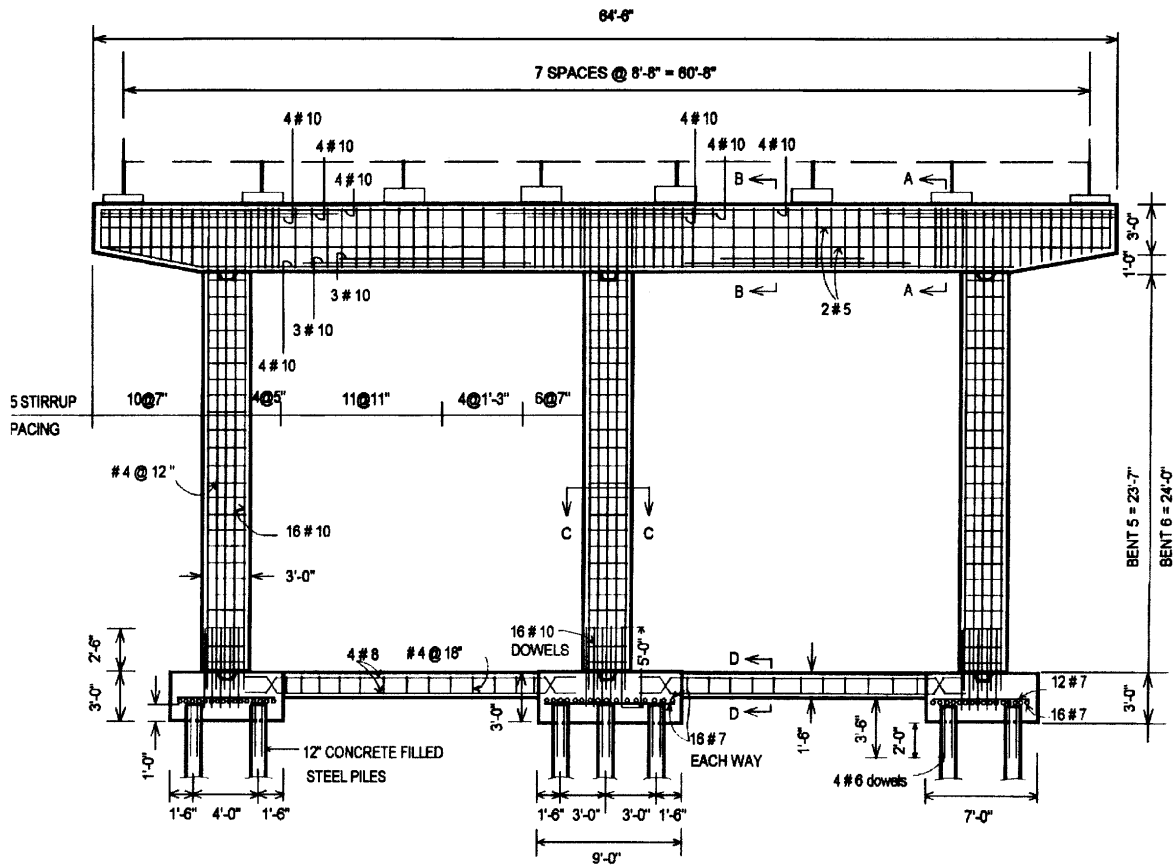


Figure 4.7 Elevation showing the original 1962 steel details

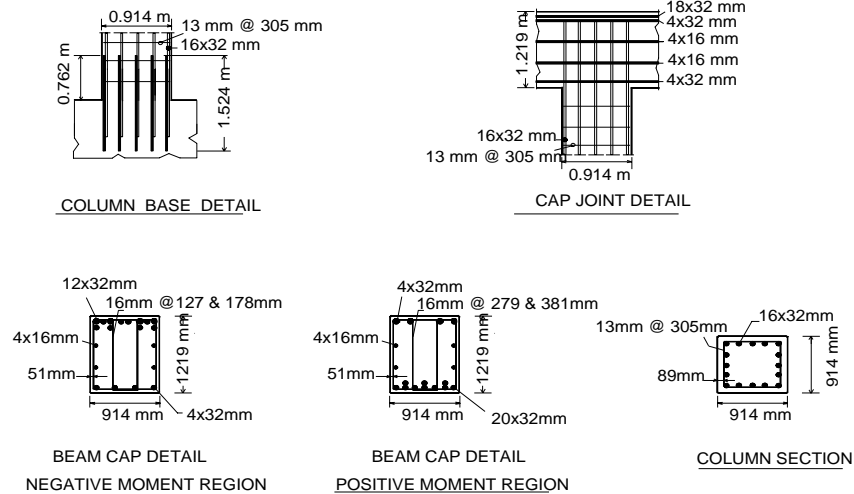


Figure 4.8 Column and beam cap section of 1962 reinforcement details

Surface Preparation

The surface preparation of the beam cap before application of the CFRP composite was done in a four-step process.

Removal of Delaminated Concrete (1)

Delaminated concrete and foreign material was removed from the surface of the bent structure. The most efficient method to remove loose debris was with jackhammers and a high-pressure water jet spray application. The basic technology of a water jet machine is to develop fine streams of water by forcing the water with high pressure through metal jet nozzles as shown in Figure 4.9.



Figure 4.9 Water jet gun and nozzle used to remove debris prior to CFRP application

The application of a water jet can be hazardous and requires unique skills and specialized equipment; all water jet application was contracted out to a local contracting company as shown in Figure 4.10.



Figure 4.10 First step in retrofit of Bent #6S: Water Jet for removing loose concrete cover

Shotcrete Application (2)

The second step was to rebuild any lost concrete cover to match the existing concrete cover thickness. Shotcrete technology was used to build up the concrete cover and bond to the existing sound concrete back to the original thickness as shown in Figure 4.11. An additional detail needed to be addressed before the shotcrete could be applied to the bottom soffit of the cap beam. A 3mm galvanized metal lathe attached with metal nailing anchors had to be applied to help the shotcrete bond to the bottom surface because of the large loss of the original cover concrete, and to overcome gravity.



Figure 4.11 Cap beam with cover layer restored to the original concrete cover thickness

Chamfered Column and Beam Cap Corner Preparation (3)

The third step was to round any corners of the square columns and rectangular cap beam. In 2000, the procedure used to round the corners of Bent #6S was grinding with standard metal hand grinders equipped with concrete grinding diamond blades. All corners were ground by hand, the only exception was where shotcrete had been applied to the cap beam. Wherever CFRP composite confinement was necessary at the shotcreted areas, a 51-mm radius was formed during the application of the shotcrete build up. The average radius obtained in the columns and beams was 51 mm. Rounding the sharp corners off the columns and cap beam was necessary to gain additional confinement for improving displacement ductility, where the CFRP composite had been applied, and to reduce stress concentrations. The benefits of grinding a radius on corners of square and rectangular shapes, when FRP composites are applied for confinement, are well known and will be discussed in a later section.

CFRP Application (4)

All areas where CFRP composite was to be applied had been finished to a smooth surface. For a better bond between the applied CFRP and smooth surfaces of the existing concrete it was necessary to roughen all concrete surfaces. All new cover areas build up by the shotcrete application were also roughened. The procedure used to roughen all surface areas was performed by water jet. This is done by adjusting the jet size in the jet spray gun and by adjusting the spray pressure of the pressure delivery system.

After all surfaces had been properly roughened, a high viscous primer epoxy resin was applied to all areas where the CFRP composite was to be installed. The resin material used on Bent #6S 2000 was Sikadur Hex 31. The resin is applied to ensure a good bond between the concrete surface and the resin used in the wet lay-up application. Also, it has been found that whenever the primer coat is not applied, gas or air from the inner concrete material is released and bubbling or delimitation occurs in the concrete-CFRP composite interface.

Bent #6S 2000 CFRP Retrofit Design Based on Previous Design of Bent #6N 1998 Experiment

After an investigation of the original as-built design it was found that there were four design deficiencies: (1) inadequate confinement of the columns, of the column lap splice region, and plastic hinge regions; (2) inadequate shear capacity of columns; (3) lack of hoop reinforcement in the bent cap joint regions; and (4) inadequate anchorage of the column longitudinal reinforcement into the bent cap and pile caps. The seismic retrofit using CFRP composites was designed to address these deficiencies. An additional retrofit measure was required in the pile-to-pile cap connections. A 38mm hole was bored then high strength Dywidag bars were epoxied in the pile-to-pile cap joint (Pantelides et. al. 1999, 2000), as shown in Figure 3.4.

The CFRP composite retrofit for Bent #6S was analyzed using the following two-step procedure: (1) based on a pushover analysis of the as-built Bent #5S, a CFRP composite retrofit was provided for flexural plastic hinge confinement of the columns and bent cap, lap-splice clamping of the column bars, and shear strengthening of the columns; and (2) after designing the CFRP composite retrofit for the columns and bent cap, the bent was reanalyzed

using DRAIN-2DX to determine the increased principal tensile stress at the bent column-cap beam joint and the increased tensile force in the longitudinal column bars framing into the joint due to the CFRP strengthening of the columns and bent cap. The second pushover analysis used a confined concrete stress-strain curve for portions of the columns and bent cap where CFRP composites were applied in step (1).

The material used in this application was a carbon fiber/epoxy resin composite unidirectional fabric and was applied at ambient temperature. The fabric and epoxy resin used were SikaWrap® Hex 103C and Sikadur® Hex 300/306. The fabric comes packaged in rolls 0.635 m wide X 15.24 m long. The fiber properties are as follows: tensile strength 3.5GPa; tensile modulus 234.4GPa; elongation 1.5%; density 0.00008 oz./mm³. The cured laminate properties are as follows: tensile strength was 958.4 MPa at a failure strain of 0.009 mm/mm; modulus of elasticity was 74.4GPa; average thickness = 1mm; average strength per 25.4 mm = 24.73 kN/layer. The CFRP confined concrete stress-strain curve used is shown in Figure 4.12; the analytical model for obtaining this curve was presented by Gergely et al. (1998). Since the cross section of the bent cap and columns are rectangular and square respectively, the strain softening plastic behavior is appropriate.

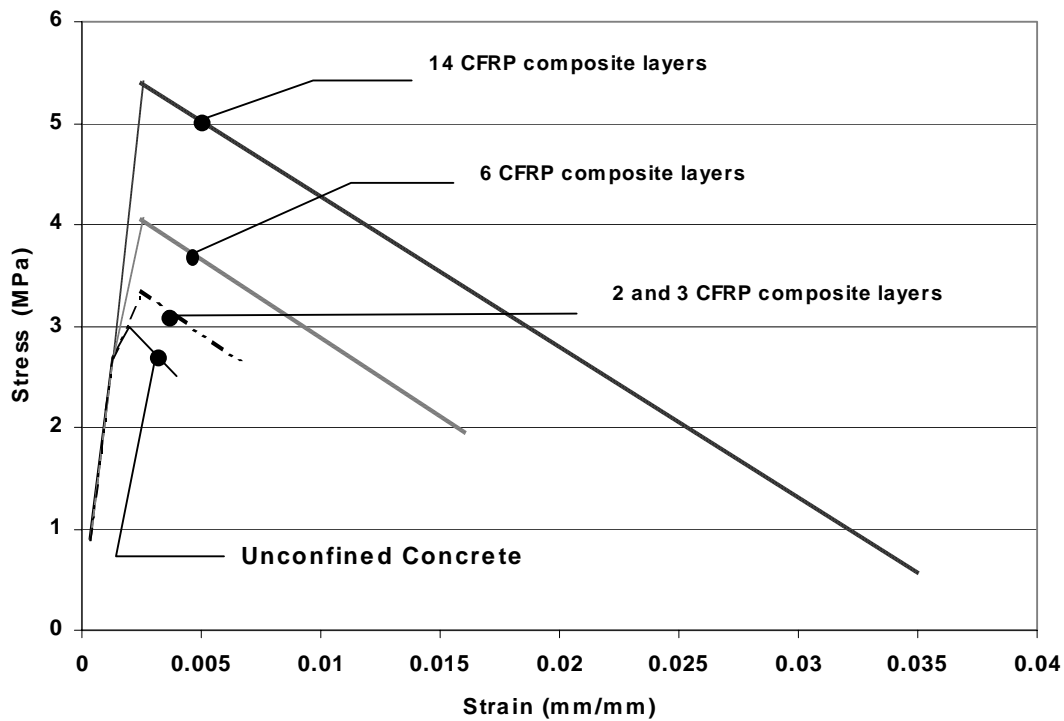


Figure 4.12 Concrete stress-strain diagrams defining the unconfined and CFRP composite confined sections used in the analytical Drain-2DX model

Flexural Hinge Confinement of Columns

To confine the plastic hinge region, the CFRP composite was designed as a square jacket using twice the CFRP thickness required for the equivalent circular jacket of diameter, D_e (Seible et al. 1997). This is recommended for rectangular columns with a size aspect ratio

less than 1.5. The CFRP jacket thickness was evaluated using the following expression (Seible et al. 1997):

$$t_j = 2 \left[\frac{0.09 D_e (\varepsilon_{cu} - 0.004) f'_{cc}}{\phi_f f_{ju} \varepsilon_{ju}} \right] \quad (4.1)$$

where: $\varepsilon_{cu} = 0.008$, defined as the ultimate concrete jacket strain; $f'_{cc} = 1.5 \times 20.7 \text{ MPa}$ defined as compressive strength of confined concrete; $f'_{ju} = 958.4 \text{ MPa}$ defined as ultimate CFRP composite tensile strength; ϕ_f = flexural capacity reduction factor taken as 0.9; $\varepsilon_{ju} = 0.013$ defined as the ultimate CFRP composite strain; and $D_e = 1.30 \text{ m}$ defined as the equivalent circular diameter. Equation 4.1 yields $t_j = 2.8 \text{ mm}$ as the thickness of the CFRP composite for flexural confinement.

An evaluation of column buckling was performed and was found to control for bending and axial loading capacity. The required thickness was found from:

$$t_j = \frac{n D_e}{E_j}; \quad \text{for } \frac{L}{D} \geq 4 \quad (4.2)$$

where: $n = 16$ is the number of longitudinal reinforcement bars; $E_j = 73 \text{ GPa}$ is the modulus of elasticity of the CFRP composite; $L = 3.66 \text{ m}$ where for a fixed-fixed condition the effective length is half the effective column height; and $D = 0.914 \text{ m}$ was defined as the diameter of the column. Equation 4.2 yields $t_j = 4.1 \text{ mm}$ as the required thickness of the CFRP composite for prevention of buckling.

The location of these layers with respect to the column height is governed by the plastic hinge length, which for a retrofitted column is (Preistley et al. 1996):

$$L_p = 0.08L + 0.15 f_{py} d_b \quad (4.3)$$

where: $L = 3.66 \text{ m}$ is the effective column length; $f_{py} = 276 \text{ MPa}$ is the yield strength of steel reinforcement; $d_b = 32 \text{ mm}$ is the longitudinal bar diameter. The plastic hinge length from Equation 4.3 was found to be 0.49 m .

Lap Splice Clamping

The CFRP composite thickness for clamping the lap-splice region was determined based on an equivalent circular jacket and was multiplied by a factor of two. The lateral clamping pressure can be found from Equation 4.4 as (Seible et al. 1997):

$$f_l = \frac{A_s f_{sy}}{\left[\frac{p}{2n} - 2(d_b + cc) \right] L_s} \quad (4.4)$$

where: $A_s = 819mm$ is the area of one longitudinal column steel bar; $f_{sy} = 276MPa$ is the yield strength of the longitudinal lap-splice bars; $p = 2.59m$ is the inside cracking perimeter along the longitudinal bars; $n = 16$; $d_b = 32.2mm$ is the diameter of longitudinal bars; $cc = 102mm$ is the concrete cover to the longitudinal bars; $L_s = 762mm$ is the lap-splice length. Equation 4.4 yields the lateral clamping stress $f_l = 0.86MPa$.

The contribution of the steel ties to the clamping stress was found using Equation 4.5:

$$f_h = \frac{0.002A_h E_h}{D_s} \quad (4.5)$$

where: $A_h = 200mm^2$ is the area of transverse ties; $E_h = 200GPa$ is the elastic modulus of the ties; $D_e = 914.4m$; and $s = 305mm$ was the tie spacing. Equation 4.5 yields $f_h = 0.185MPa$ as the contribution of the reinforcement tie clamping stress.

The thickness of the CFRP composite to clamp the lap-splice region is (Seible et al. 1997):

$$t_j = \left[\frac{D_e(f_l - f_h)}{2\varepsilon_j E_j} \right] \quad (4.6)$$

where: E_j is the modulus of elasticity of the composite (73GPa), and ε_j is the hoop strain at which lap-splice de-bonding occurs; experimental evidence suggests that this strain should be taken as 1mm/m (Seible et al. 1997). The factor 2 is due to the fact that this is a square section. The total CFRP composite thickness for the lap splice clamping from Equation 4.6 is $t_j = 11.86mm$. The location of these layers is at the bottom of the column for a length along the column equal to the lap-splice length.

Shear Strengthening of Columns

Each of the shear-resisting components was evaluated and then subtracted from the design shear, which was taken as 1.5 times the column shear at yielding. Shear strengthening was not required outside the plastic hinge region. The required thickness of the CFRP jacket inside the plastic hinge region was found from Equation 4.7 (Sieble et al. 1997):

$$t_j = \frac{\frac{V_o}{\phi_v} - (V_c + V_s + V_p)}{0.008E_j D} \quad (4.7)$$

Table 4.1 Confinement layers of CFRP composite and their locations on Bent #6S 2000

Confinement Layers						
Location	Deficiency			Tot. Thickness	Splice Length	Layers
Columns	Flexure (mm)	Shear (mm)	Lap Splice Clamping (mm)	mm	mm	Quantity
Bottom	11.2		11.2	11.2	914	14
Bottom Middle	2.0	0.5		2.5	457	3
Bottom Top	2.0			2.0	457	2
Top	4.1	0.5		4.6	914	6
Top Middle	2.5			2.5	457	3
Top Bottom	2.0			2.0	457	2
Cap Beam						
Adjacent Column Layers					457	4
Adjacent Wraps Next to 4 Layers					457	2

where: V_o = design shear (577kN); V_c = concrete shear contribution (190kN); V_s = shear contribution of ties (169kN); D = column width (914mm); E_j = modulus of elasticity of the CFRP composite; and ϕ_v = shear strength reduction factor equal to 0.85. The CFRP composite layers were applied at the top and bottom of the column for a length equal to 1.5 times the column depth, as recommended by Seible et al. (1997). The required CFRP composite thickness from Equation 4.7 is $t_j = 0.47\text{mm}$.

Flexural Hinge Confinement of Cap Beam

Since the shear and flexural capacity of the bent cap was found to be adequate, only confinement of the plastic hinges near the joints was considered. On the cap beam, a 0.46m wide CFRP composite wrap of two layers and a 0.46m wide CFRP composite four-layer wrap were applied adjacent to column-cap beam joints, for all three columns, as shown in Figure 4.13. The reason for this is that the CFRP composite placed on the columns had increased their strength, and needed to be balanced in the bent cap. An additional 0.46m CFRP wrap was placed adjacent to the four-layer wrap for all three columns to distribute any possible stress concentration at the end of the layers immediately next to the column. A final DRAIN-2DX analysis was run and it was found that the additional layers placed on the bent cap had eliminated all plastic hinge development in the bent cap for the initial design.

Required Layers after Assessment of Column and Cap Beam Deficiencies

The required CFRP composite layers for the assessed deficiencies in the columns and bent cap regions are shown in Table 4.1.

In addition to the above confinement layers there were four additional layers applied to the east joint (two layers on both sides of the cap beam along the beam axis at zero degrees) and two additional layers along the beam axis at zero degrees were applied to the center joint. The additional layers were added for investigating additional strength and will be discussed in a later section.

Shear Strengthening of Column-Cap Beam Joint-Ankle Wrap

With the design criterion to double the displacement ductility of the as-built bent, higher joint shear forces and stresses would be developed. By using DRAIN-2DX with the new CFRP composite thickness, as shown in Table 4.1, additional forces and stresses were found in the joint regions using Equations 4.8 and 4.9 as follows:

$$v_{jh} = \frac{V_{jh}}{b_{je} h_c} \quad (4.8)$$

$$v_{jv} = \frac{V_{jv}}{b_{je} h_b} \quad (4.9)$$

where V_{jh} is the horizontal joint force (1374.5kN); b_{je} is the effective joint width (0.914 m); h_c is the column width (0.914 m); v_{jh} is the horizontal shear stress (1.64MPa); V_{jv} is the vertical joint force (1116.1kN); h_b is the cap beam vertical thickness (1.22m); and v_{jv} is the vertical shear stress (1.80MPa). By finding the median average between the vertical and horizontal shear stresses (1.72MPa) and using the cap beam axial compression (-0.95MPa), the principal angle was found as $\theta_p = 38^\circ$ in the joint region by Equation 4.10:

$$\cos 2\theta_p = \frac{\sigma_x}{2\sqrt{\left(\frac{\sigma_x}{2}\right)^2 + (\tau_{xy})^2}} \quad (4.10)$$

where: σ_x is the compressive stress (-0.95 MPa); and τ_{xy} is the average shear stress (1.72 MPa). The CFRP composite shear layers were laid perpendicular to the principal shear angle at $\pm 52^\circ$ from the longitudinal axis of the bent cap.

With the increase in lateral load, the demand for the joint principal tensile stress was increased by $\Delta\sigma = (\sigma_{2b} - \sigma_{2a}) = 0.035\text{MPa}$ where σ_{2b} is the principal tensile stress in the carbon FRP composite design and σ_{2a} is the principal tensile stress in the as-built design. The CFRP layers were required at $\theta = 52^\circ$ for the most efficient lay-up angle to prevent diagonal tension and subsequent shear failure in the joint regions. These layers will be referred to as “ankle wrap” layers. In the installation phase, the ankle wrap was placed prior to the confinement layers adjacent to the columns. The adjacent column layers served a dual purpose: First, in the confinement of the cap beam adjacent to the columns and also for end clamping of the ankle wraps to prevent premature failure in the joint regions. The ankle wrap layers were laid the full width of the 0.914 m x 1.22 m joint region and were extended underneath the cap beam layers. A detailed drawing of the carbon layers is given in Figure 4.13. The number of layers required was found by using Equation 4.11:

$$F_2 = \phi_v t_j \varepsilon_j E_j \frac{d_e}{\cos \theta} \quad (4.11)$$

where ϕ_v = shear reduction factor, assumed as 1.0; θ = angle between the longitudinal axis of the member and fiber direction (52°); t_j = thickness of one composite sheet of 1mm; ε_j = average axial strain of the composite in the fiber direction, at peak horizontal load, which was taken as 2mm/m; d_e = effective joint depth equal to the joint height minus twice the effective bond length of the composite sheet to the concrete; from laboratory tests this bond length was approximately 51 mm. The joint dimension and inclination of the principal plane control the value of d_e which is equal to 0.914 m; the resulting force F_2 was 148.3kN. To find the tensile stress developed in one composite layer, F_2 is divided by the joint width ($b=0.914$ m) and by the inclined length along the crack as:

$$\sigma_f = \frac{F_2 \cos \theta}{bd_e} \quad (4.12)$$

Equation 4.12 yields $\sigma_f = 0.162 \text{ MPa}$. A number of layers each of capacity σ_f must be used to resist the principal tensile stress increase of $\Delta\sigma = (\sigma_{2b} - \sigma_{2a}) = 0.035 \text{ MPa}$ from the as-built to the retrofitted bent. The total number of layers required is:

$$L_n = \frac{\Delta\sigma}{\sigma_f} \quad (4.13)$$

which yields $L_n = 1/4$ layers. Four layers were used in the actual lay-up. After the final stages of the CFRP composite design, there was a decision made to change the foundation design used in the 1998 tests. As described earlier in this chapter, the new 2000 foundation design induced additional stresses and forces to the joint regions. It was decided to use four layers of unidirectional CFRP composite applied to both sides (two on each side of the bent cap) to form the ankle wrap. These layers were provided in both directions to resist the cyclic action of the simulated seismic loads used in the experiments.

Anchorage of Column Bars—U-Strap

In order to improve development of the longitudinal column bars ending in the column-cap bent joint and to prevent bar pullout at high lateral loads, a U-strap CFRP composite design was implemented. The straps were provided at the column edges over the longitudinal column steel and contributed to the column flexural resistance. The width of the composite straps was assumed as 356 mm, and the thickness of the composite straps was determined based on the required increment in the column tensile force from the two analyses of the bents. The incremental tensile force for the interior joint is $\Delta T = (T_b - T_a) = 118.32 \text{ kN}$, where T_b = tensile force in the retrofitted column and T_a = tensile force in the as-built column. The CFRP composite thickness required to transmit this increment force was found as:

$$t_j = \frac{\Delta T}{\phi_f w_j \varepsilon_j E_j} \quad (4.14)$$

where w_j = width of CFRP composite strap (356 mm); E_j = modulus of elasticity of the composite; ϕ_f = combined tensile and flexural capacity reduction factor, assumed as 1.0; and ε_j = effective strain developed in the composite strap, assumed as 2 mm/m. A factor of safety of 1.5 was used to ensure against premature strap failure. The required thickness was 8.0 mm; 10 layers were provided (5 layers wrapped around the bent cap and column in a U-shape, as shown in Figure 4.14).

The U-straps were clamped using one layer of CFRP composite sheet wrapped around the column over the straps in the transverse direction. Both the interior and exterior columns were retrofitted in an identical manner. There were modifications required in the U-strap lay-up dictated by the locations of the girder bearing pads. The U-strap design is shown in Figure 4.14.

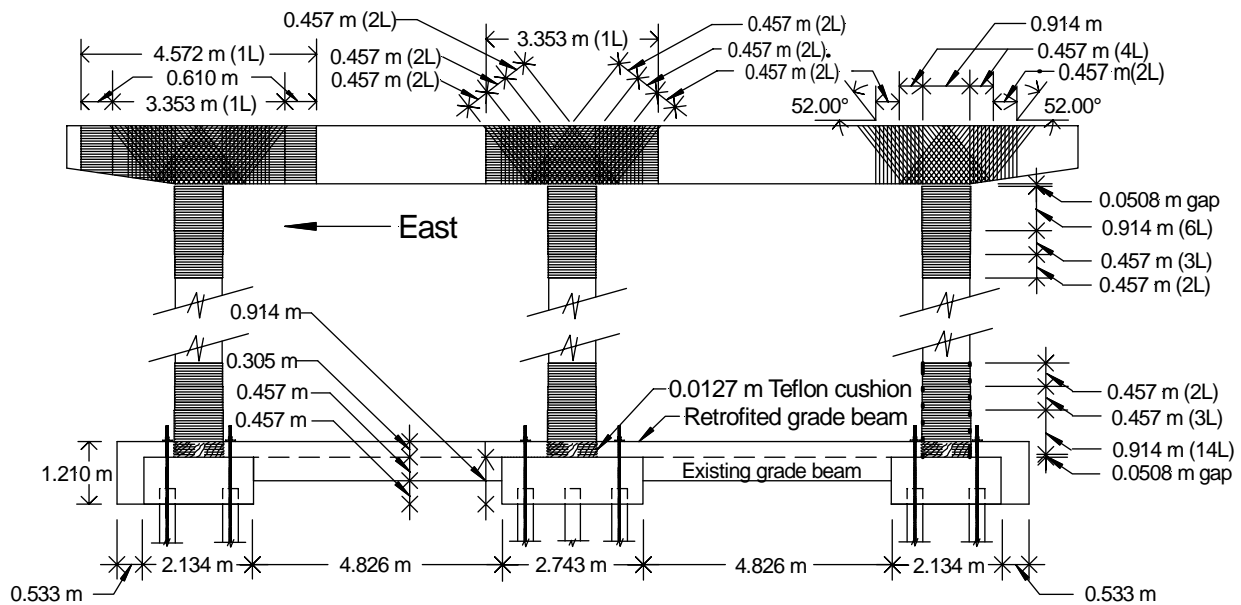


Figure 4.13 Complete CFRP composite retrofit design of Bent #6S for the 2000 test
(L = number of CFRP composite layers)

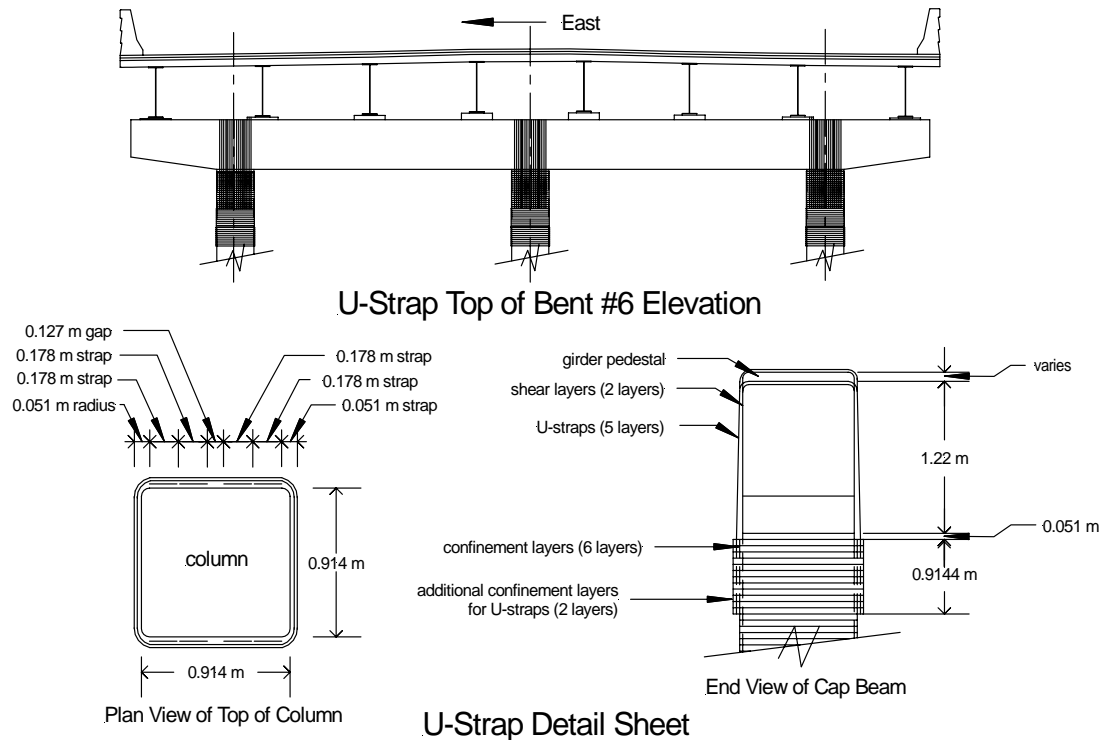


Figure 4.14 U-strap design for Bent #6S for the 2000 test

Dywidag Bar Installation

The 19.81m long piles were originally embedded into the 0.914m thick pile cap a distance of 0.305m. The existing pile locations and pile caps are shown in Figure 4.15. The connection of the piles to the pile cap consisted of four 19-mm bars extending only 0.305m into the pile cap as shown in Figure 4.16. For the lateral loads anticipated in the test, the capacity of these bars would have been exceeded and their short anchorage length would have been insufficient to resist pullout failure of the piles. To prevent this, a 38mm hole was cored through the pile cap and into the pile for a distance of 2.44m, as shown in Figure 4.16. The pile was then anchored to the pile cap using a 32mm Dywidag bar (1,030MPa ultimate stress) epoxied into the cored hole. This detail was implemented for the four corner piles of each pile cap.

Each of the pile-to-pile cap connections was designed to transfer a vertical reaction of 445kN from the pile cap to each pile. The ultimate capacity of the 32mm diameter Dywidag bar was 833kN, which is higher than the required design force. In addition to the strength of the bar, the development length was checked. The structural epoxy used to anchor the bar into the pile had a compressive strength of 128MPa and a tensile strength of 36MPa; the nominal bond stress of the concrete controlled the development length of the Dywidag bar. For a 32mm diameter bar the nominal bond stress was 2.87MPa, which is 52% of the allowable stress (ACI 1999); the required development length according to ACI Specifications was 1.56m (ACI 1999). The total length of the Dywidag anchor bar required equals the development length plus the thickness of the pile cap for a total bar length of 2.9m. A 2.9m long 32mm Dywidag bar was used for each pile cap as shown in Figure 4.16.

2.134 m square

0.914 m Column

Grade Beam

Pile Cap

0.457 m

0.305 m

1.219 m

2.9 m

0.305 m

51 mm

19 mm

32 mm Dywidag

Concrete Filled Pipe Pile

Section A-A

Foundation Design

111

providing a friction connection between the newly cast grade beam ends and the interior side surfaces of the pile caps and existing grade beam supports of Bent #6S. In addition to the friction connection, the entire grade beam structure was tied together by forming and casting additional concrete on both sides of the existing grade beam by raising the new grade beam elevation 305mm above the existing pile cap and grade beam. All new additional grade beam concrete was formed and cast monolithically. Twelve 32mm Dywidag bars (one bar for each pile with the exception of the center pile located under the center column) each with a 127mm square washer and Dywidag nut bolted the new grade beam down to the three pile caps. The twelve Dywidag pile cap connections were designed to transfer the column and pile cap moments into the modified retrofitted grade beam. Material-wise, the grade beam retrofit design required approximately 26kN of reinforcement steel and 23 cubic meters of concrete. A more comprehensive description of the grade beam design can be obtained from Cook et al. (2002) and Ward (2001). The complete retrofitted grade beam as-built drawings are shown in Figures 4.17 - 4.20.

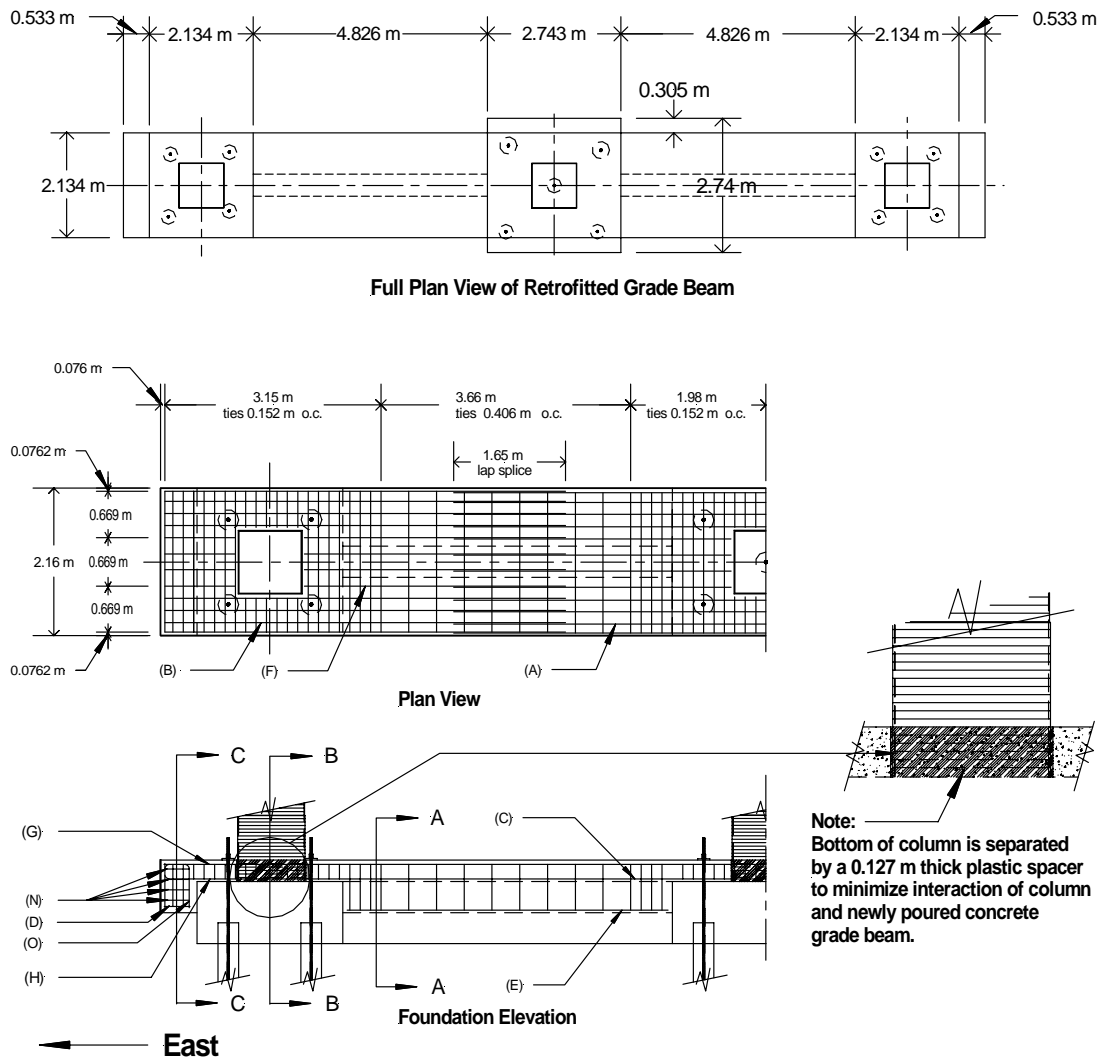


Figure 4.17 Plan view of the modified grade beam system

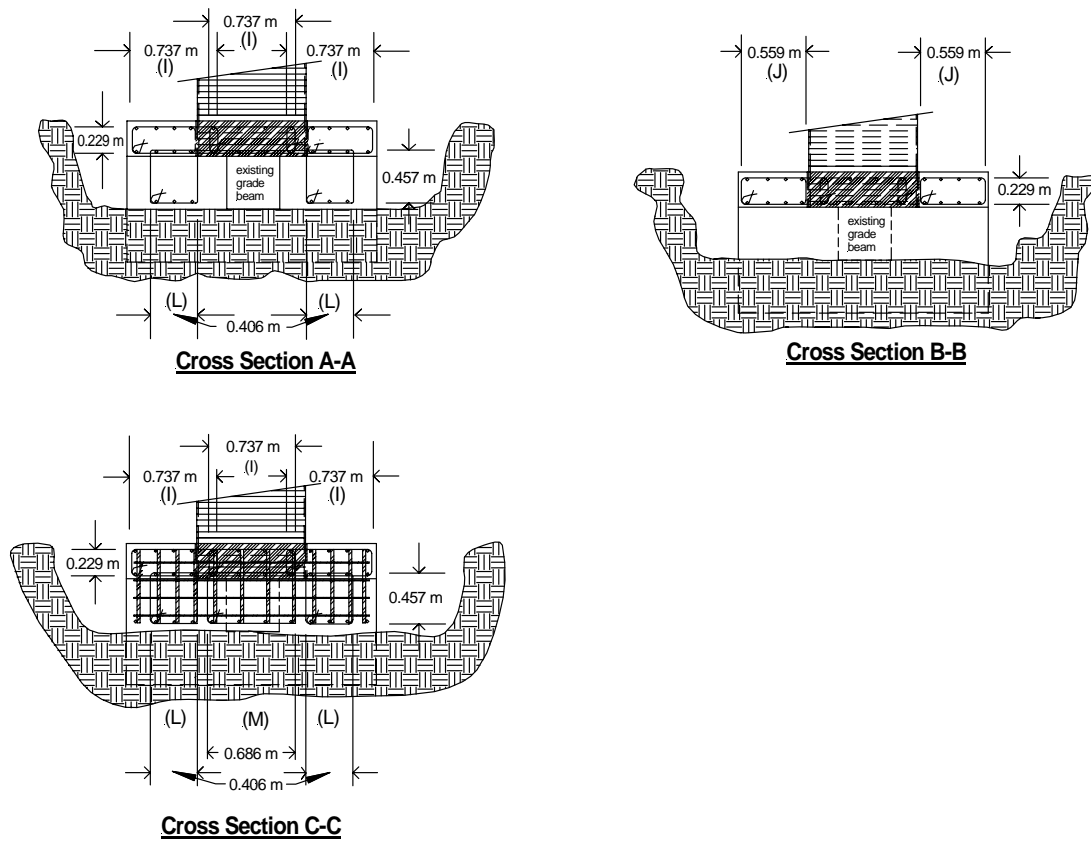


Figure 4.18 Cross-sections of the retrofitted grade beam

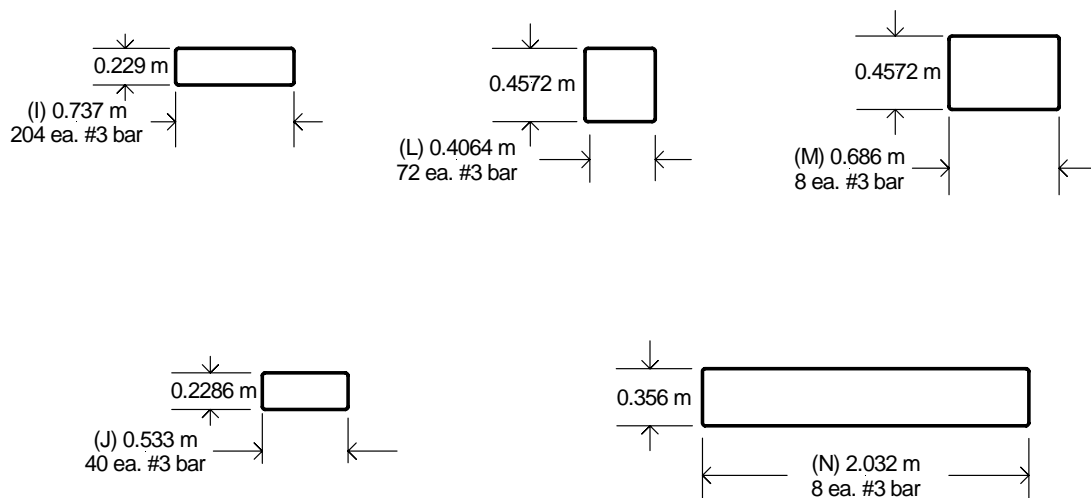


Figure 4.19 Hoop steel details used in the retrofitted grade beam

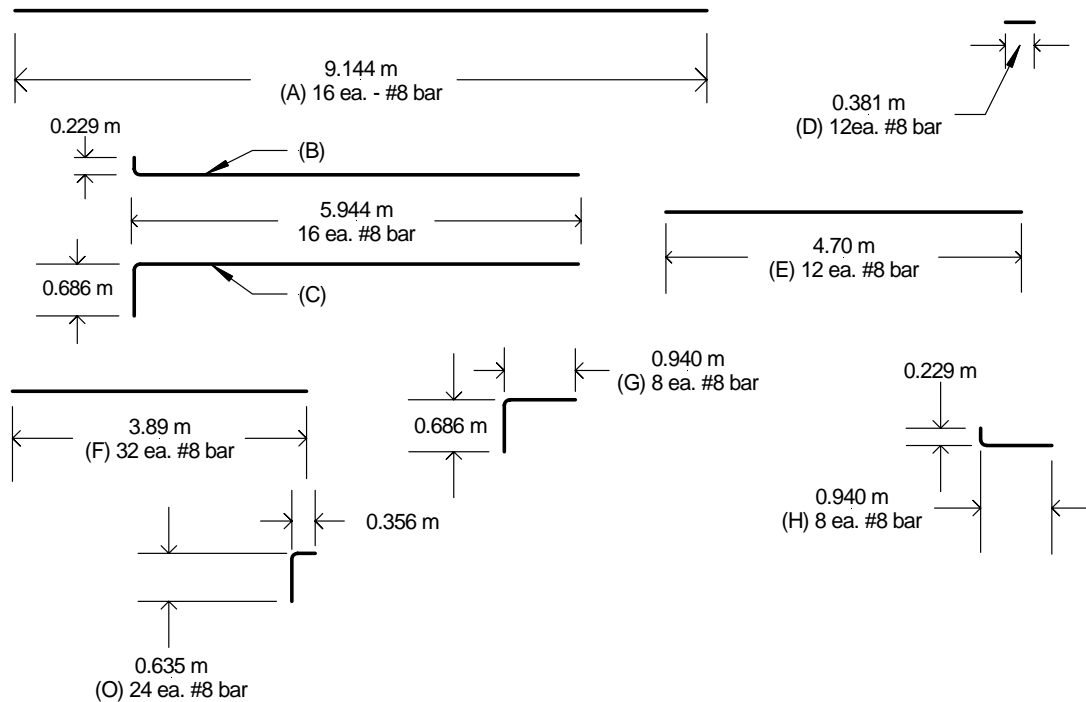


Figure 4.20 Longitudinal steel used in the retrofitted grade beam

Test Setup

The major difference in the test setup between the three bents was the foundation systems supporting the loading frame. The load frame was used to support a 2670kN capacity hydraulic actuator used for all three bent tests (Pantelides et al. 2000). For each test the actuator was attached to the end haunch sections of each cap beam and used to perform push-pull load cycles in a quasi-static test mode. A complete overview of the 2000 test setup for Bent #6S is shown in Figure 4.21.

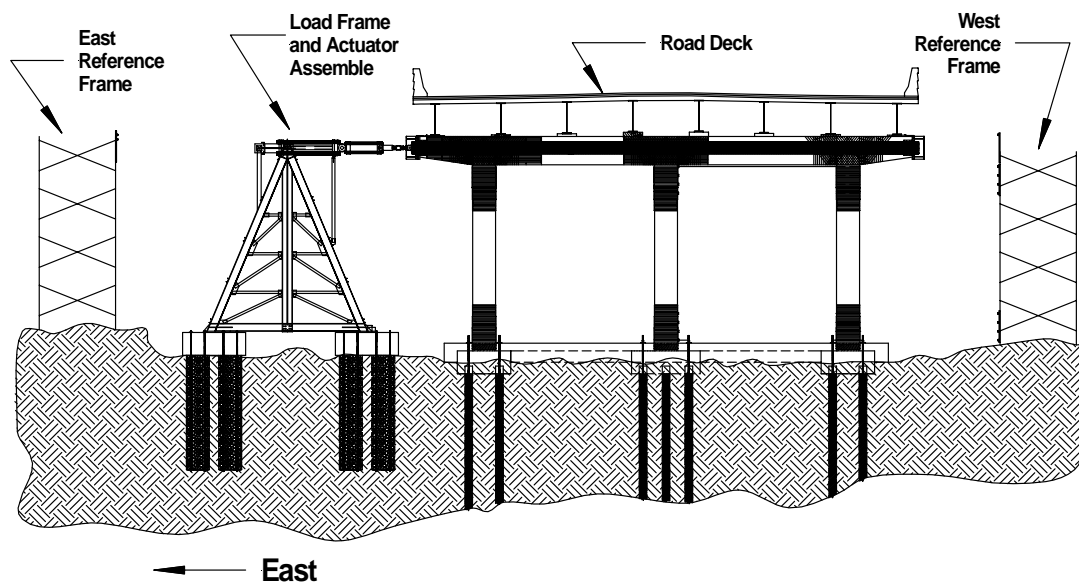


Figure 4.21 Elevation of test set-up for the May 6th and 9th 2000 Bent #6S tests

Load Frame Foundations

During the 1998 tests, the load frame foundations were constructed in a way so as to facilitate that some of the foundations could be used for both the 1998 and 2000 tests. The load frame geometry required two large foundations capable of handling very heavy vertical forces, lateral forces, and moment reactions during the tests. Also, the foundation designs needed to be capable of handling an extensive number of cycles during testing. Both foundations used to support the load frame for the Southbound Bent #6S 2000 test were existing foundations used in the Northbound 1998 Bent #6N test as well. The actuator performed a lateral push-pull cyclic loading that was transferred to the bent structure through a yoke and twenty 12.7mm cable strands connected system assembled at the cap beams, as shown in Figures 4.22 and 4.23. All reaction demands were transferred through the load frame to the load frame foundation system. The two load frame foundations were constructed of reinforced concrete and were typical in construction. Their dimensions were 2.53m wide x 7.48m long x 0.99m high. The large foundations were connected to the ground with ten geopiers per foundation that were 0.914m in diameter and extended into the ground a distance of 4.57m. A plan view of a typical foundation system is shown in Figure 4.24.



Figure 4.22 Yoke assembly attached to the East haunch end of Bent #6S



Figure 4.23 Twenty 12.7 mm cable strands used to apply the pull portion of the load for Bent #6S

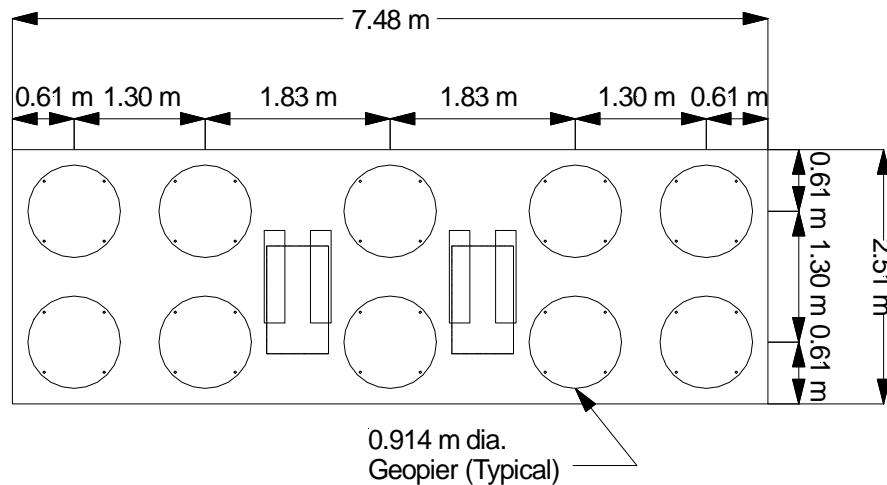


Figure 4.24 Plan view of a typical foundation and geopier system used to support the load frame used in the Bent #6S 2000 test

Load Frame

The load frame was an A-frame design with four main beam sections constructed from standard structural steel W12x65 members to transfer the compression and tension forces to the load frame foundation. Horizontal W8x31 sections were added to prevent buckling of the main beam sections. There were various diagonal steel sections added for diagonal bracing in the frame for horizontal and torsional deflection (Pantelides et al. 2000). In the 2000 tests, a 2.1 m extension was necessary and was added to the load frame; this modification was done so the load frame foundations for Bent #6N (1998) could be used again. The load frame was designed for a maximum lateral load of 1780kN with a 1.5 factor of safety (Pantelides et. al. 2000); in addition, because of modifications done on the foundation systems for the 2000 tests, the load frame needed additional welding done on the connections to ensure against frame failure. An elevation drawing of the load frame is shown in Figure 4.25.

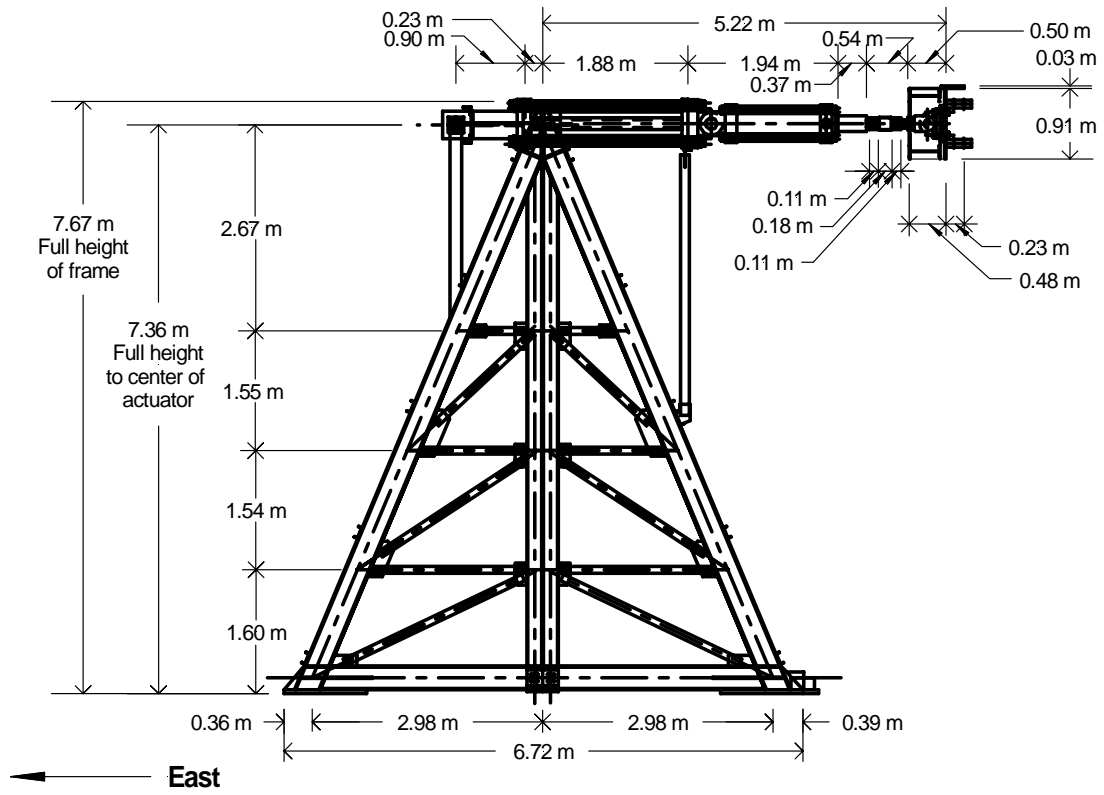


Figure 4.25 Elevation of the 2000 load frame detail with the 2.1 m extension

Road Deck Fixity on Bents #5S and #6S

After demolition, the remaining road deck between Bents #5S and Bent #6S was left in place for the tests; the deck was rigidly connected to the bent structures in the lateral direction. For the purpose of carrying out the tests for Bents #5S and #6S, modifications were made to the steel girder and cap beam connections. There were a total of eight steel girders that were connected to the top of the cap beams; these were held in place against lateral movement by keeper plates. Modifications were made on all the connections for Bents #5S and #6S to prevent unwanted torsion effects and the possibility of deck collapse. A high strength reinforced concrete box was cast around the keeper plate connections on Bent #5S to establish a pinned connection between the steel girders and cap beam, as shown in Figure 4.26. On Bent #6S sixteen heavy rollers and eight steel runways were constructed to allow the road deck to move freely for both the Bent #5S and Bent #6S tests. The roller system for Bent #6S is shown in Figure 4.27 and design details can be found in the 1998 test report (Pantelides et al. 2000).



Figure 4.26 Formed concrete pedestals on Bent #5S cap-beam



Figure 4.27 Roller and roller runways located on Bent #6S bearing plates

Instrumentation

To understand to the behavior of Bent #6S during the test, a variety of instruments were put in place to monitor the behavior of the bridge. The complete instrument setup that was installed follows.

Internal Strain Gages Attached to the Steel Reinforcement

To monitor the yielding sequence of the internal reinforcement of the bent, holes at various locations were drilled with a 102mm core drill. The holes were drilled to the steel reinforcement depth and strain gages were attached to the steel reinforcement and monitored during the test. After installing each of the strain gages, the 102mm diameter holes were filled back in with standard masonry grout that was comparable in strength to the original

concrete. The locations of the strain gages attached to the steel reinforcement are shown in Figure 4.28.

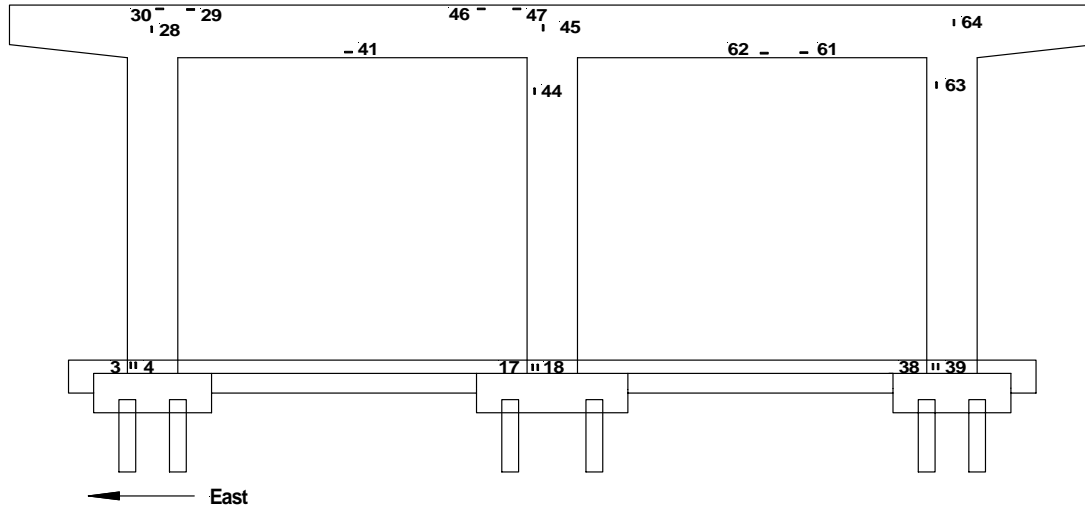


Figure 4.28 Location of the internal strain gages on the reinforcement for the Bent #6S 2000 test

Load Frame Strain Gages

Twenty strain gages were placed on the lower sections of the load frame and were used to monitor the strains in the load frame for two purposes. First, because the frame was originally designed for a maximum capacity of 1780kN there was some concern that it might not be strong enough to survive the test. Second, the gages were also used to monitor torsion effects due to the road deck gravity load and friction between the bearings and the runways constructed on Bent #6S. Also, there was some concern about misalignment of the load frame relative to the bent even though the frame was carefully placed and aligned with a transit. Fortunately, there was relatively no torsion and only small strain demands made on the load frame. The detailed location of the strain gages is shown in Figure 4.29.

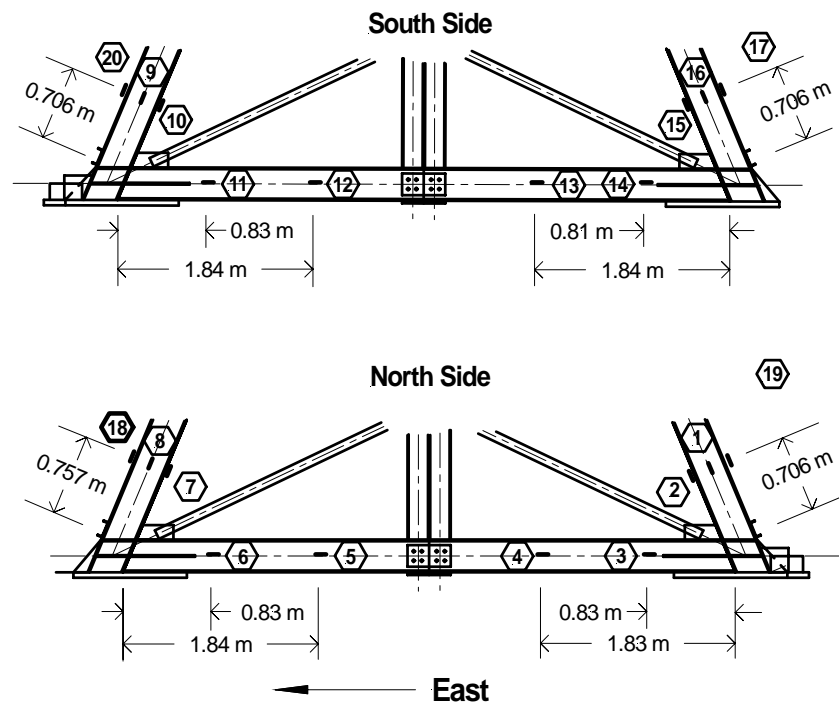


Figure 4.29 Location of the strain (F) gages on the North and South sides of the load frame

Grade Beam and Dywidag Strain Gages

Strain gages were placed on the reinforcement steel of the new reinforced concrete sections cast around the existing grade beams and pile caps. Also there were strain gages placed on the Dywidag bars used to reinforce the pile-to-pile cap connections. A detailed drawing of the locations of the strain gages placed in the new grade beam sections and the Dywidag bars is shown in Figure 4.30.

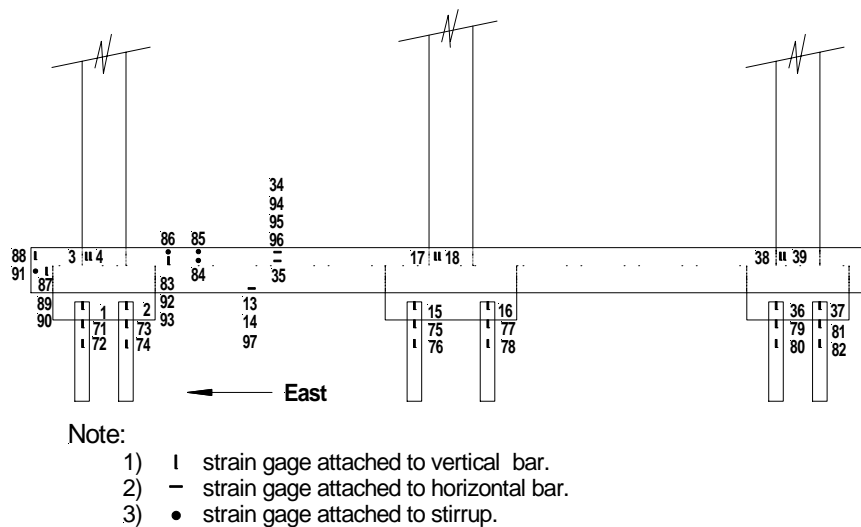


Figure 4.30 Strain gage locations in the grade beam and strain gages on the Dywidag bars in the foundations

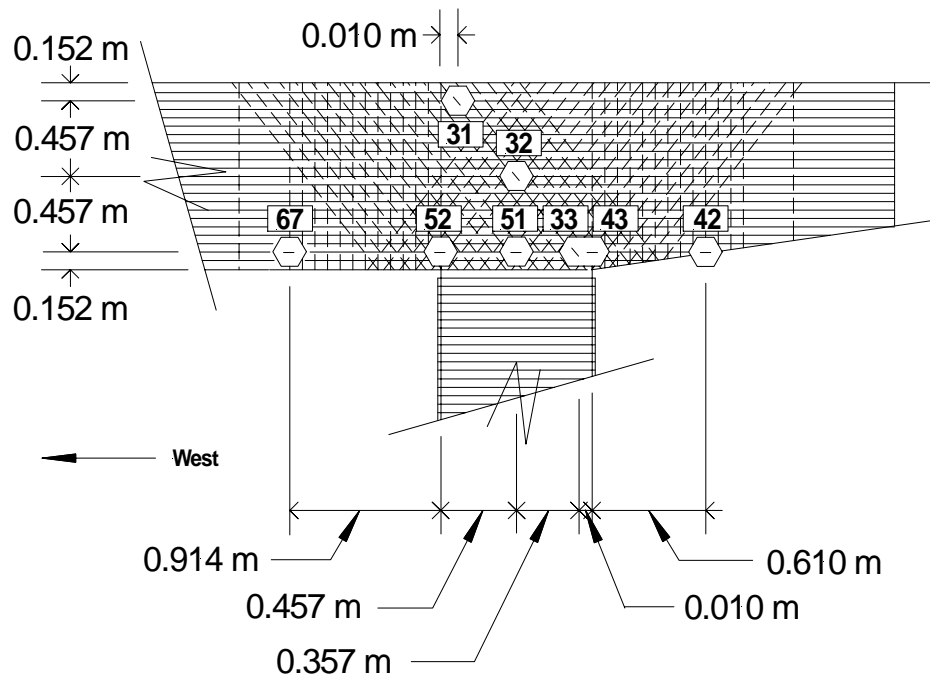


Figure 4.32 Strain gages located on the diagonal and zero layers of the East joint

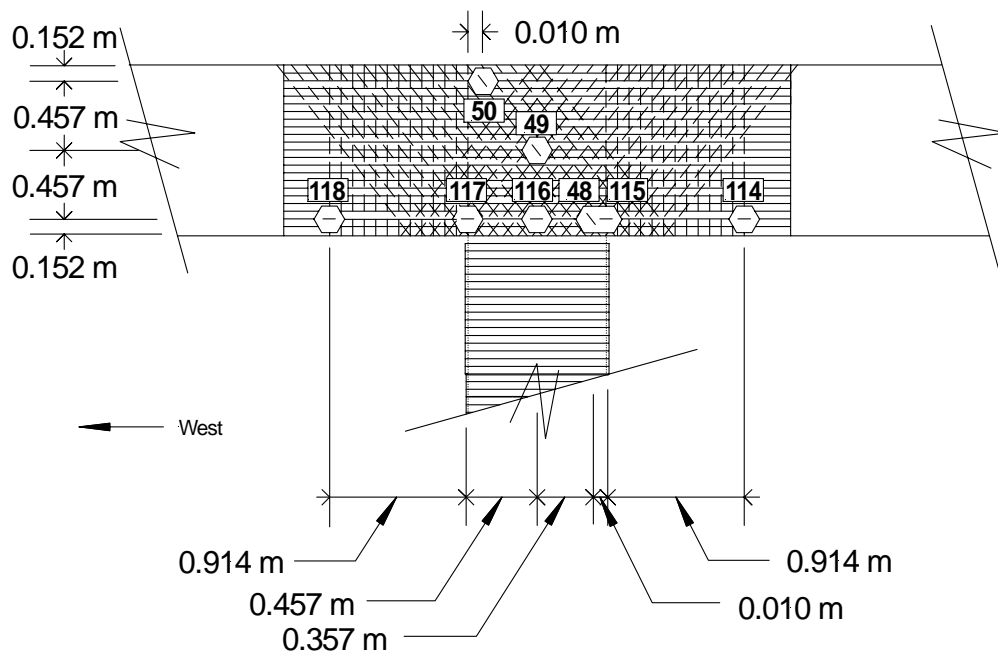


Figure 4.33 Strain gages located on the diagonal and zero layers of the Middle joint

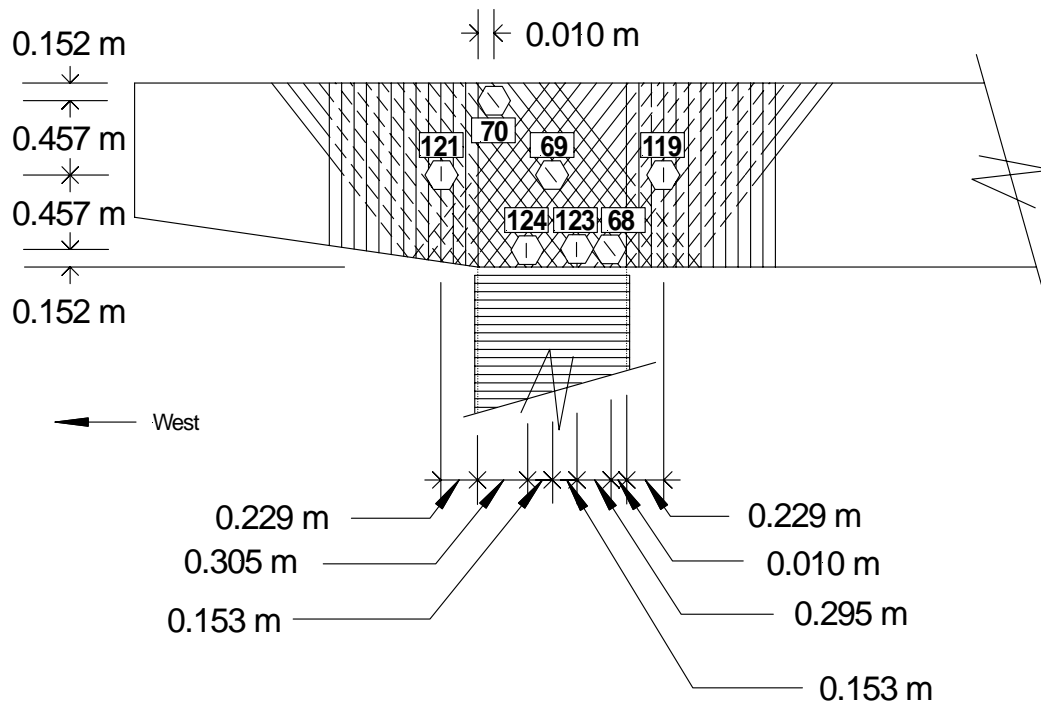


Figure 4.34 Strain gages located on the diagonal, zero, and strap layers of the West joint

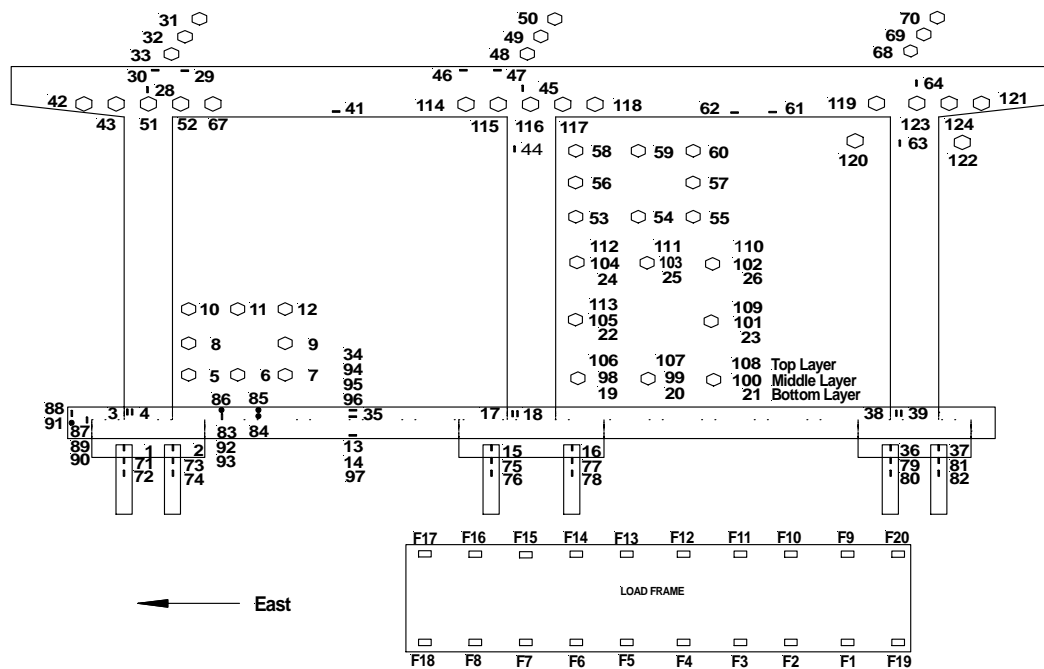


Figure 4.35 Complete view of all external strain gages installed on the load frame and Bent #6S for the 2000 test

Linear Variable Differential Transducers (LVDT) Setup

Volume LVDTs

In the first setup of LVDTs two box configurations of LVDTs were constructed around the interior column of Bent #6S 2000. The first box configuration was constructed around the bottom fourteen layers of the CFRP composite confinement layers in the plastic hinge region. A second box was constructed around the joint region on the cap beam above the interior column. The arrangement of the LVDTs consisted of two vertical LVDTs, two horizontal, one diagonal, and one each on the lower west face and upper east face of the interior column, as shown in Figure 4.36. The box arrays were used to measure joint shear strain, and volume change within the volume defined by the LVDT box arrays.

Linear Column Array

The second configuration consisted of three LVDTs installed in the vertical direction along a column and each was set to an initial length of 0.36 m. At the ends of each vertical LVDT there was a horizontal Cable Extension Displacement Transducer (DT) attached. With the horizontal and vertical displacements monitored during the test, the curvature of the center column could be measured. Drawings of the linear column arrays and horizontal DT configuration are shown in Figures 4.36.

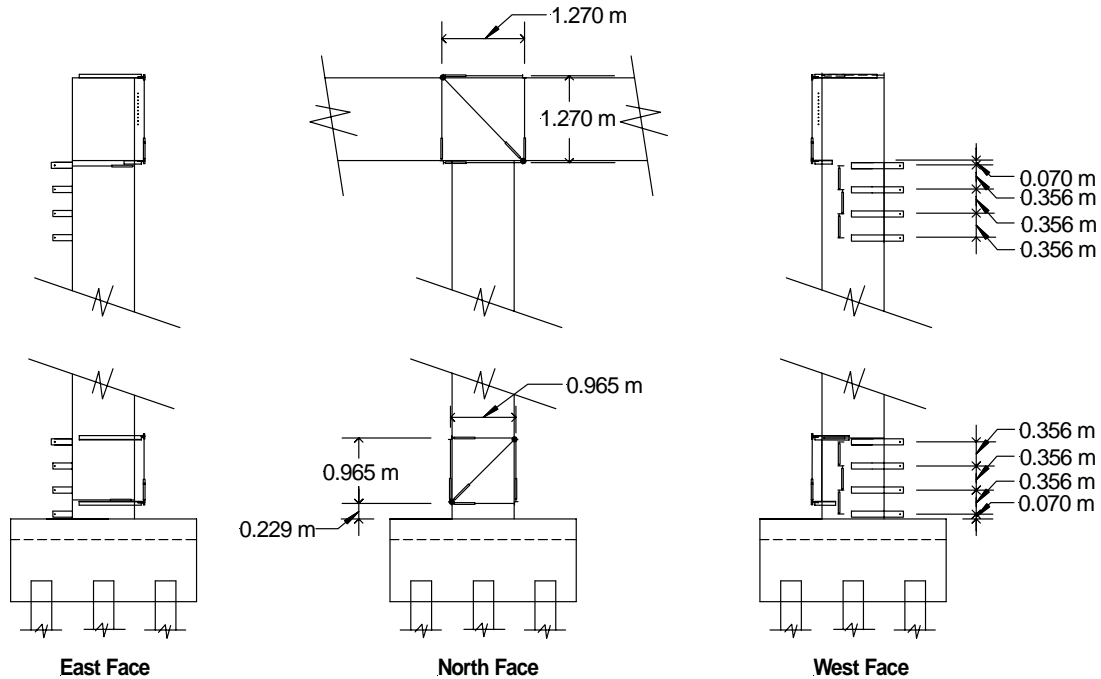


Figure 4.36 Top and bottom LVDT box arrays and linear column arrays attached to the Middle column

Cable Extension Displacement Transducers (DT)

Horizontal Cable Extension Displacement Transducers (DT)

In order to monitor the horizontal displacements during the test, two stationary reference frames made from scaffolding were erected on the West and East end of Bent #6S as shown in Figure 4.21. Eight horizontal DTs were attached to the frames to monitor the horizontal displacements of the load frame, cap beam, and the curvature of the center column as shown in Figure 4.37. The horizontal displacement of the foundations for the load frame and the grade beam were also measured during the test (Cook et al. 2002).

Vertical Cable Extension Displacement Transducers (DT)

The West end vertical displacements of the cap beam were also measured during the test. Three vertical DTs were placed in a vertical alignment on the interior column, center of the span between the interior and west end column, and on the West column. Also, at the same locations, the vertical displacement of the grade beam was measured (Cook et al. 2002). A drawing of the vertical DTs is shown in Figure 4.38.

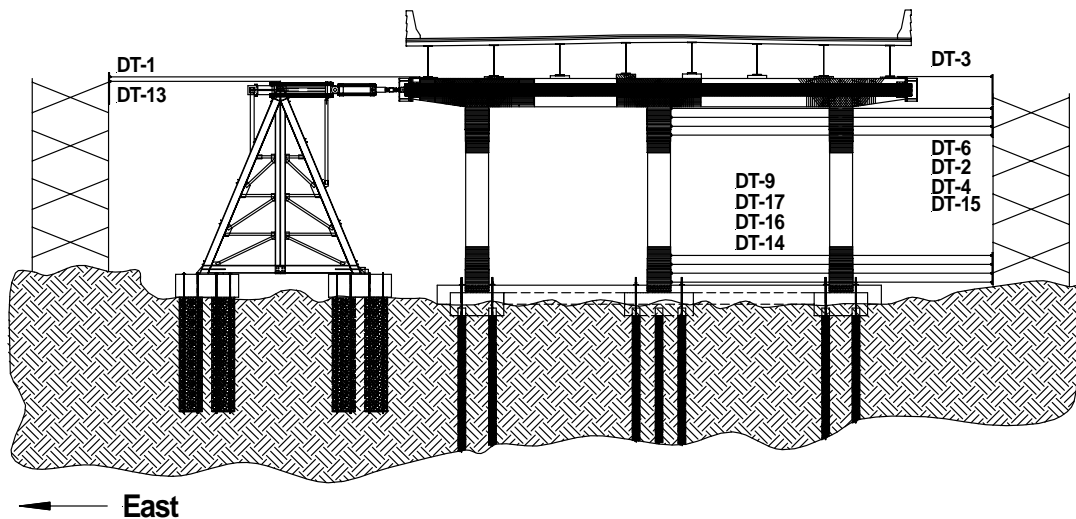


Figure 4.37 Horizontal DTs used to monitor the horizontal displacements of the load frame and cap beam during the 2000 Bent #6S test

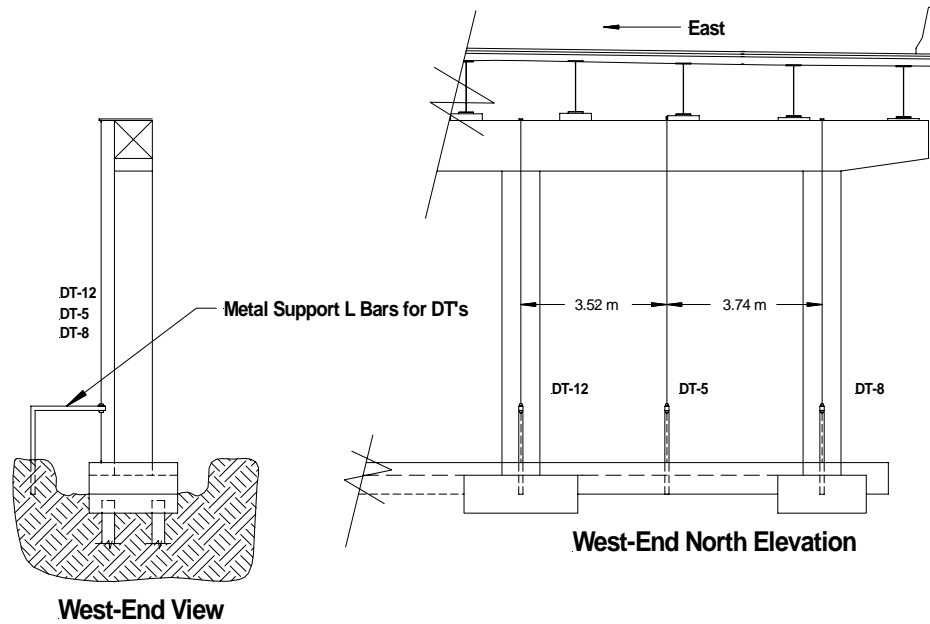


Figure 4.38 Vertical DTs used to monitor the vertical displacements of the of the cap beam and grade beam during the 2000 Bent #6S test

Because of the size and complexity of the Bent #6S test, it was necessary to test over a two-day period. An explanation of the experimental and testing conditions will be discussed further in later sections. The two days of testing were Saturday, 6 May 2000 and Tuesday, 9 May 2000. The horizontal instruments for the Tuesday, 9 May 00 test were reduced to four DTs. They were as follows: one DT attached at the foundation of the load frame, one DT attached to the top of the load frame, one DT attached to the top of the cap beam, and the last DT was attached to the grade beam. The vertical instruments were also reduced for the second test day. The instruments for the Tuesday, 9 May 2000 test were reduced to two DTs in the vertical direction to monitor the deflections of the west column and are shown in Figure 4.39.

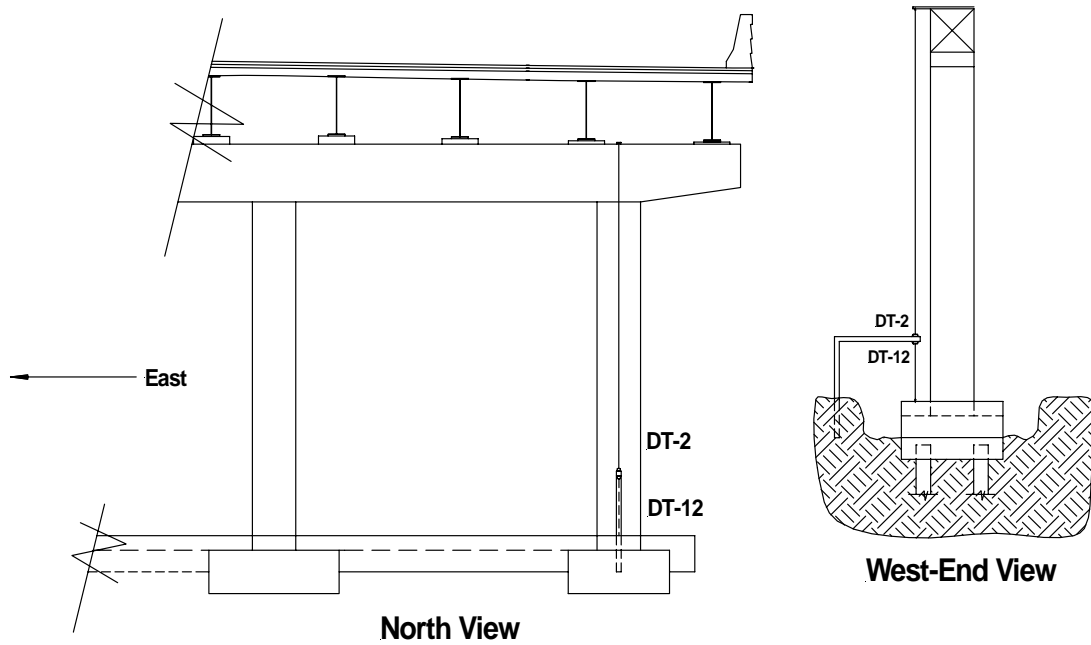


Figure 4.39 DTs used to monitor vertical displacements of the West column during the 9 May 2000 test

Experimental Conditions and Testing

Due to the complexity and the large amount of instruments used in the Bent #6S 2000 project the total testing time took two days (6 May and 9 May 2000). The weather proved to be excellent and temperatures ranged from 45 to 85 degrees Fahrenheit. The test was performed as a quasi-static cyclic test with predetermined drift displacements. Drift ratio is defined for this experiment as the horizontal displacement of the cap beam divided by the bent height, from the top of the grade beam to the center height of the column (7.64m). Each cycle was defined by first pushing the center of the cap beam to a predetermined drift then bringing the cap beam back to zero for a half cycle. The cap beam was then pulled back to the predetermined drift and back to zero again for the completion of one full cycle. Each drift cycle was repeated three times before the next drift increment was started. The predetermined step cycles for Bent #6 2000 were 0.25%, 0.50%, 1.0%, 1.5%, and in increments up to 7.0%. The actual drift steps for the test are listed in Table 4.2.

As described in earlier sections, one major difference between the Bent #6N 1998 and the Bent #6S 2000 tests was the foundation design. The foundations of the as-built Bent #5S and Bent #6S 2000 tests were of the same design and their superstructure was identical with the exception that Bent #6S was retrofitted with CFRP composites.

Table 4.2 Actual drift steps for the total system Bent #6S 2000 test

Step #	1	2	3	4	5	6	7	8	9	10	11	12	13	14
Drift %	0.28	0.53	1.0	1.4	1.9	2.8	3.8	5.1	5.5	6.0	6.2	6.4	6.7	7.0

Experimental Data

Once the testing was completed and the data was reviewed, the next task was to understand what occurred in the experiment. This section compares, where possible, the data between Bent #5S and #6S 2000 and Bent #6N 1998 tests. Comparisons have been made regarding lateral force/displacement, hysteresis, displacement ductility, cubic spline vs. the FEMA 273 curve fitting methods, and energy relationships. Also, the vertical displacements of the West column of the Bent #6S 2000 tests are included.

Displacements

Horizontal Displacements

Bent #6S was the third and last bent to be tested in the 2000 tests. From observations made from the two previous tests (Bents #4S and #5S 2000) modifications were made in positioning the load frame relative to the bent structure. Prior to the Bent #4S test, the load frame was installed by an outside contractor and was not placed in position to perform equal push and pull displacements for the test. This resulted in an overall unsymmetrical hysteresis diagram. An estimated correction was made and applied to the load frame for the Bent #5S test. The unsymmetrical loading problem was corrected, but another unforeseen problem occurred. It was difficult to drop the lateral force capacity to 80% of the peak lateral force. While the actuator total stroke length was 762 mm, its full stroke length could not be delivered to the cap beam for three reasons. There was horizontal movement in the load frame foundations, rotation in the load frame due to vertical displacements in the load frame

foundations, and stretching in tension cables during the pull portion of each cycle. A picture of the ultimate lateral displacement (102 mm) of the load frame foundation for the Bent #6S 2000 test is shown in Figure 4.40.



Figure 4.40 Horizontal displacement of load frame foundations (102 mm) on Bent #6S (2000)

To ensure that the lateral force capacity was degraded to at least 80% of the lateral peak force, the load frame was installed for an unsymmetrical displacement cycling for the Bent #6S 2000 test. Because the actuator had a higher force capacity in push than in pull, the load frame was moved forward to achieve a longer push stroke. This was successful and Bent #6S was degraded to 58% of the peak lateral force capacity. The unsymmetrical loading of Bent #6S led to some difficulty in comparing the data to the Bent #6N 1998 and Bent #5S 2000 tests. A plot showing the unsymmetrical displacements of the total system (superstructure and foundation system) is given in Figure 4.41. In Figure 4.41, the unsymmetrical loading can readily be observed. In Table 4.3 the ultimate horizontal displacements for Bent #6N 1998, Bent #5S 2000, and Bent #6S 2000 can be compared. From Table 4.3 it can be observed that the unsymmetrical loading of Bent #6S 2000 made the displacement data hard to correlate between the other two tests. As stated earlier, the Bent #6N 1998 test had no foundation displacements because the grade beam was solidly connected to the load frame foundations.

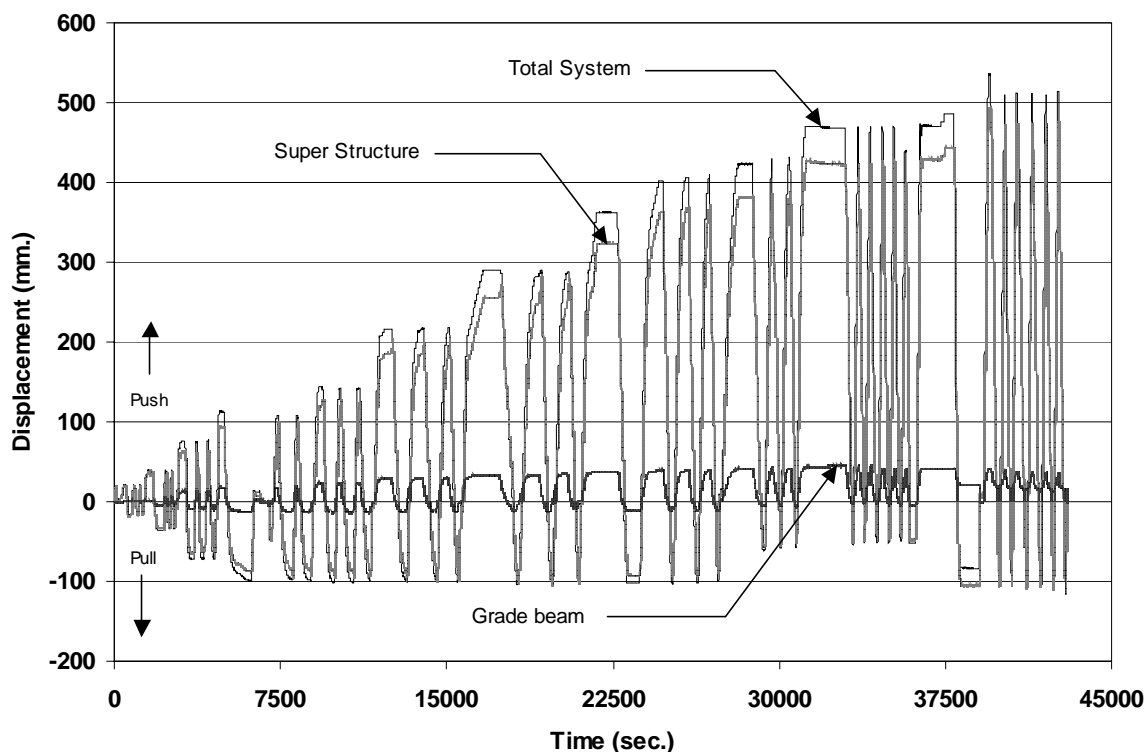


Figure 4.41 Total System, Superstructure, and Grade Beam displacements for the complete test of Bent #6S (2000)

Table 4.3 Total, superstructure, and grade beam horizontal displacements for the 1998 and 2000 tests

<u>Bent</u>	Total System		Super Structure		Grade Beam	
	Push (mm)	Pull (mm)	Push (mm)	Pull (mm)	Push (mm)	Pull (mm)
Bent #6N 1998	265	-264	N/A	N/A	N/A	N/A
Bent #5S 2000	206	-286	165	-253	41	-33
Bent #6S 2000	536	-104	494	-90	42	-14

Vertical Displacements

Three vertical columns of DT's were placed on the West end of Bent #6 to monitor any vertical deformation change during the test. The instrument set-up and locations can be reviewed in Figures 4.38 and 4.39. During the test, it was observed that there was a consistent increase in length at all three vertical instrument locations. The increased deformation can be explained as follows: First it was observed after the test, when the reinforcement concrete cover was removed, that the vertical column bars on the West column had slipped. Even after the bent's columns had been brought back to a vertical level, there was a 16 mm gap found at the top of the column longitudinal reinforcement that terminated in the West column-cap beam joint as shown in Figure 4.42. The vertical displacements of the West portion of Bent #6S are shown in Figures 4.43 - 4.46.

The total vertical displacement, from DT 8 and 2, for the West column of the superstructure was 52 mm as shown in Figure 4.45. The displacement difference between the

total displacement and the 16mm gap found in the joint region was 36mm. The additional 36mm displacement came from two conditions: yielding of the longitudinal bars in the column, at the plastic hinges, and slippage of the 0.76 m length longitudinal stub-in reinforcement in the lap splice located at the bottom of the column, shown in Figure 4.7.

All three vertical DTs showed similar displacements and it can be inferred that vertical displacements occurred on the East column as well. Slippage of the longitudinal bars located at the top and bottom joints of all three columns led to a significant reduction in stiffness for the bent structure. After the peak load capacity of the bent was reached, the lateral force capacity continued to decrease with additional drift. The top and bottom column connections were not considered to be totally fixed for the drift increase after the lateral peak load had been reached. As the drift increased, all three-column top connections were developing into complete pin connections. Also, there was a difference of 18 mm vertical displacement between the total system and the super structure. The additional displacement was accounted for by yielding in the piles (Cook et al. 2002).



Figure 4.42 West column-cap beam joint showing a permanent 16mm gap in the longitudinal column bars

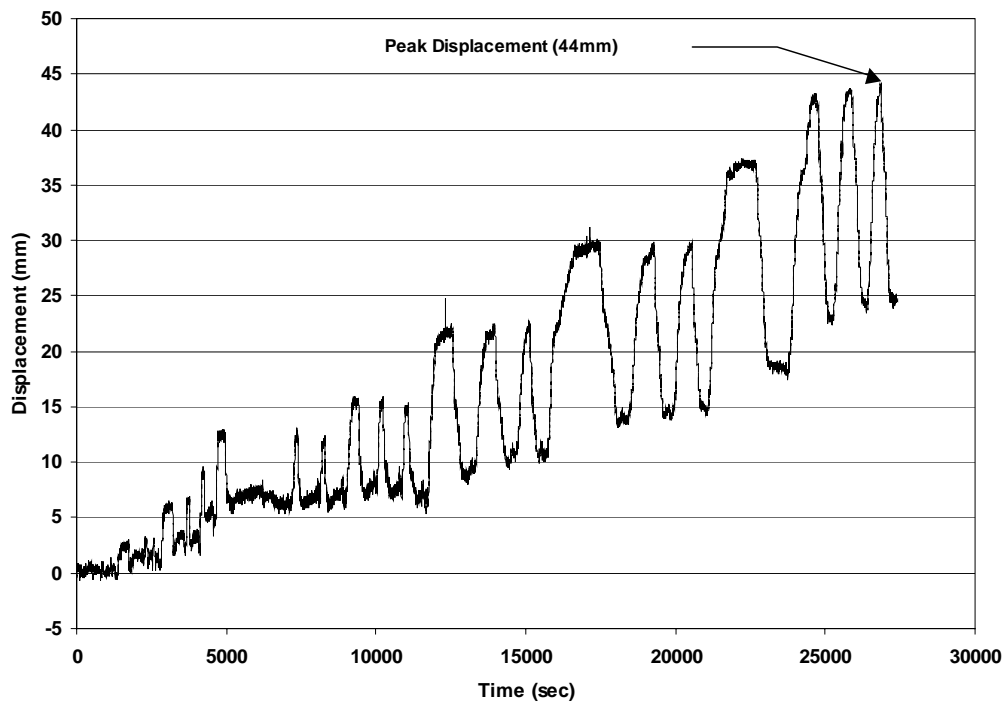


Figure 4.43 Permanent vertical deformation of the superstructure on the middle column (DT12), Bent #6S 2000 test on Saturday 6 May 00

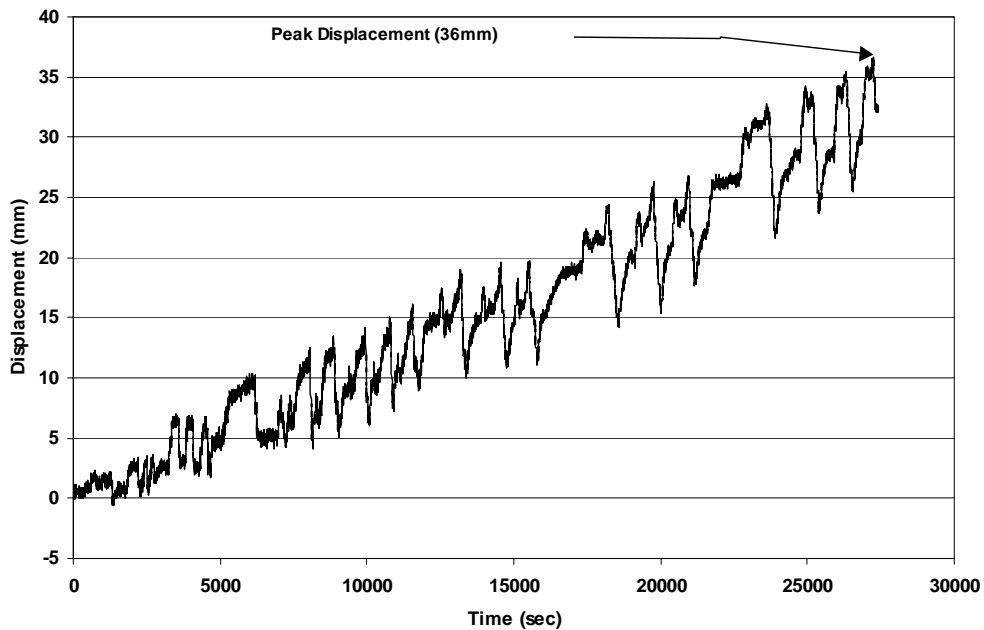


Figure 4.44 Permanent vertical deformation of the superstructure on the center span of the West portion (DT 5), Bent #6S test on Saturday 6 May 00

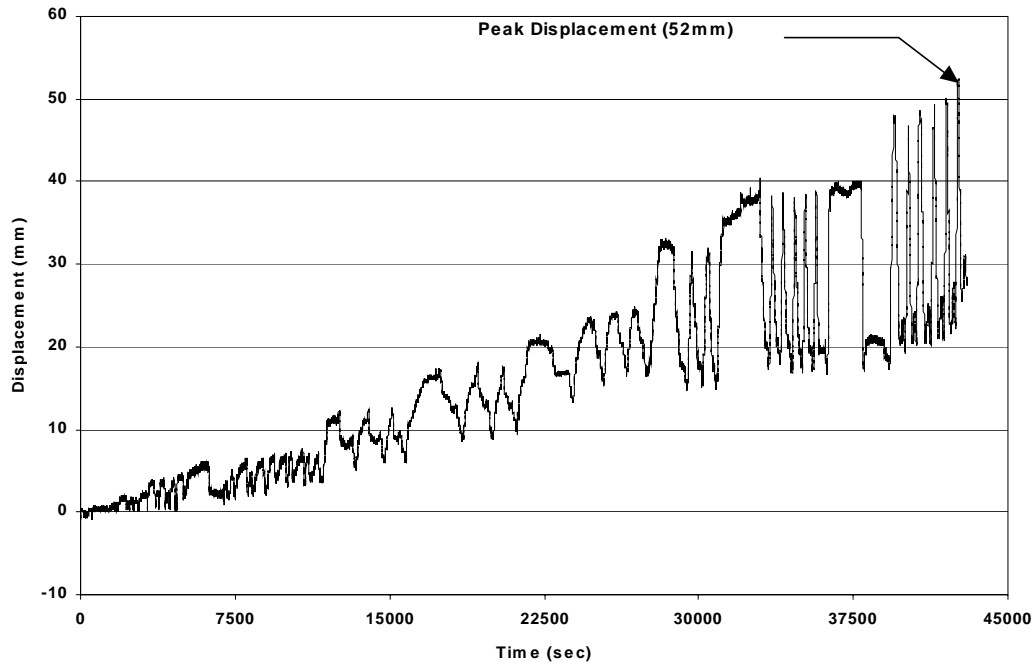


Figure 4.45 Total permanent vertical deformation of the superstructure on the West column Bent #6S 2000 test on (DT 8) and (DT 2), Saturday 6 May 00 and Tuesday 9 May 00

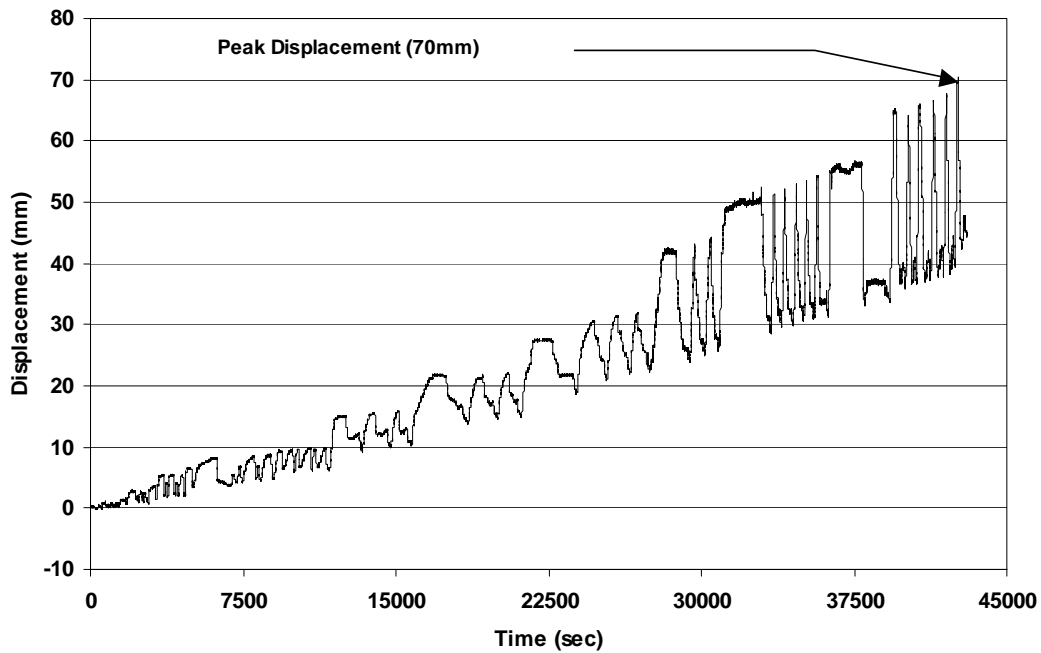


Figure 4.46 Total permanent vertical deformation of the total system on the West Column Bent #6S 2000 test on Saturday 6 May 00 and Tuesday 9 May 00

Hysteresis Curve Development

The standard approach for developing a hysteresis diagram is to take the cyclic forces and displacements from a quasi-static test and plot the force on the vertical axis against the displacement plotted on the horizontal axis. There were three basic needs for the development of a hysteresis relationship for the 1998 and 2000 tests. First, to develop force, displacement, and stiffness relationships. Second, to develop the displacement ductility of the structural system. Third, the hysteretic energy absorbed by a system can be evaluated by the definition of work. The area contained within one complete cycle describes the amount of energy capacity for one hysteresis loop. Therefore, the summation of all the areas contained in the complete hysteresis record describes the total energy absorption for an event.

Another observation is the symmetry of a hysteresis diagram with respect to the push-pull cycles. The symmetry for Bent #6N 1998, Bent #5S 2000, and Bent #6S 2000 tests can be visually estimated from Figures 4.47, 4.48, and 4.49. It is obvious that the Bent #6S 2000 CFRP composite and foundation retrofit was very successful by visually comparing it with the Bent #6N 1998 and Bent #5S 2000 tests; however, it was the most unsymmetrical.

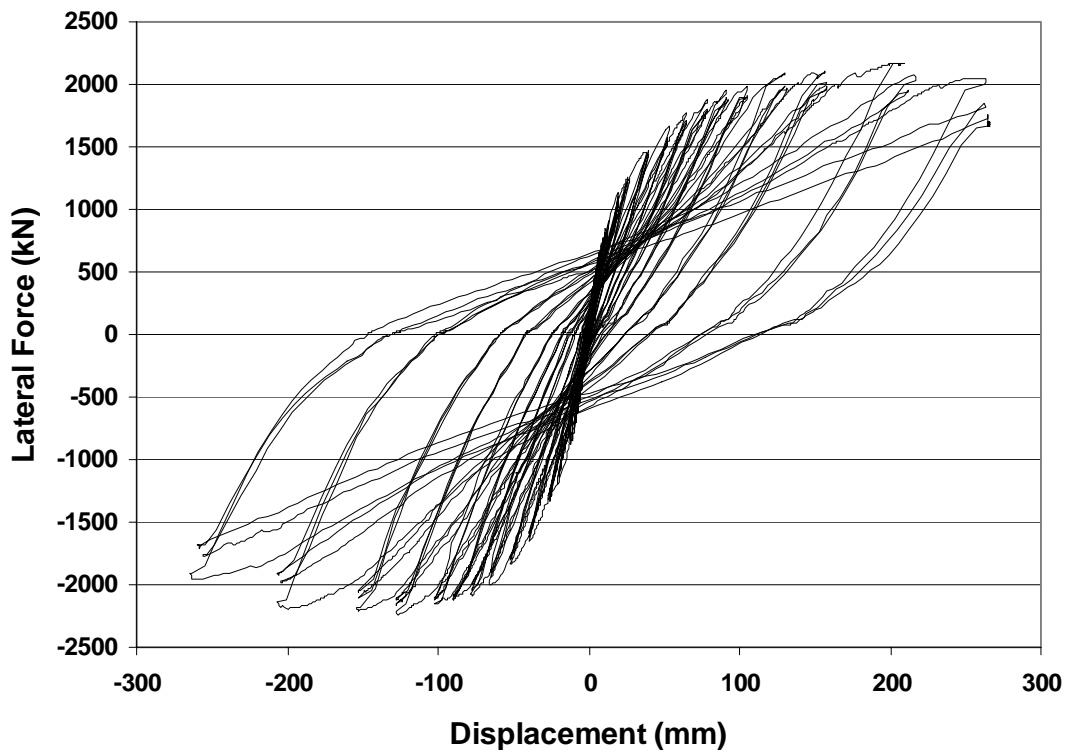


Figure 4.47 Hysteresis diagram for Bent #6N 1998 test

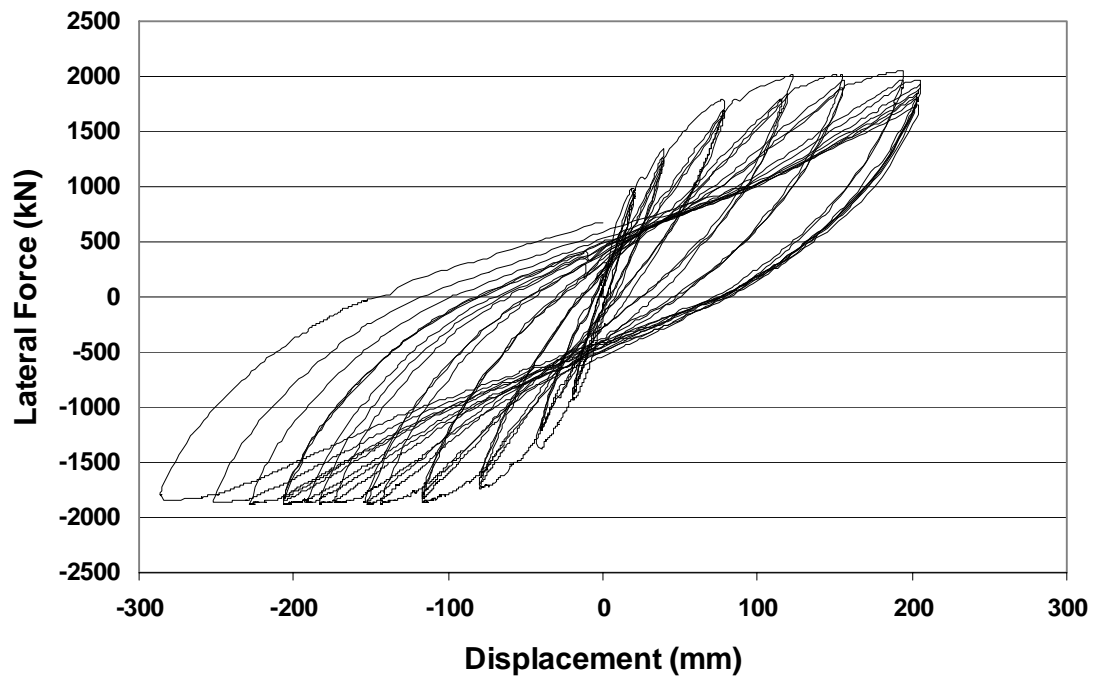


Figure 4.48 Hysteresis diagram for Bent #5S 2000 test

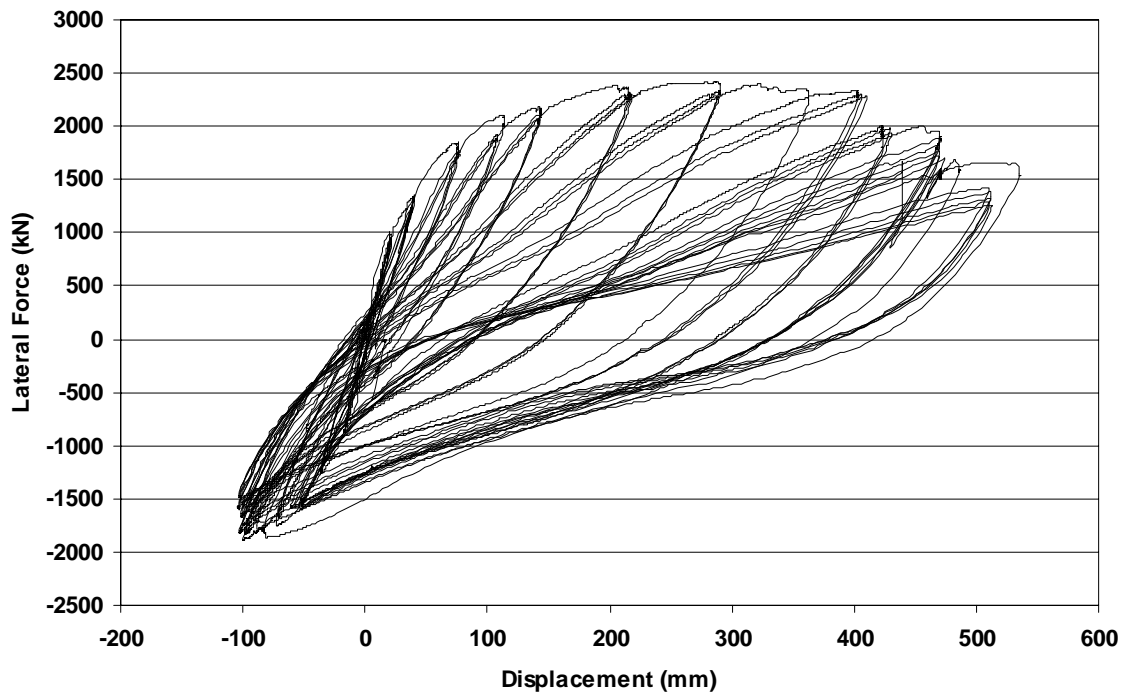


Figure 4.49 Hysteresis diagram for Bent #6S 2000 test

Force/Displacement Development

The development of the force/displacement curves involves the collection of the maximum displacements of the push/pull cycles. These displacement coordinates are matched up with their corresponding force, then averaged and plotted with the force representing the vertical axis and the displacement representing the horizontal axis. Because the Bent #6S 2000 test was unsymmetrical, special considerations needed to be made so that the skewed data was interpolated correctly. This was done with the weighted average equation, which can also be applied to symmetric loading as well.

A piecewise natural cubic spine, defined as $S(x)$, was used to plot the mean average maximum push/pull coordinates for the 1998 and 2000 tests. The lateral forces found from the weighted average equation are defined as H_i ; discrete grouped packets were defined by visual inspection and their coordinates were averaged for each group. A piecewise polynomial $S(x)$ was constructed from the grouped data coordinates to interpolate an average of the experimental maximum push/pull cycles. The interpolating polynomial $S(x)$ was weighed against the experimental extrapolated lateral force data, defined as $F(x)$ for a single variant error analysis (Duffin 2003).

A coefficient of determination (r^2) was used in the analysis and was held to a fit goal of $r^2 \geq 0.90$, on the interval of $0 \leq r^2 \leq 1$. Plots of the total system Bent #6S 2000, the superstructure for Bent #6S 2000, the push cycles only for the total system, the pull cycles only for the total system, the total system for Bent #6N 1998, and the total system for Bent #5S 2000 are shown in Figures 4.50-4.55 and Table 4.4.

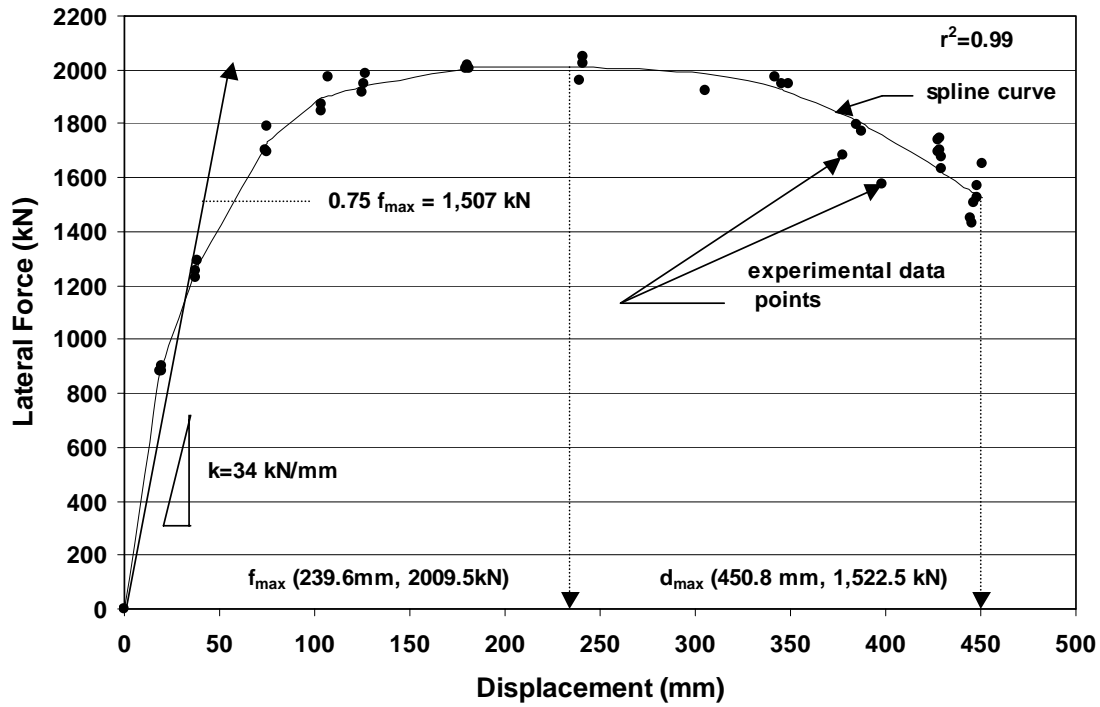


Figure 4.50 Force/displacement plot of the total system of Bent #6S 2000 test interpolated by weighted average method

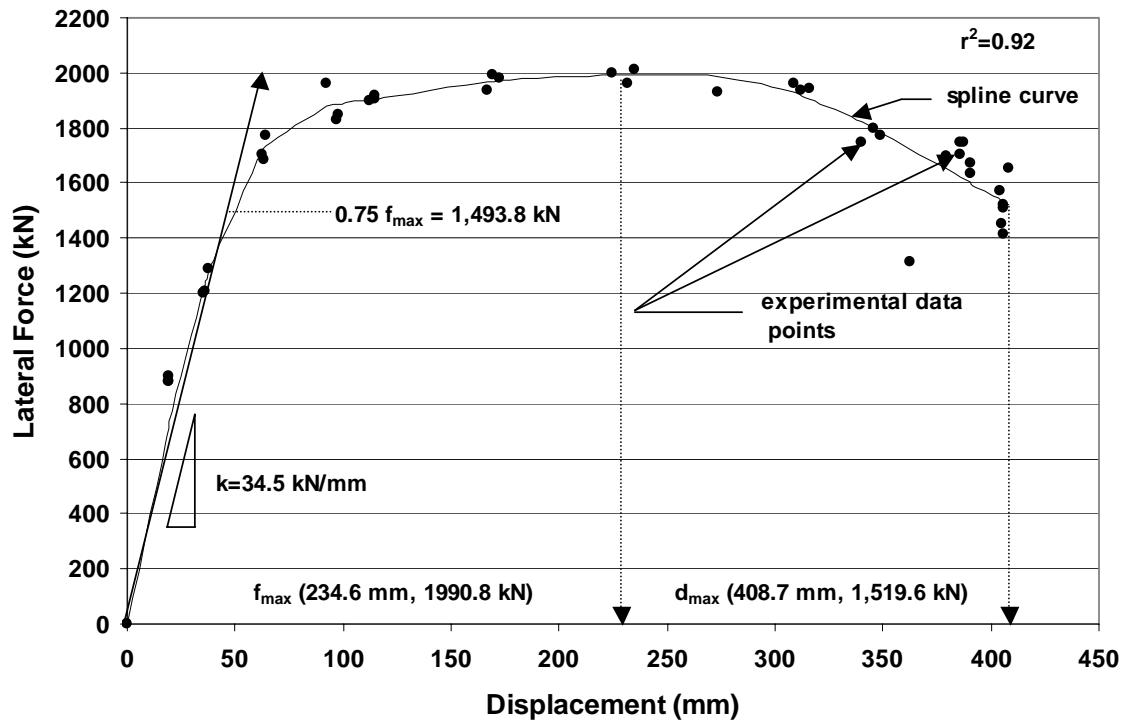


Figure 4.51 Force/displacement plot of the superstructure of Bent #6S 2000 test interpolated by weighted average method

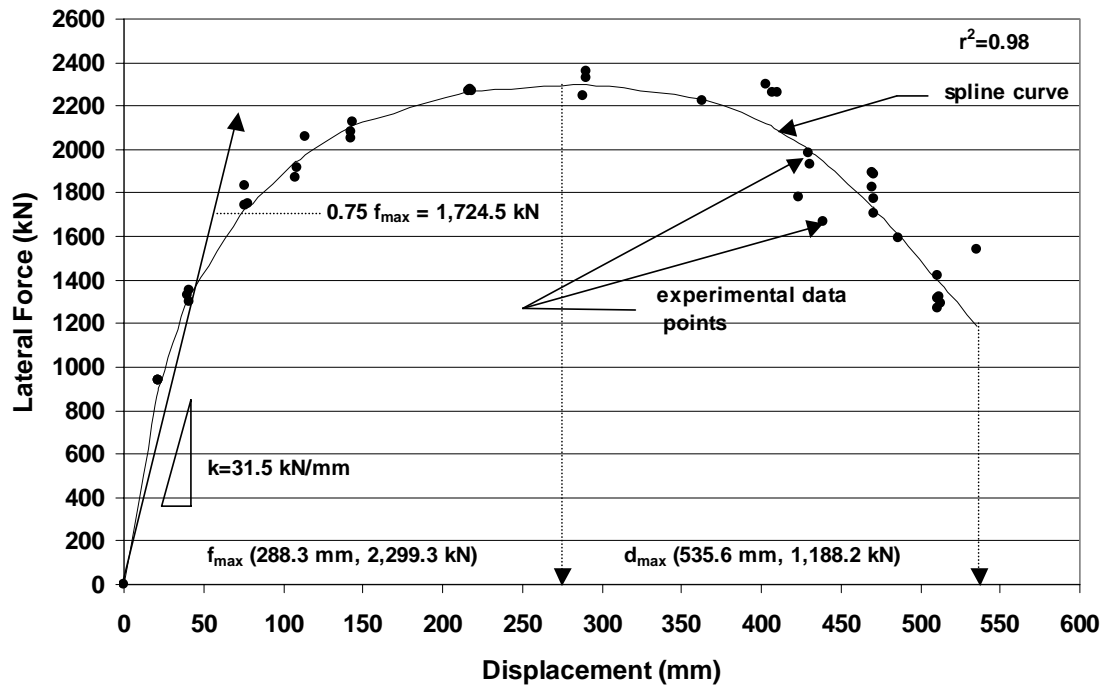


Figure 4.52 Force/displacement plot of the total system of Bent #6S 2000 push cycles only interpolated by weighted average method

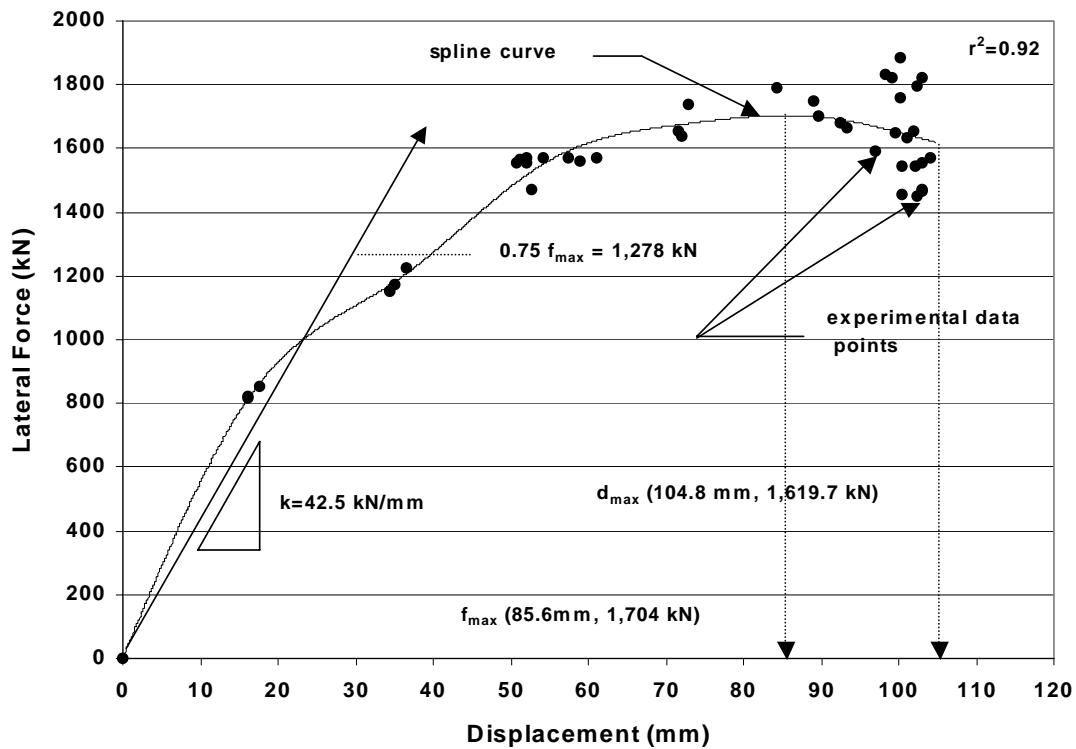


Figure 4.53 Force/displacement plot of the total system of Bent #6S 2000 pull cycles only interpolated by weighted average method

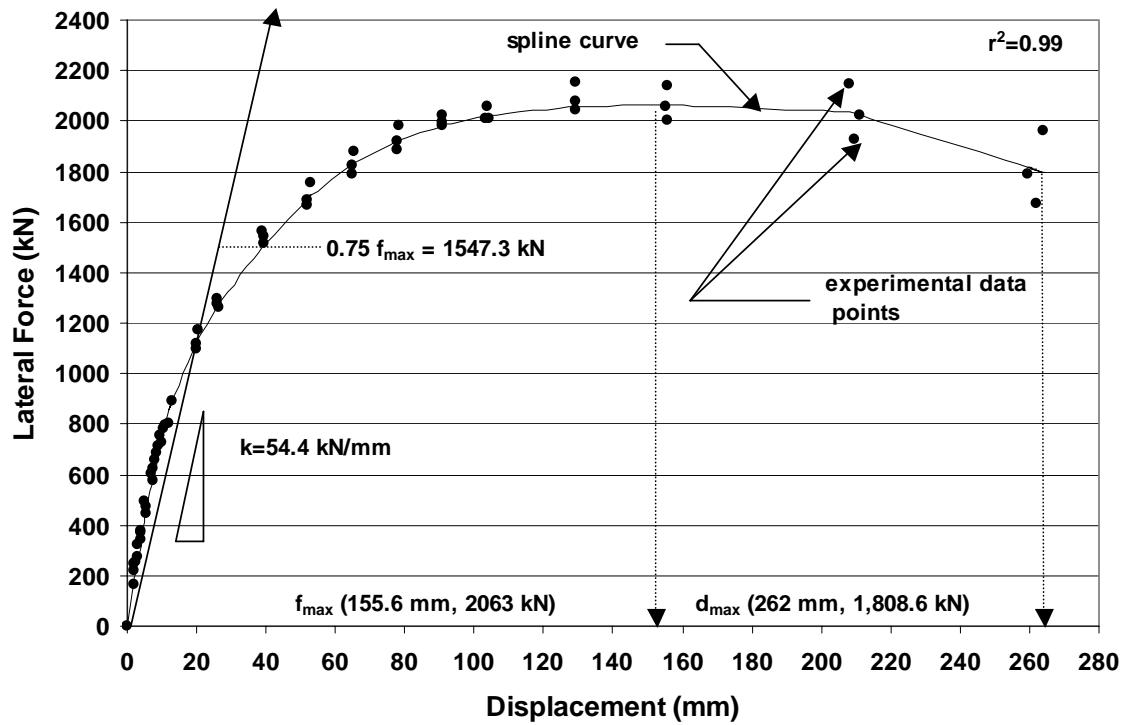


Figure 4.54 Force/displacement plot of the total system of Bent #6N 1998 test interpolated by weighted average method

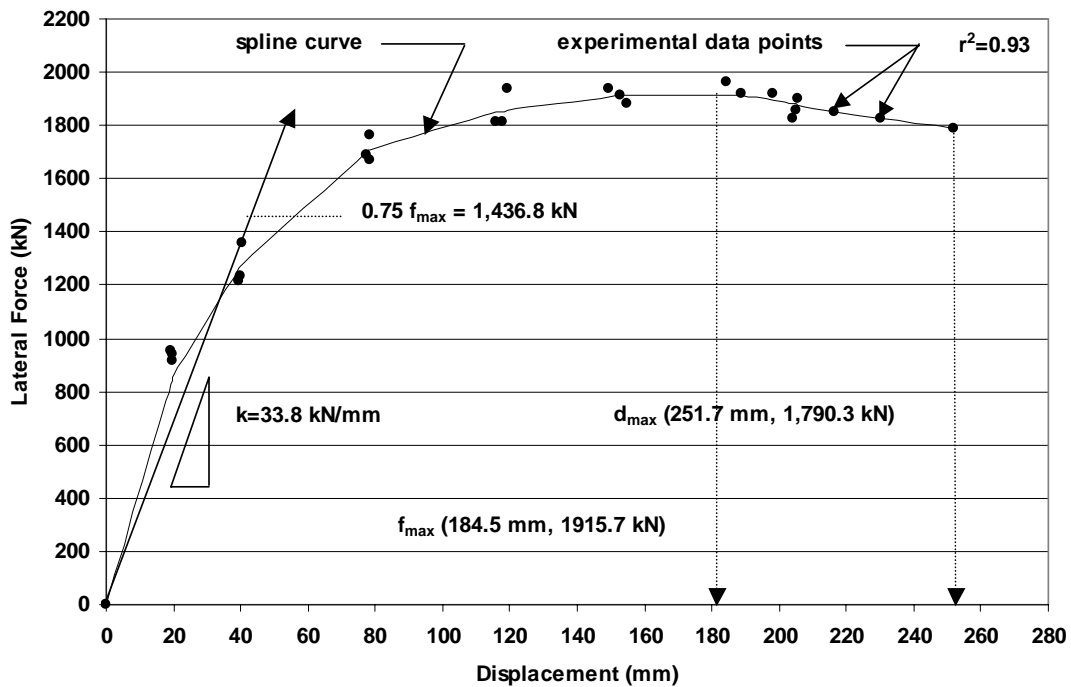


Figure 4.55 Force/displacement plot of the total system of Bent #5S 2000 test interpolated by weighted average method

Table 4.4 Load, stiffness, and displacement data for Figures 4.50–4.55

Bent Structure	Stiffness	Experimental at F_{max}		Spline at $S(x)_{max}$		Experimental at d_{max}		Spline at d_{max}	
	k (kN/mm)	d (mm)	F_{max} (kN)	d (mm)	$S(x)_{max}$ (kN)	d_{max} (mm)	F (kN)	d_{max} (mm)	$S(x)$ (kN)
Total System Bent #6 2000	34.0	241.3	2046.0	239.6	2009.5	450.8	1652.5	450.8	1522.5
Superstructure Bent #6 2000	34.5	234.7	2009.0	234.7	1990.8	408.7	1652.5	408.7	1519.2
Total System Bent #6 2000 Push	31.5	290.5	2362.6	288.3	2299.3	535.6	1542.0	535.6	1188.2
Total System Bent #6 2000 Pull	42.5	104.0	1884.0	85.6	1704.0	104.1	1570.4	104.8	1619.7
Total System Bent #6 1998	54.4	129.0	2151.0	155.6	2063.0	262.0	1670.7	262.0	1808.6
Total System Bent #5 2000	33.8	184.5	1960.3	184.5	1915.7	251.7	1790.3	251.7	1790.3

Discussion of Figures 4.50-4.55 and Table 4.4

The natural cubic spline interpolation polynomial was used in all six force/displacement curves (Duffin 2003). The spline curves were well behaved and represented the average experimental data very well. The goal of $r^2 \geq 0.90$ was easily attained and made it possible to extract other valuable information such as force/displacement relationships and the stiffness of the bent structures.

Stiffness of Structures

The stiffness shown in Figures 4.50-4.55 is an interpolated best fit line fitted to the spline curves with the yielding point of all the structures to be approximately $0.75 S(x)_{max}$ in reference to the procedure suggested by Légeron and Paultre (2000). In Table 4.4 it can be seen that the stiffness (k) for the total structure Bent #6S 2000, the superstructure Bent #6S 2000, and the total structure Bent #5S 2000 are almost identical values 34.0kN/mm, 34.5kN/mm, and 33.8kN/mm respectively. The only design difference between the total structure Bent #6S 2000 and the total structure Bent #5S 2000 test was that Bent #6S had been retrofitted with CFRP composite. This shows that the CFRP retrofit design did not significantly influence the initial stiffness of the structure. The major damage observed in the bent structure was localized at the top and bottom column plastic hinge and joint regions. The degradation in the structure's stiffness is directly related to the bar slippage in the top and bottom column joints as discussed earlier in the vertical displacement section.

Bent #6N 1998 test had the highest initial stiffness $k = 54.4$ kN/mm as shown in Table 4.4. The additional stiffness was due to the fact that the foundation system was tied to the load frame foundation with a continuous horizontal concrete strut for compression and Dywidag bars to take the tension as shown in Figure 4.5. The Bent #6N 1998 foundation system was designed to minimize rotations and displacements in the foundation system and proved to be successful.

The pull cycles were not fully developed for the displacement and loading for the Bent #6S 2000 test. As explained earlier in this Chapter, the load frame was moved forward to ensure that at least the push cycle loading would drop below 80% of F_{max} ; this and the flexibility of the load frame foundations made it impossible to fully develop the pull cycles. Also, the actuator maximum pull capacity was 1884kN and was approximately the maximum demand load placed on the actuator during the Bent #6S 2000 test. It was observed that the highest demand in the pull direction was 1,884kN at 100mm and 2,363kN at 290.5mm as shown in Figures 4.52 and 4.53. The pull demand was 80% of the push demand and is reflected in the differences found in the stiffness values that have been interpolated in Figures 4.52 and 4.53.

A plot of the stiffness degradation of the total system Bent #6S 2000, total system Bent #6S push only cycles, superstructure Bent #6S 2000, Bent #6S pull only cycles, superstructure Bent #6S 2000 total system, Bent #6N 1998, and total system Bent #5S 2000 are shown in Figure 4.56. In Figure 4.56 it can be observed that in all three bent structures the stiffness degraded at a consistent rate. Two anomalies that can be observed in Figure 4.56 are the high initial stiffness of Bent #6N 1998 and the large displacements in the Bent #6S 2000 tests as discussed earlier.

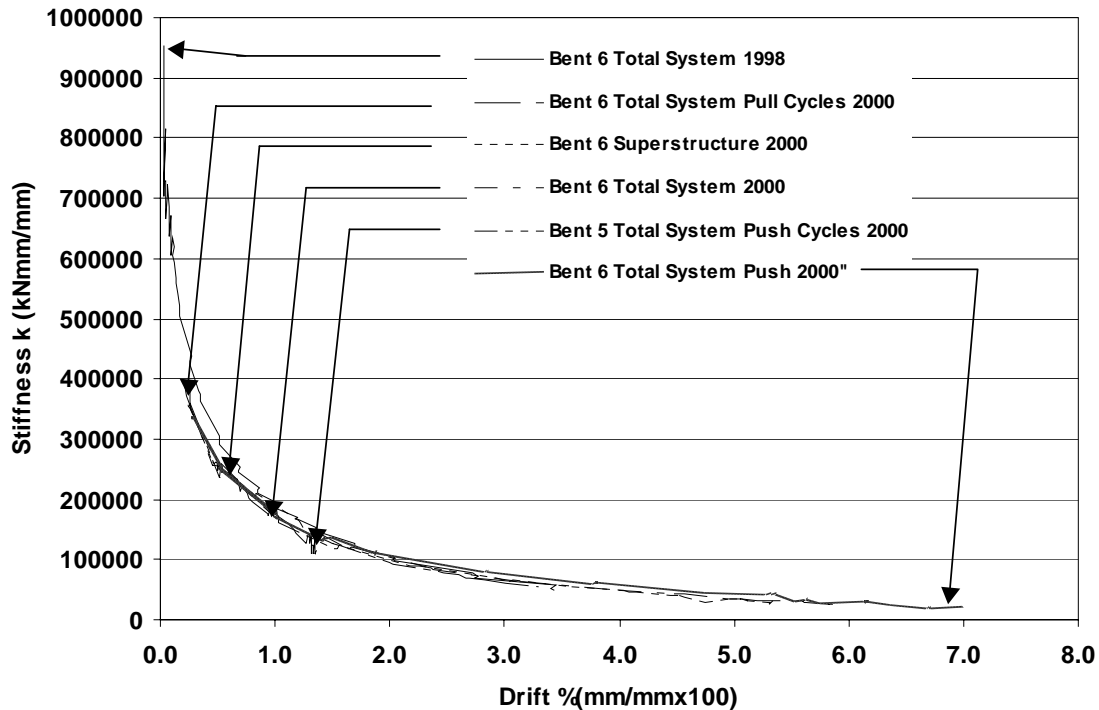


Figure 4.56 Degradation of the total system Bent #6N 1998, and total system Bent #6S 2000 pull cycles, superstructure Bent #6S 2000, total system Bent #6S 2000, total system Bent #5S 2000, and total system Bent #6S 2000 push cycles

Peak Horizontal Load Considerations

The F_{\max} maximum lateral load and displacement values found in the three tests Bent #6N 1998, Bent #5S 2000, and Bent #6S 2000 tests were (155.6mm, 2,151kN), (184.5mm, 1,960kN), and (288.3mm, 2,362.6kN). These displacements and load capacities can be directly related to the CFRP composite and foundation retrofit. Bent #6S 2000 had the largest load capacity relative to Bent #6N 1998 and Bent #5S 2000 with a percent increase of 9% and 17%, respectively. The load 9% increase from the Bent #6N 1998 to the Bent #6S 2000 tests is due to the stiffness increase provided by the U-straps applied to the column-cap beam joints. The CFRP composite application for Bent #6N 1998 was a dry lay-up and there was verification of some dry fibers found in the post-test specimens. The stiffer foundation system leads to additional stresses in the lap splice joints located at the bottom of the columns and can contribute to premature reinforcement debonding in this region.

Peak Horizontal Displacement Considerations

The maximum displacement, d_{\max} reached for Bent #6S 2000 was 535.6mm, for Bent #5S 2000 was 251.7mm and for Bent #6N 1998 was 262mm. The percentage loss of the applied force was 48% for Bent #6S 2000, 6.6% for Bent #5S 2000, and 12% for Bent #6N 1998.

Bent #6S 2000 has the largest displacement and the highest strength degradation, but overall was the most successful and its success is best represented in terms of displacement ductility that can be seen in the next section. Once again the foundation design of Bent #6N 1998 can be seen to cause premature failure due to a rigid foundation. A plot of Bent #6S 2000 mean average, Bent #6S 2000 push cycles only, Bent #5S 2000 as-built, and Bent #6N 1998 are shown for the $S(x)$ (spline average curves) in Figure 4.57. The initial stiffness k , maximum average load $S(x)_{\max}$, and the maximum displacement d_{\max} can be visually compared between the 1998 and 2000 tests.

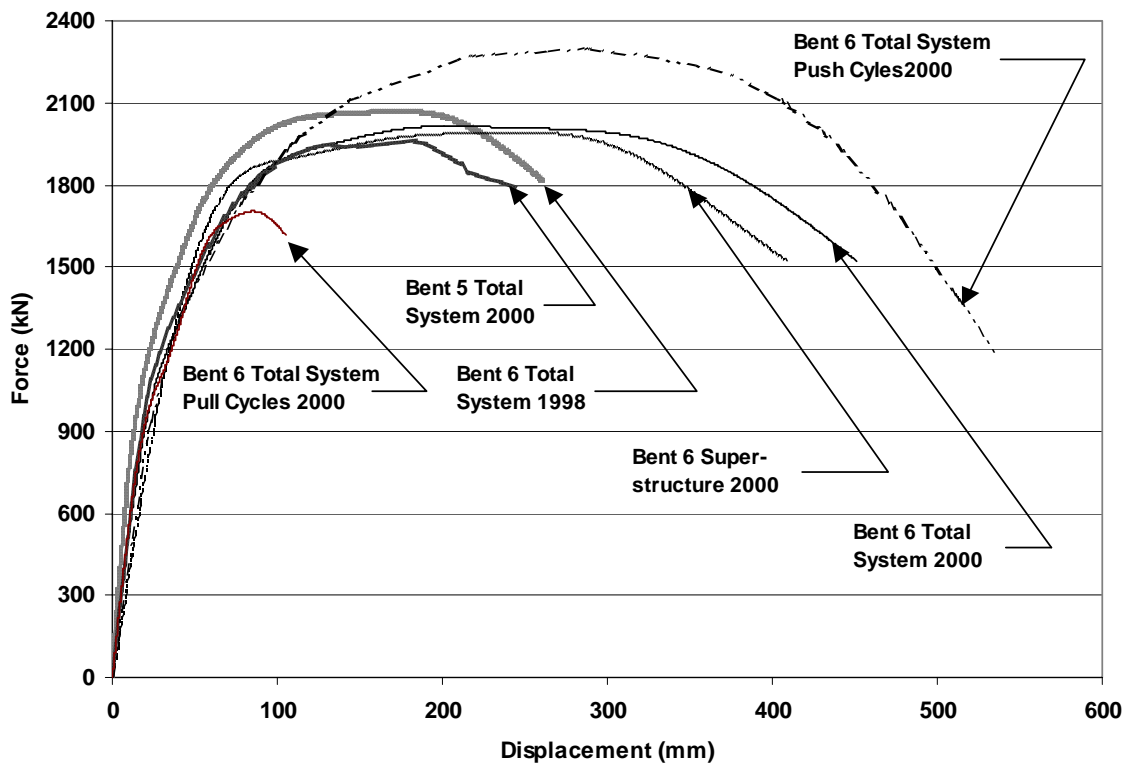


Figure 4.57 Average spline curves for the total system Bent #6N 1998, total system Bent #6S 2000 pull cycles, superstructure Bent #6S 2000, total system Bent #6S 2000, total system Bent #5S 2000, and total system Bent #6S 2000 push cycles

Ductility Relationships for Bent #5S, #6S (2000) and Bent #6N (1998)

The method used in this analysis for defining displacement ductility is a bilinear model. This approach is similar to Légeron and Paultre (2000). Six ductility curves are compared that include the total system Bent #6S 2000 mean average, the total system Bent #6S 2000 push cycles only, the total system Bent #6S pull cycles only, the superstructure Bent #6S 2000 mean average, the total system Bent #5S 2000, the total system Bent #6N 1998, as shown in Figures 4.58 - 4.63; their ductility values are listed in Table 4.5.

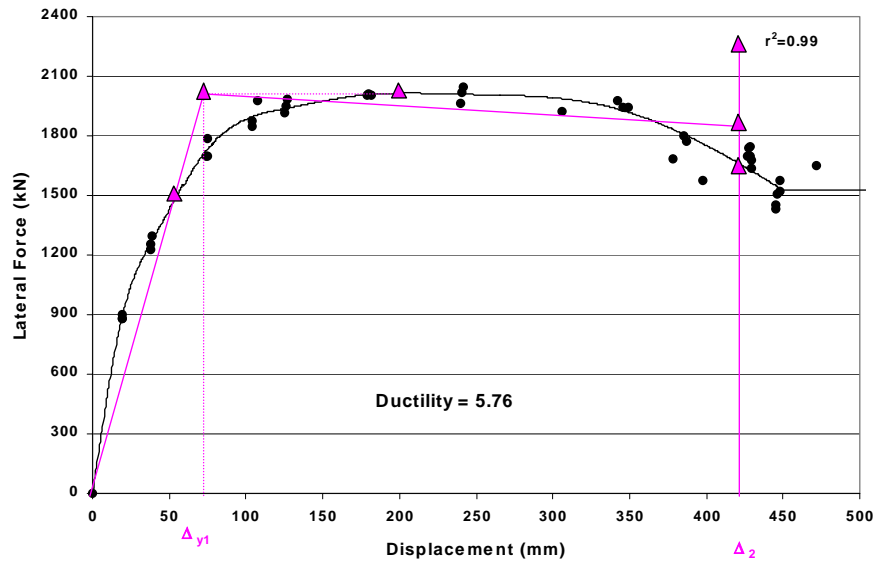


Figure 4.58 Total system Bent #6S 2000 mean average displacement ductility curve

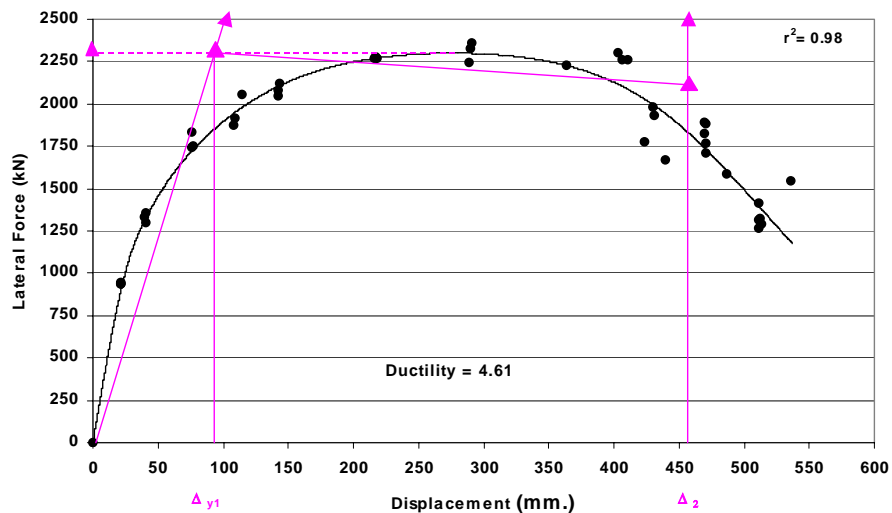


Figure 4.59 Total system Bent #6S 2000 push cycles only displacement ductility curve

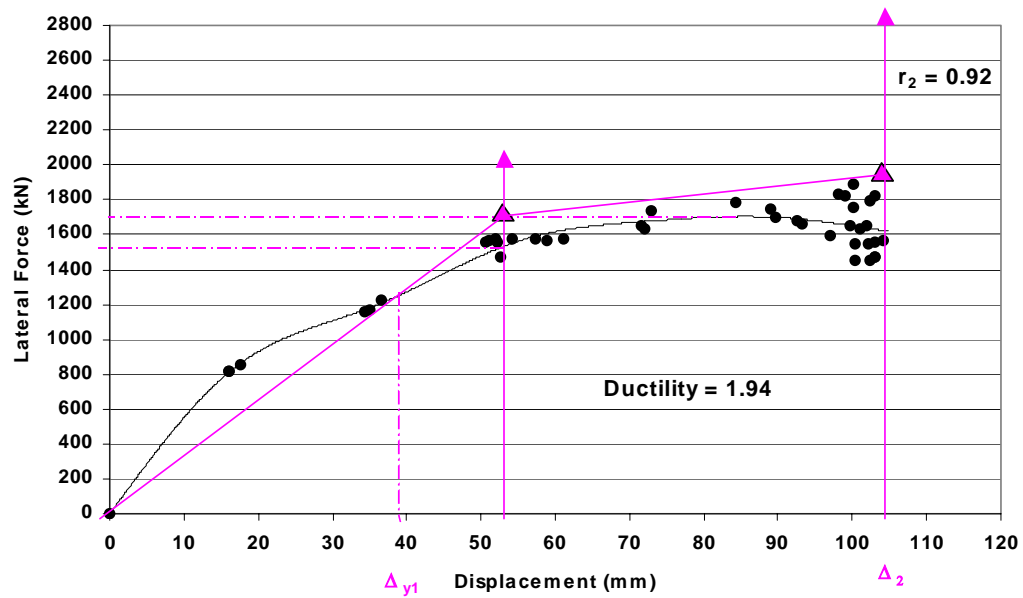


Figure 4.60 Total system Bent #6S 2000 pull cycles only displacement ductility curve

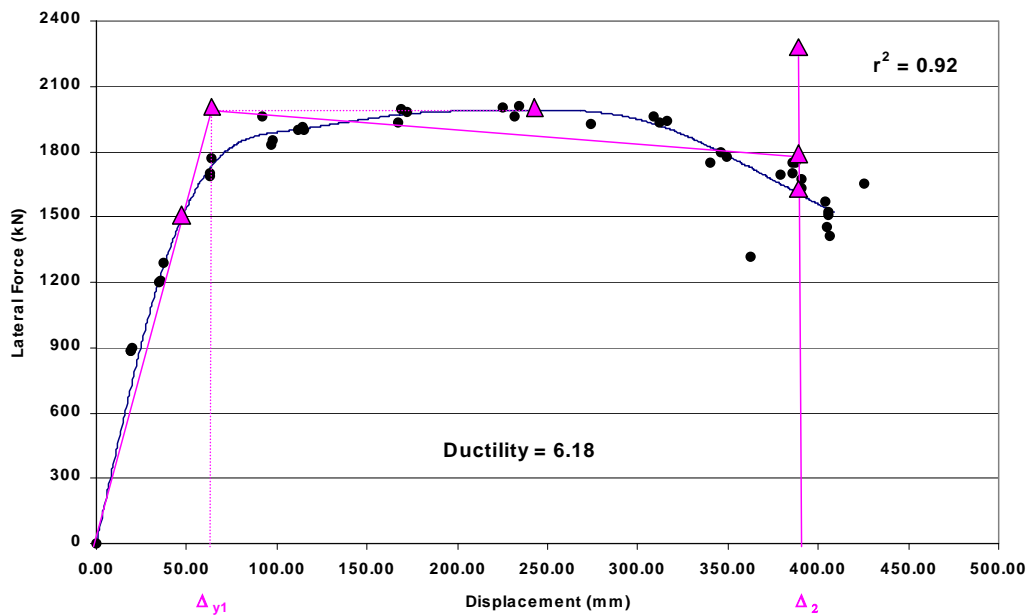


Figure 4.61 Superstructure Bent #6S 2000 mean average displacement ductility curve

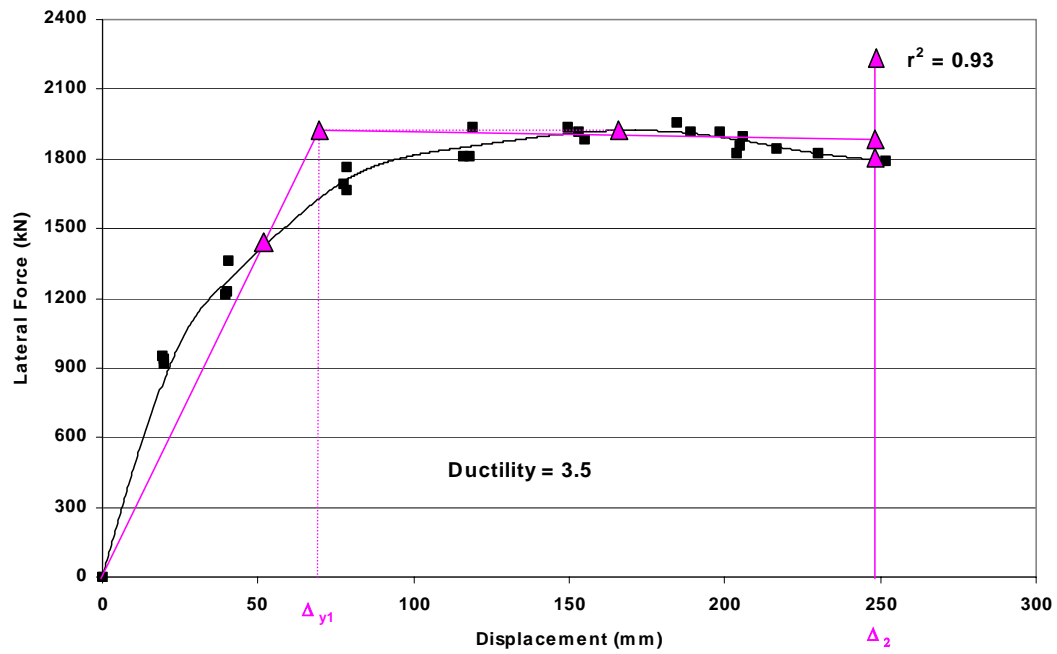


Figure 4.62 Total system Bent #5S 2000 displacement ductility curve

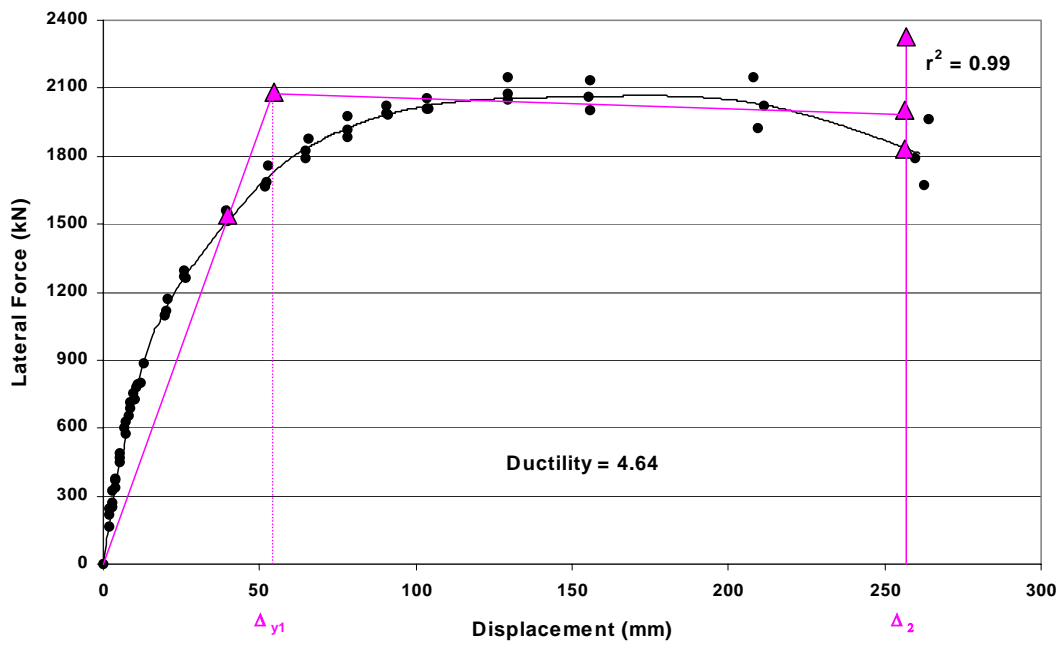


Figure 4.63 Total system Bent #6N 1998 displacement ductility curve

Table 4.5 Displacement ductility values for the 1998 and 2000 tests

	Tot. Bent #6 00	Tot. Bent #6 00 Push	Tot. Bent #6 2000 Pull	Super Structure Bent #6 00	Tot. Bent #5 00	Tot Bent #6 98
Ductility	5.76	4.61	1.94	6.18	3.5	4.64

Discussion of Figures 4.58-4.63 and Table 4.5

As discussed previously, the total system Bent #6S 2000 was tested using an unsymmetrical loading and special procedures were used to interpolate the experimental data. A weighted mean averaging method was developed to compare the unsymmetrical test against the symmetrical Bent #5S 2000 and Bent #6N 1998 tests (Duffin 2003). The Bent #6S 2000 test displacement ductility was 1.24 times larger than the Bent #6N 1998 test. This was directly related to the improved foundation system used in the Bent #6S 2000 test vs. the rigid foundation system used in the Bent #6N 1998 test. The CFRP composite retrofits were almost identical with three exceptions. First, there was a dry lay-up application used in the 1998 test vs. a wet lay-up application applied used in the 2000 test. Second, two applications of zero degree CFRP composite layers were applied to the bent cap in the East and Center column-cap beam joints. Third, the CFRP composite U-strap width in the Bent #6S 2000 test was increased. These three differences have influenced the ductility increase as well.

The Bent #6S 2000 displacement ductility was 1.65 times that of the Bent #5S 2000 test. Since both bent structures are typical, with the exception that Bent #6S was retrofitted with CFRP composites, the improvement made by the CFRP composite strengthening was exclusively responsible for the ductility increase. There is however some discrepancy between the Bent #5S and Bent #6S ductility definition. It should be noted that in the Bent #5S 2000 test, the maximum load $S(x)_{\max}$ dropped only 6.6% during the entire test, and therefore the strict definition of ductility is not applicable; moreover it is not certain that the bent would survive a 20% drop in the lateral load.

In the push and pull cycle ductility diagrams for Bent #6S (2000), the ductility values are 4.61 and 1.94, respectively. The low pull ductility 1.94 is directly related to an undeveloped force displacement, as stated earlier. Due to the unsymmetrical loading in this test, the strain hardening in the reinforcement bars and the tension and shear cracking in the concrete were also unsymmetrical. Because of the unequal loading, the push and pull ductility diagrams of Figures 4.59 and 4.60 are unrelated to Figures 4.58, 4.61 - 4.63. However, comparisons shown in Figures 4.58 - 4.63 and Table 4.5 clearly show a significant ductility increase in the Bent #6S 2000 retrofitted structure relative the Bent #6N 1998 and Bent #5S 2000 structures.

Comparisons of Curve Fitting vs. FEMA 273

In this section, a comparison of the FEMA section 273 (BSSC 1997) section on Design Parameters and Acceptance Criteria has been made for the Push and Pull cycles of the Bent #6S 2000 test against the mean average spline $S(x)$ curve, representing the total hysteresis cycles for the complete test. The weighing procedure used here is a single variant method dependent on the experimental lateral force $F(x)$ (Duffin 2003). A 99% confidence interval using a student T-distribution has been plotted around $S(x)$ to weigh a curve fitting method proposed by FEMA 273. FEMA 273 recommends taking the intersection coordinate point between the i th and the $(i-1)$ cycle for each drift step. This is to be done for all drift increase steps over the entire test; then all points are to be connected by drawing lines

between the coordinate points to form a continuous curve representing the force/displacement diagram of the experiment, as shown in Figure 3.25. The 99% confidence intervals about $S(x)$ are visually compared to the FEMA 273 procedure as shown in Figures 4.65, 4.66, 4.68, and 4.69; these figures prove that the FEMA method is conservative. This is also reflected in the ductility analysis shown in Figures 4.64 and 4.67 as compared to Figures 4.59 and 4.60.

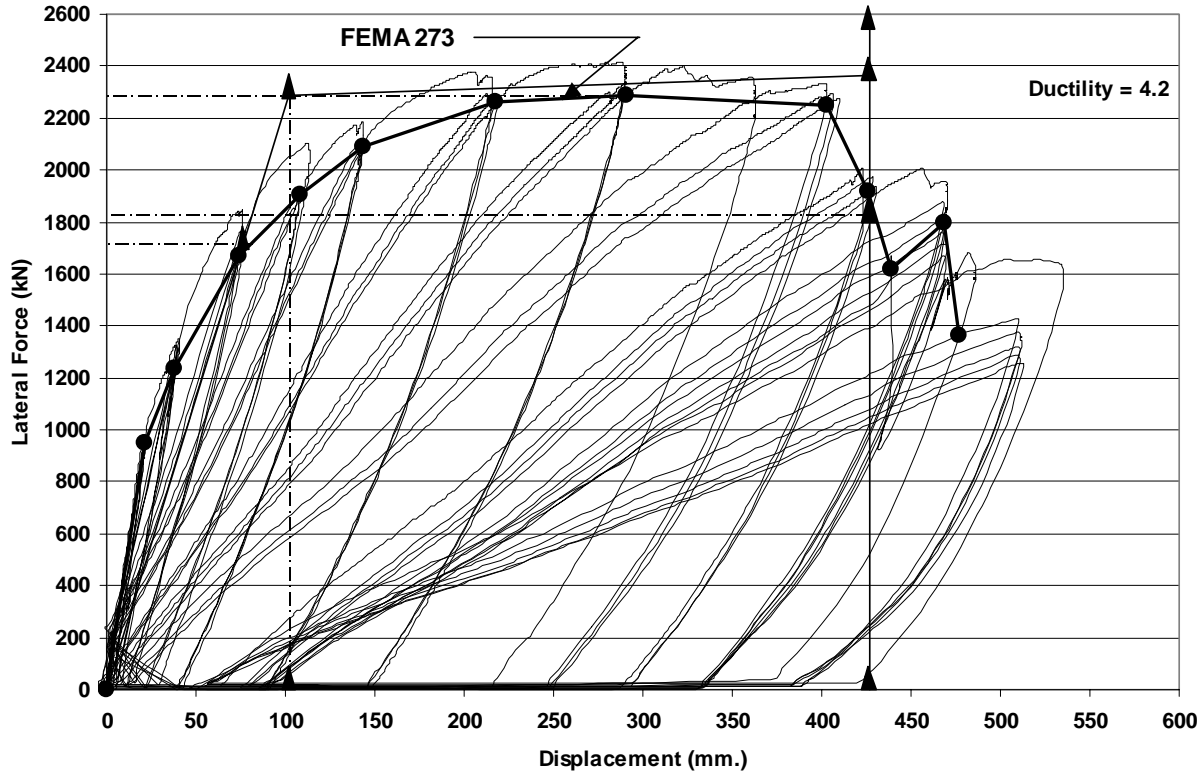


Figure 4.64 Push cycles of the backbone curve of the total system Bent #6S 2000 and the displacement ductility based on the FEMA guidelines

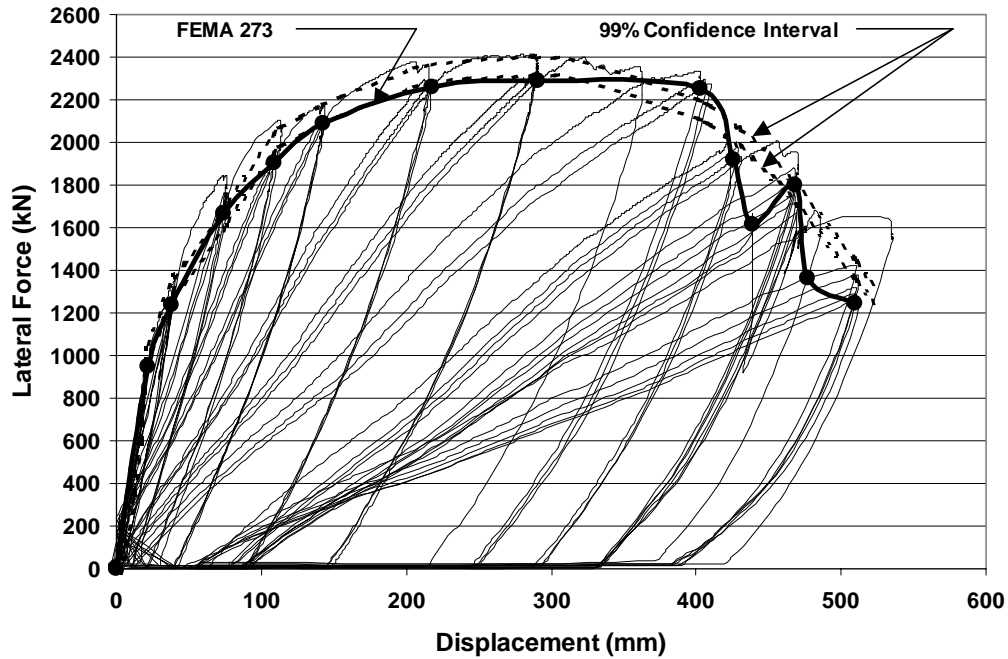


Figure 4.65 Push cycles of total system of FEMA curve and the 99% confidence intervals banded about $S(x)$ the mean average of the complete peak loads for Bent #6S 2000 test

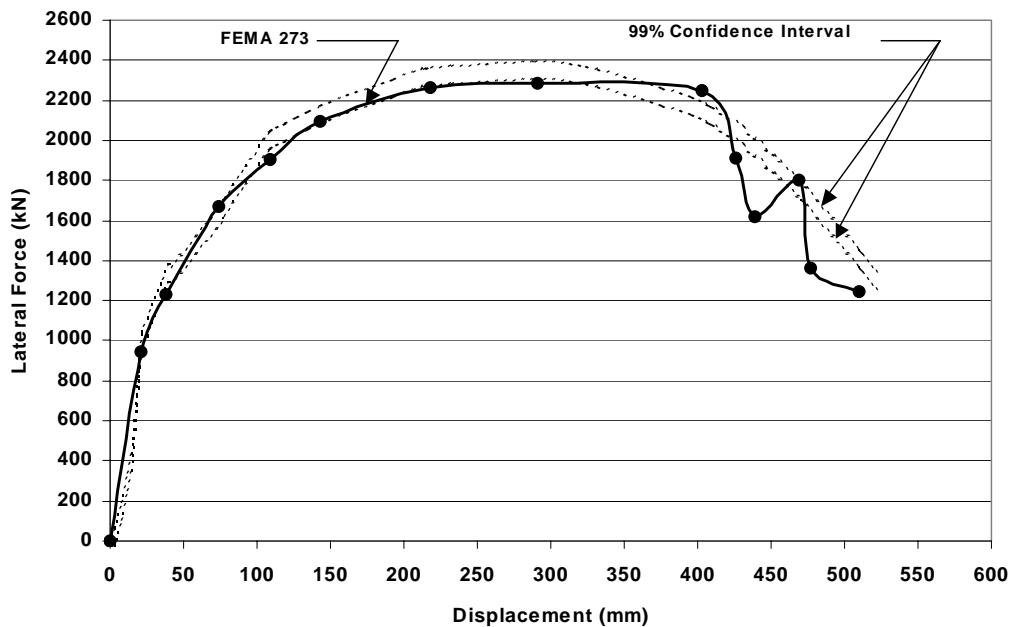


Figure 4.66 Push cycles of the 99% confidence intervals plotted around $S(x)$ the mean average of the peak vs. the recommended FEMA intersection points for the i th and the $(i - 1)$ cycles for each drift step

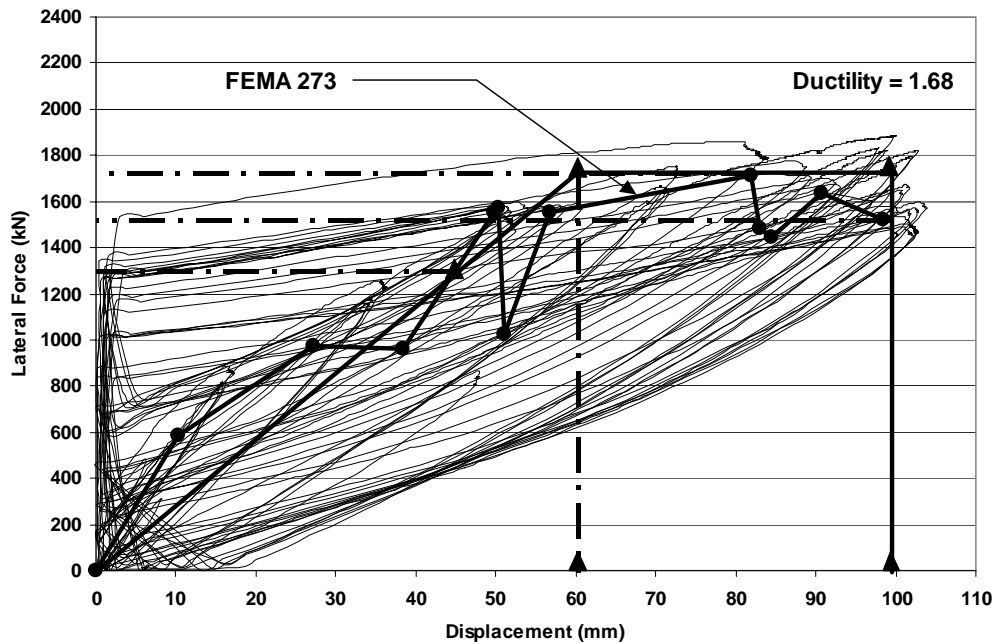


Figure 4.67 Pull cycles of the backbone curve of the total system Bent #6S 2000 and the ductility based on the FEMA guidelines

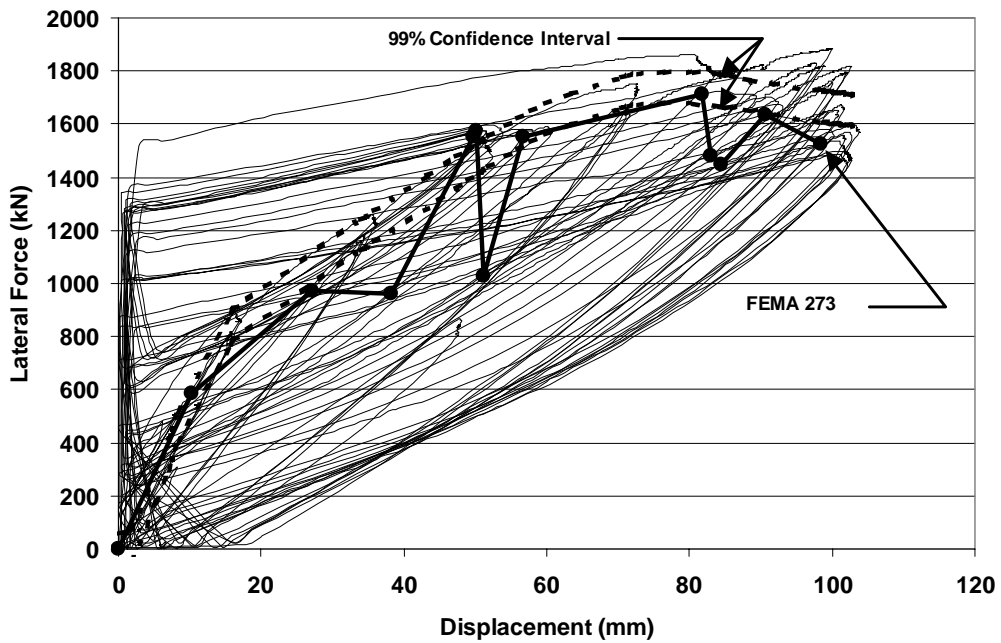


Figure 4.68 Pull cycles of total system of FEMA curve and the 99% confidence intervals banded about $S(x)$ the mean average of the complete peak loads for Bent #6S 2000

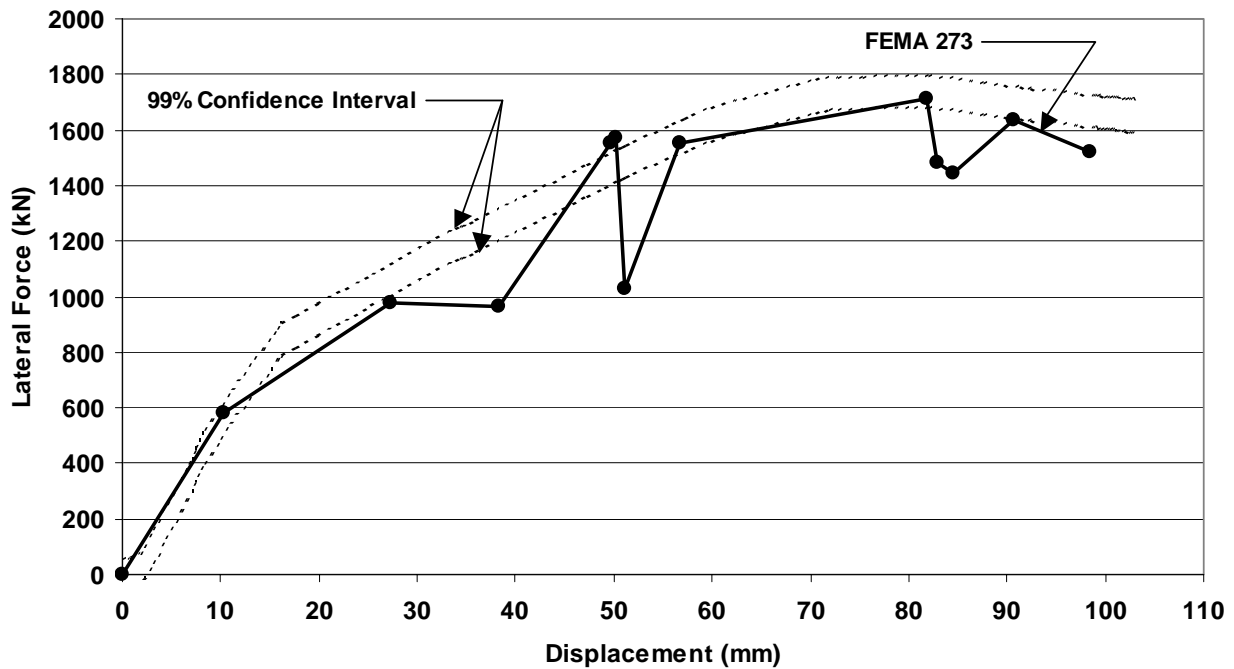


Figure 4.69 Pull cycles of the 99% confidence intervals plotted around $S(x)$ the mean average of the peak vs. the recommended FEMA intersection points for the ith and the $(ith - 1)$ cycles) for each drift step

FEMA 273 Observations and Recommendations

Observations made of the FEMA 273 curve fitting technique for force/displacement relationships show the FEMA 273 backbone to be too conservative and erratic. Also, with full-scale testing it is sometimes difficult to control the experiment to get idealistic experimental data. This was the case for Bents #4S, and #6S in the 2000 tests where the hysteresis loops were highly unsymmetrical and irregular. The spline method considers all three cycles for each drift increase representing all force/displacement points for a complete test, whereas the FEMA 273 curve fitting technique only considers the average between the 1st and 2nd cycles out of the three cycles for each drift step increment. It is recommended to use the spline fitting method shown in Figures 4.58 - 4.63, when highly skewed or irregular hysteresis loops are analyzed.

Energy Relationships

A comparison was made between the total system of Bent #6S 2000, superstructure Bent #6S 2000 (analytical model only), total system Bent #6N 1998, and total system Bent #5S 2000 tests, related to hysteretic energy dissipation. The energy of a system was defined earlier in this chapter and will be applied in this section to plot the energy per cycle for each structure. Figure 4.70 shows the hysteresis energy for the total system of Bent #6S 2000, and Figure 4.71 shows the hysteresis energy for the superstructure of the Bent #6S 2000 test. Figure 4.72 shows the hysteresis energy for the total system of Bent #6N (1998) and Figure 4.73 shows the hysteresis energy for the total system of Bent #5S (2000). A single plot showing the cumulative energy dissipation for the entire test duration for all four structures is shown in Figure 4.74.

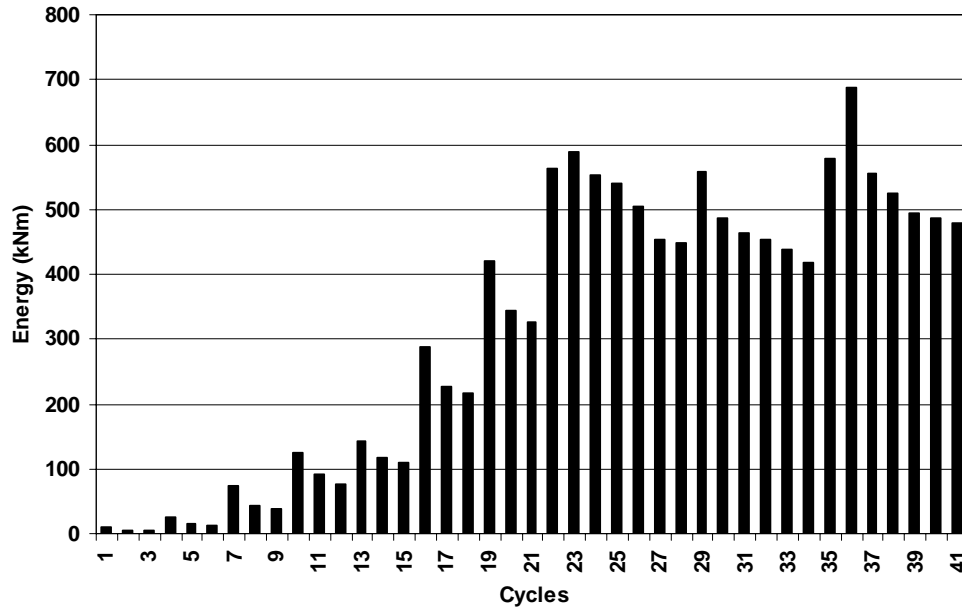


Figure 4.70 Hysteretic Energy absorbed for each cycle for the total system (Bent #6S 2000)

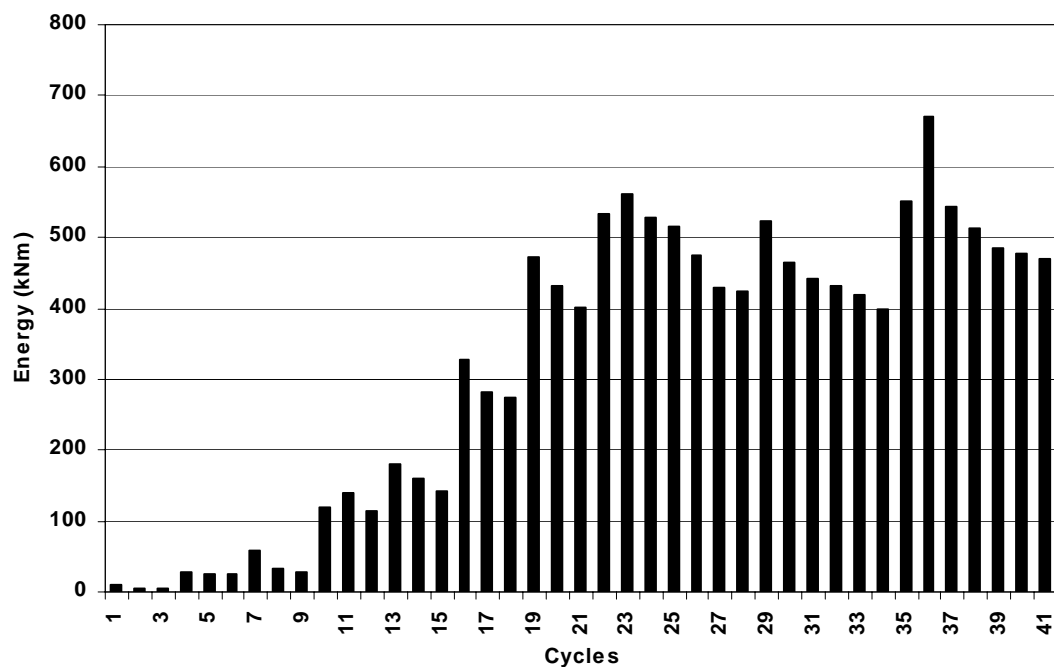


Figure 4.71 Hysteretic Energy absorbed for each cycle for the superstructure (Bent #6S 2000)

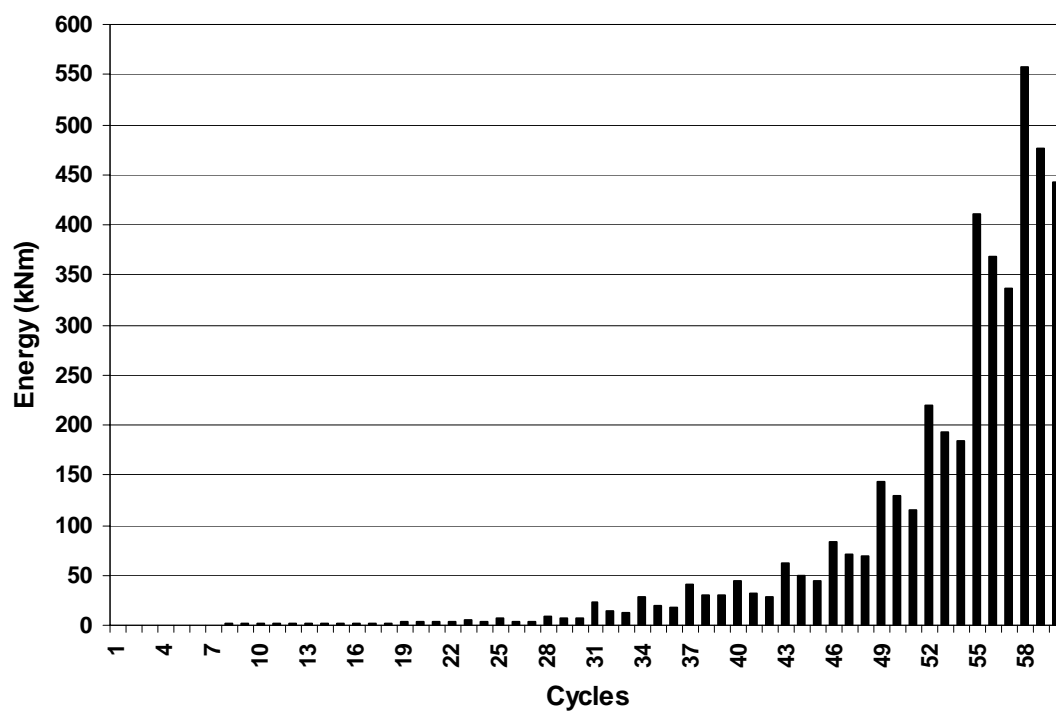


Figure 4.72 Energy absorbed for each cycle for the total system (Bent #6N 1998 test)

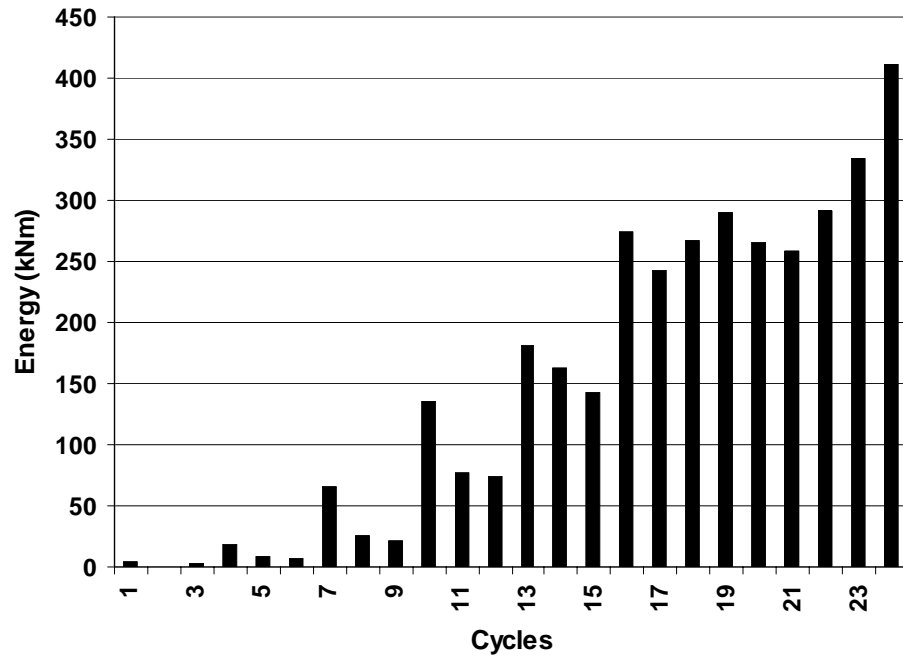


Figure 4.73 Energy absorbed for each cycle for the total system (Bent #5S 2000 test)

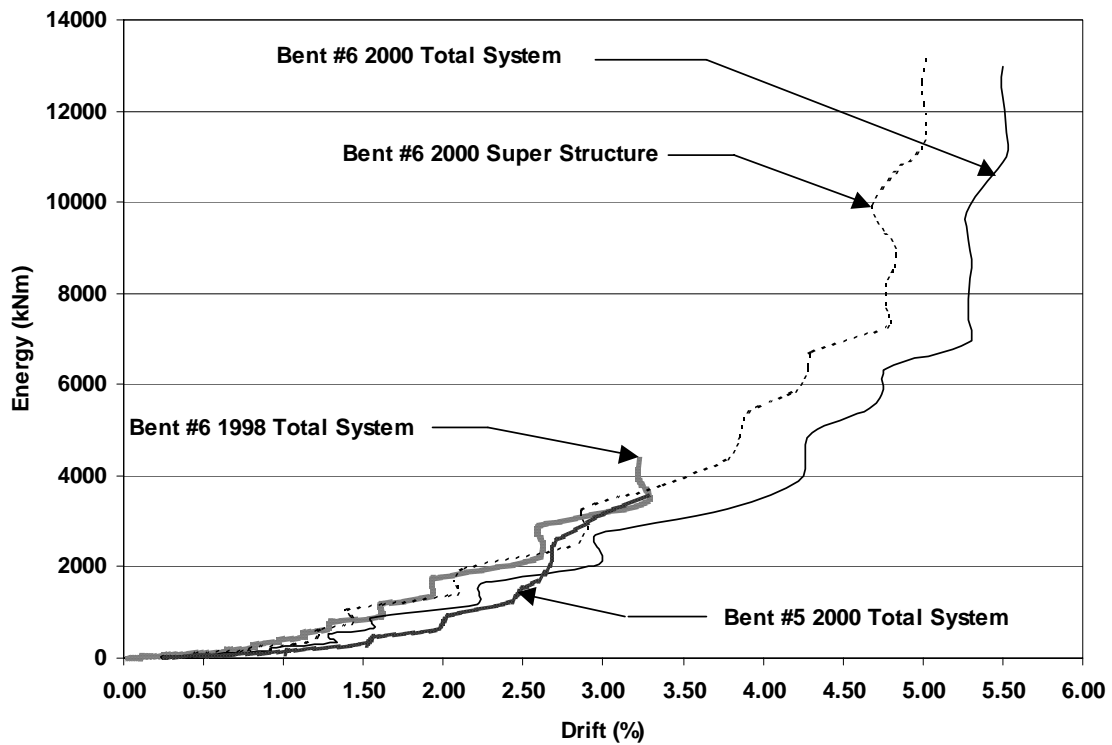


Figure 4.74 Cumulative hysteresis energy absorbed by the total system Bent #6S 2000, superstructure Bent #6S 2000, total system Bent #6N 1998, and total system Bent #5S 2000

Three energy related indices are presented E_N (Légeron and Paultre 2000), I_W (Gosain et al. 1977), and finally D_{EW} (Ehsani and Wight 1990), which were compared for the four structures using Equations 3.15-3.17. A graphical definition for the variables in Equations 3.15-3.17 is shown in Figure 4.75.

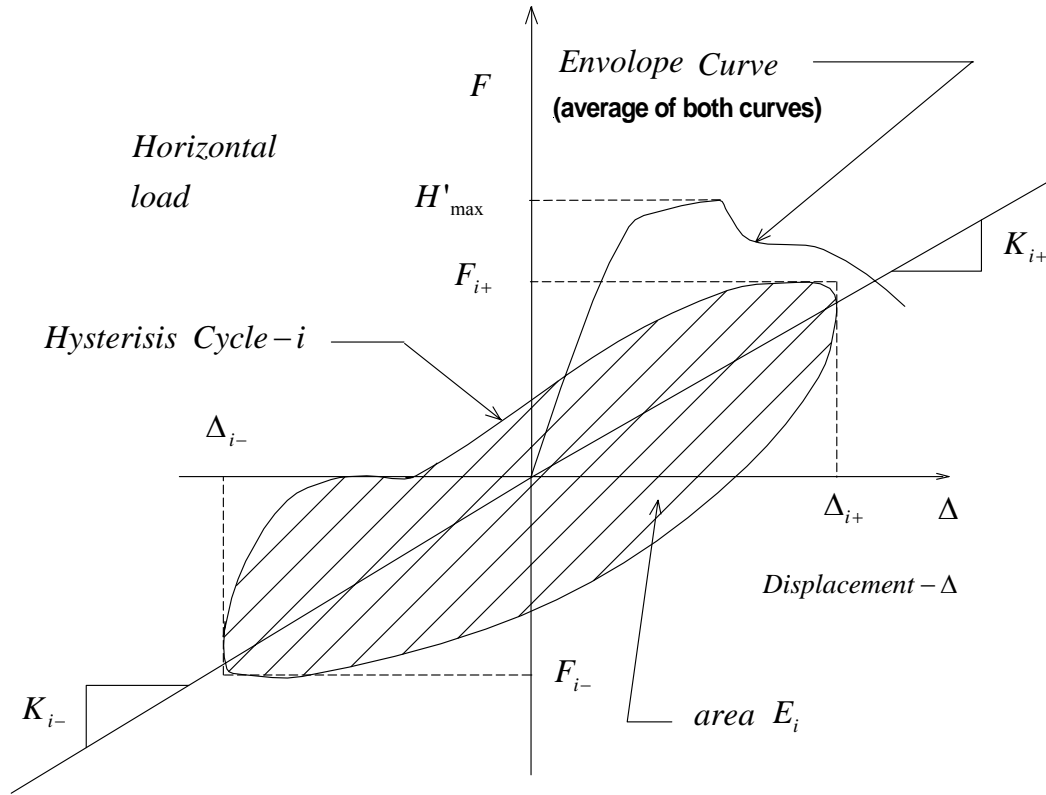


Figure 4.75 Energy dissipation for any cycle i

Discussion on Hysteretic Energy Capacity Absorption

The capacity to absorb energy can be an invaluable indicator of how well a structure will withstand damage when earthquake-induced loads or displacements are imposed on the structure. It can be observed that the highest energy absorbed for all bent structures in the 1998 and 2000 tests was that of the total system Bent #6S 2000 test. On the 36th cycle Bent #6S 2000 absorbed 689 J of energy in a test with a total of 41 cycles as shown in Figure 4.70. A decrease in the energy, for the cycles following the 36th cycle, indicates that the energy absorption capacity is decreasing and suggests that the structure has degraded and is beginning to become unstable. Also, in the total structure for Bent #5S 2000 test, the maximum energy cycle was observed on the 24th out of 24 cycles for the entire test. This indicates the structure was still stable and that severe degradation had not begun yet. During the total system Bent #6N 1998 test, the maximum energy observed was on the 57th cycle out of 60 cycles for the entire test. This indicates that the energy capacity was not decreasing at the end of the test, and degradation had just begun. It can be observed that there was a three-

cycle pattern for each drift step. Additional drift step increases needed to be performed to see if the maximum energy cycle was achieved during the test. The displacement, hysteretic energy, and cycles for the maximum energy found for each of the three tests are shown in Table 4.6.

Table 4.6 Maximum hysteretic energy cycles for the 1998 and 2000 tests

Test result of last cycle	Disp. (mm)	Cycle/Cycle _{total}	Energy of last cycle
2000 Bent #5S Mean Avg. Total System	290	24/24	412
1998 Bent #6N Mean Avg.Total System	260	57/60	557
2000 Bent #6S Mean Avg.Total System	540	36/41	688
2000 Bent #6S Mean Avg.Superstructure	490	36/41	670

The maximum energy cycle is unrelated to the lateral peak load capacity. It was observed in all tests that displacement corresponding to the peak lateral load was far smaller than the displacement of the peak energy cycle. The percentage difference for Bent #6S 2000 was 54% and 58% of the maximum energy displacement; likewise, for Bent #6N 1998 and Bent #5S 2000 total systems were found to be 49% and 40% of the maximum energy displacement. This indicates that even though the load capacity in each of these structures was starting to drop, all three structures still had substantial energy capacity and were in a very stable condition after the peak loads were observed. The displacements for the lateral peak loads are shown in Table 4.7.

Table 4.7 Peak load and displacement for the 1998 and 2000 tests

System	Disp. (mm)	Peak Load F_{max} (kN)
2000 Bent #5S Mean Avg. Total System	194	2043
1998 Bent #6N Mean Avg.Total System	128	2091
2000 Bent #6S Mean Avg.Total System	290	2362
2000 Bent #6S Mean Avg.Superstructure	283	2316

In many research studies, 80% of the peak load has been taken as the point where the maximum lateral displacement for a stable structure is defined. The displacement corresponding to the 80% peak lateral force is defined as Δ_{max} and the displacement ductility ratio is defined as displacement ductility $\mu = \Delta_{max} / \Delta_y$. Beyond the 80% load drop a structure is considered to be unstable (Légeron and Paultre 2000). The 80% of peak load capacity point and the maximum energy displacement point are related. It was found that the 80 % peak load displacement point for the Bent #6N 1998, and Bent #6S 2000, and the superstructure 2000 total system displacements were 2%, 13%, and 17 % smaller then their corresponding maximum energy displacement point. The Bent #5S 2000 test could not be used to compare because Bent #5S average spline curve $S(x)$ was found to only decrease to 6.6 % from the lateral peak load $S(x)_{max}$. The 80% of peak load maximum displacement point was observed to be a reasonable value relative to the maximum peak energy point in the 1998 and 2000 tests. The 80% $S(x)_{max}$ values are shown in Table 4.8.

Table 4.8 The 80 % $S(x)_{\max}$ lateral load peak values in the 1998 and 2000 tests

System	Disp. (mm)	80% Peak Load F_{\max} (kN)
2000 Bent #5S Mean Avg. Total System	*****	1634
1998 Bent #6N Mean Avg.Total System	265	1673
2000 Bent #6S Mean Avg.Total System	470	1890
2000 Bent #6S Mean Avg.Superstructure	420	1853

In reference to Figures 4.71-4.73, 50% of the energy absorption takes place in the few final cycles of each of the four tests. The final 50% of the energy absorption for both the total system and superstructure of Bent #6S 2000 test took place in the final 29 % of the total 41 cycles. For the total system Bent #6N 1998 and Bent #5S 2000 tests it was found that the final 50% of the energy was absorbed in the final 8.33% of 60 cycles and 21% of 24 cycles, respectively.

A final analysis was done on the 1998 and 2000 tests for the total system Bent #6S 2000, superstructure Bent #6S 2000, total system Bent #6N 1998 and total system Bent #5S 2000 tests. The normalized energy E_N defined in Equation 3.15, the work index I_w defined in Equation 3.16, and the damage index D_{EW} defined in Equation 3.17 are used to make further comparisons. In Equation 3.15, E_N defined as normalized dissipation energy has been normalized with the maximum values found in the force/displacement curve for a given test H'_{\max} and Δ_{yI} the initial yield displacement of the structure. The value E_i is the summation of the energy cycles taken over the interval of $1 \leq i \leq n$. In Equation 3.16, I_w is the work index and is normalized with H'_{\max} and Δ_{yI} . The summation of the maximum values for the peak loads and related peak displacements are summed over the interval of $1 \leq i \leq n$ cycles. For the final Equation 3.17, D_{EW} , defined as the damage index, is normalized with the values H'_{\max} and Δ_{yI} . The values K_i , Δ_i , and E_i are summed over the interval of $1 \leq i \leq n$ and are a function of the stiffness, displacements, and of the energy per cycle for a complete test. The E_N , I_w , and D_{EW} values are shown in Table 4.9.

Table 4.9 Energy, Work, and Damage Index for the 1998 and 2000 tests

System	E_N	I_w	D_{EW}
2000 Bent #5S Mean Avg. Total System	25.8	40.8	66.9
1998 Bent #6N Mean Avg.Total System	37.3	61.4	115.4
2000 Bent #6S Mean Avg.Total System	85.9	120.4	1,508.3
2000 Bent #6S Mean Avg.Superstructure	104.1	130.2	1,732.3

The values shown in Table 4.9 are representative of the field observations seen in each of the three tests. Relating the Bent #6N 1998 test to the Bent #5S 2000 test, E_N , I_w , and D_{EW} for Bent #5S 2000 are 69%, 66%, and 53% relative to Bent #6N 1998. The percentage difference between E_N and I_w is within 3% of one another and reflects the accumulated energy corresponding to their drift steps, as shown in Figure 4.74. The value for D_{EW} however shows a much higher value suggesting that more damage was sustained in Bent #6N 1998. This corresponds to the fact that D_{EW} is directly proportional to the cyclic stiffness K_i

where this reflects the stiffer foundation system constructed in the Bent #6N 1998 test. Comparing the total system Bent #6S 2000 and super structure Bent #6S 2000 values, it is shown in Table 4.9 that the E_N , I_W , and D_{EW} values are higher for the superstructure Bent #6S 2000. This was due to the fact that the normalizing value Δ_{yI} for the total structure was 74 mm and 60 mm for the superstructure accounting for the two higher values. The value D_{EW} was also normalized by Δ_{yI} , but D_{EW} is also directly proportional to the stiffness K_i and the squared value of the cyclic displacements Δ_i . The stiffness K_i and the normalized value Δ_{yI} determine the higher value D_{EW} found for the super structure. This is also consistent with field observations where the major damage was done on the columns in the superstructure. The values of E_N , I_W , and D_{EW} give valuable information that allows comparisons between the three bent structures based on energy relationships.

Finally, Table 4.9 shows clearly that more damage was sustained in the Bent #6S 2000 test compared to both the Bent #5N 1998, and the Bent #5S 2000 tests, regardless of the index used.

Performance Levels and Damage Assessment for Bent #6S

An overall description of the damage sustained by Bent #6S in the 2000 test will be made. The assessed damage can be related to four failure performance levels or stages. First, the yield and strain hardening of the reinforcement steel leading to the peak capacity and a gradual decrease in lateral capacity of the structure. Second, the concrete cracking and crushing that further decreases structural lateral capacity. Third, the loss of tensile capacity of the CFRP composite U-straps, and delamination of CFRP confinement layers in the columns and T-joints. Last, the column longitudinal reinforcement steel debonding from the concrete in the column-cap beam joints and also in the lap splice regions at the base of the columns. These four degradation stages or performance levels will lead to the complete collapse of the bridge structure during large lateral displacements in possible seismic activity. Also, some comparisons have been made between Bent #6S 2000, Bent #6N 1998, and Bent #5S 2000 tests as needed. After a generalized overview of the Bent #6 2000 structural degradation, a more in-depth evaluation of joint degradation will be presented.

Damage Assessment of Bent #6S

General Reinforcement Steel Yielding and Concrete Crushing

Two plots of the maximum push-pull lateral forces and the drift cycle vs. time are shown in Figures 4.76 and 4.77, respectively for reference. Also, a plot of the Bent #6S 2000 deflected shape at the maximum lateral load at a 3.73% drift ratio (displacement = 285mm) is presented in Figure 4.78. It should be noted that there was a 14.73mm increase in the cap beam length recorded at a 3.73% drift displacement. Three DT's were used to monitor the cap beam elongation and they were attached to the east end, middle and west end of the cap beam during the May 6th test date. The elongation was caused by the cap beam longitudinal reinforcement steel yielding and the concrete cracking in the cap beam. The drift ratio used in this report is based on the recorded West end displacements of the cap beam.

From onsite instruments and the balanced moment diagrams obtained from DRAIN-2DX analysis (Duffin 2003), the representation of the bent deflected shape was drawn as shown in Figure 4.78; the dots are the known cyclic maximum displacements recorded from the onsite instruments during the test. The inflection points for the cap beam, columns, and grade beam at a drift displacement of 3.73% are also shown in Figure 4.78; these were obtained from the moment diagram (Duffin 2003).

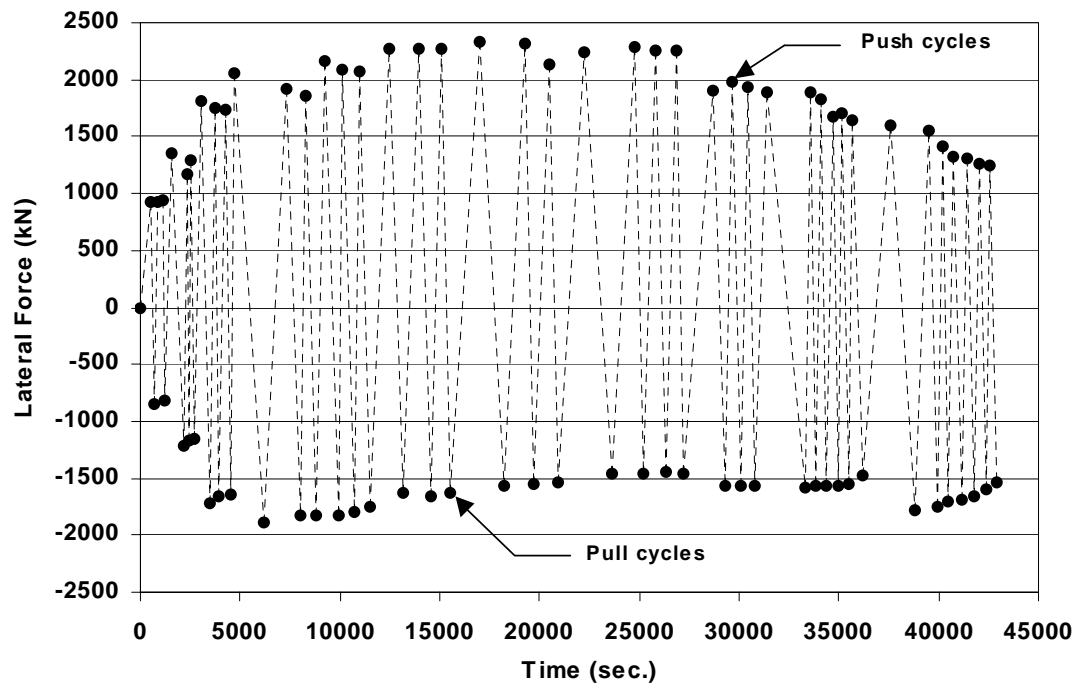


Figure 4.76 Maximum lateral push-pull forces vs. time for each cycle of the Bent #6S 2000 test

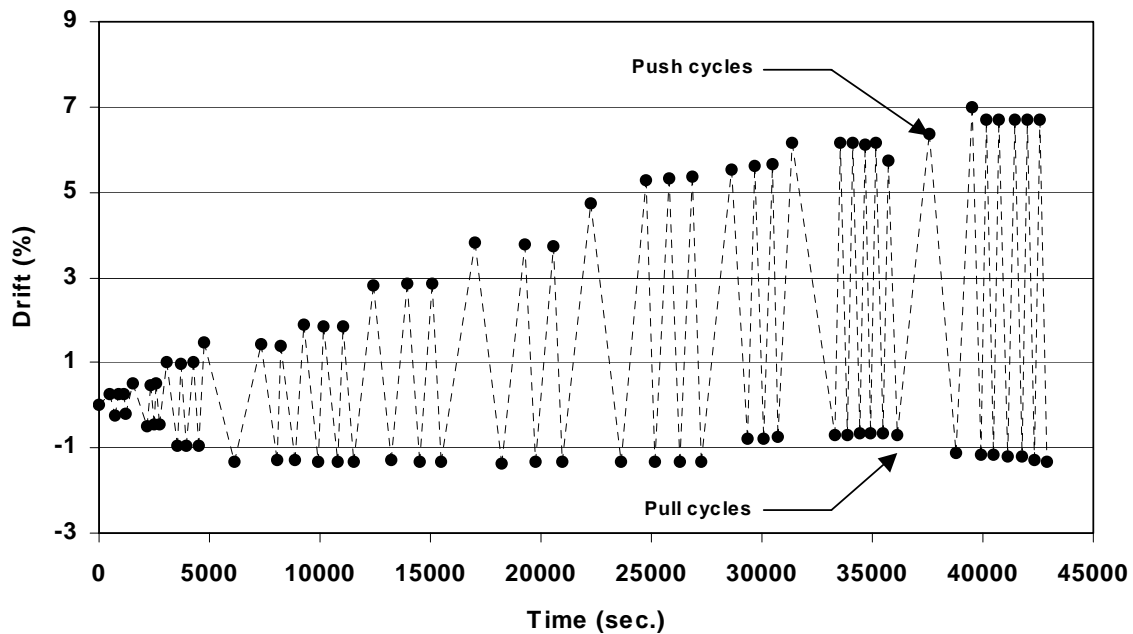


Figure 4.77 Maximum lateral push/pull drift ratio vs. time for each cycle of the Bent #6S 2000 test

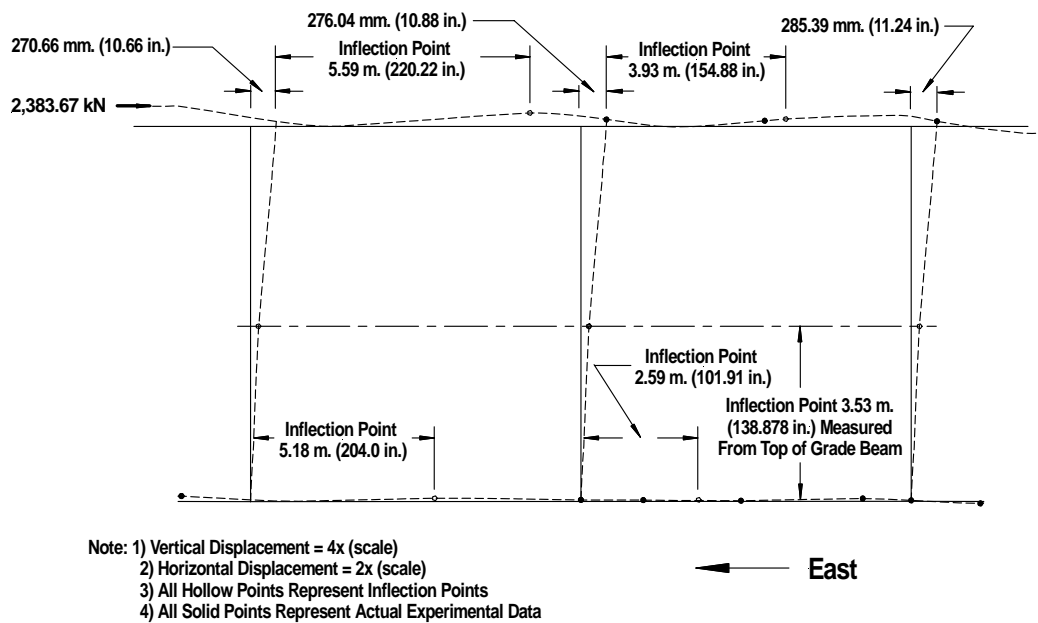


Figure 4.78 Bent #6S deflected shape for the 2000 test at the maximum lateral load and a drift ratio of 3.73%

Figures 4.79 and 4.80 show the reinforcement steel yielding in tension and concrete crushing development of degradation for the as-built (Bent #5 2000) and the retrofitted (Bent #6S 2000) structures. The plotted data shown in these two figures concurs with the information provided in Tables 4.10 and 4.11. Figure 4.81 for the as-built Bent #5S (2000) and Figure 4.82 for the CFRP retrofitted Bent #6S (2000) show the sequence of the reinforcement steel yielding and concrete crushing conditions of the two bents for the pushover analysis.

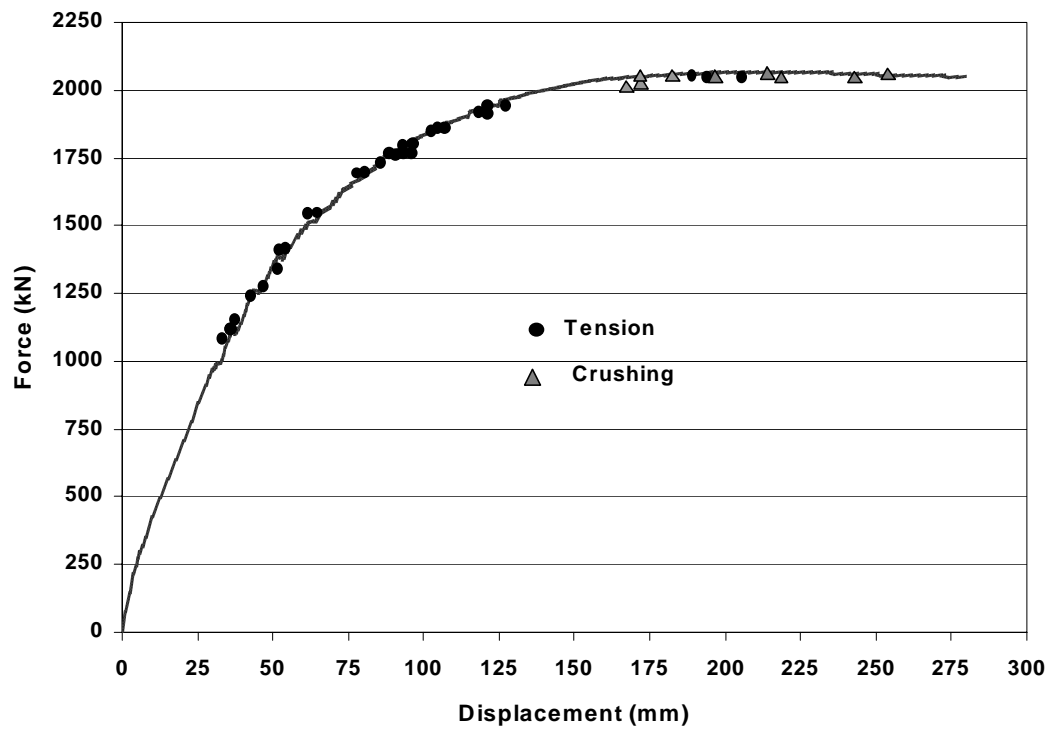


Figure 4.79 Reinforcement steel yielding and concrete crushing of the as-built Bent #5S 2000 DRAIN-2DX model lateral force/displacement curve

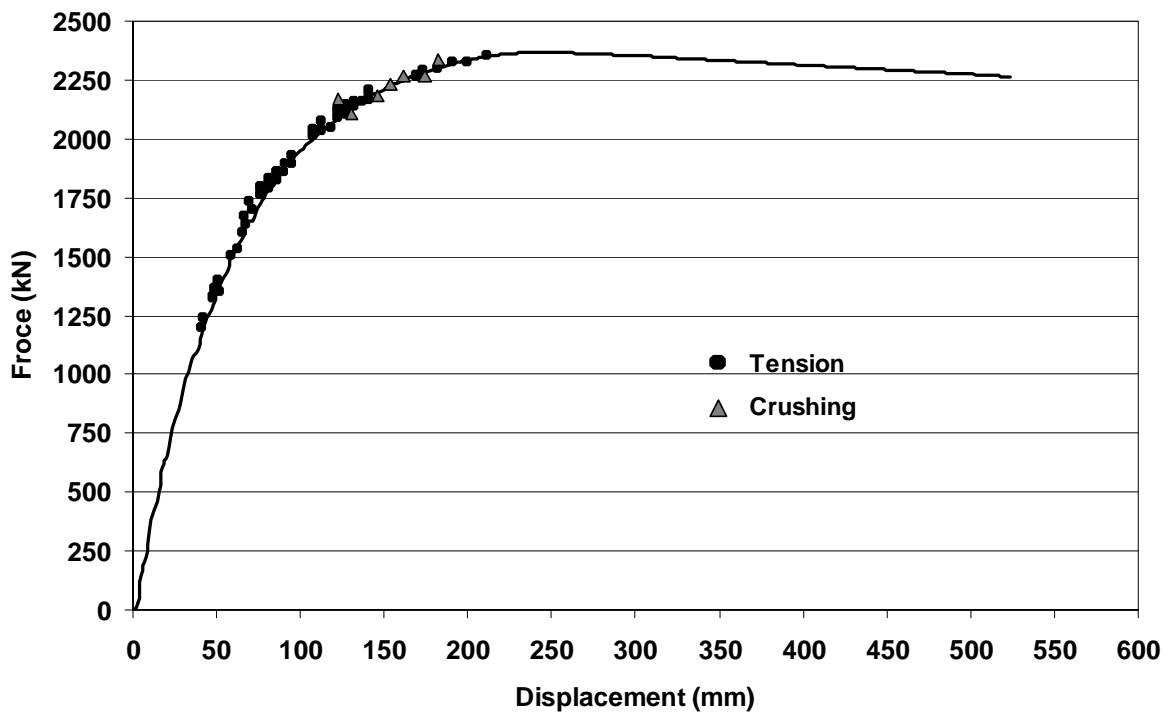


Figure 4.80 Reinforcement steel yielding and concrete crushing of the retrofitted Bent #6S 2000 DRAIN-2DX model lateral force/displacement curve

Two different reinforcement steel yielding and concrete crushing sequences are shown in Figures 4.81 and 4.82. From the pushover analysis it can be seen that the overstressing conditions in the cap beam, grade beam, and piles for the retrofitted model of Bent #6S 2000 are higher than the as-built design. The additional stresses on the Bent #6S 2000 structure are caused by higher lateral loads and displacement demands placed on the structure; there were eleven additional yielding and crushing locations on the retrofitted model vs. the as-built model from the pushover analysis. This was caused by the U-straps, which contributed additional stiffness to the columns during the initial lateral displacements. The column elements remain in a double curvature mode up to approximately a 3.73% drift (displacement = 285mm); this was the documented drift displacement at which the U-straps began to fail for the Bent #6S test, but is a noticeable increase beyond the as-built structure double curvature mode observed at 2.41% drift (displacement = 185mm). Additional capacity was gained from the CFRP composite; however, it should be noted that the retrofitted design placed an additional demand on the substructure system and this needs to be addressed when considering a seismic retrofit design of this type. The additional strength of the retrofit design of the superstructure caused yielding in the piles and additional stresses on the pile caps in the pushover analysis shown in Figure 4.82.

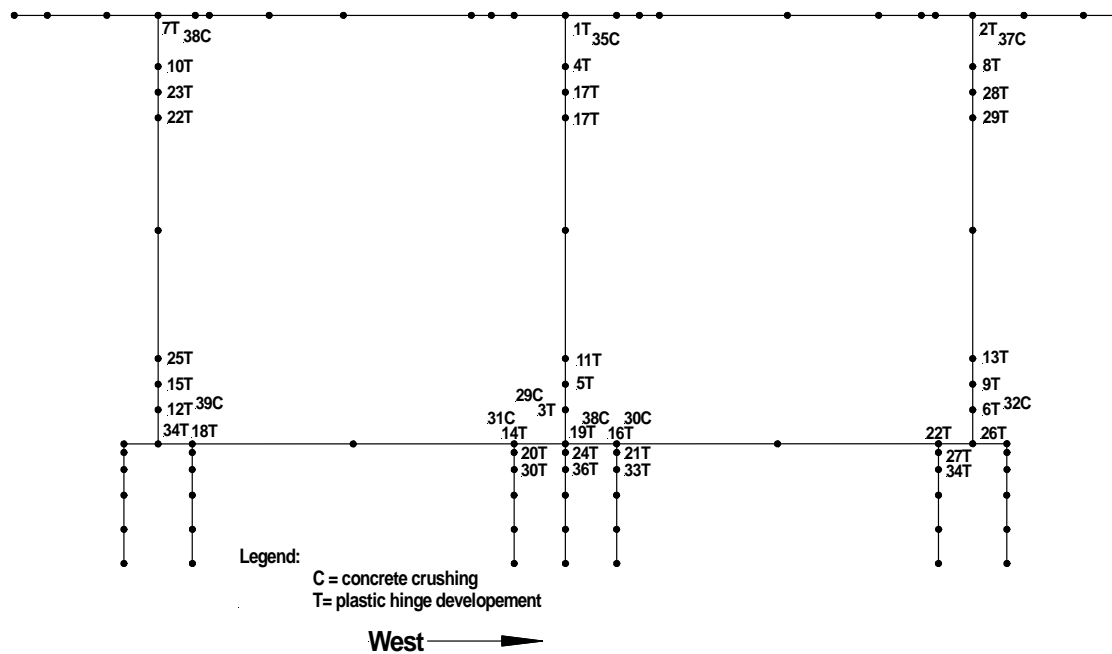


Figure 4.81 Degradation sequence represented by the reinforcement steel yielding and concrete crushing of the as-built Bent #5S 2000 DRAIN-2DX model

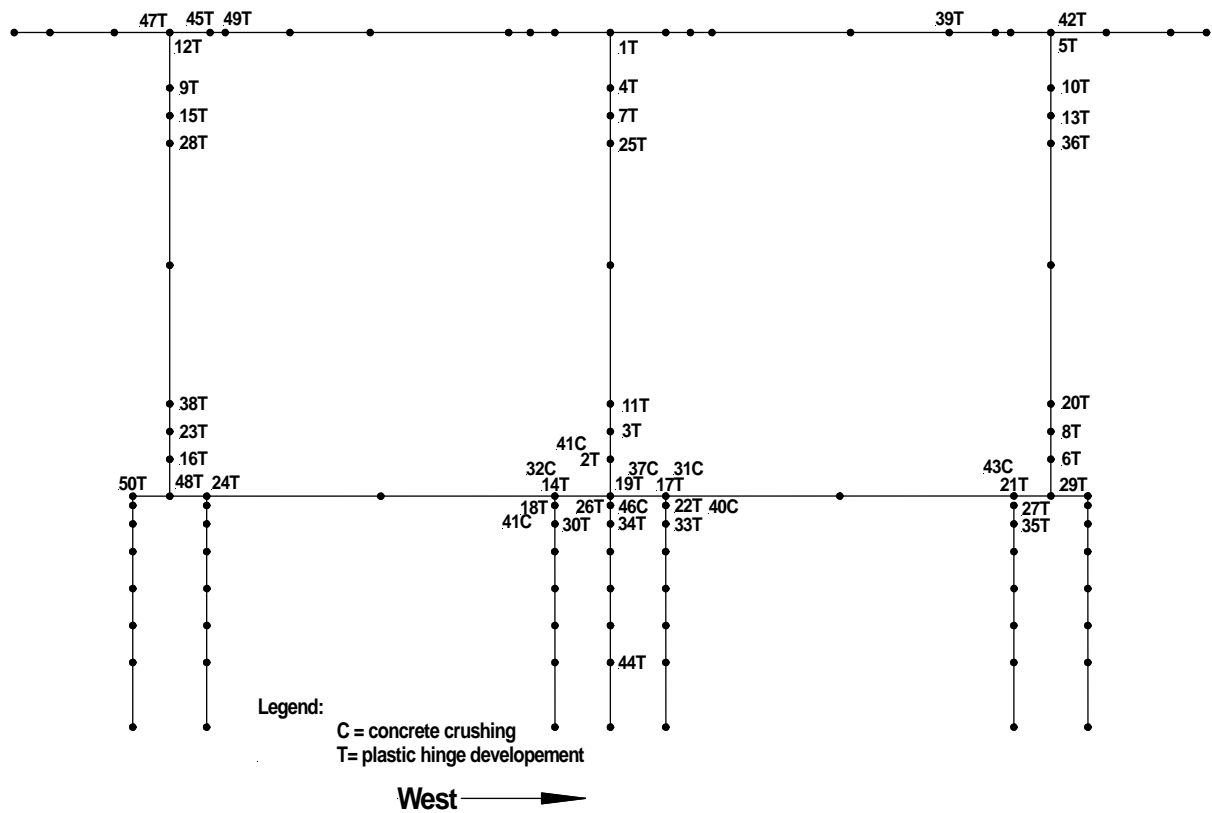


Figure 4.82 Degradation sequence of the reinforcement steel yielding and concrete crushing of the retrofitted Bent #6S 2000 DRAIN-2DX model

Table 4.10 Strains for the reinforcement yielding and concrete crushing for the as-built Bent #5S 2000

#	Element	Node	Disp. (in)	Disp. (mm)	Strain	Mode
1	139	300	1.41	35.81	0.00175	tension
2	140	308	1.73	43.94	0.00174	tension
3	5	5	1.75	44.45	0.00174	tension
4	139	298	1.80	45.72	0.00174	tension
5	5	8	1.98	50.29	0.00174	tension
6	6	6	2.07	52.58	0.00174	tension
7	138	16	2.11	53.59	0.00174	tension
8	140	299	2.36	59.94	0.00174	tension
9	6	9	2.38	60.45	0.00174	tension
10	138	297	2.60	66.04	0.00174	tension
11	8	11	2.73	69.34	0.00174	tension
12	4	4	3.17	80.52	0.00174	tension
13	9	12	3.38	85.85	0.00174	tension
14	59	28	3.46	87.88	0.00167	tension
15	4	7	3.53	89.66	0.00174	tension
16	87	31	3.62	91.95	0.00167	tension
17	136	295	3.72	94.49	0.00174	tension
18	29	26	3.85	97.79	0.00286	tension
19	73	2	3.96	100.58	0.00167	tension
20	59	52	4.07	103.38	0.00174	tension
21	87	66	4.11	104.39	0.00167	tension
22	101	33	4.18	106.17	0.00167	tension
23	135	294	4.34	110.24	0.00174	tension
24	73	59	4.48	113.79	0.00167	tension
25	7	10	4.85	123.19	0.00174	tension
26	3	3	4.86	123.44	0.00174	tension
27	101	73	4.94	125.48	0.00174	tension
28	137	296	4.97	126.24	0.00174	tension
29	5	5	6.56	166.62	-0.00400	crushing
30	87	31	6.96	176.78	-0.00400	crushing
31	59	28	7.08	179.83	-0.00401	crushing
32	6	6	7.20	182.88	-0.00401	crushing
33	88	67	7.60	193.04	0.00167	tension
34	1	1	7.76	197.10	0.00174	tension
35	139	300	8.02	203.71	-0.00400	crushing
36	74	60	8.30	210.82	0.00167	tension
37	140	308	8.32	211.33	-0.00401	crushing
38	138	16	9.66	245.36	-0.00401	crushing
39	4	4	9.85	250.19	-0.00400	crushing

Table 4.11 Strains for the reinforcement yielding and concrete crushing for the retrofitted Bent #6S 2000

#	element	node	disp(in)	disp(mm)	strain	mode
1	139	300	1.63	41.40	0.00175	tension
2	5	5	1.78	45.21	0.00175	tension
3	5	8	2.00	50.80	0.00175	tension
4	139	298	2.01	51.05	0.00175	tension
5	140	308	2.05	52.07	0.00175	tension
6	6	6	2.12	53.85	0.00174	tension
7	136	295	2.36	59.94	0.00174	tension
8	6	9	2.42	61.47	0.00174	tension
9	138	297	2.44	61.98	0.00174	tension
10	140	299	2.64	67.06	0.00174	tension
11	8	11	2.75	69.85	0.00174	tension
12	138	16	2.92	74.17	0.00174	tension
13	136	296	3.00	76.20	0.00175	tension
14	59	28	3.17	80.52	0.00167	tension
15	135	294	3.18	80.77	0.00174	tension
16	4	4	3.23	82.04	0.00174	tension
17	87	31	3.28	83.31	0.00167	tension
18	59	52	3.49	88.65	0.00167	tension
19	73	2	3.52	89.41	0.00168	tension
20	9	12	3.53	89.66	0.00174	tension
21	101	33	3.59	91.19	0.00167	tension
22	87	66	3.63	92.20	0.00167	tension
23	4	7	3.69	93.73	0.00174	tension
24	29	26	3.75	95.25	0.00287	tension
25	133	292	3.75	95.25	0.00174	tension
26	73	59	3.78	96.01	0.00168	tension
27	101	73	3.93	99.82	0.00167	tension
28	132	291	4.55	115.57	0.00174	tension
29	3	3	4.78	121.41	0.00174	tension
30	60	53	4.93	125.22	0.00167	tension
31	87	31	5.08	129.03	-0.00409	crushing
32	59	28	5.10	129.54	-0.00402	crushing
33	88	67	5.21	132.33	0.00167	tension
34	74	60	5.25	133.35	0.00167	tension
35	102	74	5.35	135.89	0.00167	tension
36	134	293	5.54	140.72	0.00174	tension
37	73	2	5.55	140.97	-0.00402	crushing
38	7	10	5.56	141.22	0.00174	tension
39	146	305	5.80	147.32	0.00167	tension
40	87	66	6.35	161.29	-0.00408	crushing
41	59	52	6.40	162.56	-0.00408	crushing
42	149	308	6.67	169.42	0.00167	tension
43	101	33	6.80	172.72	-0.00403	crushing
44	78	64	6.97	177.04	0.00167	tension
45	16	17	7.10	180.34	0.00167	tension
46	73	59	7.17	182.12	-0.00401	crushing
47	16	16	7.40	187.96	0.00167	tension
48	1	1	8.05	204.47	0.00174	tension
49	17	18	8.16	207.26	0.00167	tension
50	31	24	8.55	217.17	0.00167	tension

Specific Bent #6S 2000 Test Joint Damage Assessment

In this section all six joints are analyzed. Each joint is categorized and assessed for mechanical and material degradation. A table is presented for each individual joint, where the horizontal rows represent the mechanical and material degradation and the vertical columns represent time and drift intervals. Each interval was selected to try to best fit the sequential damage for the joints represented by onsite observations, instrumentation, and the DRAIN-2DX pushover analysis. The four drift step intervals chosen are 0% to 0.5%, 0.5% to 3.8%, 3.8% to 5.5%, and for a drift greater than 5.5%. It is documented in the following analysis that the structural frame actually transitioned into three unique frame types defined as Phase I ($0\% \leq \text{drift} \leq 4\%$) fixed-fixed column ends; Phase II ($4\% \leq \text{drift} \leq 6\%$) plastic hinged-hinged for the exterior columns and plastic hinged-plastic hinged for the middle column; and Phase III ($6\% \leq \text{drift} \leq 6.8\%$) semi fixed-hinged for the exterior columns and semi fixed-plastic hinged for the interior column.

East Column-Cap Beam Joint: Mechanical and Material Evaluation

Ankle Wrap (Diagonal) Layers

Three strain gages (SG31, SG32, and SG33) were placed on the ankle wrap layers as shown in Figure 4.32. The maximum tensile strain for the three strain gages was recorded on SG33 representing 13% of the CFRP tensile failure strain; the maximum compressive strain was recorded on SG31 and SG33 and both were 10% of the CFRP compressive failure strain. This indicates that low stress demands were placed on the ankle wrap layers during the test. A strain profile of the ankle wrap layers for push-pull cycles is shown in Figure 4.83.

Zero Layers

Five strain gages SG42, SG43, SG51, SG52, and SG67 were installed on the South face of the cap beam's two zero CFRP composite layers, as shown in Figure 4.32. The maximum tensile strain of the five strain gages was recorded on SG51 and represented 26% of the CFRP tensile failure strain; the maximum compressive strain was recorded on SG 42 and represented 8% of the CFRP compressive failure strain. Small stress demands were placed on the zero layers for the test. A strain profile of the East column-cap beam joint zero layers for the push cycles is shown in Figure 4.84.

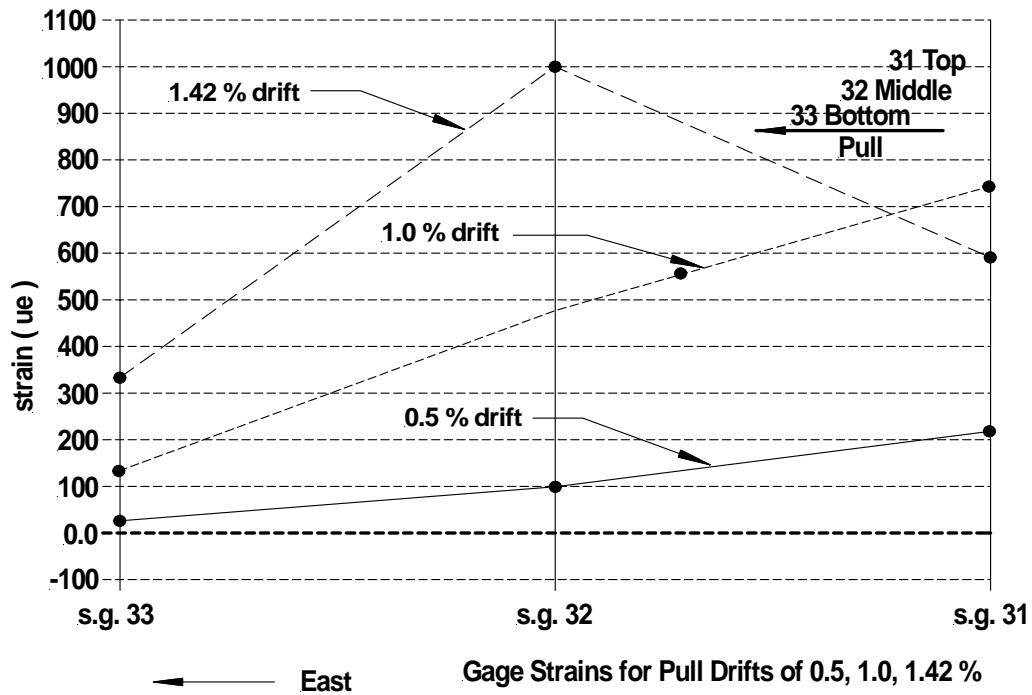


Figure 4.83 Cap-beam external CFRP composite diagonal 2 layers located in the East column-cap beam region: strain vs. %drift pull cycles for strain gages 31, 32, and 33

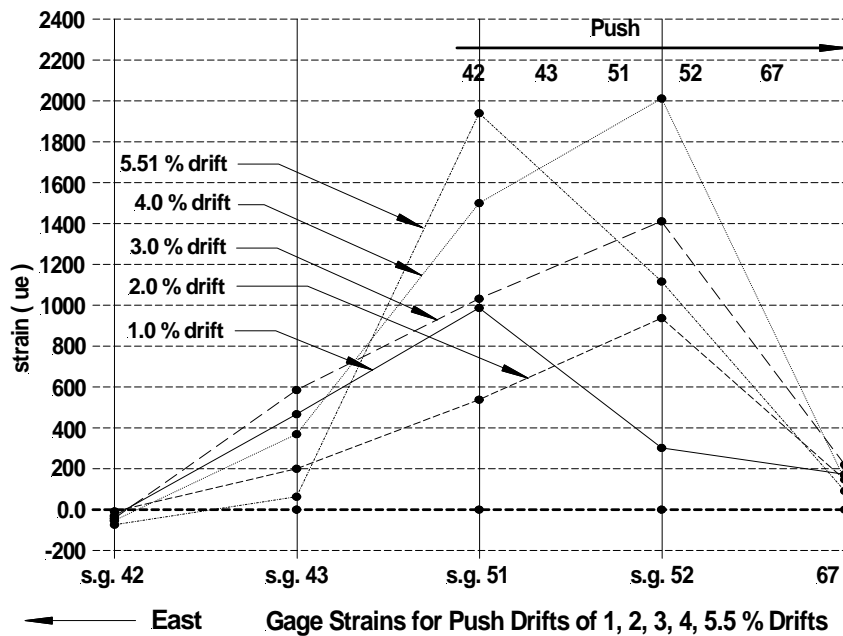


Figure 4.84 Cap-beam external CFRP composite zero 2 layers located in the East column-cap beam region: strain vs. %drift push cycles for strain gages 67, 52, 51, 43, and 42

U-Straps

No instruments were placed on the U-straps, but from onsite field observations the U-straps began to fail in tension at approximately 3.73% drift, as shown in Figure 4.85.



Figure 4.85 U-strap failure shown at 4.0% drift step

Yielding Reinforcement Steel and Concrete Crushing

Strain gage SG29 was located on the top longitudinal bars in the East joint cap beam region, as shown in Figure 4.28. The maximum tensile and compressive strains were recorded at 24% and 38% of the steel yielding strain capacity, respectively. This indicates there was relatively little lateral force demand around this location of the cap beam. An approximation of the tensile yield stress of 24.6% was found in the same general location; a strain profile for SG29 is shown Figure 4.86.

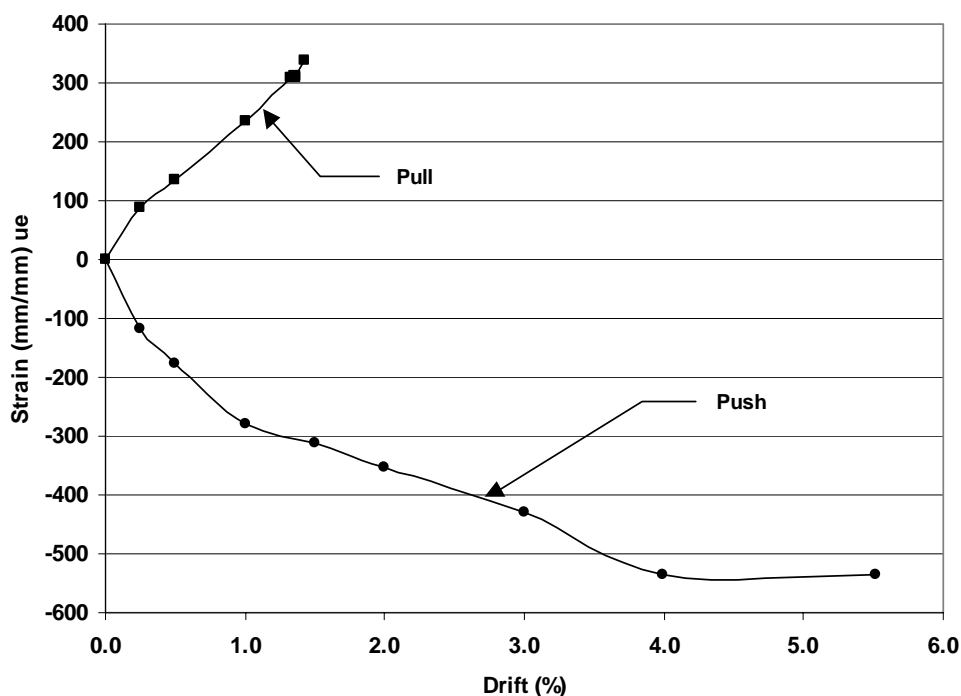


Figure 4.86 Cap-beam internal lateral reinforcement steel located in the East column-cap beam region: strain vs. % drift for SG29

From the DRAIN-2DX pushover analysis, the sequential reinforcement yielding, and concrete crushing was obtained, and there was an increase in the number of yielding and crushing points between the as-built and retrofitted designs as stated previously. The two major differences between the as-built and retrofitted joints were the confinement CFRP composite layers and the U-straps. The confinement layers improved the concrete ductility in compression and the CFRP composite U-straps and zero layers provided additional tensile capacity to the column-cap beam joints. This was indicated by no concrete crushing in the cap beam and four new yielding points that formed in the cap beam of the retrofitted structure. The reduced concrete crushing and additional yielding in the retrofitted cap beam was typical behavior for Middle and West column-cap beam joints as well. The tensile capacity can be increased very economically by using zero composite layers; applying the U-straps and adding confining CFRP composite layers to the column and the cap beam members adjacent to the joint can significantly reduce the concrete crushing in the column-cap beam joints. An example of this is shown in Figures 4.81 and 4.82 where the as-built structure column-cap beam joints have concrete crushing, whereas the retrofitted design shows no concrete crushing.

A moment curvature diagram was constructed for all six joints from the DRAIN-2DX strain data in the pushover analysis. The moment curvature analysis of the East column top and bottom plastic hinge locations shows that the moment demand and longitudinal reinforcement steel strains had increased up to a 3.0% drift ratio. After the 3.0% drift, the top column moment demand and the strain in the longitudinal reinforcement had no additional increase. Also, the moment at the bottom column remained constant, but there

was a significant increase in the longitudinal reinforcement strains beyond a 3.0% drift displacement. When additional drift displacements were applied to the structure, the rotation of the East column was transferred to the bottom column plastic hinge region approximately 700mm above the grade beam elevation. The rotation transfer occurred in the Middle and West column-grade beam joints as well. The moment curvature for the East column-cap beam joint is shown in Figure 7.9. The curvature ductility was approximately $\mu = 3.9$.

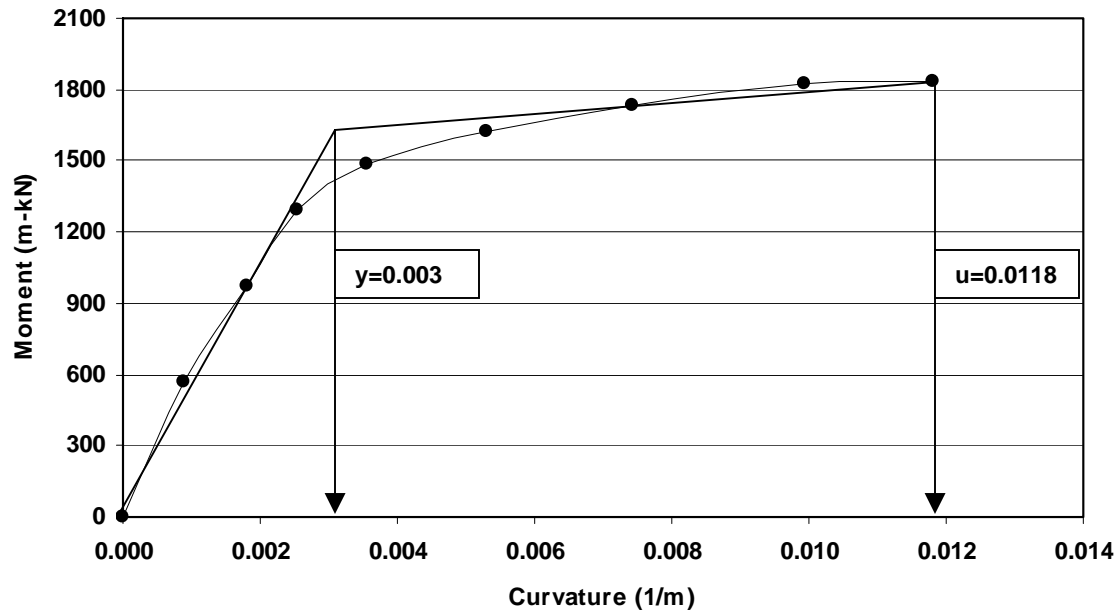


Figure 4.87 Moment curvature for the East column-cap beam joint

Joint Longitudinal Reinforcement Steel Pullout

From onsite field observations after the CFRP composite layers were removed, it was noted that there was a 4.8 mm gap at the top of the column longitudinal steel. The column longitudinal steel debonded at approximately 5.0% displacement drift. The loss of longitudinal reinforcement steel bond strength occurred in the West column-cap beam joint at approximately the same displacement drift.

Table 4.12 describes the damage for the four performance levels and refers to the relevant Figures following the Table in Figure 4.88 for surface damage and Figure 4.89 after removal of the CFRP composite and cover concrete.

Table 4.12 Damage assessment matrix for the East column-cap beam joint

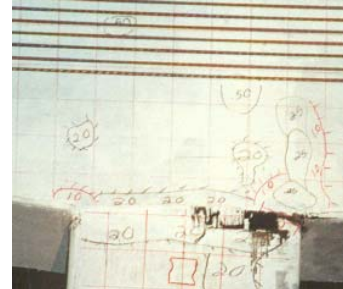
	Phase I $0 \leq \text{time} \leq 3,000$ $0\% \leq \text{drift} \leq 0.5\%$	Phase II $3,000 \leq \text{time} \leq 17,000$ $0.5\% \leq \text{drift} \leq 3.8\%$	Phase III $17,000 \leq \text{time} \leq 25,500$ $3.8\% \leq \text{drift} \leq 5.5\%$	Phase IV $\text{time} \geq 3,000$ $\text{drift} \geq 5.5$
Ankle Wrap or Diagonal Layers	Min. delaminating of layers. See Figure 4.88(a)	Additional delaminating added to Phase I. See Figure 4.88(b)	Additional delaminating added to Phase II. See Figure 4.88(c)	Additional delaminating to phase III. See Figure 4.88(d)
Zero Layers	No loss in tensile capacity. See Figure 4.88(a)	No loss in tensile capacity. See Figure 4.88(b)	No loss in tensile capacity. See Figure 4.88(c)	No loss in tensile capacity. See Figures 4.88(e) and 4.88(f)
U-Strap Layers	Small amount of delaminating. See Figure 4.88(a)	Drift 3.73% is the beginning point of the U-strap fracture. See Figures 4.88(b) and 4.88(c)	Fracture of U-strap due to excessive bending moment and tensile force on west strap. See Figure 4.88(c)	Complete U-strap failure. See Figures 4.88(d) through 4.88(f)
Confinement Layers	No lateral flexural cracks formed in CFRP composite layers	Lateral flexural cracks in confinement layers begin approximately 1.0% drift	Lateral flexural cracks do not increase after U-straps begin to fail and rotation is transferred to the bottom grade beam joint	Lateral flexural cracks do not increase after U-straps begin to fail and rotation is transferred to the bottom grade beam joint
Longitudinal Bar Yielding	No yielding. See Figure 4.88(a)	All yielding occurred in phase II. See Figure 4.80	1) West face column bars slightly buckle from confinement layers delaminating. See Figures 4.89(g) and 4.89(h). 2) Longitudinal reinforcement steel begins to de-bond at approximately 5.5% See Figure 4.89(c)	Longitudinal bars have de-bonded See Figure 4.89(c)



(a) $0\% \leq \text{drift} \leq 0.5\%$



(b) $0.5\% \leq \text{drift} \leq 3.8\%$



(c) $3.8\% \leq \text{drift} \leq 5.5\%$



(d) drift $\approx 5.5\%$



(e) drift $\approx 6.5\%$



(f) after 6.8% drift

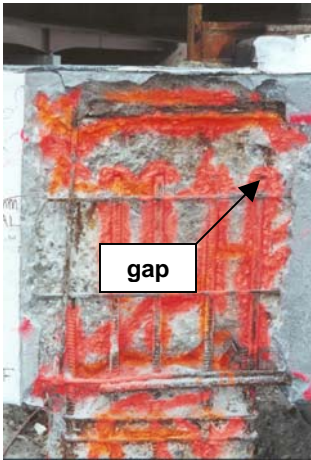
Figure 4.88 Surface damage for East column-cap beam joint



(a) Joint radial shear crack



(b) Longitudinal reinforcement bar buckle



(c) Reinforcement bar de-bonded



(d) Column flexural and shear cracks



(e) North face of East joint



(f) West face of East joint



(g) West face reinforcement bar buckle



(h) West face buckle

Figure 4.89 Internal damage for East column-cap beam joint

Middle Column-Cap Beam Joint: Mechanical and Material Evaluation

Ankle Wrap (Diagonal) Layers

The instrumentation of the ankle wrap layers and zeros for the East, Middle, and West joints are typical. The location of the strain gages applied to the diagonal and zero layers of the south face of the middle joint is shown in Figure 4.33. The maximum tensile strain on the diagonal layers was recorded on SG 48 and the CFRP tensile strain was 10% of the CFRP composite tensile failure strain; the maximum compressive strain was recorded on SG49 and was 25% of the CFRP composite compressive failure strain. From the onsite and recorded data, small stress demands were placed on the cap beam portion of the middle joint. The upper portion of the column took the majority of the damage as shown in Figure 4.90. A strain profile for the push and pull cycles is shown in Figure 4.91.



Figure 4.90 No column reinforcement steel pullout and no damage sustained on the cap beam portion of the Middle column

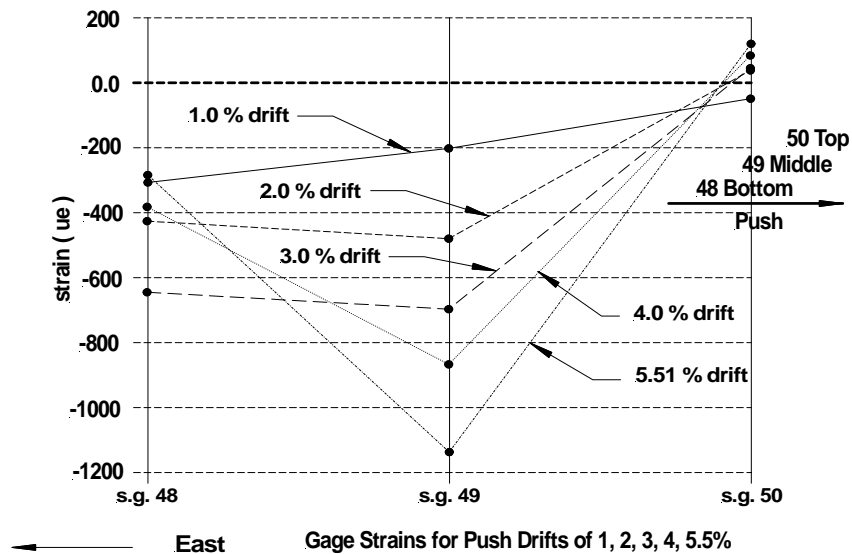


Figure 4.91 Cap-beam external CFRP composite diagonal 2 layers located in the middle column-cap beam region: strain vs. %drift push cycles for strain gages 48, 49 and 50

Zero Layers

Five strain gages were placed on the south face zero layers SG118, SG117, SG116, SG115, and SG114. Strain gage SG117 recorded the highest tensile strain which was 39% of the CFRP composite tensile failure strain; the maximum compression to failure strain was recorded on SG114 and SG116 of 6% of the CFRP composite compressive failure strain. As found in the ankle wrap section, a small stress demand was placed on the zero cap beam layers of the middle joint during the test. A strain profile for the push cycles for the zero layer strains is shown in Figure 4.92.

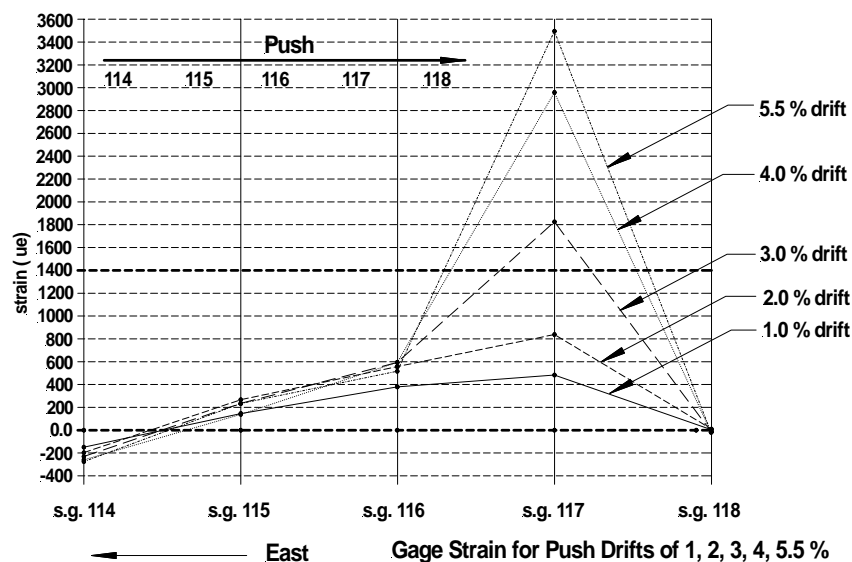


Figure 4.92 Cap-beam external CFRP composite zero 1 layer located in the middle column-cap beam region: strain vs. %drift push cycles for strain gages 118, 117, 116, 115, and 114

U-Straps

No instruments were placed on the U-straps, but from onsite observations there was no fracturing of the U-straps at the column cap beam interface for the entire test. This can be explained by noticing that there are two equal length cap beam members attached to the middle joint East and West faces. The net column-cap beam moments were distributed in almost equal proportions and this significantly reduced the tensile demand on the west U-strap for the push displacements and the same condition for the east strap for pull displacements. The proportion of the cap beam net moment on the East face was 46% and 54% for the West face for a 3.73% drift in the push direction. By comparison, the moment demand proportion for the West face of the East column-cap beam joint was 80% and 83% for the East face of the West column-cap beam joint. The excessive non-proportionate moment demands on the East and West column cap beam joints significantly increase the tensile demands on the West U-straps for both the East and West joints for a push displacement; during pull displacements, the non-proportional moments will place excessive tensile demands on the East straps. The cap beam average deflection at the Middle joint was the smallest deflection out of the three joints, as shown in Figure 4.93. Also, the U-straps for the exterior East and West joints fractured at approximately the same time and at drift displacements of 3.73% and 4.0%, respectively.

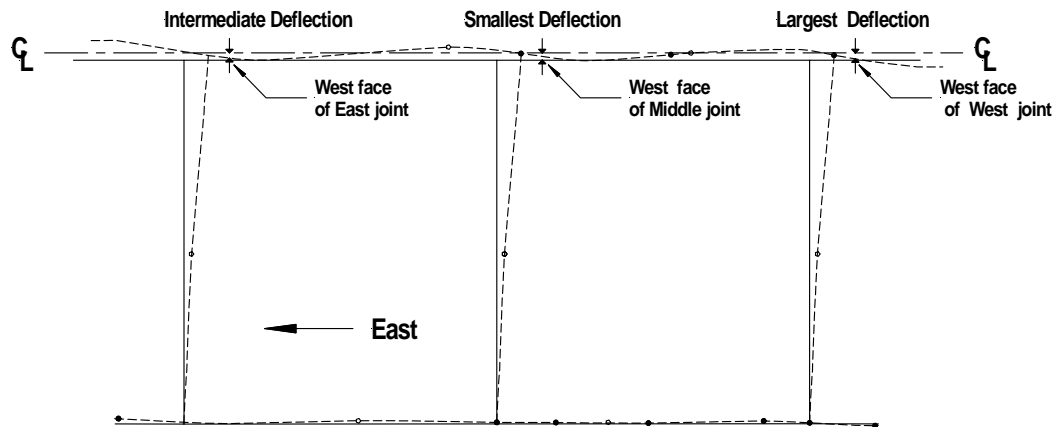


Figure 4.93 Average displacement deflections of the cap beam indicating smaller tensile demands on the middle joint U-straps

Column Confinement Layers (6 Layers) Adjacent to the Joint

Eight strain gages were placed on the midsections of the six confinement layers that lay adjacent to the column-cap beam joint, as shown in Figure 4.31. The East and West CFRP confinement layers delaminated from the concrete face at a drift ratio of approximately 2.9%. Even though the East and West confinement layers were unattached to their column faces, confinement was still provided to the column. For square columns, the confinement layers provided the maximum confinement at the corner locations; the confinement decreased at the midsection between the two corners on the same column face. Confinement also depends on geometry, such as the ratio of the lengths of the sides in a rectangular column Seible et al. (1996). Tensile capacity continued to develop in the midsection of the East face, but

diminished to almost zero on the midsection of the West face. The maximum tensile strain for the East and West faces was recorded on SG60 and was 73% of the tensile failure strain of the CFRP composite. The middle section is not, however, always the critical region of failure for a square confined geometry. The critical failure region can be at the corner for large d/r ratios and the corners can fail in compression. The Southeast corner SG58 recorded a maximum compression failure strain of $-2014\mu\epsilon$ at 5.5% drift. Considering the failure compressive strain will be at most 50% of the tensile failure strain, the corner reached approximately 45% of the CFRP compressive failure strain Barbero (1998). A strain profile of the tensile and compressive strains for the confinement layers is shown in Figure 4.94.

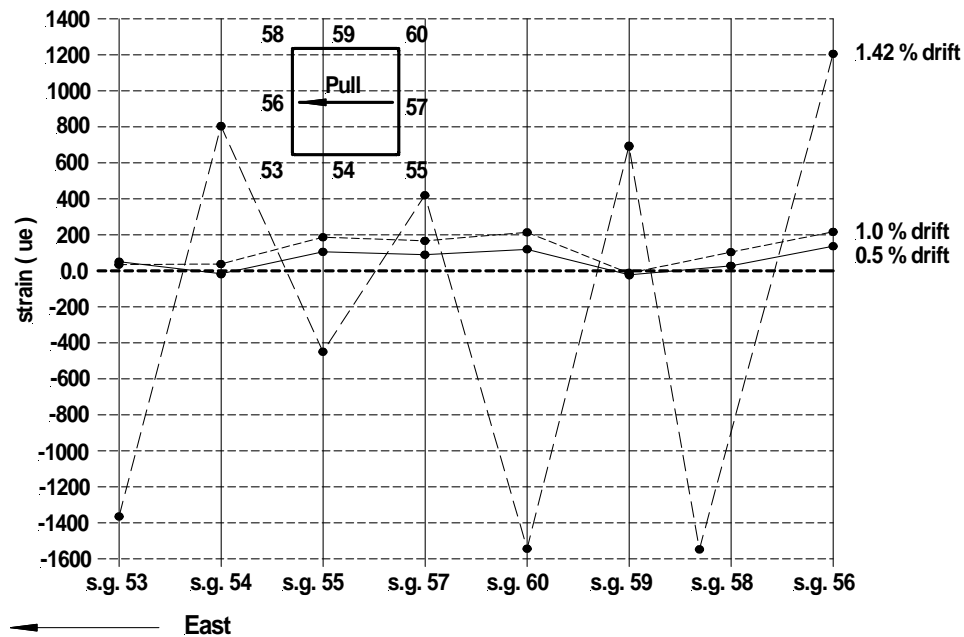


Figure 4.94 Column external CFRP composite 6 confinement layers located on the middle column top region: strain vs. %drift pull cycles for strain gages 53, 54, 55, 57, 60, 59, 58, and 56

The CFRP layers delaminated from the concrete faces for the North and South faces at approximately 4.75%. The CFRP composite layers still provided tensile confinement for both the North and South faces with recorded strains of $3,073\mu\epsilon$ and $1,853\mu\epsilon$ at a drift displacement of 5.5%. The East and West faces reached approximately 34% and 21% of the CFRP tensile failure strain, respectively. A strain profile of the tensile and compressive strains for the confinement layers is shown in Figure 4.94.

Yielding Reinforcement Steel and Concrete Crushing

Four strain gages were installed on the longitudinal reinforcement steel to monitor the internal rebar tension and compressive strains during the Bent #6 2000 test. Strain gages SG46 and SG47 were installed on the top longitudinal reinforcement in the cap beam portion of the joint. Also, two strain gages SG44 and SG45 were attached to the column's

longitudinal reinforcement. Strain gage 44 was placed approximately 305mm below the cap beam soffit in the West face of the middle column and SG 45 was placed approximately in the middle of the Middle joint in both the horizontal and vertical directions, as shown in Figure 4.28. The high strains recorded in strain gage SG44 concurs with Figure 4.90 showing large flexural damage sustained in the middle column plastic hinge region. Strain gage SG44 had the highest tensile and compressive strains and was the only gage out of the four internal strain gages that yielded. Its recorded maximum tensile and compression strains were 149% and 80% of the reinforcement steel yield strain, respectively. From Figure 4.95, it can be seen that there is no damage to the U-straps, but below the six-column confinement layers that lay adjacent to the beam cap soffit, the top portion of the column degraded due to the high flexural demands that were applied to the plastic hinge region of the column.

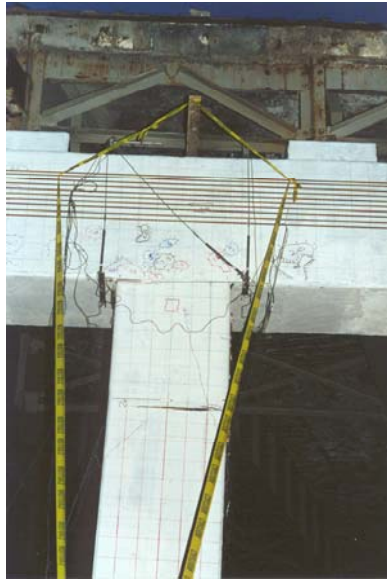


Figure 4.95 Excessive flexural demands applied to the upper column confinement layers adjacent to the cap beam soffit

Also, SG45 recorded low tensile strains of 20% of the steel yield strain, indicating that the tensile demand for the column cap beam joint was primarily absorbed by the U-straps and not by the column's interior longitudinal steel reinforcement in the joint. Strain gages SG46 and SG47 recorded low strains in the top two rows of the cap beam negative longitudinal reinforcement. Because of the presence of the two CFRP zero layers, the tensile demands were significantly reduced on the middle column-cap beam joint. Low compression strains were recorded by SG46 and SG47 as well. In the top region of the joint the compressive resistance was distributed to twelve #10 rebar and a very large cap beam width for any additional Whitney concrete compression block that may have been required for the test. The strain profile for SG44 is shown Figure 4.96. It should be noted, that the top portion of the middle column is the location of the first reinforcement yield point. This was indicated by strain gage SG44 and was also the first reinforcement yield location for the DRAIN-2DX pushover analysis. All the DRAIN-2DX pushover analysis concrete crushing points were eliminated from the entire cap beam due to the CFRP composite retrofit, as shown Figures 4.81 and 4.82.

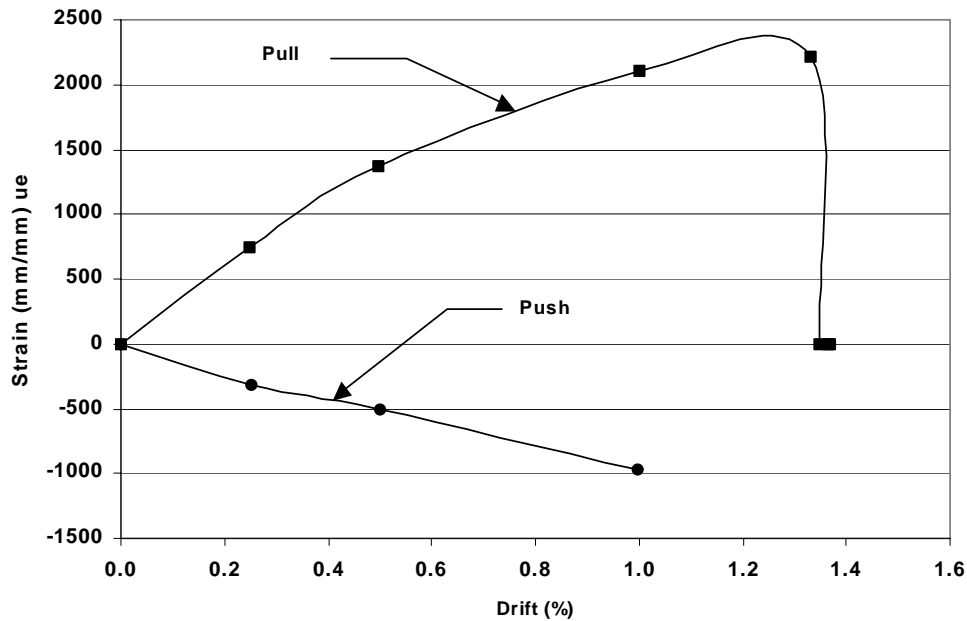


Figure 4.96 Column longitudinal reinforcement steel strain vs. drift for SG44

A moment curvature diagram was constructed for the Middle column-cap beam joint. The moment curvature behavior for the Middle column is typical as discussed previously for the East column. The moment curvature diagram for the Middle column-cap beam joint is shown in Figure 4.97. The curvature ductility was approximately $\mu = 4.7$.

Joint Longitudinal Reinforcement Steel Pullout

From onsite observations, there was no column longitudinal steel pullout. After the removal of the CFRP composite it was observed that there was no damage to the cap beam region in the Middle column-cap beam joint, as shown in Figure 4.90. Heavy damage was sustained in the top column portion of the top Middle joint.

Volumetric Change in Joint

A box configuration of LVDTs was placed around the top and bottom joint regions to monitor the volumetric change in the joints as they degraded during the test, as shown in Figure 4.95. Because most of the damage was sustained on the top portion of the middle column, there was only small volumetric change in the column cap beam portion of the middle column-cap beam joint for the push and pull cycles, as shown in Figure 4.98.

Table 4.13 describes the damage for the four performance levels and refers to the relevant Figure 4.99 for surface damage and Figure 4.100 after removal of the CFRP composite and cover concrete.

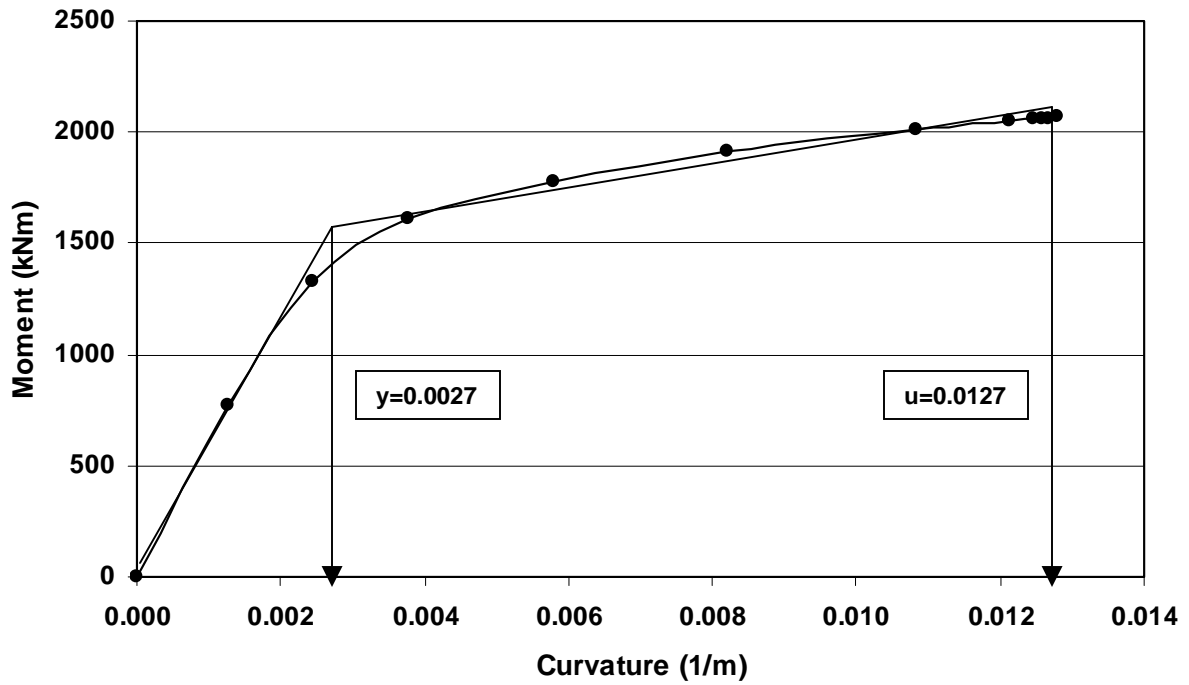


Figure 4.97 Moment curvature for the Middle column-cap beam joint

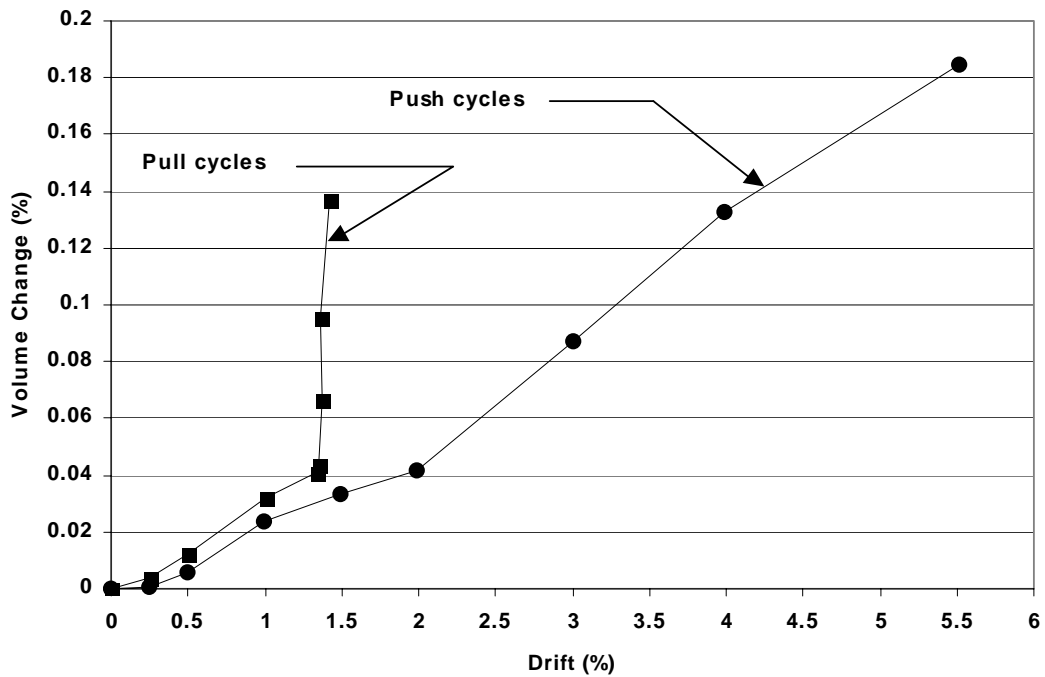


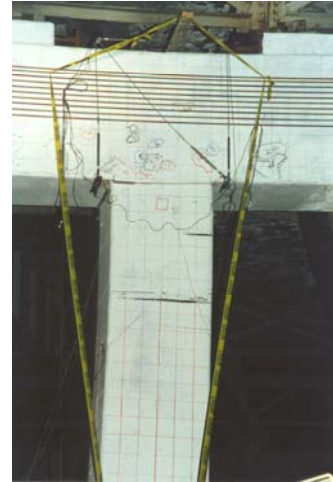
Figure 4.98 Volumetric change in the Middle column-cap beam joint

Table 4.13 Damage assessment matrix for the Middle column-cap beam joint

	Phase I $0 \leq \text{time} \leq 3,000$ $0\% \leq \text{drift} \leq 0.5\%$	Phase II $3,000 \leq \text{time} \leq 17,000$ $0.5\% \leq \text{drift} \leq 3.8\%$	Phase III $17,000 \leq \text{time} \leq 25,500$ $3.8\% \leq \text{drift} \leq 5.5\%$	Phase IV $\text{time} \geq 25,000$ $\text{drift} \geq 5.5\%$
Ankle Wrap or Diagonal Layers	No onsite documentation	Small pockets of CFRP composite delaminated on the cap beam section only. See Figure 4.99(a)	1) Additional phase II CFRP composite delaminated 2) Degradation to the top column's plastic hinge region. See Figure 4.99(b)	After the East and West U-straps failure full plastic hinge has developed in the upper column. See Figures 4.99(c)-(e)
Zero Layers.	No loss in tensile capacity	No loss in tensile capacity. See Figure 4.99(a)	No loss in tensile capacity. See Figure 4.99(b)	No loss in tensile capacity. See Figures 4.99(c)-(e)
U-Strap Layers	Small delaminating in cap beam region of joint.	Small delaminating in cap beam region of joint. See Figure 4.99(a)	Small additional delaminating in cap beam region of joint. See Figure 4.99(a)	U-straps remain in good condition throughout entire test. See Figures 4.99(d), (e)
Column CFRP Composite Confinement layers	No onsite documentation	1) Layers delaminate from columns 2) Lateral flexural damage to confinement layers as plastic hinge develops. See Figure 4.99(d)	Additional lateral flexural damage to phase II confinement layers as plastic hinge develops. See Figure 4.99(e)	Additional lateral flexural to phase III damage as plastic hinge fully develops. Full hinge has developed in lower middle column reducing demand at top of column
Longitudinal Bar Yielding	No apparent de-bonding of reinforcement bar.	1) No apparent de-bonding of reinforcement bar 2) Plastic hinge is beginning to form 2) All yielding occurred in phase II. See Figures 4.80 and 4.82	No apparent de-bonding of reinforcement bar. Further development of plastic hinge	No apparent de-bonding of reinforcement bar. Full plastic hinge developed in column



(a) $0.5\% \leq \text{drift} \leq 3.8\%$



(b) $3.8\% \leq \text{drift} \leq 5.5\%$



(c) $3.8\% \leq \text{drift} \leq 5.5\%$



(d) $\text{drift} \geq 5.5\%$



(e) $\text{drift} \approx 6.8\%$

Figure 4.99 Surface damage for Middle column-cap beam joint

After removal of the CFRP layers, onsite observations showed that the cap beam portion of the middle column-cap beam joint received no damage for the duration of the test. The extent of the damage sustained for the middle joint was absorbed entirely by the top column's plastic hinge region, as shown in Figure 4.100(a). Also, after the concrete cover was removed from the middle column-cap beam joint, onsite observation found that all the concrete cover was intact and there was no longitudinal reinforcement steel de-bonded and no gaps opened at the top of the rebar in the joint region, as shown in Figure 4.100(b).



(a) after removal of the CFRP composite



(b) after removal of the concrete cover

Figure 4.100 Internal damage for Middle column–cap beam joint

West Column-Cap Beam Joint: Mechanical and Material Evaluation

Ankle Wrap (Diagonal) Layers

Three strain gages SG68, SG69, and SG70 were placed on the ankle wrap layers, as shown in Figure 4.34. From Figure 4.101, the minimum and maximum strains for the push cycles were recorded on SG69; at a 5.5% push drift, the compression strain was $-815ue$; at a 1.4% drift the tension strain was $1619ue$. The failure to capacity strength for the compression strain was 18% and failure to capacity for tension was 18%. From onsite observations after the test, approximately 90% of the ankle wrap layers had delaminated from the as-built concrete, but there was no noticeable compression or tensile failure in the diagonal ankle layers. This indicates that there was a shear capacity reduction in the diagonal layers but they still provided some additional shear capacity for the joint for the full duration of the test, as shown in Figure 4.102.

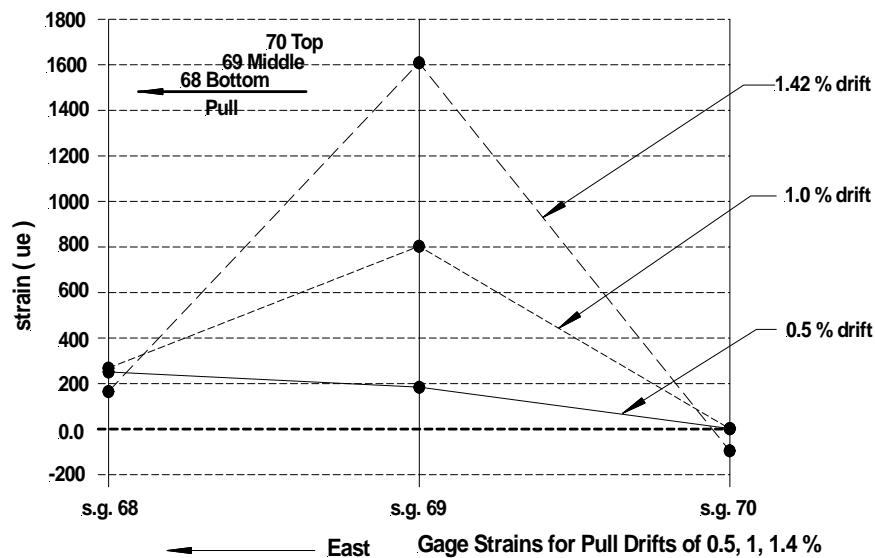


Figure 4.101 Cap-beam external CFRP composite diagonal 2 layers located in the West column-cap beam region: strain vs. %drift pull cycles for strain gages 68, 69, and 70



Figure 4.102 West column-cap beam joint ankle (diagonal) wrap and U-strap damage up to the maximum drift of 6.8%

U-Straps and Cap Beam Confinement Layers

It should be noted that no zero CFRP layers were applied to the West joint. Four strain gages SG 119, SG121, SG123, and SG124 were placed on the South face confinement layers that were adjacent to the West column-cap beam joint and the U-straps, as shown in Figure 4.34. A strain profile of the four strain gages for the push cycles is shown in Figure 4.103; SG124 recorded a maximum tensile failure strain of 34%. At a 3.0% drift ratio, strain gages SG123 and SG124 located on the U-straps recorded tensile strains of 830 $\mu\epsilon$ and 2650 $\mu\epsilon$, respectively; for 4.0% drift SG123 and SG124 recorded tensile strains of 1050 $\mu\epsilon$ and 2700 $\mu\epsilon$, respectively; and for the last recorded drift 5.5% SG123 and SG124 recorded tensile strains of 1850 $\mu\epsilon$ and 850 $\mu\epsilon$, respectively. As stated earlier, in the East column-cap beam section, it was observed that the U-straps failed at a drift ratio of 3.73% \approx 4.0%. Comparing the strain value differences for 4.0% and 5.5% for push drifts, SG124 shows a significant drop in strain while SG 123 recorded a significant increase in strain. This is the displacement drift at which the West U-strap on the West column-cap beam joint fails. Also, at 4.0% drift, the column longitudinal reinforcement steel begins to pick up additional strain as the U-straps start degrading. Unfortunately, the U-strap gages were applied to the middle-sections of the U-straps and did not reflect the ultimate failure tensile strain representative of the West edge of the West U-strap. The failure of the U-straps was caused by both tensile stress plus a bending moment stress.

For the pull cycles SG119, SG121, and SG124 show low strains for the entire test. Strain gage SG123 located on the East U-strap recorded a maximum tensile strain of 2100 $\mu\epsilon$ at 1.4% drift. The East U-strap failure mode for the two exterior columns is the same as outlined for SG124 for the pull cycles as laid out for the push cycles in the previous paragraph.

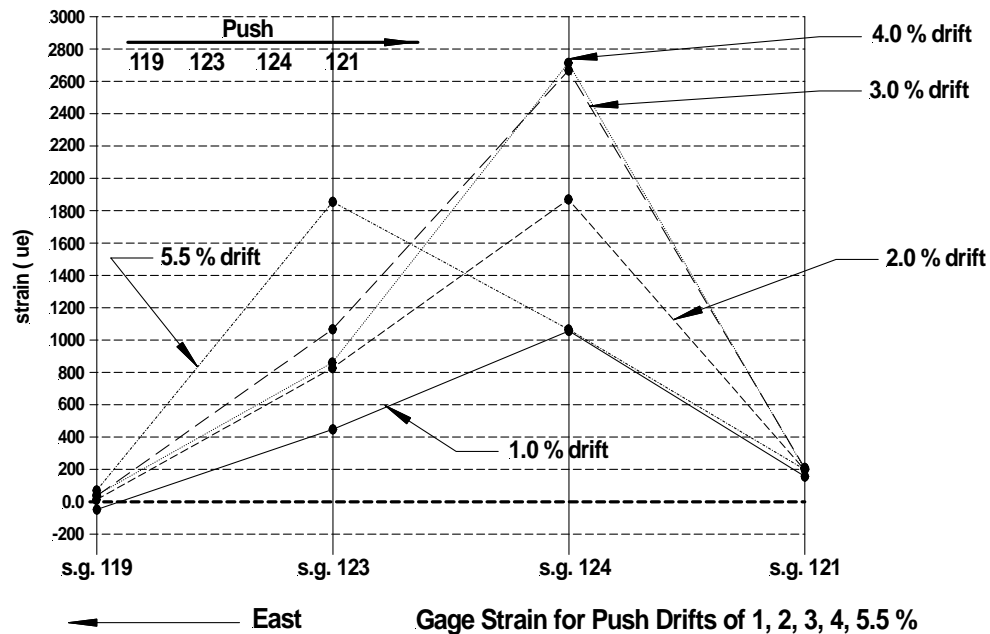


Figure 4.103 Push cycles for four CFRP composite layers SG119 and SG121; U-straps five layers SG123 and SG124

Strain gages SG119 and SG120 were applied to the vertical middle section of the four confinement layers adjacent to the column-cap beam joint. As described for the Middle column-cap beam joint, the middle layer demand is small compared to the demand placed at the corners for rectangular sections. As shown in Figure 4.103, the demand for SG119 was near zero for the complete test.

Yielding Reinforcement Steel and Concrete Crushing

Both strain gages SG63 and SG64 were attached to the column longitudinal reinforcement steel in the West column-cap beam joint, as shown in Figure 4.35. Strain gage SG63 was installed in the East column face approximately 305mm below the cap beam soffit. Strain gage SG64 was located approximately at the mid-section in the cap beam section of the West column-cap beam joint. Both SG63 and SG64 showed high tensile yield strains of 111% and 108% of the steel yield strain. This concurs with onsite observations of high flexural stresses and tensile stresses in the plastic hinge region of the upper column and cap beam after the carbon layers were removed from the West column-cap beam joint, as shown in Figure 4.104. Before the ultimate strain in the reinforcement steel could be reached, the rebar de-bonded from the concrete in the joint region and the strains began to reduce approximately at a drift ratio of 5.0%. After the U-strap failure, estimated at approximately 4.0% drift, the column longitudinal reinforcement steel in the column-cap beam region continued to pick up strain indicating that there was no rebar debonding at 4.0% drift, the beginning failure drift point for the U-straps.

After the complete failure of the U-straps at 5.0% drift, the bond capacity of the longitudinal reinforcement was reached and the reinforcement steel strains began to reduce, as shown in Figure 4.105. A comparison made between the As-built and Retrofitted DRAIN-

2DX pushover analysis shows that the yield patterns are different. Also, concrete crushing was reduced and additional longitudinal tensile demands were placed on the cap beam for the retrofitted design, as shown in Figures 4.81 and 4.82. This was typical for the East, Middle, and West column-cap beam joints. The moment curvature diagram for the West column-cap beam joint had typical moment curvature behavior as discussed in the East column section. The moment curvature diagram for the West column-cap beam joint is shown in Figure 4.106. The moment curvature was approximately $\mu = 4.3$.



Figure 4.104 West column-cap beam joint after CFRP composite layers were removed exposing moderate flexural stresses in the plastic hinge regions of the upper column

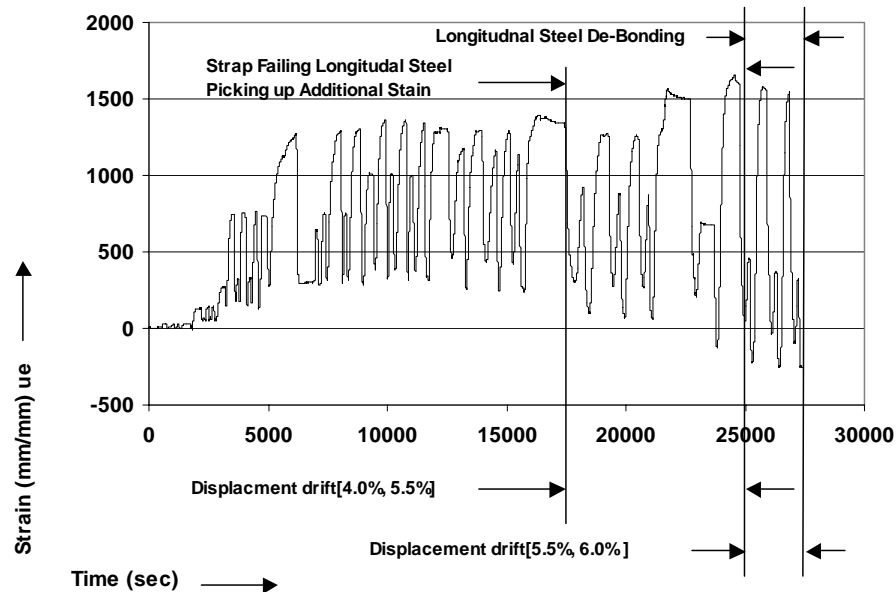


Figure 4.105 Degradation transition of the U-straps and column longitudinal reinforcement steel bond capacity

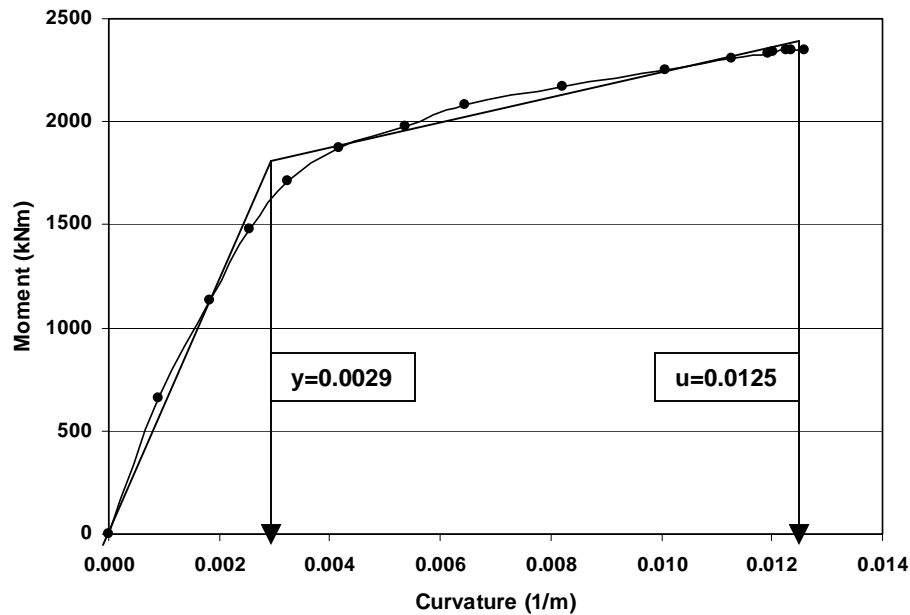


Figure 4.106 West column-cap beam moment curvature

Column Longitudinal Reinforcing in the Joint Steel Pullout

From onsite observations it was noted that there was a 16mm gap at the top of the column's longitudinal steel, as shown in Figure 4.107. The column longitudinal steel bond strength capacity was reached at approximately a 5.0% drift ratio. Once the U-straps had completely fractured, all the tensile demand was transferred to the longitudinal steel reinforcement, as shown in Figure 4.105. The West U-strap completely fractured and the total tensile demand was transferred to the column longitudinal reinforcement in the joint; the bond strength was exceeded and the joint lateral force capacity severely diminished. The failure mode for the West and East cap-beam joints was the same.

Cap Beam Flexural Crack

There was additional damage sustained on the cap beam slightly east of the West column cap beam joint. A tension crack formed starting at the top elevation of the cap beam at a distance of 1.73m from the East edge of the column. From onsite observations, the crack started to develop at approximately 4.0% drift, as shown in Figure 4.108; the crack propagated at a vertical descent adjacent and parallel to the cap beam CFRP composite confinement layers until reaching the soffit of the cap beam, as shown in Figure 4.109. This is also the East end point of the bottom row of 4-#10 rebar in the double row of negative moment longitudinal reinforcement steel installed at the top elevation of the West joint of the cap beam, as shown in Figure 4.110. The crack continued to propagate diagonally and had completely developed at a displacement drift of 5.5%. The ending point of the diagonal portion was approximately 1.0m east of the East face of the West column at an elevation approximately 280mm vertically up from the soffit of the cap beam.



Figure 4.107 Debonded column longitudinal bar observed in the joint after the concrete cover was removed from the West column-beam joint

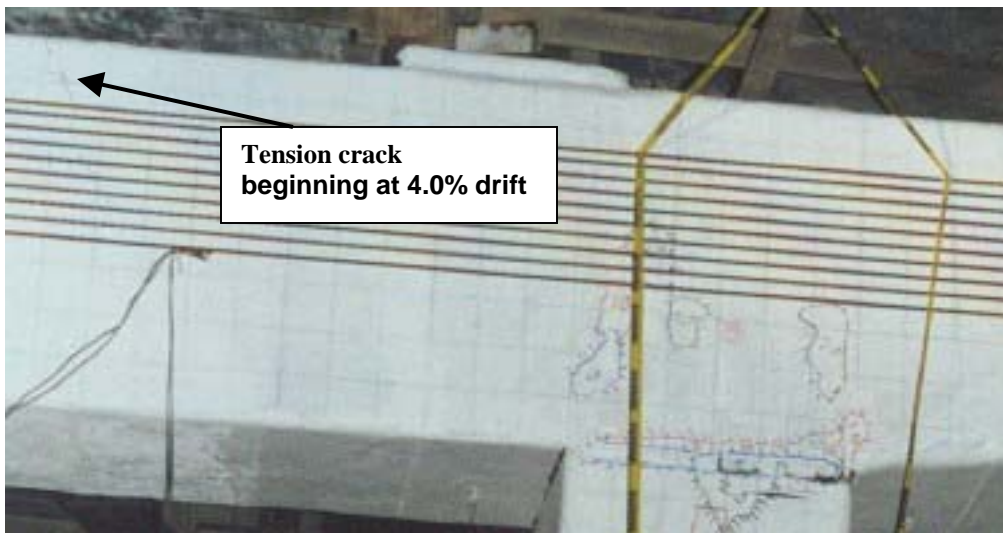


Figure 4.108 Beginning of the tension crack at 4.0% displacement drift



Figure 4.109 Flexural tension cracked cap beam section east of the West column: beginning at 4.0% drift ratio and ending at 5.5% drift

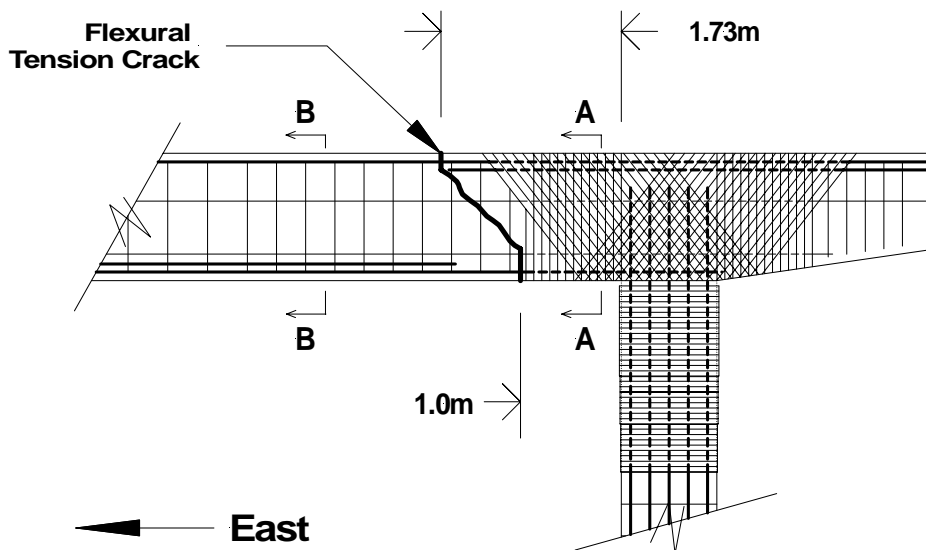


Figure 4.110 Tension crack relative to the negative moment longitudinal reinforcement steel and the CFRP confinement adjacent to the West column

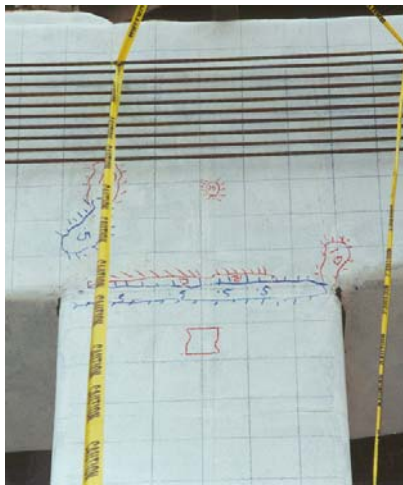
As stated earlier, the flexural tension crack began at the East end of the bottom row of the 4-#10 rebar located at the top of the cap beam negative reinforcement steel, but this also shows that the top row of the 8-#10 rebar had to yield for the crack to be able to begin. Also, the vertical last portion of the crack that ran adjacent to the CFRP composite was approximately the same height as the compression block estimated from the DRAIN-2DX as 254mm.

The size of the negative moment at 1.73m east of the East face of the West column, where the flexural tension crack first began, was estimated as 2,118kNm or 72% of the maximum negative moment located on the center cap beam West joint. This was the most likely region to fail because of the high negative moment and the insufficient tensile steel reinforcement and the absence of CFRP composite zero layers to develop enough tensile capacity in the top elevation of the cap beam to prevent yielding. From simulation results (Duffin 2003), it can be theorized that the flexural tension crack could have been prevented if two CFRP composite layers were applied to both the North and South faces of the cap beam.

Table 4.14 describes the damage for the four performance levels and refers to the relevant figures following the Table in Figures 4.111 for surface damage, Figure 4.112 after removal of the CFRP composite, and Figure 4.113 after removal of the CFRP composite and cover concrete.

Table 4.14 Damage assessment matrix of the West column-cap beam joint

	Phase I $0 \leq \text{time} \leq 3,000$ $0 \leq \text{drift} \leq 0.5$	Phase II $3,000 \leq \text{time} \leq 17,000$ $0.5 \leq \text{drift} \leq 3.8$	Phase III $17,000 \leq \text{time} \leq 25,500$ $3.8 \leq \text{drift} \leq 5.5$	Phase IV $\text{time} \geq 25,000$ $\text{drift} \geq 5.5$
Ankle Wrap or Diagonal Layers	No onsite documentation	At 1.0 drift small delaminating on cap beam around U-strap region. See Figure 4.111(a)	Additional delaminating to phase II. See Figure 4.111(b)	Some additional delaminating layers to phase III, but joint stress reduces after U-straps fracture and rebar de-bonds. See Figure 4.111(c)
U-Strap Layers and cap beam confinement layers	No degradation of U-straps. See Figure 4.111(a)	U-straps begin to fail at approximately 3.73% drift.	Failure of the West U-continues until 5.5% drift. See Figures 4.105 and 4.111(b)	Complete fracture of West U-strap. Further degradation would have occurred on the East U-strap but maximum drift for pull cycle was 1.4% See Figure 4.111(c)
Confinement Layers	No lateral flexural cracks formed in CFRP composite layers	Lateral flexural cracks in confinement layers begin approximately 1.0% drift	Lateral flexural cracks do not increase after U-straps begin to fail and rotation is transferred to the bottom grade beam joint	Lateral flexural cracks do not increase after U-straps begin to fail and rotation is transferred to the bottom grade beam joint
Longitudinal Bar Yielding and column bar pullout	No yielding from strain gages	1) No yielding in strain gages 2) All yielding occurred in phase II. See Figure 4.80	The column longitudinal reinforcement in the column and in cap beam yielded SG63 and SG64 at 4.0% drift. See Figure 4.105	1) Longitudinal rebar pulled out at 5.5%. See Figure 4.107 2) Longitudinal bar de-bonded before concrete demand was greater than the confined concrete capacity
Cap beam tension crack	No cracking	No cracking	Lateral flexural crack begins at the top elevation of cap beam at 4.0% drift and continues to crack to the soffit of cap beam at 5.5% drift. See Figures 4.108-4.109	1) Complete failure of cap beam prevented by additional support from road deck diaphragm. See Figure 4.112 2) Light damage inside reinforcement cage due to the de-bonding of the rebar reducing the bending stresses in both the cap beam and the plastic hinge region of the column. See Figure 4.113



(a) $0.5\% \leq \text{drift} \leq 3.8\%$



(b) $3.8\% \leq \text{drift} \leq 5.5\%$



(c) $\text{drift} \geq 5.5\%$

Figure 4.111 Surface damage for West column-cap beam joint



Figure 4.112 Cap beam reinforced by road deck diaphragm system preventing complete failure



(a) East face after concrete cover was removed



(b) North face after concrete cover was removed

Figure 4.113 Internal damage for West column–cap beam joint

Assessment of the East Colum -Grade Beam Joint

Confinement Layers

Eight strain gages SG5, SG6, SG7, SG8, SG9, SG10, SG11, and SG12 were installed around the midsection of the bottom fourteen CFRP composite confinement layers, as shown in Figure 4.31. Comparing SG8 and SG9 for the East-West faces and comparing SG6 and SG11 for the North-South faces, it was recorded that the confinement layers separated from the column faces approximately at 1.5% and 2.0% drift displacements. Even though the CFRP composite layers and column faces were detached, effective confinement was provided at the corners of the column in the lap splice region, as stated earlier. The flexural and shear capacity was enhanced by two modifications made to the bottom region of the column joint. First, the flexural stiffness was increased at the base of the column from the 14 CFRP composite layers that were applied to the base of the column. Second, after the 14 layers of CFRP composites were applied to the plastic hinge region, a R/C grade beam overlay was cast around all three East, Middle, and West column bases. The new grade beam elevation was set at 305mm above the original pile cap, as shown in Figures 4.16-4.18. A 13mm Teflon (HDPE) thick bushing was installed around the base of the columns to prevent damage to the bottom CFRP composite layers, as shown in Figure 4.17. The bushing acted as a cushion between the base CFRP composite layers and grade beam concrete, but the rigidity of column-grade beam joint was still significantly increased from the as-built design.

The column lap splice height above the top surface of the pile cap elevation of the as-built design was 813mm, as shown in Figure 4.7. Eight strain gages were installed at approximately 686mm above the as-built pile cap elevation, as shown in Figure 4.31. The small strains that were recorded were representative of the hoop stresses around the lap splice region. Strain gages SG9 and SG7 recorded maximum tensile and compressive strains around the middle of the 14 confinement layers as 11% of the CFRP tensile failure strain, and 9% of the CFRP compressive failure strain, respectively.

Yielding of Steel Reinforcement and Concrete Crushing

The recorded maximum tensile and compressive longitudinal reinforcement steel strains, located at the base of the column, for the retrofitted Bent #6S 2000 East column (closest column to the load frame) base were recorded at 3% and 88% of the reinforcement steel yield strain, respectively; the recorded maximum tensile and compressive yield strains for the as-built Bent #5S 2000 West column (closest column to the load frame) base were recorded at 170% and 75% of the reinforcement yield strain, respectively. Comparisons between the as-built and retrofitted design indicate that there was a reduction in the tensile demand applied to the lap splice bars of the retrofitted column due to the additional confinement clamping of the CFRP composite 14 layers.

There are three specific reasons why the CFRP seismic retrofit significantly strengthened the column lap splices. First, the CFRP confinement layers provided additional clamping capacity to the lap splice. Second, the 14 CFRP confinement layers added additional flexural stiffness to the lap splice top region and the elevation of the plastic hinge was transferred above the lap splice elevation. Last, by increasing the new

retrofitted grade-beam elevation to 305mm above the pile cap provided additional shear capacity, flexural stiffness, and confinement to the lap splice.

There was no observed cracking in the new Bent #6S 2000 grade beam overlay that encapsulated the column-grade beam joints. Two contributions prevented failure at the column-grade beam joints. First, the Teflon (HDPE) bushing that encapsulated the bottom of the column provided a cushioning effect between the columns and the retrofitted grade beam. It was observed that cracks appeared in the grade beam of the as-built Bent #5S 2000 test for smaller displacements compared to the large displacements imposed in the Bent #6S 2000 test. The connection between the new grade beam retrofit and the column faces for the Bent #5S 2000 structure was a concrete-to-concrete interface. The new column-cap beam connection was very rigid. The cracks were discussed in Chapter 3, with respect to Figures 3.22 and 3.33. Second, the Dywidag bars transferred the column-grade beam moments to the composite pile system, as shown in Figure 4.16. Further information on the grade beam and Dywidag retrofit scheme can be obtained in (Cook et al. 2002) and (Ward 2001). The moment-curvature diagram for the bottom East column is shown in Figure 4.114. The moment curvature is approximately $\mu = 13.2$, which is 3.4 times that of the east column-cap beam joint.

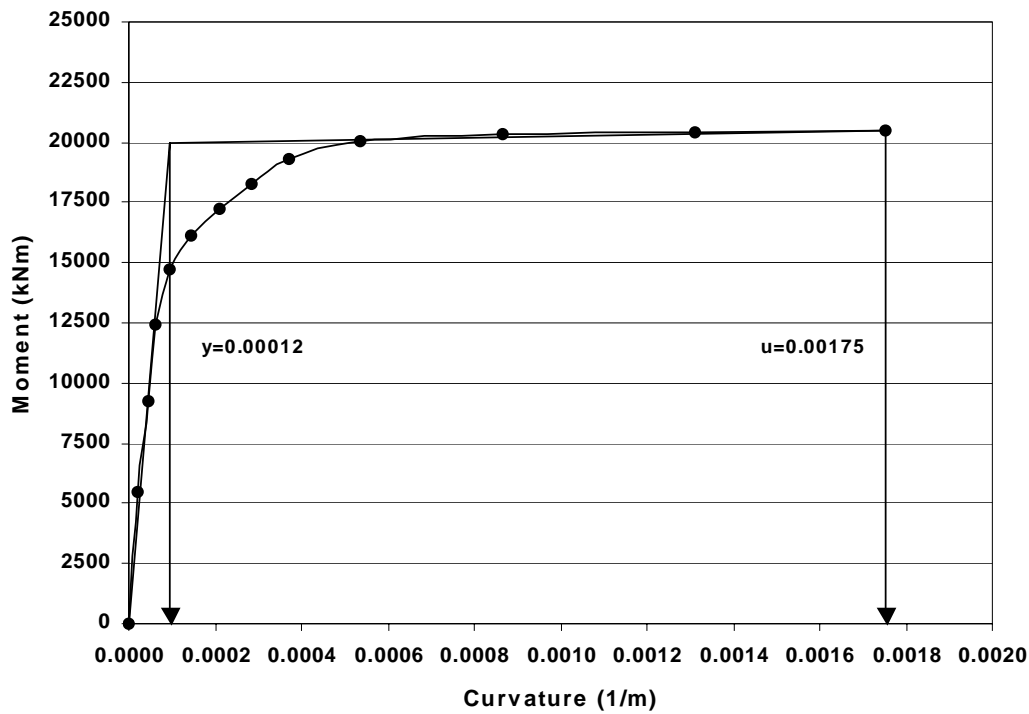
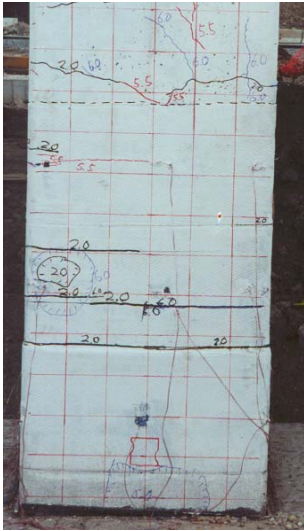


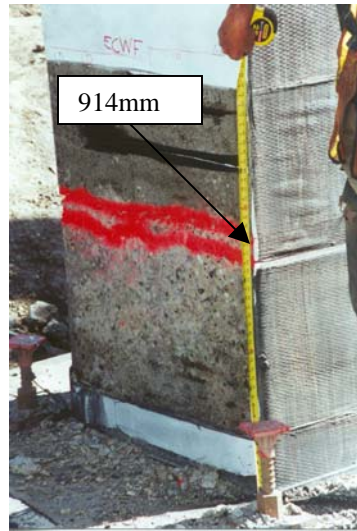
Figure 4.114 Moment curvature diagram for the East column grade beam joint

Table 4.15 Damage assessment matrix for the East column-grade beam joint

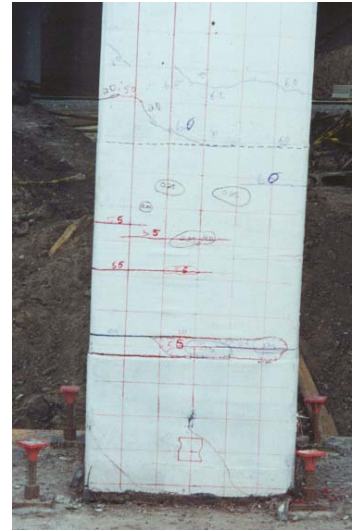
	Phase I $0 \leq \text{time} \leq 3,000$ $0\% \leq \text{drift} \leq 0.5\%$	Phase II $3,000 \leq \text{time} \leq 17,000$ $0.5\% \leq \text{drift} \leq 3.8\%$	Phase III $17,000 \leq \text{time} \leq 25,500$ $3.8\% \leq \text{drift} \leq 5.5\%$	Phase IV $\text{time} \geq 25,500$ $\text{drift} \geq 5.5\%$
Confinement layers	Hairline lateral flexural cracks beginning in the 3 layers above the lap splice region.	1) Lateral flexural cracking at 2.0% drift was transferred above the lap splice region. See Figure 4.115(c) 2) Confinement layers separate from column faces.	Additional lateral flexural cracking was added to phase II. See Figure 4.115(b)	1) Additional lateral flexural cracking was added to phase III 2) Flexural cracks formed in the unconfined concrete portion of the column above the confinement layers. See Figures 4.115(b) and 4.115(c)
Longitudinal Bar Yielding and Concrete Crushing an column bar pullout	No damage	All yielding and concrete crushing occurred in phase II. See Figure 4.80	NA	NA
Lap-splice pull-out	No damage	No damage	No damage	1) Slight amount of bar pull out on the East side of the column base after 6.0% drift. 2) Observe the difference in elevation between the East and West column base elevations. See Figure 4.115(f)
Fixed end column-cap beam and fixed end column-grade beam joints	Column end connections are fixed-fixed. See Figure 4.115(d)	Column end connections are fixed-fixed. See Figure 4.115(d)	NA	NA
Hinged end column-cap beam and fixed end column-grade beam joints	NA	NA	Column connections are plastic hinged-hinged. Column has curvature at bottom plastic hinge region. See Figure 4.115(e)	NA
Hinged end column-cap beam and semi fixed at the column-grade beam	NA	NA	NA	Column connections are semi fixed-hinged hinged. The column straightens and un-even gap at the column-grade beam interface. See Figure 4.115(f)



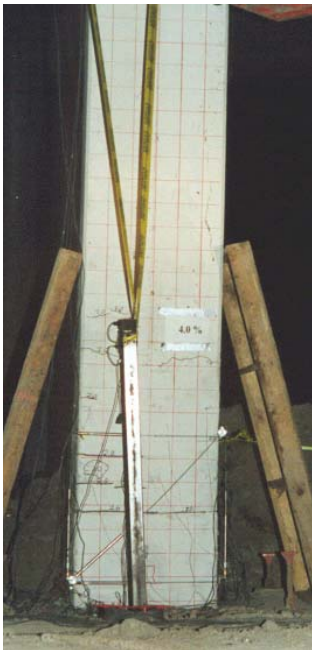
(a) Flexural cracking



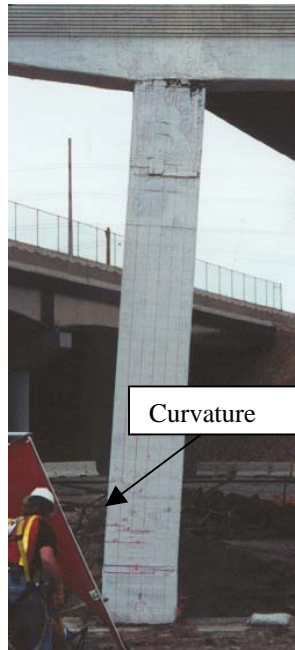
(b) Flexural cracking



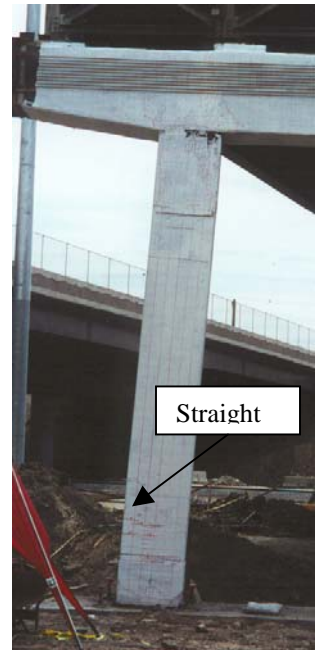
(c) Lap splice pull-out



(d) Fixed-fixed



(e) Fixed-hinged



(f) Semi fixed-hinged

Figure 4.115 Surface damage and deterioration for East column-grade beam joint

Assessment of the Middle Column-Grade Beam Joint

Confinement Layers

Three groups of eight strain gages were installed around the mid-sections of the 14, 3, and 2 CFRP composite confinement layers applied to the bottom portion of the Middle column as shown in Figure 4.31. Comparing the SG22 and SG23 for the East-West faces and comparing SG20 and SG25 for the North-South faces hoop strains in the bottom 14 confinement layers, the confinement layers on the East-West faces separated at approximately a 3.0% displacement drift, but the North-South layers stayed attached for the full duration of the first test day up to a 5.5% displacement drift. The maximum tensile strain recorded by SG23, and compressive strain recorded by SG24 in the 14 layer hoop were 15% and 12% of the CFRP tensile and compressive failure strains, respectively. A strain profile for the push drift cycles and tension-compression profile is shown in Figure 4.116.

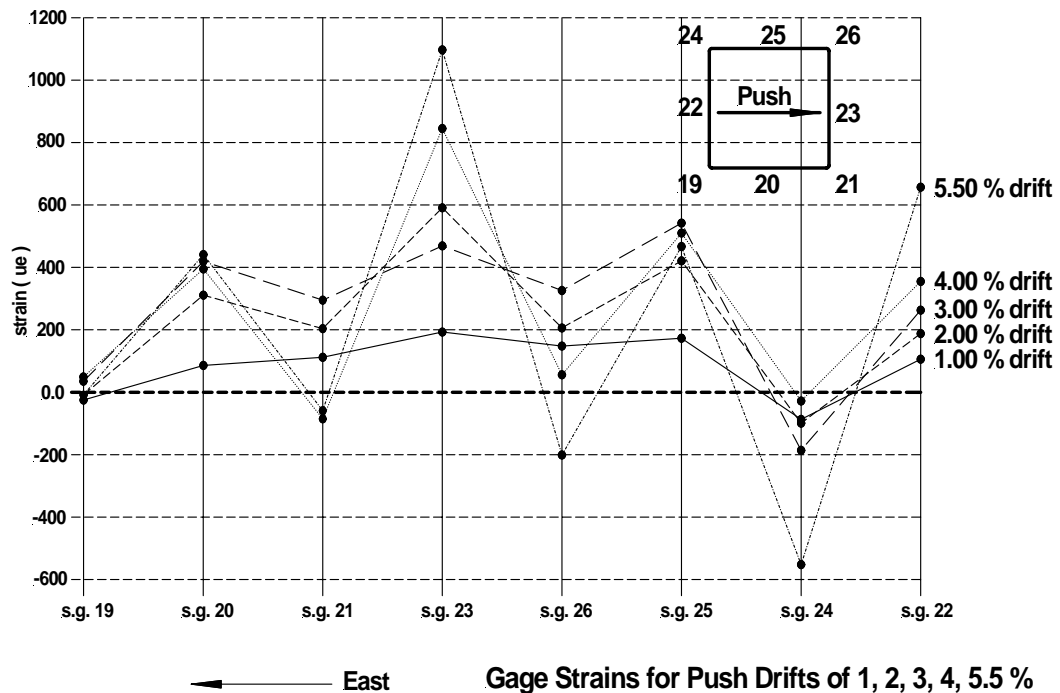


Figure 4.116 Column external CFRP composite 14 confinement layers located on the Middle column bottom region: strain vs. %drift push cycles for strain gages 19, 20, 21, 23, 26, 25, 24, and 22

Comparing the SG105 and SG101 for the East-West faces and comparing SG99 and SG103 for the North-South faces hoop strains in the middle 3 confinement layers, the confinement layers on the East-West faces and North-South layers stayed attached up to 4.0% displacement drift. The maximum tension strain recorded by SG103 and compressive strain recorded by SG100 in the 3 layer hoop were 21% and 7% of the CFRP tensile and compressive failure strains, respectively. Comparing the SG113 and SG109 for the East-West faces and comparing SG107 and SG111 for the North-South faces hoop strains in top 2 confinement layers, the confinement layers on the North-South

faces separated at approximately 1.5% displacement drift, but the East–West layers stayed attached for the full duration of the first test day up to a 5.5% displacement drift. The maximum tension recorded by SG107 and compressive recorded by SG106 on the 2 layer CFRP were 30% and 46% of the tensile and compressive failure strains, respectively. A strain profile for the push drift cycles and tension-compression profile is shown in Figure 4.117.

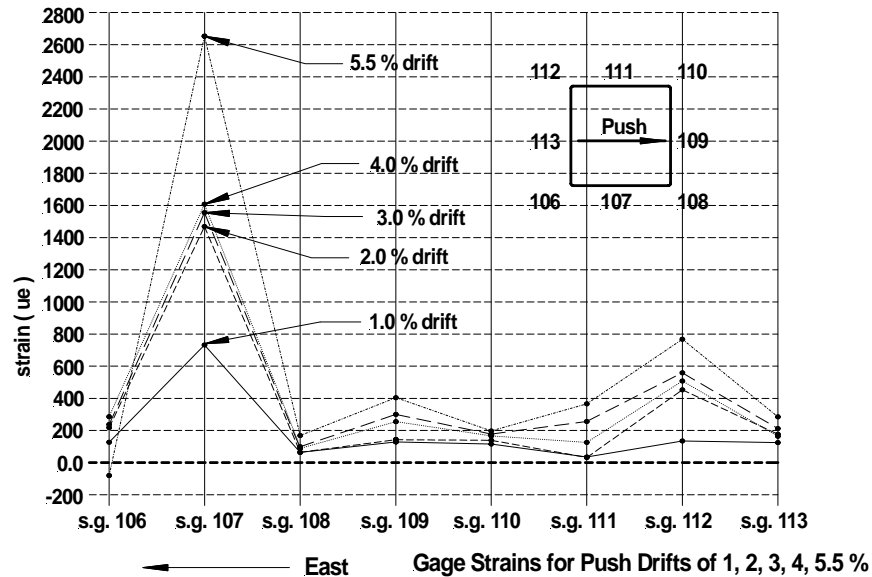


Figure 4.117 Column external CFRP composite 2 confinement layers located on the Middle column bottom region: strain vs. %drift push cycles for strain gages 106, 107, 108, 109, 110, 111, 112, and 113

The low hoop strains indicate that the demand for all confinement layers was very low. CFRP strains at strain gages SG106 and SG207 had failure safety factors in tension and compression of approximately 3.3 and 2.2, respectively. The additional flexural stiffness, shear, and contributions from the confinement layers and grade beam retrofit is similar to the analysis discussion for the confinement layers of the East column.

Yielding Reinforcement Steel and Concrete Crushing

The recorded maximum tensile and compressive yield strains for the retrofitted Bent #6SS 2000 Middle column base were recorded on SG17 as 108% and 12%, respectively; the recorded maximum tensile and compression yield strain for the as-built Bent #5 Middle column base was 115% and 108%, respectively. This suggests that the bottom confinement layers reduced the stress in the lap splice region of the middle column as described in the East column Yielding and Reinforcement section. The moment curvature for the Middle columns is shown in Figure 4.118. The behavior is similar to the moment curvature for the East column base. The curvature ductility was approximately $\mu = 27$, which is 5.7 times that of the middle column top.

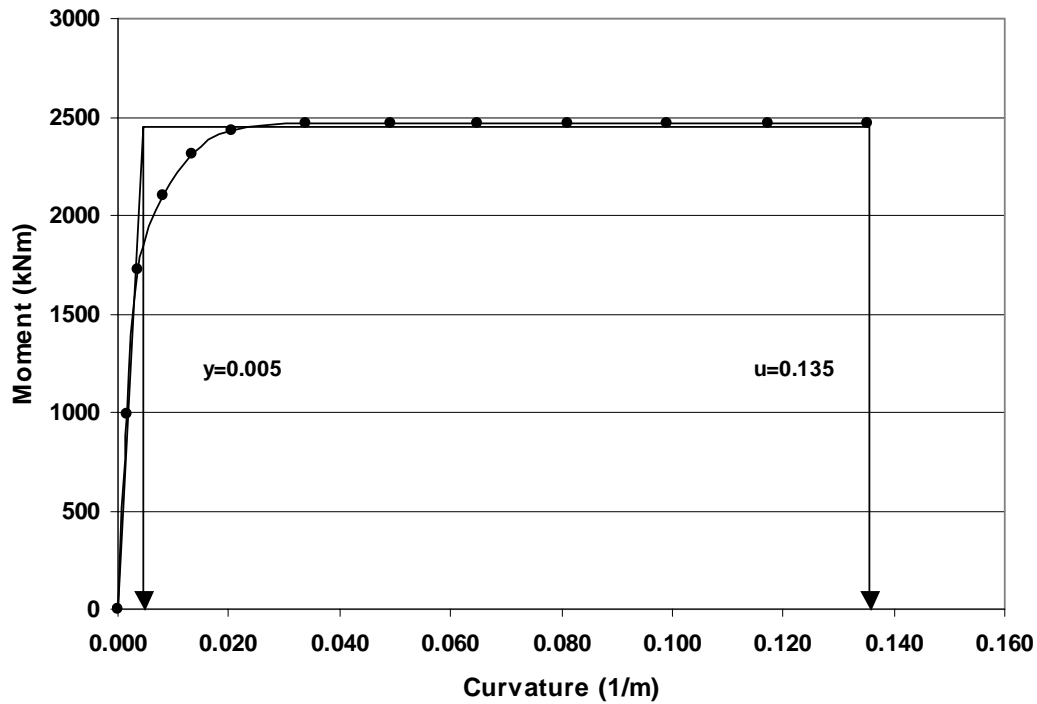


Figure 4.118 Moment curvature diagram for the Middle column–grade beam joint

Volumetric Change in Bottom Column-Grade Beam Joint

As stated earlier, a box configuration of LVDTs was placed around the bottom joint region to monitor the volumetric change in the lap splice as it degraded during the test. Because most of the damage was sustained above the lap splice region, there is only a small volumetric change in the column directly above the column-grade beam joint. The volumetric change in the push was basically zero so only the pull cycles are presented, as shown in Figure 4.119. However, this volumetric change was three times greater than the recorded volume change located at the top of the column.

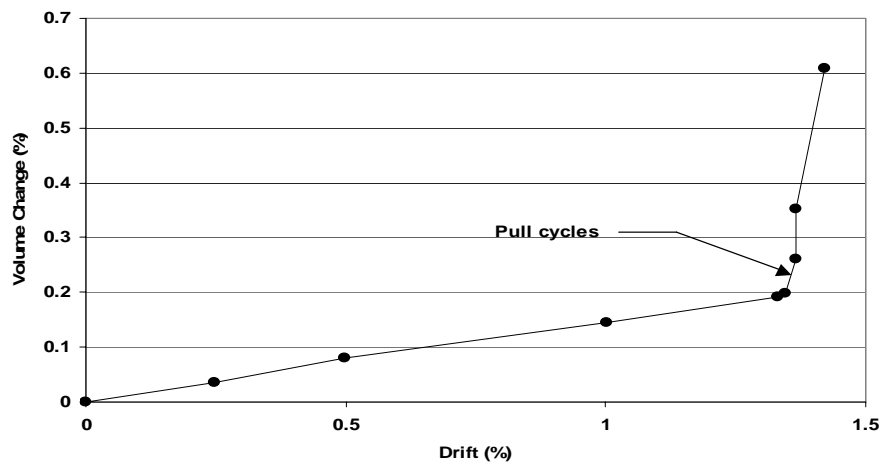
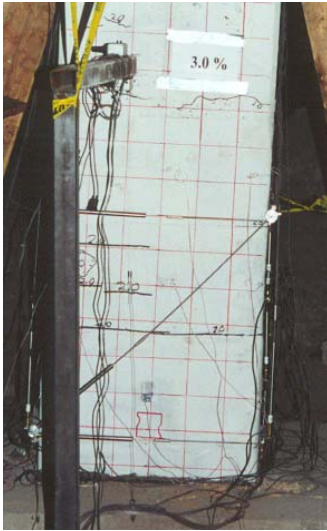


Figure 4.119 Volumetric change in the bottom Middle column-grade beam joint

Table 4.16 Damage assessment matrix for the Middle column-grade beam joint

	Phase I $0 \leq \text{time} \leq 3,000$ $0\% \leq \text{drift} \leq 0.5\%$	Phase II $3,000 \leq \text{time} \leq 17,000$ $0.5\% \leq \text{drift} \leq 3.8\%$	Phase III $17,000 \leq \text{time} \leq 25,500$ $3.8\% \leq \text{drift} \leq 5.5\%$	Phase IV $\text{time} \geq 25,500$ $\text{drift} \geq 5.5\%$
Confinement layers	Hair line lateral flexural cracks beginning in the 3 layers above the lap splice region	1) Lateral flexural cracking at 2.0% drift was transferred above the lap splice region. See Figure 4.120(b) 2) Confinement layers separate from column faces.	1) Additional Lateral flexural cracking was added to phase II. 2) Plastic hinge is fully developed	1) Additional lateral flexural cracking was added to phase III
Longitudinal Bar Yielding and Concrete Crushing and column bar pullout	No damage	1) All yielding and concrete crushing occurred in phase II. See Figure 4.80 2) SG 17 yielded at 2.0% drift	NA	NA
Lap-splice pull-out	No damage	No damage	No damage	Slight amount of bar pull out on the East side of the column after 6.0% drift. See Figure 4.120(d)
Fixed end column-cap beam and fixed end column-grade beam joints	Column end connections are fixed-fixed. See Figure 4.115(d)	1) Double curvature formed for a fixed-fixed column 2) Plastic hinges developed in the top portion and the bottom portion of the 3 layers above as-built plastic hinge region in the middle column at 3.73% drift. See Figure 4.120(b)	NA	NA
Plastic hinged end column-cap beam and plastic hinged end column-grade beam joints	NA	NA	Column connections are plastic hinge-plastic hinged. Column has curvature at bottom region. See Figure 4.115(e)	NA
Hinged end column-cap beam and semi fixed at the column-grade beam	NA	NA	NA	Column connections are semi-fixed-plastic hinged. The column straightens and uneven gap at the column-grade beam interface. See Figures 4.120(d), 4.120(e)



(a) $0.5\% \leq \text{drift} \leq 3.8\%$
Flexural cracking
above plastic hinge



(b) Flexural cracking after
confinement layers were
removed



(c) $\text{drift} \geq 6.0\%$ Lap splice pull-out



(d) $0.5\% \leq \text{drift} \leq 3.8\%$ Double curvature



(e) $\text{drift} \geq 6.0\%$ Full development of top and
bottom plastic hinges

Figure 4.120 Surface damage and deterioration for East column-grade beam joint

Assessment of the West Column-Grade Beam Joint

Confinement Layers

No confinement layer instruments were installed on the West column base for the Bent #6S 2000 test. From the onsite observations and analysis of the East and Middle column base CFRP layers, it is assumed that the tensile and compression failure strains would be comparable to the other two columns for the West column confinement layers. It was not known if the confinement layers detached from the column faces, but as discussed in the previous sections, it is evident that adequate confinement and lap splice clamping was provided to the West column lap splice region.

Yielding Reinforcement Steel and Concrete Crushing

The recorded maximum tensile and compressive strains for the retrofitted Bent #6S 2000 West column (furthest column from the load frame) base was recorded at 73% and 50% of yield; the recorded maximum tensile and compressive strains for the as-built Bent #5S 2000 East column (furthest column to the load frame) base was recorded at 72% and 54% of yield, respectively. Comparison between the as-built and the retrofitted bent strains shows that they are approximately equivalent. It should be noted, however, that the maximum drift displacement for the Bent #6S 2000 test was 6.8% where the maximum drift for the Bent #5S 2000 test was 3.75% or an 81% increase in displacement for the Bent #6S 2000 test. The overall stresses in the East, Middle, and West lap splice regions had been reduced due to the 14 layers of CFRP composite confinement layers. The 14 composite layers had significantly increased the capacity of the West column plastic hinge region.

A moment curvature analysis was performed for the base of the West column. The moment curvature for the West column is shown in Figure 4.121; the curvature ductility was approximated as $\mu = 21$, which is 4.9 times larger than that of the West column top.

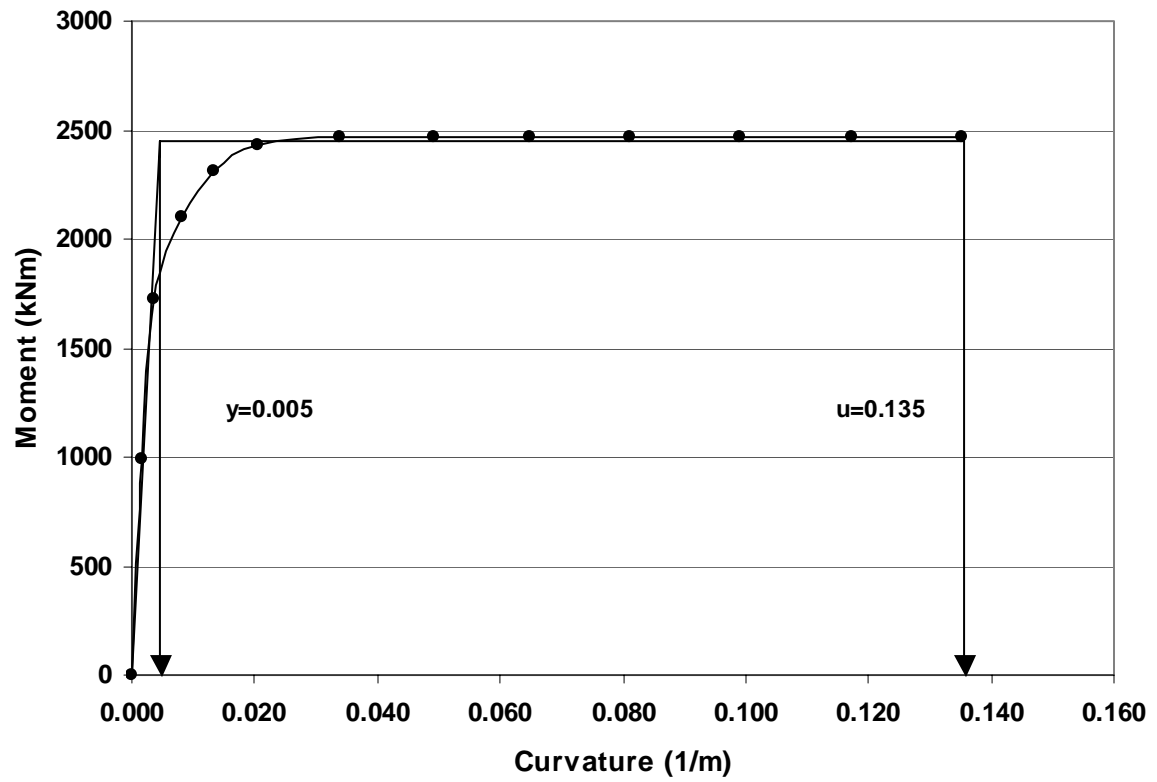
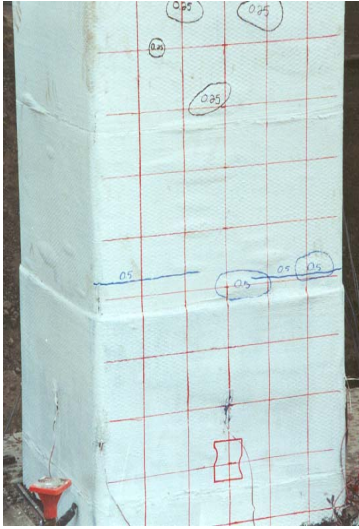


Figure 4.121 Moment curvature diagram for the West column-grade beam joint

Table 4.17 Damage assessment matrix for the West column-grade beam joint

	Phase I $0 \leq \text{time} \leq 3,000$ $0\% \leq \text{drift} \leq 0.5\%$	Phase II $3,000 \leq \text{time} \leq 17,000$ $0.5\% \leq \text{drift} \leq 3.8\%$	Phase III $17,000 \leq \text{time} \leq 25,500$ $3.8\% \leq \text{drift} \leq 5.5\%$	Phase IV $\text{time} \geq 25,500$ $\text{drift} \geq 5.5\%$
Confinement layers	Hairline lateral flexural cracks beginning in the 3 layers above the lap splice region.	1) Lateral flexural cracking at 2.0% drift was transferred above the lap splice region. See Figure 4.122(a)	Additional lateral flexural cracking were added to phase II. See Figure 4.122(b)	1) Additional lateral flexural cracking was added to phase III 2) Flexural cracks formed in the unconfined concrete portion of the column above the confinement layers. See Figures 4.122(b) and 4.122(c)
Longitudinal Bar Yielding and Concrete Crushing and column bar pullout	No damage	All yielding and concrete crushing occurred in phase II. See Figure 4.80	NA	NA
Lap-splice pull-out	No damage	No damage	No damage	1) Slight amount of bar pull out on the East side of the column base after 6.0% drift. 2) Observe the difference in elevation between the East and West column base elevations. See Figure 4.122(d)
Fixed end column-cap beam and fixed end column-grade beam joints	Column end connections are fixed-fixed. See Figure 4.122(d)	Column end connections are fixed-fixed. See Figure 4.122(d)	NA	NA
Hinged end column-cap beam and fixed end column-grade beam joints	NA	NA	Column connections are plastic hinged-hinged. Column has curvature at bottom plastic hinge region. See Figure 4.122(e)	NA
Hinged end column-cap beam and semi fixed at column-grade beam joint	NA	NA	NA	Column connections are semi fixed-hinged. The column straightens and uneven gap at the column-grade beam interface. See Figure 4.122(f)



(a) Flexural cracking



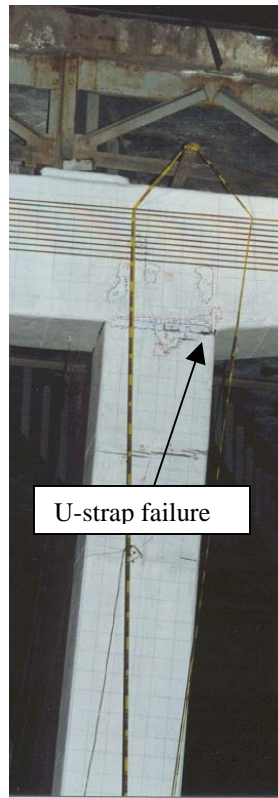
(b) Flexural cracking



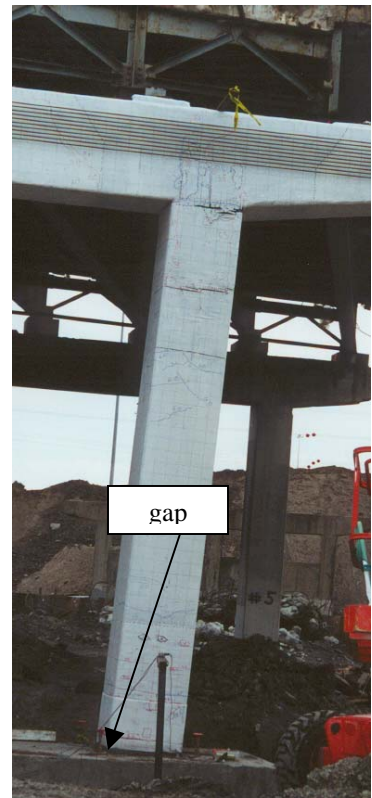
(c) Lap splice pull-out



(d) Fixed-fixed



(e) Fixed-hinged



(f) Semi fixed-hinged

Figure 4.122 Surface damage and deterioration for West column-grade beam joint

Overall Bent #6S 2000 Test Damage Assessment

At approximately 3.0% drift all of the cap beam joint rotation was transferred to the column-grade beam joints of the structure. The column-grade beam joint moment demand was constant for drifts between $3.0\% \leq \text{drift} \leq 4.6\%$. The strain in the reinforcing steel, located at the plastic hinge region, continued to increase and plasticize up to a displacement drift ratio of approximately 6.0%. However, the column deflected shape remained in double curvature for drifts between $0\% \leq \text{drift} \leq 4.0\%$, and this is defined as phase I as shown in Figures 4.124 and 4.125. It should be noted that for the moment to remain constant and lateral force to decrease, the moment arm of the column has to increase. Between the interval $3.0\% \leq \text{drift} \leq 4.0$ the column shape transformed from double curvature to single curvature to conform to these changes. Thus, for drift ratios between $4.0\% \leq \text{drift} \leq 6.8\%$ the East and West column deflected shape was in single curvature. All the rotation occurred at the plastic hinge pivot region at the bottom of the columns approximately 700mm above the grade beam elevation; this is defined as phase II and is shown in Figures 4.126 and 4.127. Beyond a 6.0% drift ratio, the lap splice bars began to debond and the fixity at the East, Middle, and West grade beam joint began to decrease; this deformed shape is defined as phase III and is shown in Figures 4.128 and 4.129.

From onsite observations, for displacement drifts between 4% and 6%, the tops of the two exterior columns pivot at the column-cap beam interface and start rigid-body rotation; at the bottom, the two exterior columns rotate approximately 700mm above the top of the grade beam where the plastic hinge develops. The Middle interior column forms two well defined plastic hinges approximately 1000mm below the cap beam soffit at the column top and 650mm above the grade beam at the bottom of the column, as shown in Figures 4.126 and 4.127. The connectivity of the exterior column end connections for drifts between $4.0\% \leq \text{drifts} \leq 6.0\%$ would be considered plastic hinged at the bottom and hinged at the top; for the interior column, the connectivity would be plastic hinge at both the top and bottom.

When the bent structure was displaced at a drift ratio between 6.0% and the ending test drift ratio of 6.8%, the bottom column-grade beam joint fixity became semi-fixed and it was observed that there was some bar slippage in the lap splice regions. The fundamental failure patterns observed and performance levels during the May 6-9, 2000, Bent #6S test are presented in a final matrix. The matrix correlates all six of the individual joints and focuses on critical failure modes observed during the test. As the structure was displaced, the joints of the structure degraded; the structural degradation transition is represented using three different structures defined as Phase I, II, and III, in the interval between $0\% \leq \text{drift} \leq 6.8\%$. Phase I is defined between $0\% \leq \text{drift} \leq 4.0\%$ in which all three columns were in double curvature; both ends of all the columns are fixed-fixed connections. Phase II is defined between $4.0\% \leq \text{drift} \leq 6.0\%$ during which the exterior column U-straps fracture and the longitudinal reinforcement in the exterior column-cap beam joints starts to pullout. The Middle joint U-straps and longitudinal reinforcement steel remained intact, but full plastic hinge pivot points developed in the top and bottom portions of the column. Also, plastic pivot points formed at the base of the East, Middle, and West columns just above the bottom 14 CFRP composite confinement layers. It should be noted that the plastic hinge pivot point was located

above the lap splice regions in all three columns. The joint connection for the East and West exterior joints would be considered plastic hinged at the bottom and hinged at the top of the columns. The Middle column (interior) top and bottom regions formed plastic hinge pivot points and plastic hinge-plastic hinge connections. Phase III, is defined between $6.0\% \leq \text{drift} \leq 6.8\%$, in which the lap splice bars pulled out and the bottom connections lateral stiffness was further decreased. A description of the fundamental damage sustained during the Bent #6 2000 test is shown in Table 4.18. A performance or pushover curve of lateral load versus drift ratio shows the three performance levels, or transition stages (phases) in Figure 4.123. Also, a drawing and a photo for the three transition stages Phases I, II, and III, are shown in Figures 4.124-4.129.

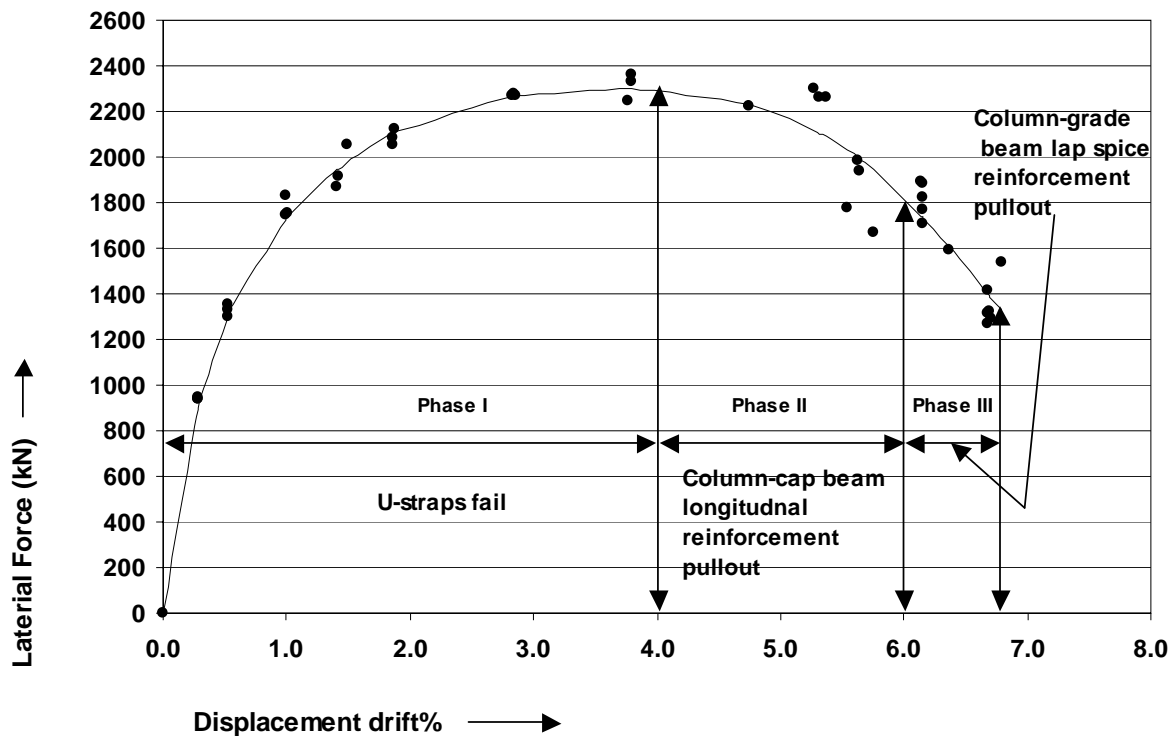


Figure 4.123 Performance levels (Phases) for Bent #6S 2000 test

Table 4.18 Overall Bent #6S 2000 test damage assessment

	Phase I 0 ≤ time ≤ 17,000 0% ≤ drift ≤ 4.0% Figures 4.124, 4.125	Phase II 17,000 ≤ time ≤ 31,400 4.0% ≤ drift ≤ 6.0% Figures 4.126, and 4.127	Phase III 31,400 ≤ time ≤ 42,900 6.0% ≤ drift ≤ 6.8% Figures 4.128, 4.129
Longitudinal reinforcement steel yielding and concrete crushing	1) All longitudinal reinforcement and concrete crushing occurred between 0.5% ≤ drift ≤ 2.8% 2) A total of 43 bar yields 3) A total of 7 concrete crushing points located in the grade beam and foundation system. See Table 4.11	NA	NA
Exterior top column U-strap fracture-failure	1) East column U-strap fracture at 3.73% drift 2) West column U-strap fracture at 4.0% drift. See Figures 4.85, 4.88(c), and 4.102	NA	NA
Middle top column plastic hinge development	At drift 4.0% a plastic hinge fully developed at the top portion of the Middle column. The pivot of the hinge developed below the top 6 layers located at 1.1m below the cap beam soffit. See Figures 4.90, 4.95, and 4.100(a)	Additional development added to phase I	Additional development added to phase II
East, Middle, and Column bottom column plastic hinge development	The bottom 14 layers confining the lap splice and grade beam transfer the plastic hinge pivot location for the East, Middle, and West base columns approximately 720mm above the new retrofitted grade beam elevation. All three base column plastic hinges begin at the beginning yielding drift of 0.5% drift. See Figures 4.115(b), 4.120(b), and 4.122(b)	Additional plastic hinge development to phase I	Additional plastic hinge development to phase II
Exterior column in the beam cap joint longitudinal reinforcement steel pull-out	NA	Longitudinal reinforcement steel pullout between 5.0% ≤ drift ≤ 6.8%. See Figures 4.89(c) and 4.107	NA
Bottom column lap splice reinforcement steel pullout	NA	NA	Longitudinal reinforcement steel pullout in the lap splice region at the East, Middle, and West column base. See Figures 4.115(c), 4.120(c), and 4.122(f)

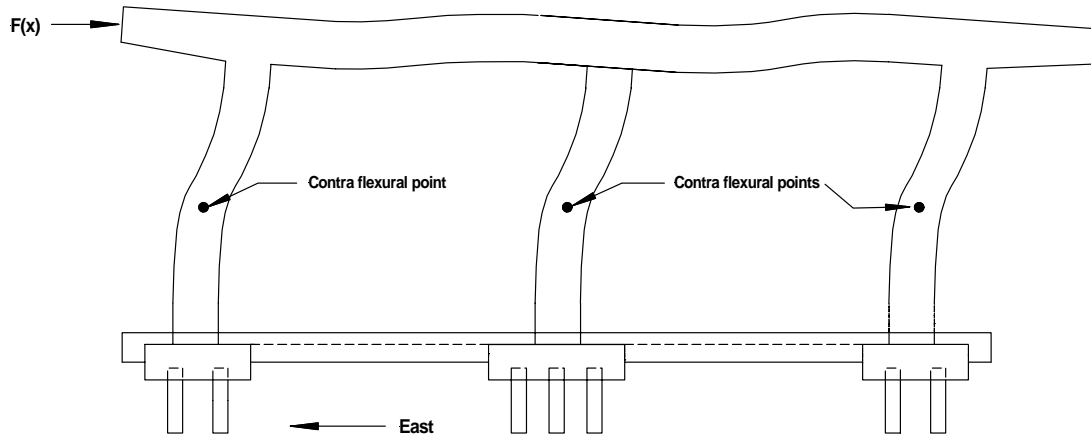


Figure 4.124 Phase I Bent #6S 2000 deflected shape between $0\% \leq \text{drift} \leq 4.0\%$



Figure 4.125 Onsite Phase I Bent #6S 2000 deflected shape between up to 4.0% drift ratio

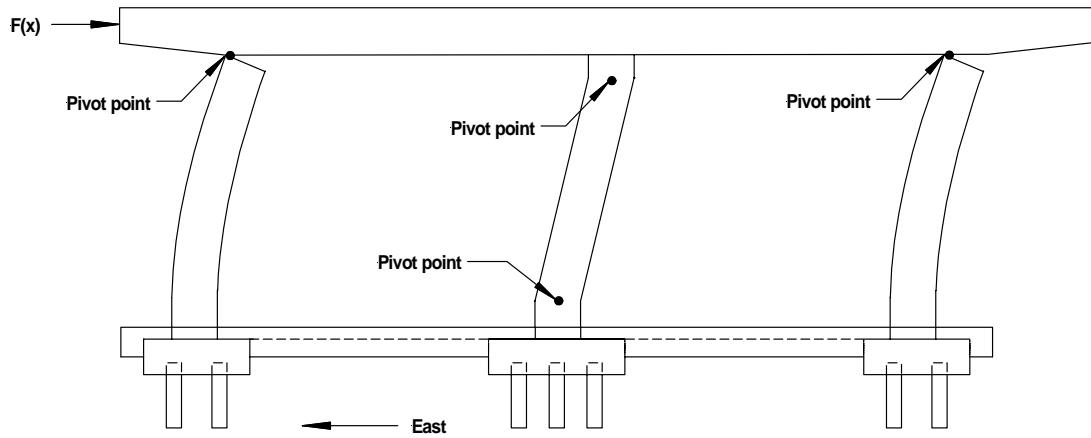


Figure 4.126 Phase II Bent #6S 2000 deflected shape between $4.0\% \leq \text{drift} \leq 6.0\%$



Figure 4.127 Onsite Phase II Bent #6S 2000 deflected shape up to 6.0% drift ratio

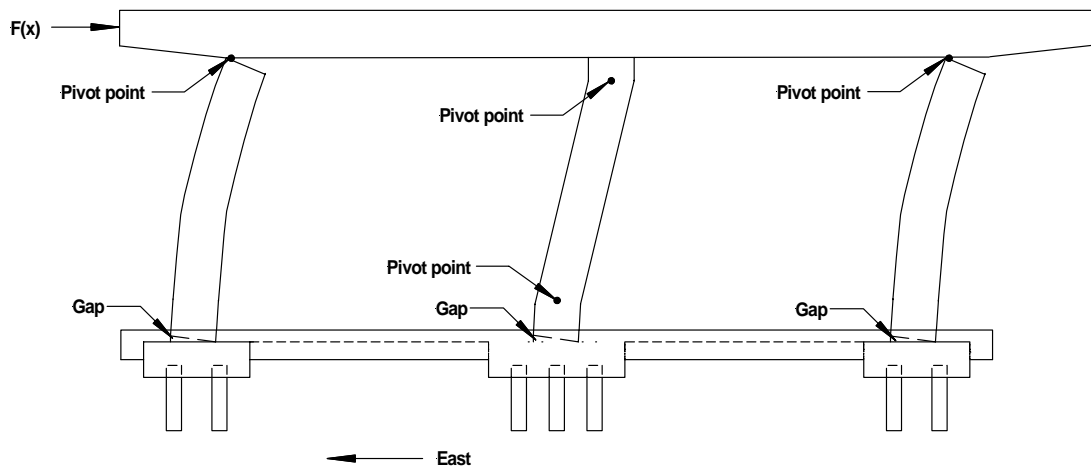


Figure 4.128 Phase III Bent #6S 2000 deflected shape between $6.0\% \leq \text{drift} \leq 6.8\%$



Figure 4.129 Onsite Phase III Bent #6S 2000 deflected shape at 6.8% drift ratio

5. CONCLUSIONS

Three bents (Bents #4S, #5S, and #6S) of the South Temple Bridge on Interstate 15 in Salt Lake City, Utah, were tested in 2000 on the Southbound lanes. The purpose of the cyclic tests was to evaluate the capacity of existing bridges for simulated seismic loads in the as-is condition, as well as in the retrofitted condition both with conventional as well as advanced composite materials.

The conclusions are described in more detail in what follows for all three bents tested; in addition, comparisons are made between the three tests and those carried out in an earlier study involving three tests of bridge bents on the Northbound lanes of the South Temple Bridge (Pantelides et al. 2000).

Bent #4S (2000)

Bent #4S was different from Bents #5S and #6S, in that before the test was performed the deck was removed and thus it had only 16.1% of the in-service dead load, whereas Bent #5S and #6S had a dead load equal to 58.0% of the in-service dead load. From the results of the test outlined in Chapter 2, it can be concluded that systematic degradation of Bent #4S occurred in three phases. In Phase I, the initial system yielding allowed for further displacement with increasing lateral loading. This was accompanied by two mechanisms: (1) many local reinforcing bars yielded at the top and bottom of the columns, and (2) cracking of the concrete in the six zones begun producing stiffness degradation.

In Phase II the third mechanism of longitudinal column bar pullout from the bent cap joints further weakened the structural system. As bars pulled out, the structural system lost continuity, and forces and moments that the system should collectively resist were transferred to other components within the system. These components were then overstressed and begun failing more quickly as evidenced by bar buckling in the top of the Center column. This bar pullout occurred in the interval from 1.0% to 2.0% drift ratio. However, although the pullout had a large effect on the structure, the structural system was still experiencing localized yielding, and the effects of concrete cracking and crushing.

Phase III started to materialize after the 2.0% drift cycles. At increasingly larger displacements, the rotations in the base joints became larger, and the prying forces on the reinforcement spread the lap splices apart. Because of this lap splice slip mechanism beginning at 2.0% drift, a steady degradation in the strength of the structure was seen; each cycle produced a little more slip and therein the strength had a steady linear drop off up to the end of the test at a 5% drift ratio; the displacement ductility of Bent #4S was bbb. The curvature ductility for the base of the columns was higher than that for the top of the columns by a factor ranging from 1.6 to 1.8 times; this demonstrates the beneficial effect of the grade beam seismic retrofit. Bent #4S absorbed the least amount of energy of all three bents at 1,827 kN-m; Bent #4S dissipated 3,566 kN-m or 1.95 times that of Bent #4S, and Bent #6S dissipated 12,984 kN-m or 7.1 times that of Bent #4S.

Bent #5S (2000)

A reinforced concrete grade beam seismic retrofit was built around the existing foundation system of Bent #5S (2000) to enhance the performance of a bridge bent under simulated seismic loads. The maximum drift ratio reached at the bent cap level was 3.8% in the pull direction and 2.7% in the push direction. Approximately 11% of the total displacement of the bridge system was due to the movement of the grade beam, foundation, piles and pile caps. The displacement ductility of the bent, including the bent cap and foundation flexibilities, the latter being the dominant effect, was 3.7.

The elastic stiffness of the superstructure was reduced to 13% of the initial elastic stiffness at the maximum drift ratio. Plastic hinge length estimates from relationships in the literature slightly underestimated the experimentally obtained plastic hinge length by 7% to 16%. The lap splices at the bottom of the columns began slipping at a steel reinforcement strain of 1.4 mm/m and a drift ratio of 2.0%. The anchorage of the longitudinal reinforcement at the top of the columns into the bent cap started degrading at a strain of 1.2 mm/m and a drift ratio of 2.0%. The principal tensile stress in the bent cap-column joint was $0.55\sqrt{f'_c}$ (MPa), and that in the pile cap-column joint was $0.68\sqrt{f'_c}$ (MPa), both of which occurred at a drift ratio of 2.0% and exceeded $0.29\sqrt{f'_c}$ (MPa), indicating joint degradation.

A performance-based evaluation according to the PEER criteria for Bent #5S (2000) produced the following five levels of performance: (1) cracking at 0.25% drift ratio, (2) yielding at 0.5% drift ratio, (3) initiation of local mechanism at 1.5% drift ratio, (4) full development of local mechanism at 2.0% drift ratio, and (5) strength degradation at 3.8% drift ratio. The column axial load, which ranged from $3.3\% f'_c A_g$ to $3.8\% f'_c A_g$ had a beneficial effect on the lateral load capacity of the bent. Comparison with the test of Bent #4S (2000) with identical details but without the deck showed that Bent #5S (2000) resisted a lateral load 1.24 times that of Bent #4S (2000). The hysteretic energy dissipated by Bent #5S (2000) was 1.95 times that of Bent #4S (2000).

The effect of the grade beam retrofit was evaluated by comparing the present test with a test of an otherwise identical bent (Bent #5N), which was tested in 1998, but did not have a grade beam retrofit. The lateral load resisted by Bent #5S (2000) was 1.4 times that of Bent #5N (1998), and the hysteretic energy dissipation was 1.98 times that of the Bent #5N (1998). These results were confirmed by comparing energy-based damage indices found in the literature. The grade beam retrofit provided higher base fixity, which in turn generated more redundancy and ductility for the foundation-superstructure system. The grade beam retrofit was successful in improving the seismic performance of a bent with substandard reinforcement details and should be considered in the seismic retrofit design of similar bridges.

Bent #6S (2000)

By comparing the lateral displacement performance of the Bent #6S (2000) retrofitted vs. the retrofitted Bent #6N (1998) and the as-built Bent #5S (2000) bridge structures, the Bent #6S (2000) lateral performance level was improved significantly. A moment distribution analysis of the road deck and parapet curb walls was conducted to increase the accuracy of

the loading distribution used for modeling purposes for the Bent #6S (2000) design. There was an overall 20% gravity load increase added to the Bent #6S (2000) model because of additional layers of asphalt applied to the road deck over forty years of service that were not included in the Bent #6N (1998) and Bent #5S (2000) analysis.

Significant progress was made by changing the 1998 foundation detail to the new grade beam design used in the 2000 test. Three natural design characteristics in the grade beam design significantly enhanced the overall performance of the 2000 bent structures. First, by changing the elevation of the grade beam 305mm above the existing pile cap elevation, using a R/C overlay, the reinforcement steel at the base shear location was doubled by elevating the column-cap beam joint 305mm, and thus defining a new base shear location where the new base steel reinforcement was in the midsection of the lap spliced bars located at the base of the columns. Second, the new grade-beam elevation increased the stiffness of the column-grade beam joint in the lap splice region. The elevated grade beam combined with the bottom 14 layers of CFRP composite was responsible for transferring the plastic hinge pivot location above the lap splice. Last, because of the increased fixity at the column-cap beam joint, the base moment demands were transferred more efficiently into the composite pile sub grade system. This is evidenced by the curvature ductility for the base of the columns, which was higher than that for the top of the columns by a factor that ranged from 3.4 to 5.7 times. This shows the great contribution of the CFRP composite in confinement, strengthening, and energy absorption of the columns, thus postponing any impending failure due to a large earthquake.

The Bent #6S (2000) test was modeled for computer analysis using non-linear models; it represents well both the substructure and superstructure of the bridge bent. Substructure elements and nodes were included and modeled the soil stiffness values against the deep foundation system. A pushover analysis evaluation was conducted on the substructure and foundation system vs. the onsite test data and was found to be very representative of the actual test. Because computer analysis was used so extensively as the major design aid to solve for the shears, moments, stresses, and strains for the Bent #6S (2000) analysis, it was necessary to use simple basic solution methods to check the reliability of the pushover analysis against the actual test.

Different CFRP composite lay-up applications were used for the Bent #6 1998 and 2000 tests. In 1998, a dry lay-up application was used and a wet lay-up application was used for the 2000 tests. After onsite damage assessments of the 1998 and 2000 tests, dry fibers were found in the 1998 lay-up but no dry fibers found in the 2000 test. With the wet lay-up application, the saturation of the material is more controlled and fibers are completely saturated with resin. It is therefore recommended to use the wet lay-up technique whenever possible.

The initial stiffness was slightly increased from 33.8kN/mm to 34.0kN/mm comparing the Bent #5S (2000) (no CFRP composite) and Bent #6S (2000) structures with the same grade beam system. The additional stiffness gain is small but can be related entirely to the composite portion of the retrofit. Comparing the maximum lateral capacity, Bent #6S (2000) had a capacity of 2,151 kN, whereas Bent #5S (2000) had a capacity of 1,960 kN; therefore there was a 10% increase from the as-built bent to the CFRP-composite retrofitted bent.

Different enhancements were made between the Bent #6N (1998) and Bent #6S (2000) CFRP composite retrofitted structures. Comparing the displacement ductility between Bent #6S (2000), Bent #5S (2000) and Bent #6N (1998), the displacement ductilities were 5.76,

3.50, and 4.64, respectively. The displacement ductility difference between the Bent #5S (2000) (no CFRP composite) and Bent #6S (2000), an increase of 65%, is reflective of the CFRP composite retrofit applied to the Bent #6 2000 structure. The displacement ductility increase of 24% from Bent #6N (1998) to Bent #6S (2000) (both retrofitted with CFRP composites) is reflective of two different foundation systems and an improved CFRP design. Bent #6S (2000) had four zero layers applied to the East column-cap beam joint, two zero layers to the Middle column-cap beam joint, and no zero layers applied to the West column-cap beam joint.

At the peak lateral load corresponding to a drift ratio of 3.73%, a flexural tension crack formed in the west region of the cap beam adjacent to the West column joint. Through analytical simulation it was found that four zero layers applied to the West joint region would have prevented the tension crack in the cap beam from happening. The hoop strains in the CFRP composite retrofitted columns were found to be relatively small, and the largest tensile and corner compression strain for the confinement layers were 73% and 45% of the tensile and compressive failure strains, respectively.

Observations made of the FEMA 273 curve fitting technique for force/displacement relationships show the FEMA 273 backbone to be too conservative and erratic. Also, the FEMA 273 curves are not well behaved for unsymmetrical data, such as actual seismic induced displacements and the data for the Bent #6S test. Three energy indices were used to assess the Normalized energy, Work index, and Damage index for Bents #5S and #6S (2000) and Bent #6N (1998). The Bent #6S (2000) test shows the highest values for all three indices; these results are reasonable with respect to the larger peak lateral load and displacement imposed on the Bent #6S (2000) test.

From the damage assessment of the test of Bent #6S, it was determined that the two-bay structural frame of the three-column bent transitioned into three unique frames corresponding to three performance phases over the total degradation process. Phase I is for a drift ratio from 0% up to 4%, at which point the CFRP composite U-straps fracture at the beam cap-column joint of the east and west columns. During Phase I, the column deflected shape remained in double curvature for all three columns. After a drift ratio of 4.0%, which initiated Phase II, the exterior column end connections became plastic hinges at the bottom and hinges at the top; for the interior column a plastic hinge developed at both the top and bottom. At approximately 6.0% drift ratio, the column-cap beam longitudinal reinforcement started to pull out; further degradation occurred in the lap splices at the bottom of the columns up to a drift ratio of 6.8%; the range from 6.0% to 6.8% drift ratio defines Phase III. In Phase III, the fixity at the East, Middle, and West column-grade beam joint began to decrease and the bent behaved like a mechanism.

Closure

The research carried out during this project and presented in this report has contributed to a greater understanding of the design, material properties, strength, and ductility of existing interstate reinforced concrete bridges that have been in service for 35 years or more and have similar specifications to the South Temple Bridge. The project has also uncovered the performance of the grade beam reinforced concrete overlay as a good seismic retrofit technique. The enhancements and improved performance of a bridge bent with the grade beam retrofit were shown in the testing of all three bents. The very beneficial seismic retrofit of the superstructure with carbon fiber reinforced polymer composites, in addition to the

grade beam, was demonstrated from the results of testing Bent #6S. The authors are of the opinion that such seismic retrofits utilizing conventional and advanced composite materials can greatly benefit the existing infrastructure.

6. REFERENCES

- Alkhardji, T. (2001). "Destructive testing of a highway bridge strengthened with FRP systems." Ph.D. Dissertation, Dept. of Civil Eng., University of Missouri – Rolla, Rolla, Missouri.
- American Association of State Highway and Transportation Officials, Inc., (AASHTO). (1998). "Standard Specifications for Highway Bridges." *SI Units*, 2nd Edition, Washington, DC.
- American Concrete Institute, (ACI). (1999). "Building Code Requirements for Structural Concrete and Commentary." ACI 318-99, Farmington Hills, Michigan.
- American Society for Testing Materials (ASTM). (1999). "ASTM C 42, Standard Test Method for Obtaining and Testing Drilled Cores and Sawed Beams of Concrete." West Conshohocken, PA.
- Building Seismic Safety Council (1997). "NEHRP Guidelines for the Seismic Rehabilitation of Buildings." FEMA Publication 273, Washington, DC.
- Cook, C. R., Lawton, E. C., and Pantelides, C. P. (2002). "Soil-structure interaction of bridge bents subjected to lateral loads." *7th Nat. Conf. Earthq. Engrg., Proceedings*, Boston, MA, 21-25 July 2002, Paper 00405.
- Darwish, I.S., Saiidi, M.S., and Sanders, D.H. (1999). "Seismic retrofit of hinged and fixed reinforced concrete bridge columns with short bar anchorage in footings." *ACI Struct. J.*, 96(6), 988-996.
- Duffin, J. B. (2003). "Design of CFRP jackets for seismic strengthening of existing bridges and experimental verification." M.Sc. Thesis, Dept. of Civil and Env. Eng., University of Utah, Salt Lake City, Utah.
- Eberhard, M. O., and Marsh, M. L. (1997). "Lateral-load response of a reinforced concrete bridge." *J. Struct. Eng.*, 123(4), 451-460.
- Ehsani, M. R., and Wight, J. K. (1990). "Confinement steel requirements for connections in ductile frames." *J. Struct. Eng.*, 116(3), 751-767.
- Gamble, W.L., and Hawkins, N.M. (1996). "Seismic retrofitting of bridge pier columns." *Proc. Struct. Congress XIV*, ASCE, Reston, VA, Vol. 1, 16-23.
- Gergely, I., Pantelides, C.P., Nuismer, R.J., and Reaveley, L.D. (1998). "Bridge pier retrofit using fiber-reinforced plastic composites." *J. of Composites for Construction*, 2(4), 165-174.

Gergely, J., Pantelides, C.P., and Reaveley, L.D. (2000). "Shear strengthening of RCT-joints using CFRP composites." *J. of Composites for Construction*, 4(2), 56-64.

Gosain, K. N., Brown, H. R., and Jirsa, J. O. (1977). "Shear requirements for load reversals on RC members." *J. Struct. Div.*, ASCE, 103(7), 1461-1476.

Griezic, A., Cook, W.D., and Mitchell, D. (1999). "Seismic retrofit of existing bridge columns with hinges." ACI Special Publication, SP187, 205-234, Farmington Hills, Michigan.

Hognestaed, E., Hanson, N., and McHenry, D. (1955). "Concrete stress distribution in ultimate strength design." *ACI Journal*, 52(6), 455-479.

Hose, Y. D., Silva, P. F., and Seible, F. (2000). "Development of a performance evaluation database for concrete bridge components and systems under simulated seismic loads." *Earthq. Spectra*, 16(2), 413-442.

Iihoshi, C., Fukuyama, H., Matsumoto, Y., and Abe, S. (1999). "Strengthening effect of reinforced concrete elements with polyacetal fiber sheets." American Concrete Institute, Report SP-188-58, 659-669, FRPRCS-4, Farmington Hills, Michigan.

Katsumata, H. et al. (1988). "A study with carbon fiber for earthquake-resistant capacity of existing reinforced concrete column." *Proceedings, 9th Conference on Earthquake Engineering*, Tokyo, Japan, Vol. 7, 517-522.

Katsumata, H., Kimura, K., and Murahashi, H. (2001). "Experience of FRP strengthening for Japanese historical structures." *Proc. Intern. Conf. FRP Composites in Civil Eng.*, Elsevier Science, New York, V. 2, 1001-1008.

Lam, L., and Teng, J.G. (2002). "Strength models for Fiber-Reinforced Plastic-confined concrete." *J. Structural Engineering*, 128(5), 612-623.

Lau, K.-T., and Zhou, L.-M. (2001). "The mechanical behavior of composite-wrapped concrete cylinders subjected to uniaxial compression load." *Composite Structures*, 52(2) 189-198.

Légeron, F., and Paultre, P., (2000). "Behavior of high-strength concrete columns under cyclic flexure and constant axial load." *ACI Struct. J.*, 97 (4), 591-601.

Lowes, L.N., and Moehle, J.P. (1999). "Evaluation and retrofit of beam-column T-joints in older reinforced concrete bridge structures." *ACI Struct. J.*, 96(4), 519-532.

Machida, A. (1997). "Seismic retrofitting of reinforced concrete structures. Present status and issues." *Semento Konkurito (Cement and Concrete)*, Japan, 606(10), 16-21.

- Masuo, K., Morita, S., Jinno, Y., and Watanabe, H. (2001). "Advanced wrapping system with CF-anchor – seismic strengthening of RC columns with wing walls." *Proc. FRPRCS-5*, Thomas Telford, London, U.K., Vol . 1, 299- 308.
- McLean, D. I., and Marsh, M. L. (1999). "Seismic retrofitting of bridge foundations." *ACI Struct. J.*, 96(2), 174-182.
- Mirmiran , A., Shahawy, M., Samaan, M., Hazem E., Mastrapa, J.C., and Pico, O. (1998). "Effect of column parameters on FRP-confined concrete." *J. of Composites for Construction*, 2(4), 175-185.
- Monti, G., Nistico, N., and Santini, S. (2001). "Design of FRP jackets for upgrade of circular bridge piers." *J. of Composites for Construction*, 5(2), 94-101.
- Moran, D.A., and Pantelides, C.P. (2002). "Stress-strain model for fiber-reinforced polymer-confined concrete." *J. Compos. Constr.*, 6(4), 233-240.
- Mutsuyoshi, H., Ishibashi, T., Okano, M., and Katsuki, F. (1999). "New design method for seismic retrofit of bridge columns with continuous fiber sheet- performance-based design." American Concrete Institute, Report SP-188-21, 229-241, FRPRCS-4, Farmington Hills, Michigan.
- Panagiotakos, T. B., and Fardis, M. N. (2001). "Deformations of reinforced concrete members at yielding and ultimate." *ACI Struct. J.*, 98(2), 135-148.
- Pantelides, C.P., Gergely, J., Reaveley, L.D., and Volnyy, V.A. (1999). "Retrofit of RC bridge pier with CFRP advanced composites." *J. Structural Engineering*, 125(10), 1094-1099.
- Pantelides, C.P., Gergely, J., Marriottt, N., and Reaveley, L.D. (2000). "Seismic rehabilitation of concrete bridges: Verification using in-situ tests at South Temple Bridge on Interstate 15." *Res. Report*, UUCVEEN 00/1, Dept. of Civil and Envir. Eng., University of Utah, Salt Lake City, Utah.
- Pantelides, C.P., Gergely, J., and Reaveley, L.D. (2001). "In-situ verification of rehabilitation and repair of reinforced concrete bridge bents under simulated seismic loads." *Earthquake Spectra*, 17(3), 507-530.
- Pantelides, C.P., and Gergely, J. (2002). "Carbon-fiber-reinforced polymer seismic retrofit of RC bridge bent: Design and in situ validation." *J. of Composites for Construction*, 6(1), 52-60.
- Pantelides, C. P., Duffin, J. B., Ward, J., Delahunty, C., and Reaveley, L. D. (2002). "In-situ tests at South Temple Bridge on Interstate 15." *7th Nat. Conf. Earthq. Engrg., Proceedings*, Boston, MA, 21-25 July 2002, Paper 00209.

Park, R., Rodriguez, M., and Dekker, D.R. (1993). "Assessment and retrofit of a reinforced concrete bridge pier for seismic resistance." *Earthquake Spectra*, 9(4), 781-801.

Prakash, V., Powell, G. H., and Campbell, S. (1993). "*DRAIN-2DX base program description and user guide: version 1.10.*" Report No. UCB/SEMM-93/17, University of California at Berkeley, Berkeley, California.

Priestley, M.J.N., Seible, F., and Anderson, D.L. (1993). "Proof test of a retrofit concept for the San Francisco double-deck viaducts, Part 1: design concept, details, and model." *ACI Struct. J.*, 90(5), 467-479.

Priestley, M.J.N., Seible, F., and Calvi, G.M. (1996). *Seismic Design and Retrofit of Bridges*. John Wiley & Sons, Inc., New York, New York.

Saadatmanesh, H., Ehsani, M.R., and Limin, J. (1996). "Seismic strengthening of circular bridge pier models with fiber composites." *ACI Struct. J.*, 93(6), 639-647.

Saadatmanesh, H., Ehsani, M. R., and Limin, J. (1997a). "Repair of earthquake-damaged RC columns with FRP wraps." *ACI Struct. J.*, 94(2), 206-215.

Saadatmanesh, H., Ehsani, M.R., and Jin, L. (1997b). "Seismic retrofitting of rectangular bridge columns with composite straps." *Earthquake Spectra*, 13(2), 281-304.

Saatcioglu, M., and Grira, M. (2001). "Seismic performance and design of concrete columns confined with CFRP grids." *Proc. Intern. Conf. FRP Composites in Civil Eng.*, Elsevier Science, New York, V. 2, 1227-1234.

Seible, F., Priestley, M.J.N., Hegemier, G.A., and Innamorato, D. (1997). "Seismic retrofit of RC columns with continuous carbon fiber jackets." *J. of Composites for Construction*, 1(2), 52-62.

Seible, F., and Priestley, M.J.N. (1999). "Lessons learned from bridge performance during the Northridge earthquake." ACI International, Report SP-187-3, 29-55, *Seismic Response of Concrete Bridges*, ed. K. Krishnan, Farmington Hills, Michigan.

Seible, F., Innamorato, D., Baumgartner, J., Karbhari, V., and Sheng, L.H. (1999). "Seismic retrofit of flexural bridge spandrel columns using fiber reinforced polymer composite jackets." American Concrete Institute, Report SP-188-78, 919-931, FRPRCS-4, Farmington Hills, Michigan.

Seible, F. (2001). "Seismic retrofit of RC columns with continuous carbon fiber jackets." *Proc. Intern. Conf. FRP Composites in Civil Eng.*, Elsevier Science, New York, V. 1, 817-824.

Sheikh, S. A. (2001). "Use of FRP composites for seismic upgrade of concrete columns." *Proc. Intern. Conf. FRP Composites in Civil Eng.*, Elsevier Science, New York, V. 1, 901-908.

Spoelstra, M. R., and Monti, G. (1999). "FRP-confined concrete model." *J. of Composites for Construction*, 3(3), 143-150.

Sritharan, S., Priestley, M.J.N., and Seible, F. (1999). "Enhancing seismic performance of bridge cap beam-to-column joints using prestressing." *PCI J.*, 44(4), 74-91.

Ward, J. (2001). "Assesment of in-situ lateral load test of a reinforced concrete bridge bent." M.Sc. Thesis, Dept. of Civil and Env. Eng., University of Utah, Salt Lake City, Utah.

Xiao, Y., Priestley, M. J. N., and Seible, F. (1996). "Seismic assessment and retrofit of bridge column footings." *ACI Struct. J.*, 93(1), 79-94.